Department of Applied Geology

Timing and Kinematics of Mesozoic-Cenozoic Mountain Building and Lithospheric Thinning in the Eastern North China: Constraints from Geochronology and Thermochronology

Liping Liu

This thesis is presented for the Degree of
Doctor of Philosophy
Of
Curtin University

October 2014

DECLARATION

To the best of my knowledge and belief this thesis contains no material previously published by any other person except where due acknowledge has been made. This thesis contains no material which has been accepted for the award of any other degree or diploma in any university.

Liping Liu

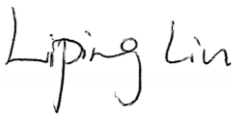

Date: 17/10/2014

ABSTRACT

The Dabie-Sulu orogenic belt in central eastern China is best known for the widespread occurrence of ultrahigh-pressure (UHP) metamorphic rocks, a protolith of which was subducted to >100 km depths beneath the North China block, overprinted by UHP metamorphism, and finally exhumed to the surface. The Sulu UHP belt is offset from the Dabie UHP metamorphic belt by approximately 500 km of left-lateral strike-slip displacement along the Tan-Lu fault. It remains controversial as to what role the Tan-Lu fault played during collision-exhumation along the Dabie-Sulu orogenic belt. Current models in the literature include the transform fault model, lithospheric indentation model, crustal detachment model and rotational collision model. The thermal history of the Sulu UHP belt, and surrounding regions such as the Jiaobei region in the north and the Luxi region in the west, may thus provide valuable insights into the collision process. In addition, eastern North China is also one of the best studied regions for lithospheric thinning, which is commonly believed to have occurred since the Mesozoic. This event should also have been recorded in the regional thermal history. This study utilizes zircon U-Pb geochronology and multiple thermochronometry methods including mica and hornblende $^{40}Ar/^{39}Ar$, zircon and apatite fission-track, and zircon and apatite (U-Th)/He dating to more fully constrain the thermal evolution of the region, thus shedding new light on the collision process between the North China and the South China blocks, as well as on the lithospheric thinning process.

$^{40}Ar/^{39}Ar$ and zircon (U-Th)/He data show that the Sulu UHP terrane experienced a prominent cooling event at ca. 210–160 Ma. This event is interpreted as representing an erosional response to northward thrust-driven uplift of the UHP rocks and can be best explained by the crustal detachment model. A subsequent episode of exhumation took place between ca. 125 Ma and 90 Ma as recorded by zircon (U-Th)/He data. This event was more pronounced in the northern section of the UHP terrane, whereas in the southern section, the zircon (U-Th)/He system retained Jurassic cooling ages of ca. 180–160 Ma. The mid-Cretaceous episode of exhumation is interpreted to have resulted from the removal of a thickened enriched mantle lithosphere, and crustal extension. A younger episode of exhumation was recorded by apatite fission-track and (U-Th)/He ages at ca. 65–40 Ma. Both the 125–

90 Ma event and the 65–40 Ma event are interpreted to represent episodic thinning of the lithosphere along the Sulu orogenic belt in an extensional environment, likely linked to the roll-back of the Western Pacific subduction system

Thermochronologic and geochronologic analyses performed in the Jiaobei region, provide additional constraints on the timing of deformation and exhumation pertaining to the Mesozoic collision between the South and North China blocks. Three distinct episodes of deformation (D_1, D_2 and D_3) were previously found in the Jiaobei region. D_1 features penetrative foliations and mineral stretching lineations in Precambrian metamorphic basement and is constrained to have taken place at ca. 1974–1834 Ma as recorded by muscovite and hornblende $^{40}Ar/^{39}Ar$ data. D_2 is marked by cleavages transposing the primary bedding in the Neoproterozoic-upper Paleozoic Penglai Group, and by WNW trending, NE-verging folds in the Precambrian basement. Exhumation at ~260 Ma could be related to D_2 deformation and represent the tectonic exhumation of the overriding plate resulting from initial continental collision. D_3 deformation is characterized by NNE-trending inclined folds subparallel to the dominant strike of foliations in the Sulu orogenic belt. Zircon (U-Th)/He data indicate westward-advancing exhumation from 196 ± 9 Ma to 164 ± 7 Ma, which is partly concomitant with exhumation of the ultrahigh-pressure rocks in the Sulu orogenic belt. The latter two directions of structural orientation and associated exhumation can be best explained by a crustal detachment model. In addition, mica $^{40}Ar/^{39}Ar$, zircon fission-track and (U-Th)/He data from Upper Jurassic-Lower Cretaceous granitoids reveal exhumation episodes in an extensional context at ~130–90 Ma and at ~65–40 Ma, again testifying to episodic lithospheric thinning.

Fission-track and (U-Th)/He results on zircon and apatite reveal multiple tectonic events in the Luxi region during the Phanerozoic. Zircon fission-track ages of 442–309 Ma and the large dispersion of zircon (U-Th)/He ages (738–484 Ma), along with the absence of the Upper Ordovician–Lower Carboniferous strata, suggest that this region underwent slow denudation from the Late Ordovician to early Carboniferous. Triassic to Late Jurassic crustal shortening in the region did not fully exhume the Archean rocks to depths of ca. 8 km, indicating that crustal exhumation during the SCB-NCB collision was not as severe here as in the region east of the Tan-Lu fault. During the Early Cretaceous, extension-related denudation exhumed the Archean rocks above ca. 8 km and yielded uniform single-grain ZHe ages.

Apatite fission-track and (U-Th)/He ages of 60–40 Ma reveal an episode of rapid exhumation during early Cenozoic. The latter two episodes of exhumation, synchronous throughout the entire study region, reflect episodic lithospheric thinning in eastern North China.

Widespread late Mesozoic granitoids in the Jiaobei region are potential records of crustal thickening associated with the North China-South China collision and/or subsequent lithospheric thinning in the North China block. To unravel the petrogenesis of two major episodes of granitoid formation, *in-situ* zircon U-Pb-Hf isotopic and whole-rock geochemical analyses were carried out on the Linglong-Luanjiahe granites and the Guojialing granodiorites, and on mafic microgranular enclaves (MMEs). LA-ICP-MS zircon U-Pb dating revealed that the Linglong granites and mafic enclaves crystallized in the Late Jurassic (157–148 Ma). They show high concentrations of Ba (1505–2809 ppm) and Sr (530–1544 ppm), low Y contents (< 20 ppm), high LREE contents with variable LREE/HREE ratios, and negative HFSE anomalies. Strongly negative zircon εHf(t) values (−27 to −18) indicate that the Linglong granites were sourced from an Archean lower continental crust. The Linglong granites and enclosed MMEs are cogenetic. Fractionation of hornblende and allanite mainly controlled the REE pattern. All these geochemical and isotopic features, in combination with low magma temperatures (645–780 ℃), suggest that the Linglong granites were unlikely to have formed by dehydration melting of amphibolite with garnet as a residue. High concentrations of Ba and Sr indicate high solubility of plagioclase in water-rich magmas. Therefore, the Linglong granites are interpreted to have been formed by water-fluxed melting of biotite gneiss or the lower continental crust. The Luanjiahe granites, with a zircon U-Pb age of 159 ± 1 Ma, may have been derived from melting of younger sources as revealed by their higher εHf values (−18 to −11). The crustal detachment model can best accommodate the diverse conditions required for generation of the granitoids, such as multiple sources, temperature build up, and external water responsible for the geochemical patterns of the Linglong-Luanjiahe granites. The Guojialing granodiorites were emplaced during 127–124 Ma with contemporaneous mafic igneous rocks. The granodiorites and MMEs also have high LREE/HREE ratios and negative HFSE anomalies. The occurrence of MMEs and less negative εHf(t) values (−23 to −10), relative to the Linglong granites, suggest the involvement of mantle components in the sources. Fractionation of hornblende and titanite probably played

a major role in the depletion of REE contents at high silica contents. Similar εNd(t) values, higher initial $^{87}Sr/^{86}Sr$ ratios and hornblende fractionation trends, relative to contemporaneous mafic rocks, indicate that the Guojialing granodiorites were differentiated from an enriched mantle-derived mafic magma with minor crustal contamination. This magmatic event was likely linked to the thinning of an enriched mantle lithosphere in the Early Cretaceous.

Overall, the pre-160 Ma exhumation history in the Sulu orogenic belt and the Jiaobei region, together with activities in the Tan-Lu fault at 221–181 Ma and at ~160 Ma, can best be explained by the crustal detachment model. The two episodes of exhumation, in the Early Cretaceous and the early Cenozoic, likely reflect two episodes of lithospheric thinning in the eastern North China block. The lithospheric thinning may have been controlled primarily by extension due to roll-back of the subducting Western Pacific oceanic slab.

ACKNOWLEDGEMENTS

This thesis would not have been accomplished without the support and contributions from the following individuals over the past four years. First and foremost, I would like to thank my principal supervisor, Prof. Zheng-Xiang Li, for providing me the opportunity to work on this interesting project. I appreciate the adequate freedom that he offered regarding my research topic. His constructive criticism and inspiring discussions opened my mind and helped me to learn a lot in terms of fieldtrip planning, data presentation and ways of thinking. I am always amazed at the way he thinks about a certain scientific question. The very high standard he sets for research and supervision will continue to influence me. Sincere gratitude must be given to my associate supervisor Dr. Martin Danišík for training me in thermochronology techniques, assistance with acquiring fission track data and for his patience and encouragement when helping me to solve problems. I am also grateful to Prof. Sanzhong Li for supporting the fieldtrips and mineral separation, and for discussing structural interpretations. Thanks to Dr. Kongyang Zhu for his insightful discussion and help with fieldtrip during the granite study.

I thank Associate Professors Fred Jourdan and Noreen Evans for helping with $^{40}Ar/^{39}Ar$, (U-Th)/He data and LA-ICP-MS U-Pb analyses, and discussions about data interpretation. Much appreciation is given to Noreen as well for the highly efficient proofreading. I also thank Drs Allen Kennedy, Daniel Dunkley, Richard Taylor and Mr Hao Gao for providing much support for SHIRMIP zircon U-Pb analysis and instrument setup. I thank Ms Elaine Miller and her SEM team for training and help with CL imaging. Mr Bradley McDonald provided much help during the acquisition of (U-Th)/He and U-Pb data. Ms Celia Mayers taught me how to pick minerals and measure dimensions under microscopes. A/Prof. Norman Pearson provided much support in zircon Hf analysis and Prof. Wuxian Li assisted whole rock geochemistry analysis. Also, thanks to Prof. Peter Kamp for the opportunity to visit and obtain (U-Th)/He data at the University of Waikato, New Zealand.

Thanks to Xin Liu, Pengcheng Wang, Shan Yu and Hongcai Wang for their company in office and during sampling fieldtrips, regardless of hot or bad weathers. I would also express many thanks to members from our Curtin research group, including Xuan-Ce Wang, Chongjin Pang, Wei-Hua Yao, Ni Tao, Yingchao Liu and Hui-Qing Huang. Interaction with them deepened my knowledge in geology, geochronology, geochemistry and thermochronology. I thank Curtin University, China Scholarship Council, the Australian Research Council, and the Institute for Geoscience Research (TIGeR), for offering me a generous PhD scholarship and funding my research.

At last, I would like to thank my parents and brother for their encouragement and support during the entire study. Thanks to Chunguang for being here with me when possible.

TABLE OF CONTENTS

DECLARATION I

ABSTRACT II

ACKNOWLEDGEMENTS VI

TABLE OF CONTENTS VIII

LIST OF FIGURES XIV

LIST OF TABLES XX

CHAPTER 1 INTRODUCTION 1

1.1 Introduction 1

1.2 Objectives 5

1.3 Research methods 5

1.4 Thesis structure 6

CHAPTER 2 GEOLOGICAL SETTING 7

2.1 The Sulu orogenic belt 7

2.2 The Jiaobei region 9

2.3 The Luxi region 10

CHAPTER 3 ANALYTICAL METHODOLOGY 12

3.1 SHRIMP zircon U-Pb dating 12

3.2 LA-ICP-MS zircon U-Pb dating 13

3.3 $^{40}Ar/^{39}Ar$ dating 13

3.4 Fission-track analysis 15

3.4.1 Basics of fission-track method 15

3.4.2 Laboratory analysis 16

3.5 (U-Th)/He dating 17

3.5.1 Basics of (U-Th)/He dating 17

3.5.2 Laboratory analysis 19

3.6 Major and trace element analyses 19

3.7 Zircon Hf isotope 20

CHAPTER 4 THERMOCHRONOLOGY OF THE SULU ULTRAHIGH-PRESSURE METAMORPHIC BELT 21

4.1 Introduction 21

4.2 Sampling 22

4.3 Results 23

4.3.1 SHRIMP zircon U-Pb results 23

4.3.2 $^{40}Ar/^{39}Ar$ data 27

4.3.3 Zircon fission-track and (U-Th)/He data 29

4.3.4 Apatite fission-track and (U-Th)/He data 30

4.4 Inverse modelling 31

4.5 Interpretation and Discussion 37

4.5.1 Effect of radiation damage on zircon He diffusion and fission-track annealing 37

4.5.2 Thermal history and tectonic implications 38

4.5.3 Thermal history of the UHP terrane 40

4.5.4 Implication of 210–160 Ma cooling for the NCB-SCB collision model 41

4.5.5 Implication for lithospheric thinning from 125–90 Ma and 65–40 Ma exhumation events 44

4.5.6 65–40 Ma exhumation and tectonic implication 45

4.6 Conclusions 46

CHAPTER 5 THERMOCHRONOLOGICAL AND STRUCTURAL CONSTRAINTS ON THE CRUSTAL EVOLUTION OF THE JIAOBEI REGION48

5.1 Introduction 48

5.2 Structural Deformation 50

5.3 Analytical Results 53
5.3.1 SHRIMP Zircon U-Pb Ages 53
5.3.2 $^{40}Ar/^{39}Ar$ Ages 56
5.3.3 Zircon Fission-Track and Zircon (U-Th)/He Data 59
5.3.4 Apatite Fission-Track and Apatite (U-Th)/He Data 62
5.3.5 Inverse modelling 63
5.4 Discussion 66
5.4.1 Timing of deformation 66
5.4.2 Implication for the South China-North China Collision 68
5.4.3 Extensional Tectonics and Implication for Lithospheric Thinning 71
5.5 Conclusions 73
CHAPTER 6 THERMOCHRONOLOGY OF THE LUXI REGION 75
6.1 Introduction 75
6.2 Sampling 76
6.3 Results 76
6.3.1 Zircon fission-track and (U-Th)/He data 76
6.3.2 Apatite fission-track and (U-Th)/He data 78
6.4 Interpretation and Discussion 81
6.4.1 Implication for a weak crustal shortening in the early Mesozoic 81
6.4.2 Implication for two episodes of lithospheric thinning 82
6.5 Conclusions 85
CHAPTER 7 PETROGENESIS OF LATE MESOZOIC ADAKITE-LIKE GRANITOIDS IN THE JIAOBEI REGION, EASTERN NORTH CHINA 86
7.1 Introduction 86
7.2 Sampling and petrology 87
7.3 Results 91
7.3.1 Zircon U-Pb ages and Hf isotopes 91

7.3.2 Major and trace elements 97

7.4 Discussion 101

7.4.1 Petrogenisis of Linglong granites and Luanjiahe granites 101

7.4.2 Petrogenesis of Guojialing granodiorite 104

7.4.3 Tectonic implications 105

7.5 Conclusion 109

CHAPTER 8 SYNTHESIS 111

8.1 Introduction 111

8.2 Collision between the SCB and NCB 111

8.2.1 Exhumation of the Sulu UHP rocks and in the Jiaobei region 111

8.2.2 Formation of the Tan-Lu fault 114

8.2.3 Crustal melting 117

8.3 Mesozoic–Cenozoic lithospheric thinning 117

8.3.1 A thickened continental crust in the early to mid-Mesozoic 117

8.3.2 Metasomatised lithospheric mantle 118

8.3.3 Temporal variations in the Cretaceous magmatic composition 118

8.3.4 Extension and subsidence since the Cretaceous 119

8.3.5 Lithospheric thickening during mid- to late Cenozoic 120

8.3.6 Two episodes of exhumation 120

8.3.7 Implication for the mechanism of lithospheric thinning 121

8.4 Conclusions 122

8.4.1 Implications for Mesozoic continental collision 122

8.4.2 Implications for lithospheric thinning 123

REFERENCES 124

APPENDICES 155

Appendix Table 4.1 SHRIMP zircon U-Pb results for samples from the Sulu UHP belt 155

Appendix Table 4.2 $^{40}Ar/^{39}Ar$ results for granites and metamorphic rocks in the Sulu UHP belt 159

Appendix Table 4.3 ZFT ages for samples in the Sulu UHP belt............. 162

Appendix Table 4.4 Zircon (U-Th)/He data for samples in the Sulu UHP belt.. 163

Appendix Table 4.5 Apatite fission-track data for samples in the Sulu UHP belt.. 166

Appendix Table 4.6 Apatite (U-Th)/He data for samples in the Sulu UHP belt.. 167

Appendix Table 4.7 Compilation of U-Pb, Ar/Ar, (U-Th)/He results in the Sulu UHP-HP belt.. 169

Appendix Figure 4.1 Radiation damage and grain size effects on the AHe, ZHe and ZFT ages.. 181

Appendix Table 5.1 Sample information for thermochronology study in the Jiaobei region 184

Appendix Table 5.2 SHRIMP zircon U-Pb results for samples from the Jiaobei region 186

Appendix Table 5.3 $^{40}Ar/^{39}Ar$ results for granites and metamorphic rocks in the Jiaobei region 194

Appendix Table 5.4 Zircon and apatite (U-Th)/He data for samples in the Jiaobei region 201

Appendix Table 6.1 Zircon and apatite fission-track results for the Luxi region 207

Appendix Table 6.2 Zircon and apatite (U-Th)/He results for the Luxi region 208

Appendix Table 7.1 Sample locations and mineral assemblages for the late Mesozoic igneous rocks in the Jiaobei region 213

Appendix Table 7.2 LA-ICP-MS zircon U-Th-Pb isotope data for the late Mesozoic igneous rocks from the Jiaobei region...................................... 215

Appendix Table 7.3 LA-ICPMS zircon Hf isotope data for the late Mesozoic igneous rocks from the Jiaobei region....................................... 230

Appendix Table 7.4 Major and trace element data for the late Mesozoic igneous rocks in the Jiaobei region.. 238

LIST OF FIGURES

Figure 1.1 Geologic sketch map of the NCB (shaded area in inset) (Gao et al., 2008), subdivided into the Western Block (WB), Eastern Block (EB), and Trans-North China Orogen (TNCO) (Zhao et al., 2005). NSGL is the North–South Gravity Lineament (Griffin et al., 1998). Qinling, Dabie and Sulu denote the orogenic belt formed during collision between the NCB and the SCB. The Dabie-Sulu orogenic belt (blue) is offset by the Tan-Lu fault. Inset shows major tectonic divisions of China. 2

Figure 1.2 Tectonic models proposed for the Mesozoic collision between the NCB and SCB. A. Transform fault model modified after Okay et al. (1993) and Yin and Nie (1993). This model claims that the suture had opposing polarity in the subduction zone when the two blocks collided: in the region east of the Tan-Lu fault, the subduction zone was south dipping, implying the NCB was the lower plate, whereas in the region west of the Tan-Lu fault the SCB was subducted along a north dipping subduction zone. Southward propagation of thrust stacks and normal faults exhumed the high grade metamorphic rocks in the Dabie orogenic belt; B. Lithospheric indentation model modified after Yin and Nie (1993). A salient block existed in the northern margin of the SCB, indentation of which caused the concomitant left-slip motion of the Tan-Lu fault and southward thrusting in the southern margin of the NCB; C. Crustal detachment model after Li (1994). The Dabie-Sulu orogenic belt was aligned along a linear suture at the start of collision and was later displaced by northward motion of the Sulu orogenic belt along a crustal detachment, with the Tan-Lu fault acting as a sinistral strike-slip “tear” fault mainly in the upper crust; D. Rotational collision model after Zhang (1997), Gilder Gilder et al. (1999), and Xu et al. (2009a). The SCB rotated clockwise with respect to the NCB and collided from east to west. 3

Figure 2.1 Geologic map and subdivision of the study area including the Luxi region and the Jiaodong Peninsula separated by the NNE striking Tan-Lu fault. The Jiaodong Peninsula is subdivided by the Wulian-Qingdao-Yantai fault into the Jiaobei region and the Sulu UHP belt. Pt–Paleoproterozoic. 8

Figure 3.1 Representative track length distributions for spontaneous tracks, after Gleadow et al. (1986b). 16

Figure **3.2** The T–t graphs for the five model thermal histories which all yield an apatite (U-Th)/He age of 40 Ma, after Wolf et al. (1998) and Brown et al. (2013)... 18

Figure 3.3 Apatite (U-Th)/He age as a function of structural depth in a 20 ℃/km geothermal gradient for the time–temperature histories shown in Figure 3.2, after Wolf et al. (1998). 18

Figure 4.1 Location and geological map of Shandong Peninsula (a and c) and distribution of the Early Cretaceous rift basins and metamorphic core complexes (MCC) in eastern North China (b) (modified after Zhu et al. (2012a)). Cross section (d) shows the structure of the Sulu (UHP-HP) metamorphic terrane (modified after Xu et al. (2006c)) along the A-B transverse in Figure 1b. Figure 1a is modified after Suo et al. (2012). BBB: Bohai Bay Basin, SYSB: South Yellow Sea Basin ; WQY: Wulian-Qingdao-Yantai. 22

Figure 4.2 Representative cathodoluminescence (CL) images showing the internal structure of the zircon grains. Spot number and corresponding $^{206}Pb/^{238}U$ ages for all samples except $^{207}Pb/^{206}Pb$ ages for 10JD05 are shown next to the analytical spots. 25

Figure 4.3 SHRIMP zircon U-Pb plots of metamorphic rock and granite samples. Mean age for younger than 1 Ga ages refers to $^{206}Pb/^{238}U$ age and $^{207}Pb/^{206}Pb$ age for older than 1 Ga ages. 26

Figure 4.4 $^{40}Ar/^{39}Ar$ age spectrum for dated samples. Note 10SD041B, 11LX196 and 10SD062B results were obtained from multiple grains. 28

Figure **4.5** ZHe, AFT and AHe ages in eastern Sulu UHP terrane (a). Projection of ZHe data along cross section A-A’ showing an increasing trend with distance away from Wulian-Qingdao-Yantai fault (b). ZHe ages-elevation plot (c). 32

Figure 4.6 Thermal modelling results of thermochronological data in time-temperature diagrams modelled with the HeFTy program. The shaded polygons demonstrate contours of acceptable fit curves (green) and good fit curves (magenta). Dark grey bar: ZHe partial retention zone; light grey bar: apatite fission-track partial annealing zoneAHe partial retention zone; MTL: mean track length in μm, A “good” result corresponds to the goodness of fit value 0.5 or higher. The dot lines represent dividing lines for different cooling episodes. Note the pre-160 Ma cooling paths in a, c and e are actually not constrained by modelling parameters and less reliable regarding cooling style. 36

Figure 4.7 Comparison of $^{40}Ar/^{39}Ar$ results and ZHe ages in the Sulu ultrahigh-pressure–high pressure metamorphic terrane. The northern ultrahigh pressure terrane (NUHP) has a wider K-feldspar age spectrum and younger minimum age compared to the southern ultrahigh pressure terrane (SUHP) and high pressure terrane (HP), which indicates partial reheating of NUHP by the Early Cretaceous magmatism. Legend for rocks is the same as **Figure 4.1**. Hbl: Hornblende, Ms: Muscovite, Bt: Biotite, K: K-feldspar, KAr: K-feldspar $^{40}Ar/^{30}Ar$. Dataset for the figure is provided in the Appendix Table 4.7 40

Figure 4.8 Cooling paths for different components of the Sulu ultrahigh pressure-high pressure terrane. The dataset for this figure is provided in Appendix Table 4.7. 42

Figure 4.9 Cooling history of major components of the Sulu UHP terrane and related tectonothermal events........ 43

Figure 4.10 Kinematic process (a) of the Sulu UHP-HP terrane predicted by the crustal detachment model and corresponding cooling path (b)........ 44

Figure 5.1 Geological map of the Jiaodong Peninsula showing the lithology, structures and sample locations. Three crustal cross sections in the lower panel show the geometry of structures. The DEF cross sections was modified after SBGB (1996). Inset map shows the tectonic location of the study area. Bold letters shaded by white circles represent the location of each figure in Figure 5.2. 50

Figure 5.2 Characteristics of D_1, D_2 and D_3 structures in the Jiaobei region. (A) F_1 rootless intrafolial folds in the Archean Complex (GPS: N37°16.012', E120°53.902'). (B) Intrafolial fold F_1 and gneissic layering S_1 in the Archean Complex (GPS: N37°13.688', E120°57.938'). (C) Spaced cleavage S_3 cross-cutting S_2 foliation in the Penglai Group (GPS: N37°24.951', E120°59.875'). (D and E) S_2 Cleavage refolded by NE-striking anticline (B_3) with primary bedding preserved in the Penglai Group (GPS: N37°24.869', E121°00.417'). (F) S_1 foliation refolded by D_3 deformation with the axial plane foliation (f_2) dipping southeast in the Jingshan Group (36°48.460', E120°42.046'). Locations of the observations are referred to Figure 5.1. 52

Figure 5.3 SHRIMP U-Pb zircon concordia age plots and cathodoluminescence (CL) images for samples from the Jiaobei region........ 55

Figure 5.4 $^{40}Ar/^{39}Ar$ age spectrum from the Precambrian basement. Note: 10SD201 was degassed in the furnace. 58

Figure 5.5 (a) New $^{40}Ar/^{39}Ar$ ages, zircon fission track and zircon (U-Th)/He ages for the Jiaodong Peninsula. (b) Time-space exhumation patterns across the Jiaodong Peninsula. Ages were plotted onto the A-B cross section following the curvatures of Upper Jurassic-Lower Cretaceous plutons in the Jiaobei region, whereas ages in the Sulu orogenic belt were plotted directly onto the cross section. Ages in the Sulu orogenic belt were cited from Chapter 4. Two $^{40}Ar/^{39}Ar$ ages with star symbol in the Jiaobei region were after Faure et al. (2003a) and Hacker et al. (2009). 62

Figure 5.6 Zircon U-Pb, AFT and AHe ages for the Jiaodong Peninsula. AFT and AHe results in the Sulu orogenic belt were adopted from chapter 4. The starred Zircon U-Pb age was cited from Tam et al. (2011). Two ages from the Penglai Group with §signs were originally reported in Zhu et al. (1994b). 63

Figure 5.7 Inverse modelling of representative samples from the Jiaobei region. APAZ: apatite partial annealing zone; APRZ: apatite partial retention zone; ZPRZ: zircon partial retention zone; ZPAZ: zircon partial annealing zone. C-projected track length is used for the histogram. 65

Figure 5.8 Schematic map and lithospheric cross sections showing the kinematic process for the Mesozoic collision between South China and North China blocks, modified after Li (1994) and Li (1998). 70

Figure 5.9 Whole rock εNd(t) versus ages for Cretaceous mafic rocks in the Jiaodong Peninsula. Data sources are: Guo et al. (2004), Yang et al. (2004), Guo et al. (2005a), Yan et al. (2005), Zhang et al. (2008b), Liu et al. (2009b),Kuang et al. (2012a), Kuang et al. (2012b), Cai et al. (2013), and Ma et al. (2014b). 72

Figure 6.1 Geolological map of the Luxi region and locations of samples collected during this study. The first two letters of sample codes are not shown in the figure for a succinct view. Pt = Proterozoic. 76

Figure 6.2 Radial plots of ZFT data (upper panels) and correlation between single-grain age and U concentration (lower panels). 77

Figure 6.3 Histogram of ZHe ages from samples where no weighted mean age was calculated. 78

Figure 6.4 Radial plots of AFT results. The large relative error arises from low U abundance in the apatite. 79

Figure 6.5 Inverse modelling results for representative samples with pairwise ages and those with track length data. Ages shown in each panel were used to constrain cooling paths that can reproduce the measured results. Note: all the high temerpature constraints were drawn artificially in order to reveal the cooling through ZPRZ. The constraint box for 11LX053A around 140 Ma comes from the ZFT age reported in Guo (2014). AHe age for 11LX030 is not used because it failed to yield cooling paths when it is incorporated into the modelling. 84

Figure 7.1 Sketch map of North China (a) and geological map of the Jiaobei region (b) showing distribution of Mesozoic magmatic rocks. Symbols in Figure. 1a: red intrusions (Early Cretaceous), blue granitoids (Jurassic), green intrusions (Triassic). This figure 1a is modified after Sun and Yang (2013)... 87

Figure 7.2 Field, hand specimen and SEM microphotographs of the Mesozoic rocks from the Jiaobei region. All microphotographs were taken using Hitachi TM3030 Tabletop Microscope integrated with SwiftEDS3000 at Curtin University (Accelerating voltage = 15kV, Filament current = 1850 mA). Mineral abbreviations: Afs (Ba): alkali feldspar rich in barium, Aln: allanite, Ap: apatite, Bt: biotite, Chl: chlorite, Hbl: hornblende, Pl: plagioclase, Qz: quartz, Ttn: titanite, Zrn: zircon....... 89

Figure 7.3 Representative zircon CL images from dated samples. Spot numbers and $^{206}Pb/^{238}U$ ages are shown with analysed spots.. 93

Figure 7.4 Zircon LA-ICP-MS U-Pb results. The dash circles refer to analyses excluded for calculation of weighted mean $^{206}Pb/^{238}U$ age.. 95

Figure **7.5** Diagram of Hf isotopic evolution in zircons from the Linglong granite, Luanjiahe granite, Guojialing granodiorite and Early Cretaceous dioritic intrusion. The Hf isotopic data for the Luanjiahe granite were cited from Jiang et al. (2012). . 97

Figure 7.6 Whole rock geochemical plots for the samples in the study and from the literature. (a): $FeO_t/(FeO_t+MgO)$ versus SiO_2, after Osborn (1979) and Frost et al. (2001), U = Northeast Umnak Island, Aleutian Islands, C = Cascades, western United States; (b): Molar $Al_2O_3/(Na_2O+K_2O)$ versus $Al_2O_3/(CaO+Na_2O+K_2O)$; (c): Na_2O+K_2O-Cao versus SiO_2, after Frost et al. (2001); d: Sr-Rb-Ba plot, after Tarney and Jones (1994). Data quoted in the plot include Hou et al. (2007),Zhang et al. (2010a), Jiang et al. (2012), Yang et al. (2012c), and Ma et al. (2013) for Linglong and Luanjiahe granites and Guojialing granodiorite; Guo et al. (2004), Yang et al. (2004), Liu et al. (2009b), Kuang et al. (2012b) and Ma et al. (2014b) for coeval mafic rocks to the Guojialing granodiorite in the Jiaobei region.............................. 99

Figure 7.7 Trace element patterns of the Mesozoic magmatic rocks normalized to the global average continental upper crust (Rudnick and Gao, 2003). Data quoted in the plot include Hou et al. (2007), Zhang et al. (2010a), Jiang et al. (2012), Yang et al.

(2012c), and Ma et al. (2013) for Linglong and Luanjiahe granites and Guojialing granodiorite; Guo et al. (2004), Yang et al. (2004), Liu et al. (2009b), Kuang et al. (2012b) and Ma et al. (2014b) for coeval mafic rocks to the Guojialing granodiorite in the Jiaobei region. 100

Figure 7.8 εNd(t) versus initial $^{87}Sr/^{86}Sr$ diagram plotted with published data. Data quoted in the plot include Hou et al. (2007),Zhang et al. (2010a), Jiang et al. (2012), Yang et al. (2012c), and Ma et al. (2013) for Linglong and Luanjiahe granites and Guojialing granodiorite; Guo et al. (2004), Yang et al. (2004), Liu et al. (2009b), Kuang et al. (2012b) and Ma et al. (2014b) for coeval mafic rocks to the Guojialing granodiorite in the Jiaobei region. 102

Figure 7.9 Cl chondrite-normalized $(Dy/Yb)_{CN}$ and $(La/Sm)_{CN}$ ratios versus SiO_2 for mafic rocks and granitoids. Normalization values are from Sun and McDonough (1989). 103

Figure 7.10 Tectonic model for the geneses of Late Jurassic Linglong and Luanjiahe granites and Guojialing graondiorites, modified after Li (1998). 108

Figure 8.1 (a) zircon fission-track and (U-Th)/He ages across the Sulu orogenic belt and the Jiaobei region. (b) Cooling history of the Sulu UHP rocks constrained by ages obtained by zircon U-Pb, 40Ar/39Ar of mica, hornblende and feldspar, and zircon (U-Th)/He methods. 113

Figure 8.2 The crustal detachment model after Li (1998) which could explain exhumation process of the Sulu UHP rocks and the Jiaobei region. 113

Figure 8.3 Representative $^{40}Ar/^{39}Ar$ results for three well studied segments (Dabie, Zhangbaling and Sulu) within the Tan-Lu fault zone, modified after Zhu et al. (2010). The full dataset is presented in Table 8.1. For brevity, not all results are shown in the figure. Letters in parenthesis represent minerals analysed by $^{40}Ar/^{39}Ar$ dating; phengite (P), biotite (B), muscovite (M). 115

Figure 8.4 Paleogeography of the eastern NCB from the Late Jurassic to the Early Cretaceous (after Wang (1985).NSGL — North-South Gravity lineament. 119

LIST OF TABLES

Table 0.1 Samples studied in the Sulu UHP belt..23
Table 0.2 Summary of geochronology and thermochronology data in the Sulu UHP belt..33
Table 0.1 Published $^{40}Ar/^{39}Ar$ ages from the Tan-Lu fault 116

CHAPTER 1 INTRODUCTION

1.1 Introduction

The Dabie-Sulu orogenic belt in central eastern China is well known for its occurrence of ultrahigh-pressure (UHP) metamorphic rocks, protolith of which was subducted to > 100 km depth beneath the North China block (NCB), overprinted by UHP metamorphism, and finally exhumed to surface (Zheng et al., 2003). The Sulu UHP metamorphic belt is offset from the Dabie UHP belt by approximately 500 km of left-lateral strike-slip displacement along the Tan-Lu fault (**Figure 1.1**), however, the role of this fault during the collision-exhumation process along the Dabie-Sulu orogenic belt remains controversial. There are a number of models competing to explain to explain the Mesozoic collision between NCB and the South China block (SCB), including the transform fault model (Okay and Şengör, 1992; Okay et al., 1993), lithospheric indentation model (Yin and Nie, 1993), crustal detachment model (Li, 1994; Li, 1998) and rotational collision model (Zhang, 1997; Gilder et al., 1999; Hacker et al., 2004) (**Figure 1.2**). Understanding the metamorphism and kinematics of the Dabie-Sulu orogenic belt would help to elucidate the kinematics of continental collision and general mountain building processes. Past work has focused on geochemical processes in the continental collision zone (Zheng et al., 2012), characterizing the timing and P-T conditions of metamorphism and partial melting during subduction and exhumation (e.g., Yao et al., 2000; Ye et al., 2000a; Yang et al., 2003b; Zhang et al., 2009b; Zong et al., 2010a; Zong et al., 2010b; Liu and Liou, 2011; Zheng et al., 2011; Liu et al., 2012; Chen et al., 2013). A number of structural and geophysical studies have been carried out to improve our understanding of the kinematics of the Dabie-Sulu orogenic belt (e.g., Ratschbacher et al., 2000; Yang, 2002; Faure et al., 2003a; Faure et al., 2003b; Xu et al., 2006c; Lin et al., 2009; Suo et al., 2009; Li et al., 2011). However, due to repeated structural and metamorphic overprinting of the UHP rocks, it has been extremely difficult to restore unequivocal kinematic indicators and constrain the timing of deformation events. Sedimentary and structural evidence from outside the Dabie-Sulu orogenic belt is, therefore, important for constraining the evolution of the entire orogen. So far, only limited work has been carried out outside the UHP or high-pressure (HP) metamorphic core of the Dabie-Sulu orogenic belt (e.g., Grimmer et al., 2003; Dong et al., 2004; Meng et al., 2007; Li et al., 2009).

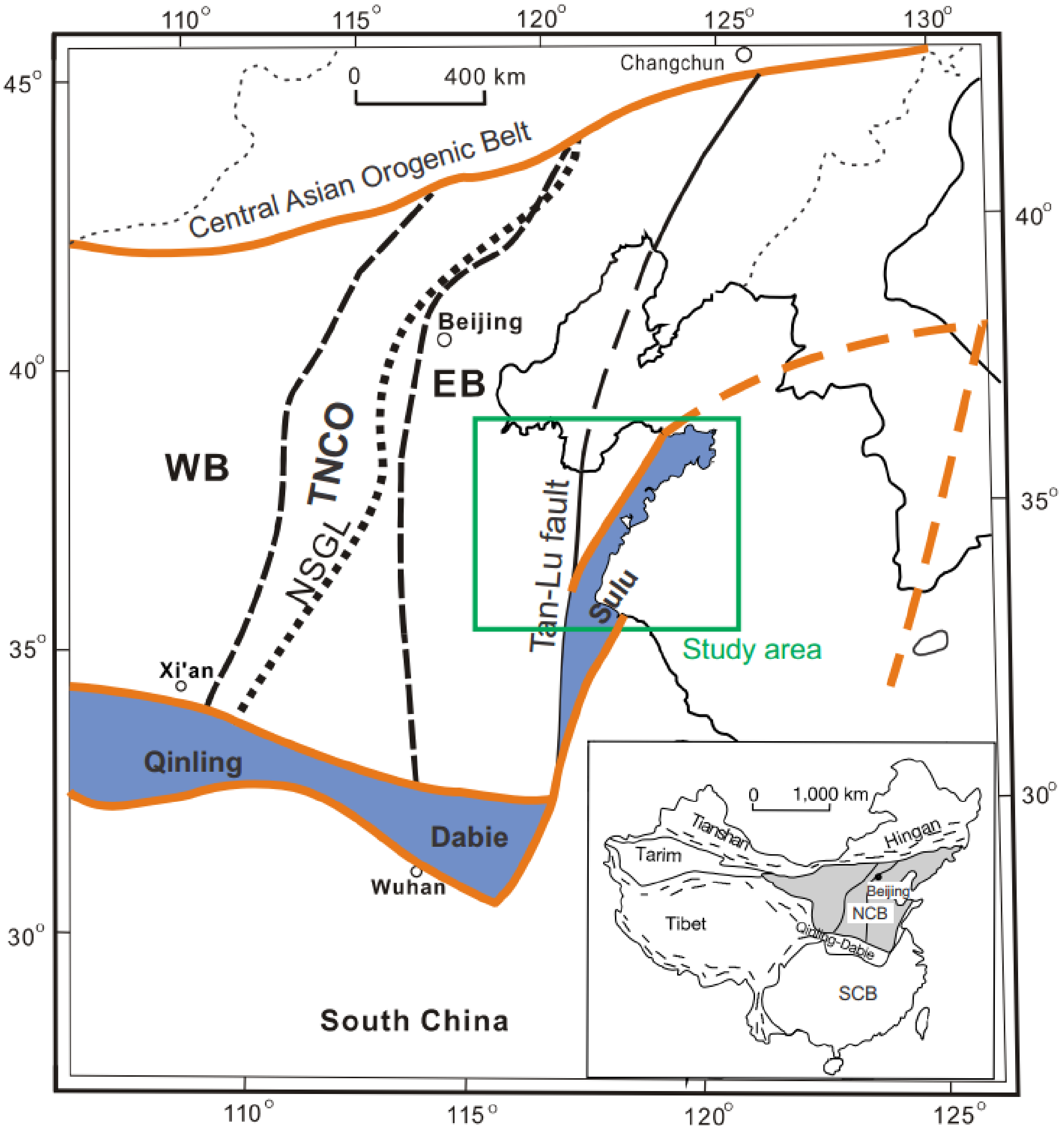

Figure 1.1 Geologic sketch map of the NCB (shaded area in inset) (Gao et al., 2008), subdivided into the Western Block (WB), Eastern Block (EB), and Trans-North China Orogen (TNCO) (Zhao et al., 2005). NSGL is the North–South Gravity Lineament (Griffin et al., 1998). Qinling, Dabie and Sulu denote the orogenic belt formed during collision between the NCB and the SCB. The Dabie-Sulu orogenic belt (blue) is offset by the Tan-Lu fault. Inset shows major tectonic divisions of China.

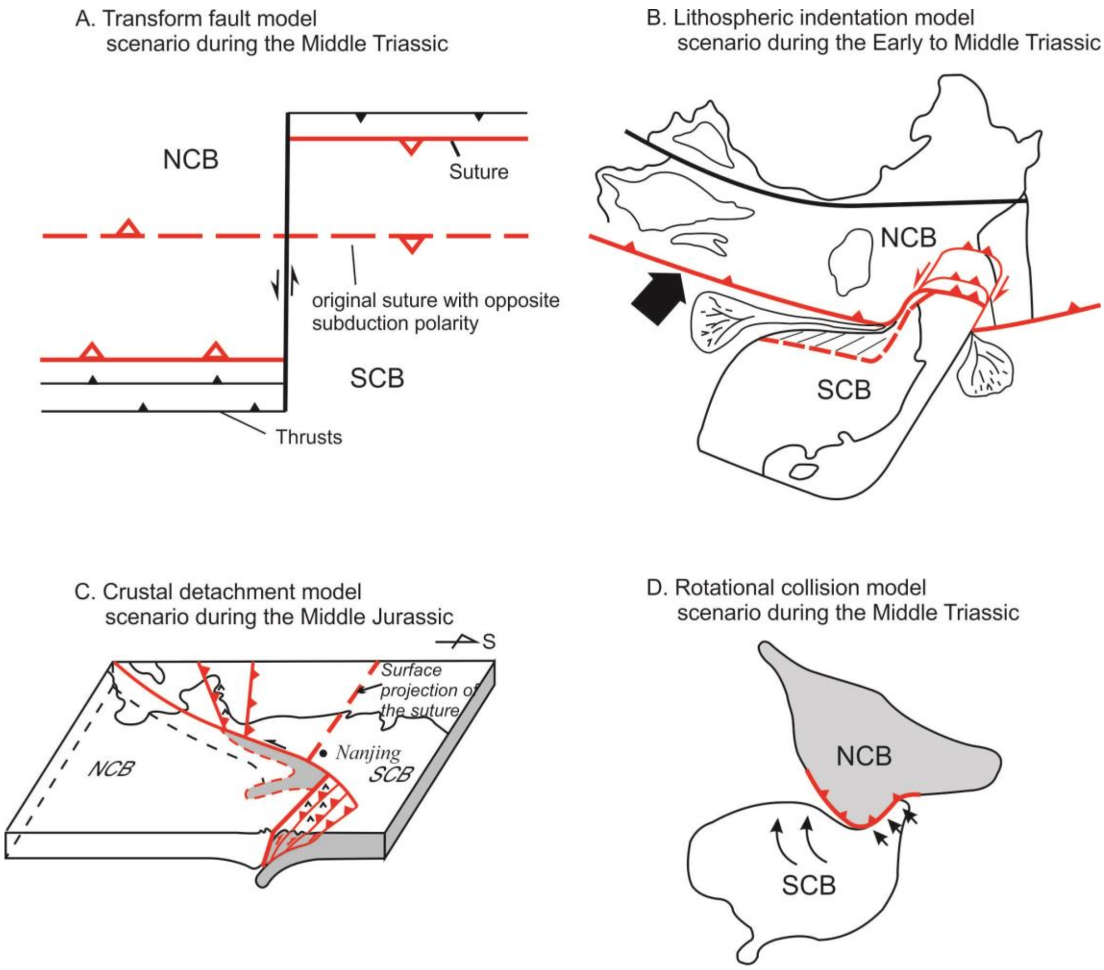

Figure 1.2 Tectonic models proposed for the Mesozoic collision between the NCB and SCB. A. Transform fault model modified after Okay et al. (1993) and Yin and Nie (1993). This model claims that the suture had opposing polarity in the subduction zone when the two blocks collided: in the region east of the Tan-Lu fault, the subduction zone was south dipping, implying the NCB was the lower plate, whereas in the region west of the Tan-Lu fault the SCB was subducted along a north dipping subduction zone. Southward propagation of thrust stacks and normal faults exhumed the high grade metamorphic rocks in the Dabie orogenic belt; B. Lithospheric indentation model modified after Yin and Nie (1993). A salient block existed in the northern margin of the SCB, indentation of which caused the concomitant left-slip motion of the Tan-Lu fault and southward thrusting in the southern margin of the NCB; C. Crustal detachment model after Li (1994). The Dabie-Sulu orogenic belt was aligned along a linear suture at the start of collision and was later displaced by northward motion of the Sulu orogenic belt along a crustal detachment, with the Tan-Lu fault acting as a sinistral strike-slip "tear" fault mainly in the upper crust; D. Rotational collision model after Zhang (1997), Gilder Gilder et al. (1999), and Xu et al. (2009a). The SCB rotated clockwise with respect to the NCB and collided from east to west.

Thermochronology provides a powerful tool to reveal spatial and temporal patterns of rock movements relative to Earth's surface (exhumation), which may be associated with thrusting (e.g., Metcalf et al., 2009), normal faulting (e.g., Armstrong et al., 2003) and/or concomitant erosion. By far, the most commonly used thermochronometers are (U-Th)/He and fission-track dating of zircon and apatite (e.g., Gallagher et al., 1998; Farley, 2002; Donelick et al., 2005; Reiners, 2005; Tagami, 2005), and $^{40}Ar/^{39}Ar$ dating of mica, feldspar and hornblende (e.g., McDougall and Harrison, 1999; Kelley, 2002a), which collectively provide constraints on crustal processes at temperatures below approximately 300–550 ℃ (Reiners and Brandon, 2006). So far, only a little (U-Th)/He and fission-track work has been carried out either within or outside the Sulu orogenic belt (Liu et al., 2009c; Siebel et al., 2009). Therefore, a thermochronologic study, in conjunction with regional tectonic and magmatic analyses, will potentially provide new insights into the kinematics of the collisional process of the Dabie-Sulu orogenic belt.

The collisional process between the SCB and NCB ended no later than the Late Jurassic (Li, 1994; Yin and Nie, 1996; Gilder et al., 1999). The Linglong granitic pluton, which was emplaced to the north of the Sulu UHP belt in the Late Jurassic, is commonly regarded to have been derived from partial melting of a thickened crust with multiple sources from the Archean basement of the NCB and the Sulu UHP belt (Hou et al., 2007; Jiang et al., 2012; Yang et al., 2012c; Ma et al., 2013). Understanding the origin of this pluton, and in particular, how the materials in the Sulu orogenic belt became a source for the Linglong pluton, may help to decipher the collisional process in the Sulu orogenic belt.

The most conspicuous tectonic event in eastern North China after the continental collision was lithospheric thinning, manifested as replacement of up to 120 km thickness of ancient lithospheric root by a much thinner juvenile mantle lithosphere (Menzies et al., 1993; Griffin et al., 1998; Xu, 2001; Yang et al., 2010). Mantle xenoliths from Ordovician diamondiferous kimberlites consisted mainly of garnet facies harzburgite and suggested that a cold (heat flow of ~40 mW/m^2), thick (~200 km) (Griffin et al., 1998), and refractory Archean lithospheric mantle with Os model ages and Re depleted ages of 2.5 – 3.2 Ga existed in the Paleozoic (Gao et al., 2002; Wu et al., 2006b; Zhang et al., 2008a). In contrast, mantle xenoliths from Cenozoic basalts were characterized by spinel facies lherzolite (Fan et al., 2000) and revealed a hot (heat flow of 80 mW/m^2) (Menzies and Xu, 1998), thin (80–120 km), fertile and juvenile lithospheric mantle with mixed ancient and modern mantle components (Gao et al., 2002; Wu et al., 2003; Wu et al., 2006b; Chu et al., 2009; Liu et al., 2014b). Two notable, and possibly mutually relevant, mechanisms have been proposed for lithospheric thinning: delamination (Gao et al., 1998; Gao et al., 2004; Xu et al., 2006b; Deng et al., 2007; Liu et al., 2009b) and thermo-mechanical-chemical erosion (Menzies et al., 1993; Menzies and Xu, 1998; Xu, 2001; Zheng et al., 2007). The delamination hypothesis requires that the delaminated lower crust of the NCB hybridised the lithospheric mantle, leaving melts derived from the partial melting of the delaminated eclogite to be intruded as adakitic rocks and those derived from the hybridized mantle to form the basaltic and high-Mg andesitic rocks (Gao et al., 2009). Topographic uplift is commonly cited consequence from lithospheric delamination. A thick and stiff lithosphere, however, can retard or prevent uplift (Elkins-Tanton, 2007). Subsequent upwelling of the asthenosphere could possibly induce extension of the lithosphere. The thermo-mechanical-chemical erosion model, on the other hand, predicts two episodes of lithospheric thinning, the first being characterised by melting of the enriched lithospheric mantle in the Early Cretaceous and the second characterised by melting of the asthenosphere in the Late Cretaceous–early Cenozoic (Xu et al., 2009b). The essence of this model is that extension, possibly linked to the subduction of Western Pacific plate (Xu, 2007), caused the thinning of lithosphere and the sequential partial melting of enriched lithospheric mantle and asthenosphere. Documentation of exhumation history, either arising from topographic uplift and crustal extension, will shed new lights on the process of lithospheric thinning.

1.2 Objectives

The thesis aims to

- Constrain the timing and styles of compressional deformation in the NCB adjacent to the Sulu UHP belt in relation to the SCB-NCB continental collision;
- Investigate the sources and petrogenesis of the Upper Jurassic granitoids;
- Reveal temporal and spatial variation of exhumation pertaining to lithospheric thinning;
- Test tectonic models for continental collision and the mechanisms of lithospheric thinning.

1.3 Research methods

The project utilized multiple-system thermochronology, SHRIMP zircon U-Pb geochronology and field structural observation to identify deformation and exhumation related to continental collision and lithospheric thinning. The thermochronometers include $^{40}Ar/^{39}Ar$ dating of mica and hornblende, and fission-track and (U-Th)/He dating of zircon and apatite. Laser ablation inductively coupled plasma mass spectrometry (LA-ICP-MS) zircon U-Pb dating, major and trace element analyses and *in situ* zircon Hf isotope were carried out to investigate the sources and petrogenesis of the Upper Jurassic granitoids.

1.4 Thesis structure

This thesis starts with Chapter 1, introducing the scientific questions related to the Dabie-Sulu orogenic belt, the objectives and an overview of methods employed during the dissertation. This is followed by Chapter 2, reviewing the geological setting of the Sulu orogenic belt and peripheral regions. Chapter 3 describes the methods by which the data in the thesis were acquired. Chapters 4–6 reconstruct the exhumation history of the Sulu UHP belt, the Jiaobei region and the Luxi region, respectively, using multiple-system thermochronology. The tectonic implication of the exhumation/deformation is discussed in terms of the SCB-NCB collision and lithospheric thinning. Chapter 7 focuses on the origin of the Upper Jurassic-Lower Cretaceous granitic plutons and discusses their genetic relationship with the SCB-NCB collision and lithospheric thinning. Chapter 8 outlines the exhumation histories in the three regions and integrates them with numerous geologic phenomena into a self-consistent tectonic scenario for eastern North China since the Mesozoic.

CHAPTER 2 GEOLOGICAL SETTING

The NCB is one of the Earth's old Archean cratons, preserving crustal remnants as old as 3.8 Ga (Liu et al., 1992). Paleoproterozoic collisions between sub-blocks, amalgamated the NCB into a coherent craton (Zhao et al., 2001b; Wilde et al., 2002; Zhao et al., 2005; Zhai and Santosh, 2011; Zhao et al., 2011). During the Phanerozoic, the NCB underwent a complex tectonic interaction with multiple neighbouring blocks. Progressive subduction along the northern margin formed the accretionary Central Asian Orogenic Belt (CAOB) (**Figure 1.1**) with the final closure of the Paleo-Asian Ocean occurring in the Permian along the Solonker suture (Xiao et al., 2003; Windley et al., 2007). In the Jurassic, this newly accreted plate amalgamated with the Siberia plate in the north along the Mongol-Okhotsk suture (Kravchinsky et al., 2002; Tomurtogoo et al., 2005). In the southern margin, collision of the NCB with the SCB started by the Early Triassic (Zhao and Coe, 1987) and ended no later than Late Jurassic (Li, 1994; Yin and Nie, 1996), which formed the Qinling-Dabie-Sulu orogenic belt (**Figure 1.1**). The Paleo-Pacific (Izanagi) plate may have begun to interact with the eastern margin of the NCB from the Jurassic (Maruyama, 1997; Wu et al., 2007). The study area consists of three regions with distinctive geologic locations, litholoies and deformation histories. They are the Sulu orogenic belt, the Jiaobei region and the Luxi region, which are introduced below.

2.1 The Sulu orogenic belt

The Sulu ultrahigh pressure (UHP) belt is geographically located in the southern part of the Jiaodong Peninsula and is separated from the NCB by the northwest dipping Wulian-Qingdao-Yantai fault (**Figure 2.1**) (Zhai and Liu, 1998; Wallis et al., 1999; Zhai et al., 2000). High-pressure metamorphic rocks outcrop to the southeast.

The Sulu UHP belt is composed dominantly of banded gneisses enclosing layers or lenses of eclogite, coesite-bearing marbles and peridotites (Liou et al., 1996; Ye et al., 2000b; Zhang et al., 2003b; Zhang et al., 2010b). Micro-diamond and coesite occur as inclusions in minerals such as garnet, clinopyroxene and zircon, indicating temperature-pressure conditions of 750–850 ℃ and >28 kbar consistent with UHP metamorphic conditions (Xu et al., 2006c). The timing of regional UHP metamorphism in the Sulu orogen spans from 243 ±4 Ma to 218 ±2 Ma based on U-Pb dating of zircon (containing UHP mineral inclusions) from a wide range of rocks, including eclogite, amphibolite, marble, quartzite, ortho- or paragneisses (Ames et al., 1996; Ye et al., 2000b; Liu et al., 2003; Liu et al., 2005; Liu et al., 2006b; Liu et al., 2007; Liu et al., 2009a; Zong et al., 2010a; Liu and Liou, 2011; Leech and Webb, 2013). Zircon cores commonly preserved protolith U-Pb ages of ca. 790 to 700 Ma and 2.05 to 1.85 Ga (Ames et al., 1996; Zheng et al., 2004; Tang et al., 2008; Zheng et al., 2008), suggesting an affinity to the SCB. The UHP rocks are interpreted as having been recrystallized during Triassic subduction of SCB crustal materials to a depth of approximately 200 km (Ye et al., 2000a; Yang et al., 2003b). Syn-exhumation syenite and gabbro were emplaced at ca. 210 Ma as indicated by zircon U-Pb data (Zhao et al., 2012).

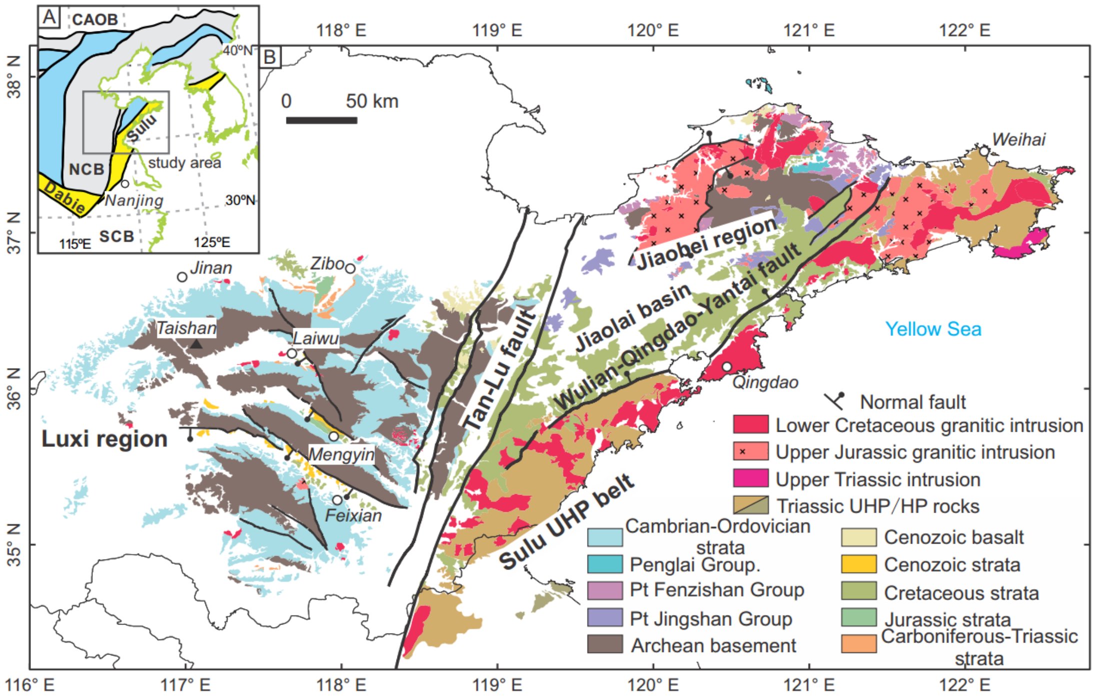

Figure 2.1 Geologic map and subdivision of the study area including the Luxi region and the Jiaodong Peninsula separated by the NNE striking Tan-Lu fault. The Jiaodong Peninsula is subdivided by the Wulian-Qingdao-Yantai fault into the Jiaobei region and the Sulu UHP belt. Pt–Paleoproterozoic.

The UHP rocks were intruded by massive Upper Jurassic to Lower Cretaceous granitoids (Guo et al., 2005b; Yang et al., 2005b; Zhang et al., 2010a; Jiang et al., 2012; Yang et al., 2012c), and overlain by Cretaceous clastic and bimodal (mafic and felsic) volcanic rocks (Fan et al., 2001; Guo et al., 2005a) as well as sparse Cenozoic sedimentary and Neogene basaltic rocks.

2.2 The Jiaobei region

The Jiaobei region is located in the northwestern part of the Jiaodong Peninsula and has a distinctive crustal nature relative to the Sulu UHP-HP belt to the southeast of the Wulian-Qingdao-Yantai fault (Tang et al., 2007; Zhang et al., 2014) (**Figure 2.1**). The northwest dipping normal fault controlled the deposition of the Cretaceous strata in the Jiaolai basin (Zhu et al., 2012a) and is generally regarded as a post-collision extensional fault. However, beneath the Jiaolai basin, seismic profiles showed suspect imbricate thrusts truncated by the Wulian-Qingdao-Yantai fault (Wu et al., 2006a), suggesting that it is unlikely to be the boundary fault operating during the collision.

The Jiaobei region is the southernmost segment of the Jiao-Liao-Ji Belt, one of three major Paleoproterozoic orogenic belts emplaced during the formation of the coherent NCB. It comprises five main lithological units:

(1) Meso-Neoarchean tonalite-trondhjemite-granodiorite (TTG) gneisses, granulites, amphibolites and metamorphosed supracrustal rocks (Tang et al., 2007; Jahn et al., 2008; Liu et al., 2013a; Wu et al., 2014);

(2) Paleoproterozoic meta-volcanic and meta-sedimentary successions (marbles, gneisses, leptites and mica schists) metamorphosed at the ~1.95–1.85 Ga (Wan et al., 2006; Zhou et al., 2008d; Tam et al., 2011; Zhang et al., 2014). They are generally in detachment fault contact with underlying Archean rocks and are divided into greenschist-lower amphibolite facies Fengzishan Group in the north and upper amphibolite-granulite facies Jingshan Group in the south (**Figure 2.1**).

(3) Proterozoic (?) meta-sedimentary rocks of the Zhifu Group and Penglai Group. The Zhifu Group is located on an island northeast of the Jiaobei region and consists mainly of greenschist to amphibolite facies quartzites and schists. Provenance of the detrital zircons showed an affinity to the NCB and deposition after ca. 1844 Ma (Liu et al., 2013b). The Penglai Group, represented mainly by slates, quartzites, marbles and limestones, is locally in detachment contact with the underlying Precambrian basement and generally assigned to the Neoproterozoic, but an early Paleozoic age was also suggested on the basis of bivalves and brachiopod

fossils (Ji and Zhao, 1992). It has been a subject of debate as to whether the Penglai Group has a tectonic affinity to the NCB or the SCB (Li et al., 2007b; Zhou et al., 2008b; Chu et al., 2011).

(4) Upper Jurassic and Lower Cretaceous granitoids. A great number of zircon U-Pb studies indicate the Upper Jurassic and Lower Cretaceous granitoids were emplaced during 160–144 Ma and 130–115 Ma, respectively (Wang et al., 1998; Zhang et al., 2003c; Goss et al., 2010; Zhang et al., 2010a; Yang et al., 2012c; Ma et al., 2013; Yang et al., 2014b).

(5) Cretaceous volcano-sedimentary rocks with little Cenozoic strata in the extensional Jiaolai basin (Fan et al., 2001; Ling et al., 2009).

2.3 The Luxi region

Neoarchean magmatic rocks and supracrustal assemblages constituted the oldest rocks exposed in the western Shandong Province. They consist mainly of quartzite, biotite gneiss, amphibolite, meta-volcanic rocks, phyllite and banded iron formation, mostly deformed and subjected to greenschist- to amphibolite-facies metamorphism. Recent SHRIMP zircon U-Pb dating indicated that these supracrustal rocks and trondhjemite-tonalite-granodiorite (TTG) rocks formed from 2.75–2.50 Ga (Du et al., 2005; Wan et al., 2010; Wang et al., 2010; Wan et al., 2011; Wan et al., 2012; Peng et al., 2013b; Peng et al., 2013a; Wang et al., 2013). The Archean rocks were intruded by mafic dykes at ~1.8 Ga (Hou et al., 2006; Wang et al., 2007b) and ~1.2 Ga (Peng et al., 2013c). In contrast to the Jiaobei region, no metamorphic event has been found to occur in the Paleoproterozoic. Unconformably overlying the Archean rocks are the late-Precambrian Tumen Group comprising nonmetamorphosed siliciclastic rocks, and Cambro-Ordovician marine carbonates. The Tumen Group contains the youngest detrital zircons dated at ~1.2 Ga. Silurian, Devonian, and Lower Carboniferous strata are absent due to denudation in the early Paleozoic. The Upper Carboniferous is represented by a coal-bearing succession comprising dominantly sandstone and shale, intercalated with limestone. The entire Permian was dominated by terrestrial sedimentation and the strata are in conformable contact with the Upper Carboniferous rocks. There are few Triassic sedimentary outcrops in the west Shandong and Bohai Bay region (Li et al., 2012a; Li et al., 2013) except localized Fenghuangshan Formation sediments that unconformaby overlie

Permian strata in the Zibo basin (Yang et al., 2013). The Jurassic succession unconformably overlies older rocks and is predominantly composed of siliciclastic sediments with coal seams. Their depositional age was constrained by detrital zircon provenance analysis as Middle–Late Jurassic (Li et al., 2013; Yang et al., 2013). The Cretaceous strata mainly consist of intermediate-basic volcanic and clastic rocks. The Paleogene is comprised primarily of fluvial and alluvial sediments. The Cretaceous and Paleogene strata are mainly distributed within the half-graben basins controlled by NW-trending normal faults.

The Luxi region shows evidence for three stages of magmatic activity since Mesozoic. The Tongshi complex consists predominantly of monzonite and syenite, emplaced at ~180 Ma, and interpreted to have originated from either an asthenospheric mantle or the Neoarchean–Paleoproterozoic crust (Xu et al., 2004a; Lan et al., 2012). The second stage magmatic event is characterized by intrusive rocks such as diabase, gabbro and diorite, and andesitic and basaltic volcanic rocks in the fault controlled basins. Available chronological data constrain this magmatic event to occur between 144 Ma and 112 Ma (Qiu et al., 2001; Zhang et al., 2002; Liu et al., 2008b; Ling et al., 2009; Yang et al., 2012a and references therein; Yang et al., 2012d). Neogene and quaternary alkaline basalts were mainly erupted in the Luxi area close to the Tan-Lu fault (Luo et al., 2009; He et al., 2011; Zeng et al., 2011).

The Cambro-Ordovician sedimentary cover dips at less than 30° and WNW- and NNE-trending Jura-type or open folds developed in the Luxi region between the late Middle Triassic and the Late Jurassic (Qi et al., 2004; Li et al., 2005). Subsequent block faulting is characterized by development of a series of NW striking, south dipping faults, which controlled the present-day distribution of Meso-Cenozoic strata in half graben basins (Yan et al., 1996; Li et al., 2012a).

CHAPTER 3 ANALYTICAL METHODOLOGY

3.1 SHRIMP zircon U-Pb dating

Zircons were separated from crushed rock samples by conventional magnetic and high-density liquid separation. Grains were handpicked and mounted in epoxy resin discs, ground to approximately half-grain thickness, and coated with a 40 nm layer of gold to produce a resistance of 15–25 Ω across the mount surface. Internal structure of zircons was inspected by cathodoluminescence (CL) imaging using a Phillips XL30 scanning electron microscope or Zeiss EVO 40XVP SEM located in the Department of Imaging and Applied Physics at Curtin University.

Sensitive High Resolution Ion Microprobe (SHRIMP) zircon U-Pb isotopic analyses were conducted at the John de Laeter Centre of Mass Spectrometry, Curtin University (see details in De Laeter and Kennedy (1998)). A 25–30 µm diameter spot was created by an O^{2-} primary beam at 10 keV with intensity of 1.8–2.5 nA to sputter secondary ions from the surface of the zircon mineral. The sample surface was cleaned prior to data collection by rastering of the primary beam for 2 minutes over the target area. Data for each spot were collected in sets of six scans through the 9 mass peaks of $^{196}Zr_2O^+$, $^{204}Pb^+$, Background, $^{206}Pb^+$, $^{207}Pb^+$, $^{208}Pb^+$, $^{238}U^+$, $^{248}ThO^+$, $^{254}UO^+$. The absolute abundances of U, and Th isotopes were determined with reference to 91500 zircon standard ($^{206}Pb/^{238}U$ age = 1065 Ma, U = 81 ppm (Wiedenbeck et al., 1995)) or BR266 zircon ($^{206}Pb/^{238}U$ age = 559.0 ± 0.3 Ma, U = 909 ppm (Stern, 2001)). U-Pb calibration standards included Plešovice (Sláma et al., 2008) and TEMORA 2 (Black et al., 2004). Every four unknown zircon analyses were typically bracketed by one analysis on Plešovice/TEMORA 2 zircon during each session. Uncertainties assigned to all isotopic ratios and dates for individual analyses include uncertainty arising from counting statistics and common-Pb correction. Ratios and dates based on $^{238}U/^{206}Pb^*$ include an external uncertainty related to the reproducibility of the standard $^{238}U/^{206}Pb^*$ measurements. The uncertainty arising from calibration against the reference standard is also included in individual $^{238}U/^{206}Pb^*$ ratios and dates reported in data tables. The correction for initial common-Pb utilized measured $^{204}Pb/^{206}Pb$ and contemporaneous common-Pb isotopic compositions determined according to the model of Stacey and Kramers

(1975). Data were reduced by SQUID 2.5. Regressions, concordia ages, and weighted average ages were calculated using Isoplot 3.75 (Ludwig, 2012). Spots with values of $^{206}Pb_c$ (fraction of common ^{206}Pb in total ^{206}Pb) >1% were usually rejected. Values of MSWD (mean square of weighted deviates) and Probability for concordia ages are for X-Y weighted mean and X-Y equivalence. Uncertainties at 2σ levels are displayed on Concordia and weighted mean plots; the errors on weighted mean ages and concordia ages are reported at the 95% confidence level.

3.2 LA-ICP-MS zircon U-Pb dating

Laser ablation inductively coupled plasma mass spectrometry (LA-ICP-MS) zircon U-Pb analyses were conducted at AGOS-GeoHistory Laser Ablation ICPMS Facility, Curtin University, using an Agilent 7700s quadrupole ICP-MS coupled with Resonetics M-50 193nm ArF excimer laser ablation system. Following a 40s period of gas background analysis, zircon was ablated for 30 seconds at a 7 Hz repetition rate in a ultra-high purity He-N_2 atomosphere using a 33 μm beam (23 μm for 13JD40A and 13JD40F) and laser energy of 10 J/cm^2. Zircon 91500 was used as a secondary standard, to monitor the reproducibility and the stability of the instrument. During each session, the sequence started with NIST 610, 91500 and Plešovice, and then twenty unknowns were bracketed by two Plešovice, four 91500 and two NIST 610. Plešovice was used to monitor and correct for both instrumental drift and down-hole fractionation. Twenty isotopes were scanned during each analysis, including those necessary for U-Pb dating (^{235}U, 238U, ^{232}Th, ^{204}Pb, ^{206}Pb, ^{207}Pb and ^{202}Hg) and some major and trace elements (Si, Ti, REE). International glass standard NIST 610 was used as the primary standard to calculate elemental concentrations (using ^{29}Si as the internal standard element) and to correct for instrument drift. Precision is better than 5% for most elements based on repeated analyses of secondary internal standards. U-Pb data reduction was performed using the U-Pb Geochronology 3 data reduction scheme in Iolite 2.5 (Paton et al., 2010; Paton et al., 2011). Concordia and weighted mean age calculation were carried out by Isoplot 3.75 (Ludwig, 2012).

3.3 $^{40}Ar/^{39}Ar$ dating

Unaltered minerals were carefully handpicked optically under a binocular microscope. The selected hornblende and mica minerals were further leached in diluted HF for one minute and then thoroughly rinsed with distilled water in an ultrasonic cleaner.

Samples were loaded into eight large wells of two 1.9 cm diameter and 0.3 cm depth aluminum discs (I15t40h and I12t25h). These wells were bracketed by small wells that included Fish Canyon sanidine (FCs) as a neutron fluence monitor for which an age of 28.294 ± 0.036 Ma (1σ) was adopted (Renne et al., 2011). The discs were Cd-shielded (to minimize undesirable nuclear interference reactions) and irradiated for 40 hours in the US Geological Survey nuclear reactor (Denver, USA) in the central position during two separate irradiations. The mean J-values was computed from standard grains within the small pits. The specific J value to each sample is referred to Appendices $^{40}Ar/^{39}Ar$ tables. Mass discrimination was monitored using an automated air pipette and provided a mean value of 1.006127 ± 0.0038 to 1.006309 ± 0.003522 per dalton (atomic mass unit) relative to an air ratio of 298.56 ± 0.31 (Lee et al., 2006). The correction factors for interfering isotopes were $(^{39}Ar/^{37}Ar)_{Ca} = 7.30x10^{-4}$ (± 11%), $(^{36}Ar/^{37}Ar)_{Ca} = 2.82x10^{-4}$ (± 1%) and $(^{40}Ar/^{39}Ar)_{K} = 6.76x10^{-4}$ (± 32%).

Most samples were step-heated using a 110 W Spectron Laser Systems, with a continuous Nd-YAG (IR; 1064 nm) laser rastering over the sample of either naked single grain, or grain populations wrapped in 0-blank Nb foil, for 1 minute to ensure a homogenously distributed temperature. The multi-grain hornblende from sample 10SD201 was heated in a Pond Engineering© furnace, where the temperature was monitored using a thermocouple directly in contact with the crucible. The gas was purified in a stainless steel extraction line using three SAES AP10 getters (or two SAES AP10 getters, one GP50 getter) and one liquid nitrogen condensation trap. Ar isotopes were measured in static mode using a MAP 215-50 mass spectrometer (resolution of ~500; sensitivity of $4x10^{-14}$ mol/V) with a Balzers SEV 217 electron multiplier primarily using 9 to 10 cycles of peak-hopping. The data acquisition was performed with the Argus program written by M.O. McWilliams run in a LabView environment. The raw data were processed using the ArArCALC software (Koppers, 2002) and the ages were calculated using the decay constants recommended by Renne et al. (2010). Blanks were monitored every 3 to 4 steps and typical ^{40}Ar blanks range from 1 x 10-^{16} to 2 x 10-^{16} mol. Our criteria for the determination of a plateau are as follows: plateaus must include at least 70% of ^{39}Ar. The plateau should be distributed over a minimum of 3 consecutive steps, agreeing at 95% confidence level and satisfying a probability of fit (P) of at least 0.05. Plateau ages are given at the 2σ level and are calculated using the mean of all the plateau steps, each weighted by the inverse variance of their individual analytical error. All sources of uncertainty are included in the calculation.

3.4 Fission-track analysis

3.4.1 Basics of fission-track method

The fission-track method is based on accumulation of damage tracks which result from spontaneous nuclear fission decay of ^{238}U in nature. When a ^{238}U atom decays by spontaneous fission, two high energy fragments are produced that travel through the lattice of the host mineral in opposite directions, thus causing tiny linear damage zone called fission track (Fleischer et al., 1975). The naturally born tracks are referred to as spontaneous tracks. Because the fission track is tiny and can be only observed under a transmission electron microscope, chemical etching was introduced (Price and Walker, 1962) to enlarge the tracks so that they could be counted under an optical microscope. Like other isotopic dating methods, abundance or ratio of the parent and daughter products must be measured in order to calculate an age. For fission-track analysis, the daughter is represented by the spontaneous fission track and the parent is ^{238}U. The abundance of daughter product is determined by counting the number of spontaneous tracks on a given surface of a mineral grain. The ^{238}U abundance is commonly determined using external detector method (Gleadow, 1981; Gleadow et al., 2002). The sample is bombarded with thermal neutrons in nuclear reactors to induce fission of ^{235}U atoms and induced fission tracks are recorded on a mica external detector. Abundance of ^{238}U is derived on the basis of the constant $^{238}U/^{235}U$ ratio of natural uranium ($^{238}U/^{235}U$ = 137.88) (Stacey and Kramers, 1975). After irradiation, only the external detector is etched to reveal induced fission tracks.

Fission tracks are not stable and can anneal/shorten after formation. The annealing is known to be dependent upon temperature, chemical composition and crystallographic orientation. Dpar and Cl wt% are useful indicators of fission track annealing kinetics in apatite. Dpar is the etch pit diameter parallel to the crystallographic c-axis (Burtner et al., 1994). Apatite grains with relatively low values of Dpar (≤1.75 μm for apatite grains etched for 20 s in 5.5 M HNO_3 at 21 ℃) anneal relatively rapidly (Donelick et al., 2005).

An important advantage of the fission-track method is that length distribution data is employed to constrain the interpretation of fission-track ages. Different styles of thermal history result in different patterns of length distribution (Gleadow et al., 1986a; Gleadow et al., 1986b)(**Figure 3.1**). The undisturbed volcanic type, characteristic of volcanic rocks, represents rapid cooling to relatively low surface temperatures. Apatite grains that have spent a significant period of time within the fission-track annealing zone will show various patterns of broader length distribution. The undisturbed basement type represents monotonic cooling from temperatures above about 120 ℃. More complex, multi-stage thermal histories will produce the even broader 'mixed' distributions. When the peaks in such a distribution are clearly resolved, as in the bimodal case, the distribution is indicative of a two-stage history with an older generation of tracks shortened during a later thermal event, and a new generation of long tracks produced subsequently. Such a bimodal distribution is particularly useful, giving information on the timing as well as the severity of the thermal event (Gleadow et al., 1986a; Gleadow et al., 1986b; Gleadow et al., 2002).

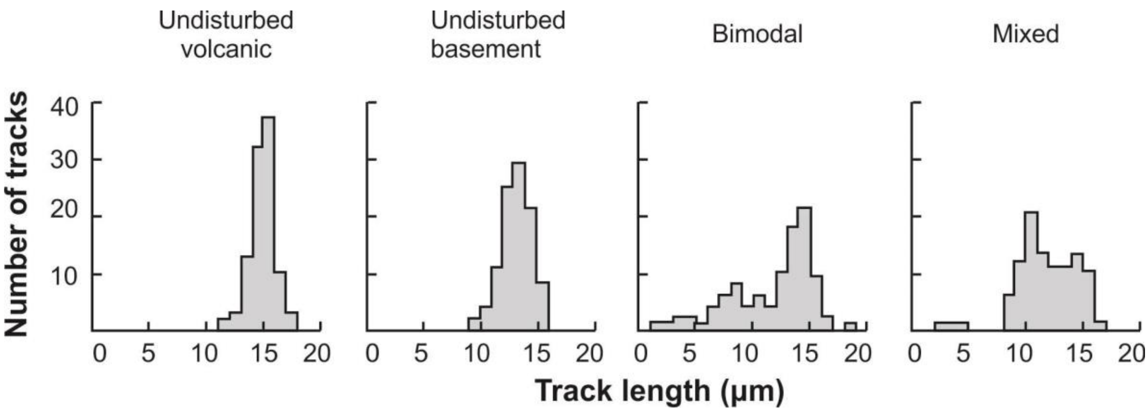

Figure 3.1 Representative track length distributions for spontaneous tracks, after Gleadow et al. (1986b).

3.4.2 Laboratory analysis

Apatite and zircon fission-track (AFT and ZFT) analyses were carried out at the University of Waikato (New Zealand) using the external detector method (Gleadow, 1981) and the ζ age calibration approach (Hurford and Green, 1983) to determine the fission-track age. Analytical procedures followed the protocols described by Danišík et al. (2007). Apatite and zircon grains were embedded in epoxy and Teflon mounts, respectively. Prepared mounts were then polished to 4π geometry and etched to reveal spontaneous tracks. Apatites were etched in 5.5 M HNO_3 solution for 20 seconds at 21 ℃ (Donelick et al., 1999). Zircons were etched in a eutectic mixture of KOH and NaOH at 215 ℃ for 3 to 16 hours (Zaun and Wagner, 1985). Etched samples were then covered by low-uranium muscovite sheets and enclosed with age standards and dosimeter glasses (CN-5 with 12 ppm U for apatite and CN-2 with 38 ppm U for zircon) into a plastic container prior to irradiation in the nuclear reactor at Oregon State University. Under neutron flux, fission tracks induced by fission of ^{235}U were recorded in the mica external detector. After irradiation, the mica detectors were etched with 40% HF for 30 minutes at 21 ℃ to reveal induced tracks. Tracks in apatite, zircon and mica detectors were counted with 1250x magnification using a dry objective. Fission-track ages were calculated using TrackKey 4.2g (Dunkl, 2002). Horizontal confined ‘tracks in tracks’ were measured in the c-axis parallel surfaces of apatite and were normalized for crystallographic angle using a c-axis projection (Donelick et al., 1999; Ketcham et al., 2007b). The annealing properties of apatite were assessed by measuring Dpar (Burtner et al., 1994).

3.5 (U-Th)/He dating

3.5.1 Basics of (U-Th)/He dating

(U-Th-Sm)/He dating is based on the production of α-particles (^4He) from U, Th and Sm decay (Farley and Stockli, 2002). Quantities of parent and daughter isotopes define the accumulation time through closure temperature. While radiogenic Pb is normally completely preserved in the phase being dated since mineral formation and cooling, He gas escapes more readily from host minerals, during radioactive decay (α-ejection), cooling and subsequent low-temperature heating episodes (diffusion). A temperature window (partial retention zone) exists between when the He gas starts to be retained in the mineral and when it is completely preserved. The retentivity of He varies with temperature, mineral features such as grain size and shape, and degree of radiation damage (Dodson, 1973; Farley, 2002; Flowers et al., 2007; Brown et al., 2013; Guenthner et al., 2013).

One challenging aspect of (U-Th)/He dating is that the cooling paths corresponding to a specific age, are not exclusive. For example, despite their different t–T paths, all five temperature histories in **Figure 3.2** yield indistinguishable apatite (U-Th)/He ages of 40 Ma (Wolf et al., 1998). However, the five paths can be resolved in an age-depth plot and a 1.5 km long elevation profile is sufficient to distinguish them from each other (**Figure 3.3**) (Wolf et al., 1998). Another approach is pairwise analysis of apatite by fission-track and (U-Th)/He methods. Given their different closure temperatures, this approach provides important cross-validation of these two independent techniques.

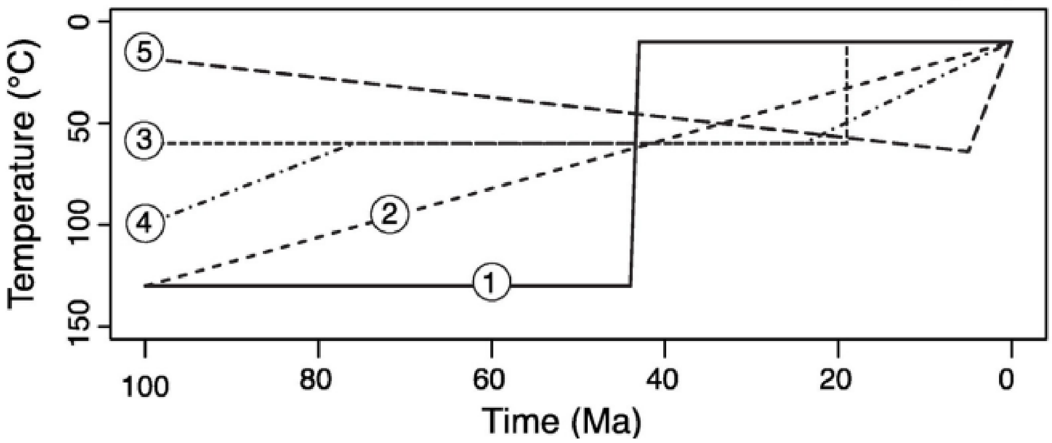

Figure **3.2** The T–t graphs for the five model thermal histories which all yield an apatite (U-Th)/He age of 40 Ma, after Wolf et al. (1998) and Brown et al. (2013).

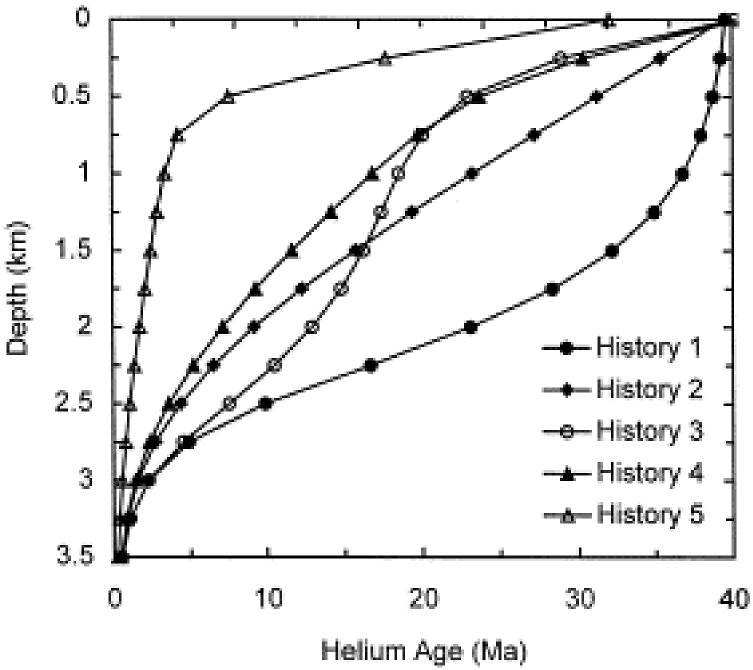

Figure 3.3 Apatite (U-Th)/He age as a function of structural depth in a 20 ℃/km geothermal gradient for the time–temperature histories shown in Figure 3.2, after Wolf et al. (1998).

3.5.2 Laboratory analysis

Single crystals of apatite and zircon (3 to 6 per sample) were dated by (U-Th)/He methods. Prior to dating, grains were inspected under cross-polarized transmitted light to eliminate grains with inclusions and damage, and selected grains were photographed and measured in order to calculate a correction factor F_t for alpha ejection (Farley et al., 1996).

(U-Th)/He dating was conducted at the University of Waikato and Curtin University. Both analyses followed standard analytical procedures including whole crystal laser gas extraction for He and isotope dilution inductively coupled plasma mass spectrometry for U, Th and ± Sm (see Evans et al. (2005) and Danišík et al. (2012) for details). Total analytical uncertainty was computed as the square root of the sum of squares of weighted uncertainties on U, Th, Sm and He measurements and used to calculate the error on raw He ages. The raw zircon (U-Th)/He (ZHe) and apatite (U-Th)/He (AHe) ages were corrected for α-ejection by F_t correction after Farley et al. (1996). A 5% uncertainty was imposed on the F_t value and incorporated into calculated errors on corrected ZHe and AHe ages. Replicate analyses of Durango apatite (n = 17) and Fish Canyon Tuff zircon (n = 12) measured as internal standards yielded mean (U-Th)/He ages of 31.6 ± 0.8 Ma and 28.0 ± 0.4 Ma, respectively. These are in excellent agreement with the Durango (U-Th)/He age of 31.02 ± 1.01 Ma (McDowell et al., 2005) and the Fish Canyon Tuff zircon (U-Th)/He age of 28.3 ± 1.3 Ma (Reiners, 2005).

3.6 Major and trace element analyses

Major elements were analysed using a Rigaku ZSX100e wavelength dispersive X-ray fluorescence spectrometer at the Guangzhou Institute of Geochemistry, Chinese Academy of Sciences, with relative standard errors less than 2%. Trace elements were analysed by a Perkin-Elmer ELAN 6000 inductively coupled plasma source mass spectrometer at the Guangzhou Institute of Geochemistry, Chinese Academy of Sciences, following the procedures described by Li et al. (2002), with relative standard errors less than 3%.

3.7 Zircon Hf isotope

The Lu-Hf isotope analysis of zircon was undertaken in the Geochemical Analysis Unit, GEMOC Key Centre in the Department of Earth and Planetary Sciences, Macquarie University, Sydney following the methods of Griffin et al. (2000) and Pearson et al. (2008).

Hf-isotope analyses were carried out *in-situ* using a New Wave UP-213 laser-ablation microprobe, attached to a Nu Plasma multi-collector ICPMS. The UP213 system is fitted with a large-format two-volume cell. Laser operating conditions included a beam diameter of ca. 55 μm (30–40 μm for 13JD040A and 13JD040F), a 5 Hz repetition rate and energy of 0.015 mJ (fluence 6 J/cm^2). This resulted in total Hf signals of 2−4 × 10^{-11} A, depending on conditions and the Hf contents. Typical ablation times were 100–120 seconds, resulting in pits 40–60 μm deep. He carrier gas transported the ablated sample from the laser-ablation cell via a 30 ml Savillex mixing chamber to the ICPMS torch. Interference of ^{176}Lu on ^{176}Hf is corrected by measuring the intensity of the interference-free ^{175}Lu isotope and using ^{176}Lu/^{175}Lu = 0.02669 (De Bievre and Taylor, 1993) to calculate ^{176}Lu/^{177}Hf. Similarly, the interference of ^{176}Yb on ^{176}Hf has been corrected by measuring the interference-free ^{172}Yb isotope and using ^{176}Yb/^{172}Yb to calculate ^{176}Yb/^{177}Hf. The appropriate value of ^{176}Yb/^{172}Yb was determined by spiking the JMC475 Hf standard with different concentrations of Yb, and determination of the value of ^{176}Yb/^{172}Yb (0.587) required to yield the value of ^{176}Hf/^{177}Hf obtained on the pure Hf solution. Detailed discussions regarding the overlap corrections for ^{176}Lu and ^{176}Yb are provided in Pearson et al. (2008). Analyses of standard zircons Mud Tank and Temora illustrate the precision and accuracy obtainable on the ^{176}Hf/^{177}Hf ratio, despite the severe corrections on ^{176}Hf. Mud Tank and Temora zircons yield analytical ^{176}Hf/^{177}Hf ratios of 0.282509 ± 29 (n = 51) and 0.282717 ± 28 (n = 27), respectively. These results are consistent with solution data of Woodhead and Hergt (2005). The typical 2SE precision on the ^{176}Hf/^{177}Hf ratios presented here is ±0.00002, equivalent to ±0.7 εHf unit. Initial ^{176}Hf/^{177}Hf ratios were calculated using measured ^{176}Lu/^{177}Hf ratios and the ^{176}Lu decay constant of 1.867 ×10^{-11} yr^{-1} (Söderlund et al., 2004). For the calculation of ε_{Hf} values, chondritic values from Blichert-Toft and Albarède (1997) were adopted.

CHAPTER 4 THERMOCHRONOLOGY OF THE SULU ULTRAHIGH-PRESSURE METAMORPHIC BELT

4.1 Introduction

The Dabie-Sulu orogenic belt, well-known for ultrahigh-pressure metamorphic (UHP) rocks, formed as a result of collision between the South China and the North China blocks (SCB and NCB, respectively) during Early Triassic-Middle Jurassic times (Zhao and Coe, 1987; Yin and Nie, 1993). The orogenic belt was displaced ~530 km along the Tan-Lu fault (Okay and Şengör, 1992) (**Figure 1.1**). Questions remain regarding the timing of this displacement and the mechanisms controlling continental collision east of the Tan-Lu fault. Published models include the transform-fault model (Okay and Şengör, 1992; Okay et al., 1993), indentation model (Yin and Nie, 1993), crustal detachment model (Li, 1994; Li, 1998) and rotational collision model (Zhang, 1997; Gilder et al., 1999; Hacker et al., 2004) (**Figure 1.2**). The validity of these models can be tested by reconstructing the thermal history of the Dabie-Sulu orogen.

Apart from the collisional process, it has been widely acknowledged that the eastern NCB has undergone widespread lithospheric thinning with up to 120 km of lithospheric root removed since the Mesozoic (Menzies et al., 1993; Griffin et al., 1998; Xu, 2001). Removal of a relatively cold and dense lower lithosphere can cause surface uplift and exhumation of crustal rocks (Foster and John, 1999) which can be recorded by low temperature thermochrometers.

In this chapter, a combination of SHRIMP zircon U-Pb, mica and hornblende $^{40}Ar/^{39}Ar$, zircon and apatite fission-track, and zircon and apatite (U-Th)/He geo- and thermochronometers, covering the temperature range from 900 °C to 40 °C, are used to reconstruct cooling trajectories of metamorphic rocks and Mesozoic intrusive rocks in the Sulu orogen. These new results, combined with available geological constraints, allow us to reconstruct the exhumation history of the Sulu UHP terrane, and to evaluate the existing tectonic models for the SCB–NCB collision, as well as the process of lithospheric thinning in the NCB.

4.2 Sampling

To investigate post-metamorphism exhumation processes in the Sulu UHP terrane, thirteen samples were collected from the footwall of the Wulian-Qingdao-Yantai fault (**Figure 4.1** and **Table 4.1**). The rock types range from Neoproterzoic granitic gneiss and Triassic UHP rocks to Lower Cretaceous intrusive rocks. One sample (11LX178B) was collected from the foliated Neoproterozoic granite, with affinity to the SCB, on the hanging wall of the Wulian-Qingdao-Yantai fault (Zhou et al., 2003; Huang et al., 2006; Zhou et al., 2008a). Although it is unclear if this sample experienced UHP metamorphic conditions, in view of the post-orogenic age of the Wulian-Qingdao-Yantai fault and the SCB affinity of the outcrop, it is preliminarily considered as being from the Sulu UHP terrane.

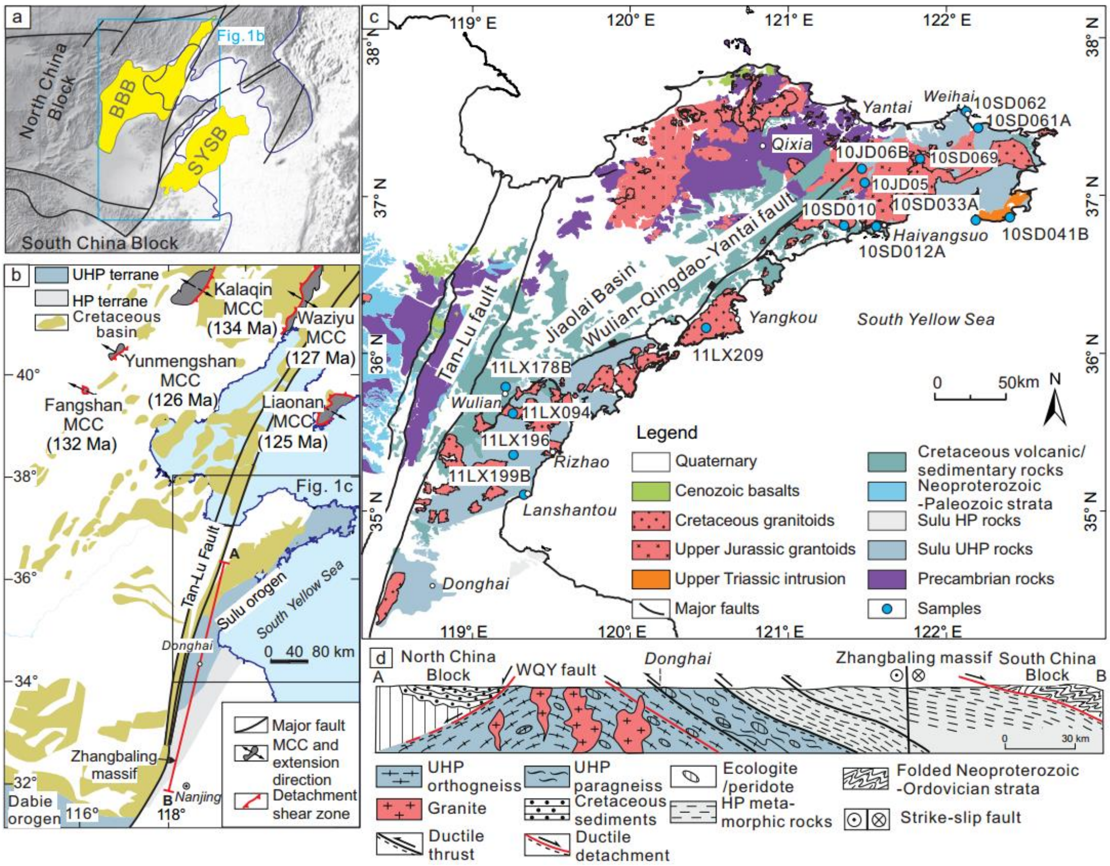

Figure 4.1 Location and geological map of Shandong Peninsula (a and c) and distribution of the Early Cretaceous rift basins and metamorphic core complexes (MCC) in eastern North China (b) (modified after Zhu et al. (2012a)). Cross section (d) shows the structure of the Sulu (UHP-HP) metamorphic terrane (modified after Xu et al. (2006c)) along the A-B transverse in Figure 1b. Figure 1a is modified after Suo et al. (2012). BBB: Bohai Bay Basin, SYSB: South Yellow Sea Basin ; WQY: Wulian-Qingdao-Yantai.

Table 4.1 Samples studied in the Sulu UHP belt

Sample	Latitude (N °)	Longitude (E °)	Elevation (m)	Lithology	Stratigraphic age
10JD05	37.0813	121.4793	69	Marble	Paleoproterozoic
10JD06B	37.1675	121.4684	154	Granite	Upper Jurassic
10SD010	36.8086	121.3571	55	Granite	Upper Cretaceous
10SD033A	36.8430	122.1912	7	Granitic gneiss	Upper Triassic
10SD061A	37.4253	122.2063	86	Granitic gneiss	Upper Triassic
10SD062	37.5352	122.1350	98	Amphibolite	Upper Triassic
10SD069	37.2331	121.8373	86	Granite	Lower Cretaceous
10SD41B	36.8620	122.4072	7	Quartz syenite	Upper Triassic
11LX094B	35.6187	119.2580	104	Monzonite	Lower Cretaceous
11LX178B	35.7849	119.2130	128	Foliated granite	Neoproterozoic
11LX196	35.3250	119.2513	108	Banded granitic gneiss	Upper Triassic
11LX199B	35.1042	119.3295	71	Granitic gneiss	Upper Triassic
11LX209	36.1599	120.4814	123	Alkali feldspar granite	Lower Cretaceous
10SD012A	36.8265	121.5714	21	Amphibolite	Upper Triassic (?)

4.3 Results

4.3.1 SHRIMP zircon U-Pb results

Results of SHRIMP U-Pb analyses are shown in Appendix Table 4.1. Zircon crystals from granitic gneiss sample 10SD033A displayed euhedral core-rim structure with rims of low luminescence and variably irregular, homogenous or zoned cores (**Figure 4.2**a). Thirty-one spots were analysed on twenty-five zircon grains. Twelve analyses on zircon cores yielded a concordia Neoproterzoic ^{206}Pb/^{238}U age of 762 ± 4 Ma (MSWD = 1.3, P = 0.17, n = 12), which is indistinguishable from the weighted mean ^{206}Pb/^{238}U age of 761 ± 6 Ma (MSWD = 1.99, P = 0.03, n = 12) (**Figure 4.3**a). Five of six analyses on rims plot on the concordia curve but yielded a mean ^{206}Pb/^{238}U age with MSWD = 7.6 and P = 0, suggesting that these analyses are discordant from each other and only yield an estimated age around 226 Ma. The remaining eleven spots lie in a discordant line. Th and U concentrations for rims are 18–74 ppm and 877–1671 ppm, respectively, in contrast to 123–531 ppm and 202–456 ppm for cores, indicating U-enriched rims for these zircons. Th/U ratios of the concordant core spots range from 1.45 to 0.52, implying a magmatic origin. Th/U ratios of zircon rims are 0.08–0.002, suggesting a metamorphic origin. Therefore, the 226 Ma estimate is interpreted as the Triassic metamorphic recrystallization age and 762 ± 4 Ma as the crystallization age of the Neoproterzoic protolith.

Zircon grains from granite sample 10JD06B were elongated, euhedral and showed core-rim structures in CL images. Rims were characterized by oscillatory zoning while most cores were homogenous and irregular (**Figure 4.2**b). Sixteen analyses were performed on fourteen zircon grains. Two analyses on cores yielded discordant $^{206}Pb/^{238}U$ ages of 218 ± 5 Ma and $^{206}Pb/^{238}U$ age of 714 ± 18 Ma, respectively and Th/U ratios of 0.73. Thirteen out of the remaining fourteen analyses on rims yielded a weighted mean $^{206}Pb/^{238}U$ age of 159.7 ± 1.3 Ma (MSWD = 1.17, P = 0.30, n = 13) (**Figure 4.3**b) and Th/U ratios between 0.24–0.11. One analysis with an older age of 168 ± 2 Ma and a low Th/U ratio of 0.01 was treated as an outlier and excluded from the weighed mean age calculation. Of the concordant analyses, four analyses yield a concordia age of 160.3 ± 2.8 Ma (MSWD = 2.1, P = 0.054, n = 4). The granite is interpreted to have crystallized at 159.7 ± 1.3 Ma.

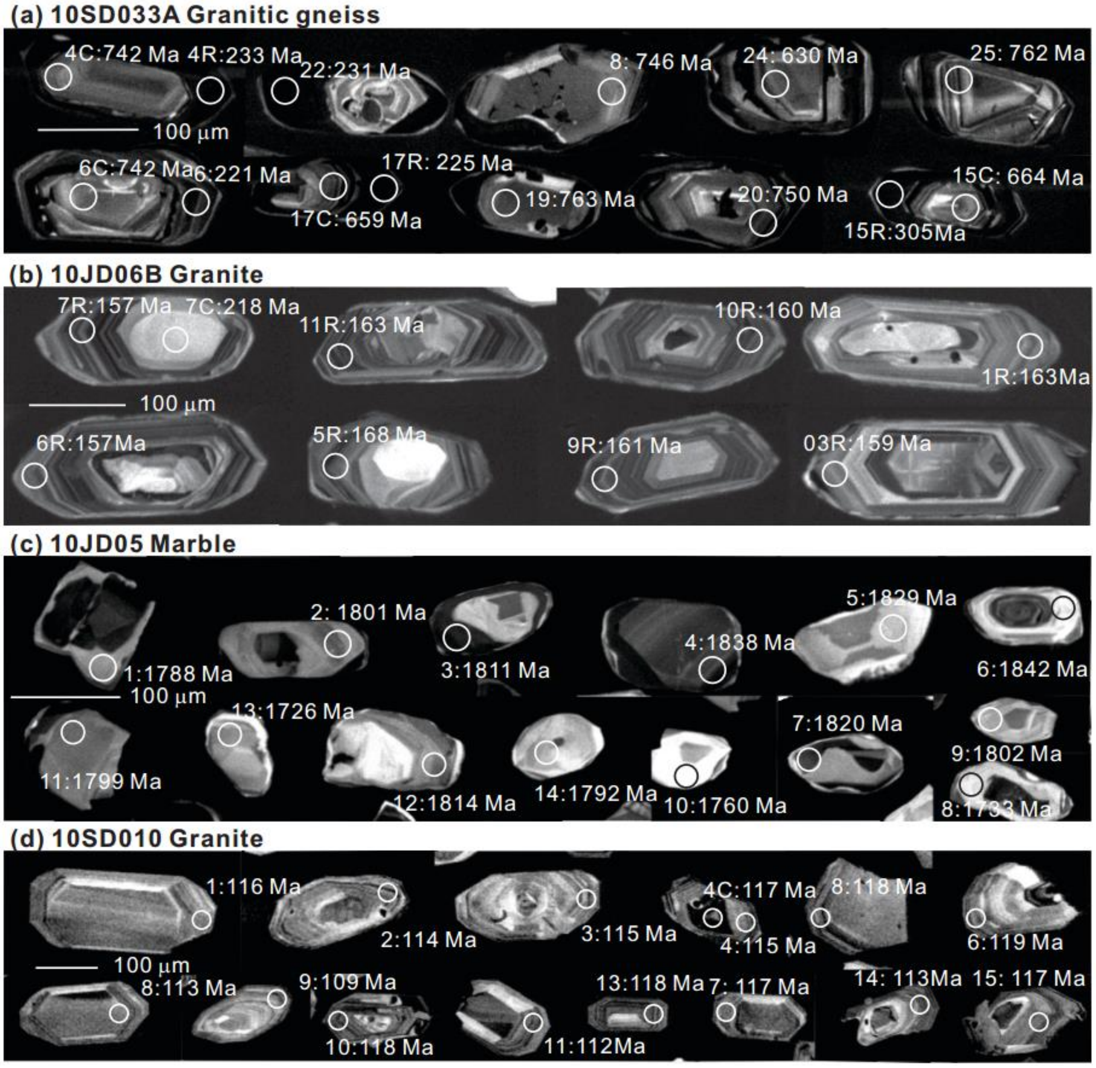

Figure 4.2 Representative cathodoluminescence (CL) images showing the internal structure of the zircon grains. Spot number and corresponding $^{206}Pb/^{238}U$ ages for all samples except $^{207}Pb/^{206}Pb$ ages for 10JD05 are shown next to the analytical spots.

Zircon grains from marble sample 10JD05 were primarily stubby, highly luminescent, structureless or nebulously-zoned (**Figure 4.2**c). Twenty analyses were made on nineteen zircon grains that form a discordant line with intercepts of apparent ages at 1799 ± 17 Ma and 206 ± 89 Ma (MSWD = 3.0). Thirteen concordant analyses yielded a weighted mean $^{207}Pb/^{206}Pb$ age of 1814 ± 10 Ma (MSWD = 1.7, P = 0.055, n = 13) and five yielded a concordia age of 1818 ± 18 Ma (MSWD = 1.8, P = 0.069, n = 5) (**Figure 4.3**c). Th/U ratios of these spots were 0.99–0.23. Two analyses were performed on a single grain that did not show distinctive structures relative to others in the CL images, but yielded $^{206}Pb/^{238}U$ ages of 147.9 ± 1.5 and 146.3 ± 2.5 Ma and Th/U ratios of 0.05 and 0.06, respectively. No grains with an intermediate apparent age in the Pb loss line were dated; hence the two younger ages may not bear geological significance. 1814 ± 10 Ma is interpreted as the timing of metamorphism, which is consistent with Sm-Nd isochron ages from mafic granulites about 30 km to the east (Zhai et al., 2000).

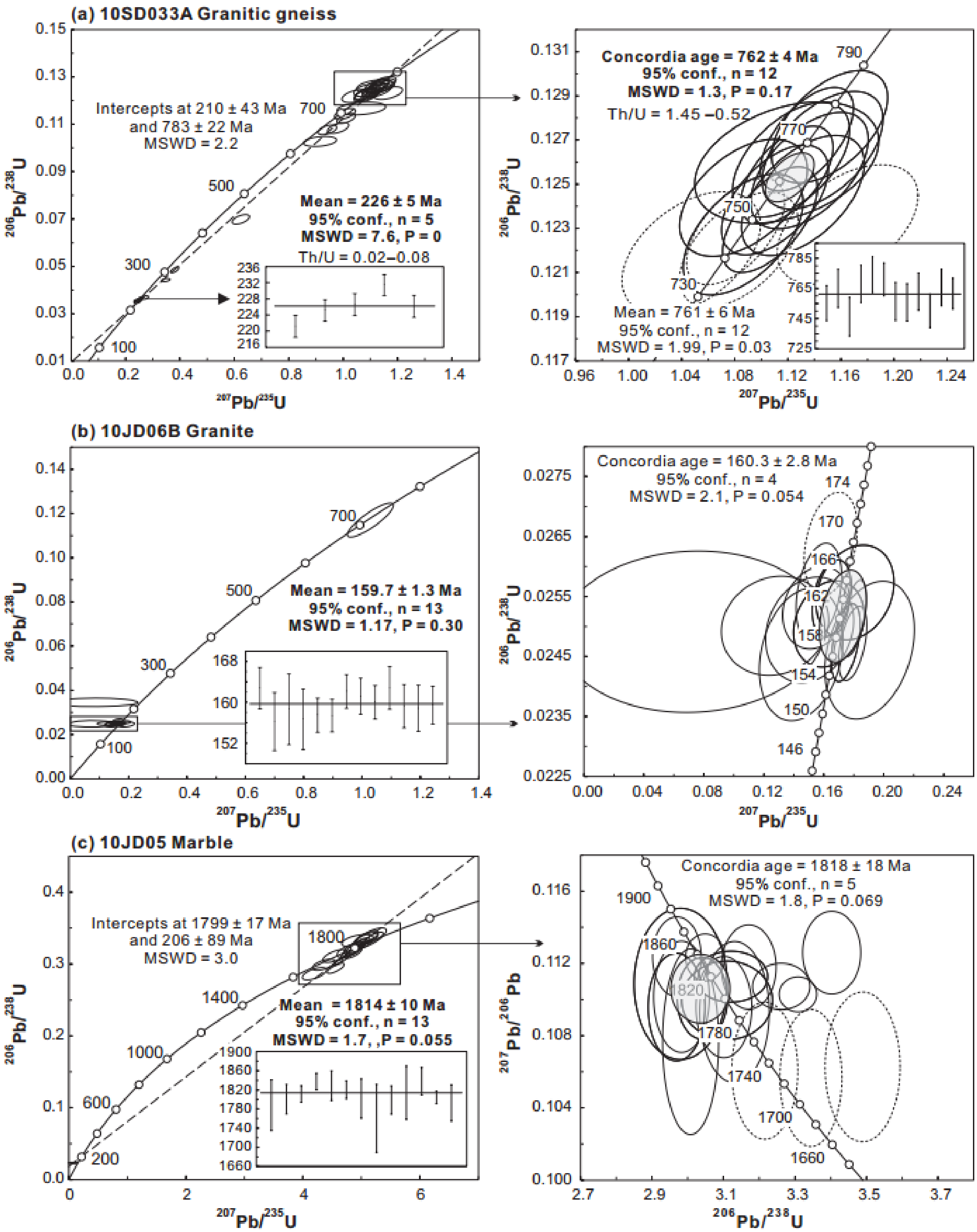

Figure 4.3 SHRIMP zircon U-Pb plots of metamorphic rock and granite samples. Mean age for younger than 1 Ga ages refers to $^{206}Pb/^{238}U$ age and $^{207}Pb/^{206}Pb$ age for older than 1 Ga ages.

Zircons from granite sample 10SD010 had euhedral and transparent morphology and exhibited oscillatory zoning in CL images (Figure 4.2d). Eighteen analyses were run on seventeen zircon grains. Two spots yielded younger and discordant ages compared with the others, possibly due to the unusually large common-Pb measurements, and therefore are considered to be outliers. The remaining sixteen analyses with Th/U ratios of 2.17–0.71 yielded a weighted mean age of 115.8 ± 1.2 Ma (MSWD = 1.45, P = 0.11, n = 16), identical with the concordia age of 115.3 ± 1.2 Ma (MSWD = 1.5, P = 0.064, n = 12) (Figure 4.3d). The granite is interpreted to have been emplaced at 115.8 ± 1.2 Ma.

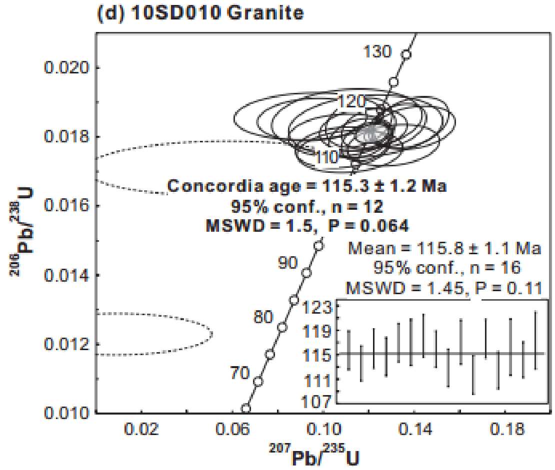

Figure 4.3 (continued).

4.3.2 $^{40}Ar/^{39}Ar$ data

All but one Late Triassic metamorphosed or intrusive rock yielded Late Triassic $^{40}Ar/^{39}Ar$ ages (Appendix Table 4.2 and **Figure 4.4**). Biotite package from sample 10SD041B yielded a plateau age at 212.9 ± 2.5 Ma (MSWD = 0.94; P = 0.46 **Figure 4.4**), identical to zircon U-Pb ages (211 ± 2 Ma–215 ± 5 Ma) (Chen et al., 2003; Yang et al., 2005a; Zhao et al., 2012). Hornblende package from amphibolite sample 10SD062B yielded a plateau age of 202 ± 15 Ma plagued by a large uncertainty due to the small sample size analysed (**Figure 4.4**b). We note that this age is consistent with a hornblende $^{40}Ar/^{39}Ar$ age of 205 ± 3 Ma reported by Faure et al. (2003a) from a sample located nearby. The single muscovite grain from gneiss sample 11LX199B was characterized by an increasingly older age spectrum until 90% ^{39}Ar was released (**Figure 4.4**c), after which the steps yielded slightly younger apparent ages. While no definitive age could be determined, a rough estimate based on a weighted average is ~215 Ma. Step heating $^{40}Ar/^{39}Ar$ results on gneiss sample 11LX196 multi-grain biotites yielded a logarithmic shape age spectrum approaching 100 Ma (**Figure 4.4**d). This result suggests that the biotite was crystallized before

100 Ma. The shape of the age spectrum also indicates partial Ar loss due to thermally activated diffusion caused by reheating during a thermal event younger than < 50 Ma.

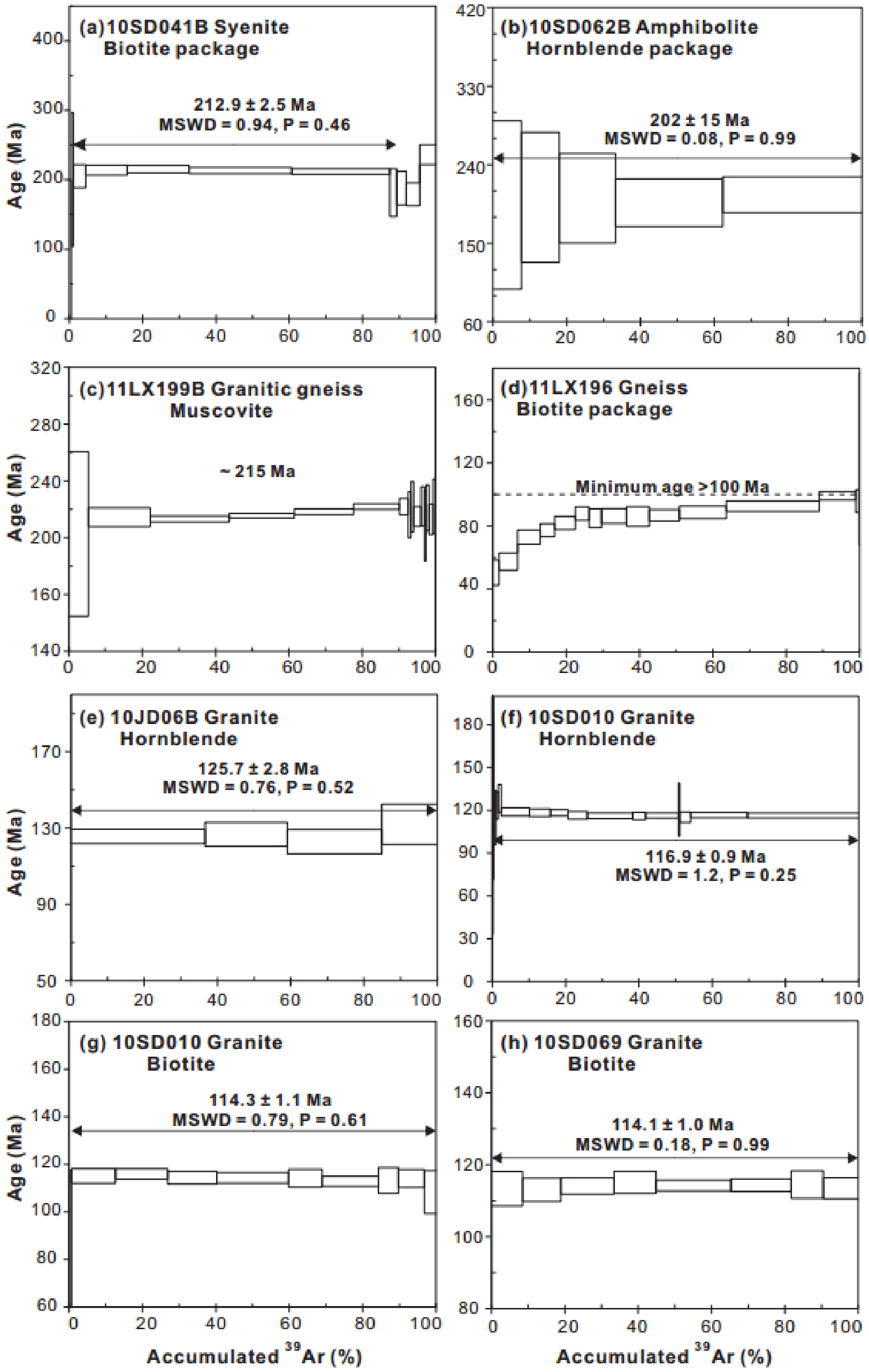

Figure 4.4 $^{40}Ar/^{39}Ar$ age spectrum for dated samples. Note 10SD041B, 11LX196 and 10SD062B results were obtained from multiple grains.

The hornblende grain from Upper Jurassic granite 10JD06B produced a concordant age spectrum with a plateau age of 125.7 ± 2.8 Ma (MSWD = 0.76, P = 0.52) (**Figure 4.4**e). Hornblende and biotite from granite 10SD010 yielded a plateau age of 116.9 ± 0.9 (MSWD = 1.2, P = 0.25) Ma and 114.3 ± 1.1 Ma (MSWD = 0.79, P = 0.61), respectively (**Figure 4.4**f and g), both indistinguishable within error from the SHRIMP U-Pb zircon age of 115.8 ± 1.1 Ma (**Figure 4.3**d). Incremental heating of a biotite grain from granite sample 10SD069 yielded a plateau age of 114.1 ± 1.0 Ma (MSWD = 0.18, P = 0.99) (**Figure 4.4**h).

4.3.3 Zircon fission-track and (U-Th)/He data

The results for zircon fission-track and zircon (U-Th)/He analyses are summarized in **Table 4.2** and detailed data are presented in Appendix Table 4.3 and Appendix Table 4.4, respectively.

ZFT analyses on four Upper Jurassic–Lower Cretaceous granitoid samples (10JD06B, 11LX209, 10SD010 and 11LX094B) all passed the chi square test ($P(\chi^2) >$ 0.27) and yielded ages of 85 ± 4, 93 ± 6, 108 ± 7 and 101 ± 6 Ma, respectively. Samples from Triassic metamorphic rocks and the Neoproterozoic granite yielded the central ages of 82 ± 5 (11LX199B), 96 ± 5 Ma (10SD061A), 125 ± 6 Ma (10SD033A) and 128 ± 8 Ma (11LX178B).

ZHe ages for twelve samples generally fell within two populations: > 160 Ma and 120–90 Ma. In the southern Sulu UHP terrane, sample 10SD041B (collected from the Upper Triassic syenite) yielded a mean age of 176 ± 8 Ma (MSWD = 1.7, P = 0.14), showed a positive linear correlation between corrected ages and radiation dose (α/g) (Appendix Figure 4.1b), and featured a long residence in ZHe partial retention zone (ZHePRZ). The ZHe ages are systematically younger than the biotite $^{40}Ar/^{39}Ar$ age (213 ± 2 Ma, Figure 4a) and zircon U-Pb ages (215 ± 5 Ma to 211 ± 2 Ma) (Chen et al., 2003; Yang et al., 2005a; Zhao et al., 2012). About two kilometres southwest of the Upper Triassic syenite, the Upper Triassic metamorphosed gneiss 10SD033A yielded a mean age of 168 ± 9 Ma (MSWD = 0.93, P = 0.45) and did not exhibit any obvious correlation between ages and radiation dose or radius (Appendix Figure 4.1b). To the northern Sulu UHP terrane, single grain ZHe ages from 11LX178B vary from 143 ± 8 Ma to 203 ± 103 Ma and show a roughly positive correlation between ages and radiation dose (Appendix Figure 4.1b). ZHe ages for 10SD033A and 11LX178B are approximately 45 Ma older than corresponding ZFT data, whereas the opposite relationship is expected given the relatively higher closure temperature of the ZFT system (230 ± 50 ℃ for ZFT sytem (Tagami and Shimada, 1996; Brandon et al., 1998) and 180 ± 20 ℃ for ZHe system (Reiners et al., 2004)).

This phenomenon will be discussed later in section 4.5.1. Other Upper Triassic or older crystallized or recrystallized rocks in the northern Sulu UHP terrane revealed mid- to Late Cretaceous ZHe ages, similar to Upper Jurassic and Lower Cretaceous granitoids samples. The ZHe ages of sample 11LX199B ranged from 83 ± 4 Ma to 105 ± 6 Ma. 10SD061A, 10JD05 and 10SD012A yielded mean ZHe ages of 102 ± 7 Ma (MSWD = 2, P = 0.13), 96 ± 5 Ma (MSWD = 0.74, P = 0.57), and 91 ± 6 Ma (MSWD = 1.1, P = 0.33), respectively. With respect to the granitoids, ZHe ages for granite sample 10JD06B, which intruded at 159.7 ± 1.3 Ma (**Figure 4.3**b), ranged from 85 ± 5 Ma to 101 ± 6 Ma and exhibited a positive correlation with radiation dose but a negative relationship with radius (Appendix Figure 4.1b). Sample 10SD010 from the Lower Cretaceous granite yielded a ZHe age range from 78 ± 4 Ma to 95 ± 6 Ma. Sample 10SD069 yielded a mean ZHe age of 90 ± 5 Ma (MSWD = 0.70, P = 0.59). Samples 11LX209 and 11LX094B from Lower Cretaceous granites yielded a mean ZHe age of 85 ± 5 Ma (four of five analyses, MSWD = 1.08, P = 0.36) and 115 ± 5 Ma (MSWD = 1.9, P = 0.08), respectively. From a spatial distribution point of view, ZHe ages increase with distance away from Wulian-Qingdao-Yantai fault (**Figure 4.5**a and **Figure 4.5**b), suggesting a gradation of cooling through the ZHePAZ (200–160 ℃). There is no correlation between ZHe ages and elevation (**Figure 4.5**c).

4.3.4 Apatite fission-track and (U-Th)/He data

The results for apatite fission-track and apatite (U-Th)/He analyses are summarized in **Table 4.2** and detailed data are presented in Appendix Table 4.5 and Appendix Table 4.6, respectively.

AFT ages range from 46 ± 3 Ma to 62 ± 4 Ma and are younger than ZHe ages (**Table 4.2**), which is consistent with the lower closure temperature of the AFT system (~110–60 ° C) (Wagner et al., 1989; Dumitru, 2000). All samples passed the chi-square test (P > 69.5%) and statistically form one population. Dpar values for 10SD033A and 11LX178B which yielded the oldest (62 ± 4 Ma) and youngest AFT (46 ± 3 Ma) ages, respectively, average 1.75 and 1.65 μm, suggesting a lower resistance to annealing for fission tracks (Carlson et al., 1999; Donelick et al., 2005). Dpar values for the other samples average from 2.04 to 2.98 μm, indicating higher resistivity to annealing. Similar to the ZHe spatial pattern in the eastern part of the Sulu UHP terrane, AFT ages show a weak positive relationship with increasing distance from WQY fault, rising from 49 ± 3 Ma to 62 ± 4 Ma (**Figure 4.5**c). Eight AFT ages were acquired, but only one sample had a sufficient number of confined fission tracks for length measurement due to the low uranium concentration in the apatites. A mean track length derived from sample 11LX178B in the northern Sulu UHP terrane was 13.9 μm with a standard deviation of 1.1 μm (**Table 4.2**). The track length distribution was weakly bimodal (**Figure 4.6**f), suggesting a moderate cooling through the apatite fission-track partial annealing zone (AFTPAZ).

Four AHe ages also show an increase from 35 ± 4 Ma (10JD06B) close to the Wulian-Qingdao-Yantai fault to 45 ± 3 Ma (10SD010 and 11LX209) and 77 ± 5 Ma (10SS033A) further from the fault (**Figure 4.5**a and **Table 4.2**), suggesting the footwall experienced a variable cooling through the apatite He partial annealing zone. Some AHe ages show correlation with grain size within a sample. A good correlation between AHe age and grain size can be observed in 11LX199B and 10JD06B (Appendix Figure 4.1a), which, therefore, cannot yield mean AHe ages. AHe ages from 11LX199B range from 27 ± 3 Ma to 80 ± 8 Ma and those from 10JD06B range from 30 ± 3 Ma to 51 ± 5 Ma. Radiation damage is also observed in 10JD06B, where AHe ages correlate positively with effective U content (eU) (Flowers et al., 2007), but no obvious correlation exists for the remaining samples (Appendix Figure 4.1). 11LX094 yielded a younger ZHe age range from 23 ± 2 Ma to 39 ± 4 Ma.

4.4 Inverse modelling

Thermal histories of the samples were modelled using the HeFTy 1.8 modelling program (Ketcham, 2005) using ZFT, AFT (age and lengths when applicable), and representative single grain ZHe and AHe data. The starting point of the time-temperature path was constrained by $^{40}Ar/^{39}Ar$ data in the form of a constraint box, dimensions of which were determined by the closure temperature range (biotite: 300 ± 50 ℃ (Harrison et al., 1985), muscovite: 350 ± 50 ℃ (Hames and Bowring, 1994), hornblende: 500 ± 50 ℃ (Harrison and McDougall, 1981)) and 2σ error of ages. ZFT data were incorporated into inverse modelling by drawing a constraint box around ZFT partial annealing zone (230 ± 50 ℃). For samples 10SD033A and 11LX178B, with ZHe ages significantly older than ZFT ages, we modelled ZFT and ZHe ages separately, although radiation damage is likely responsible for the mismatch (see discussion in section 6.1). The end point of the time-temperature path was set to 12 ± 2 ℃ according to the present mean temperature in the study area. The Monte-Carlo search algorithm was set to terminate when the number of good paths exceeded 20 at least. Specifically, the high temperature constraint of 10JD05 sample was estimated from the timing and temperature of regional amphibolite-facies metamorphism. $^{40}Ar/^{39}Ar$ ages obtained in this study were used as initial constraints for samples 10JD06B, 10SD010, 10SD41B, 11LX199B and 10SD069. For samples 11LX209 and 11LX094B, each ZFT age was used as the high temperature constraint. Constraints for 10SD033A, 11LX178B and 10SD061A were inferred from $^{40}Ar/^{39}Ar$ results from Hacker et al. (2009), Zhou et al. (2008c), Faure et al. (2003a) and 10SD062 in this study, respectively. The kinetic parameters for annealing and diffusion models for AHe, ZHe and AFT were adopted from Farley (2000); Reiners et al. (2004); Ketcham et al. (2007a), respectively.

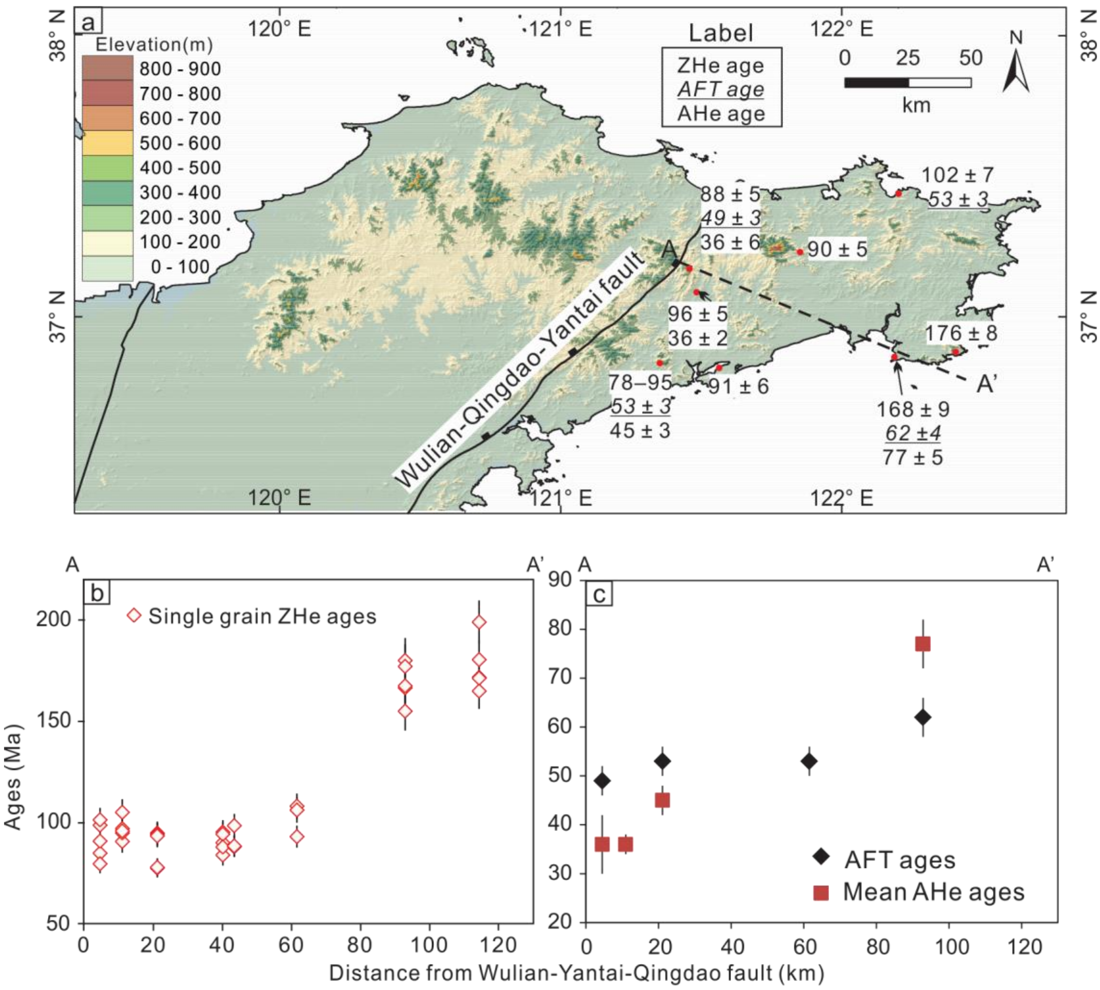

Figure **4.5** ZHe, AFT and AHe ages in eastern Sulu UHP terrane (a). Projection of ZHe data along cross section A-A' showing an increasing trend with distance away from Wulian-Qingdao-Yantai fault (b). ZHe ages-elevation plot (c).

Table 4.2 Summary of geochronology and thermochronology data in the Sulu UHP belt

	SHRIMP zircon U-Pb ±2σ	$^{40}Ar/^{39}Ar$ ± 2σ	ZFT ± σ	ZHe ± SE	AFT ± σ	N(L)	*C-axis projected MTL	SE	SD	Dpar	AHe ± SE
	Ma	Ma	Ma	Ma	Ma		µm	µm	µm	µm	Ma
10JD05	1814 ±10			96 ±5							36 ±2
10JD06B	159.7 ±1.3	125.7 ±2.8 (Hbl)	85 ±4	85 ±5 to 101 ±6	49 ±3					2.26	30 ±3 to 51 ±5
10SD010	115.3 ±1.2	116.9 ±0.9 (Hbl) 114.3 ±1.1 (Bt)	108 ±7	78 ±4 to 95 ±6	53 ±3					2.17	45 ±3
11LX209			93 ±6	78 ±4 to 116 ±6	55 ±5					2.04	45 ±5
10SD033A	~ 226		125 ±6	168 ±9	62 ±4					1.75	77 ±5
10SD041B		212.9 ±2.5 (Bt)		176 ±8							
10SD061A			96 ±5	102 ±7	53 ±3					2.98	
10SD062		202 ±15 (Hbl)									
10SD069		114.1 ±1.0 (Bt)		90 ±5							40 ±2 to 66 ±5
11LX178B			128 ±8	143 ±8 to 203 ±11	46 ±3	98	13.94 (12.69)	0.11	1.13 (1.64)	1.65	
11LX094B			101 ±6	115 ±5	54 ±4					2.08	23 ±2 to 39 ±4
11LX196		> 100 Ma (Bt)									
11LX199B		≈ 215 Ma (Mus)	82 ±5	92 ±5 or 95 ±5	52 ±6					2.3	27 ±3 to 80 ±8
10SD012				91 ±6							

*C-axis projected mean track length after (Ketcham et al., 2007b). Number in the bracket is the parameter without the c-axis projection.

Inverse modelling of eleven samples suggest three episodes of cooling in the Sulu UHP terrane (**Figure 4.6**). The first episode, from 350 to 180 ℃, occurred from the Late Triassic (~ 210 Ma) to ~160 Ma, and is shown by samples in the southern section of the UHP terrane (**Figure 4.6**a, c, and e, as recorded by ZHe ages of 10SD033A, 11LX178B and 10SD041B).

In contrast, modelling results of ZFT ages of 10SD033A and 11LX178B do not show rapid cooling during 210–160 Ma; instead, these samples did not cool through 250 ℃ until as late as 140 Ma (**Figure 4.6**b and d). The first rapid cooling for them occurred sometime during Cretaceous–early Cenozoic. This modelling result disagrees with a 196–172 Ma cooling over 350–150 ℃ shown by K-feldspar multiple domain diffusion (MDD) modelling results of Chen et al. (1992). Therefore, the ZHe ages of 10SD033A and 11LX178B are more compatible than their ZFT ages with the K-feldspar $^{40}Ar/^{39}Ar$ results and consequently support a cooling episode during 210–160 Ma. We note that this cooling episode is defined by the $^{40}Ar/^{39}Ar$ and ZHe age constraints only, and that the style and rate of cooling cannot be constrained by the HeFTy modelling. Detailed data points and cooling paths are given in Figure 4.8.

The second cooling episode for other samples, from 350 to 180 ℃, took place between ~125 Ma and ~90 Ma, and was found only in the northern part of the UHP terrane as clearly recorded by granite samples 10JD06B, 10SD010, 11LX209, 11LX094 and 11LX196 (**Figure 4.6**i–m) and somewhat less clearly recorded by metamorphic rock samples 11LX199B, 10SD061A and marble 10JD05 (**Figure 4.6**f-h). The third cooling episode occurred predominantly at ~65–40 Ma with the onset and termination ages of the relatively rapid cooling varying among the samples. Samples 11LX178B and 11LX094 show a cooling since the Miocene, which possibly reflects a local exhumation in the southwest of the Sulu UHP terrane.

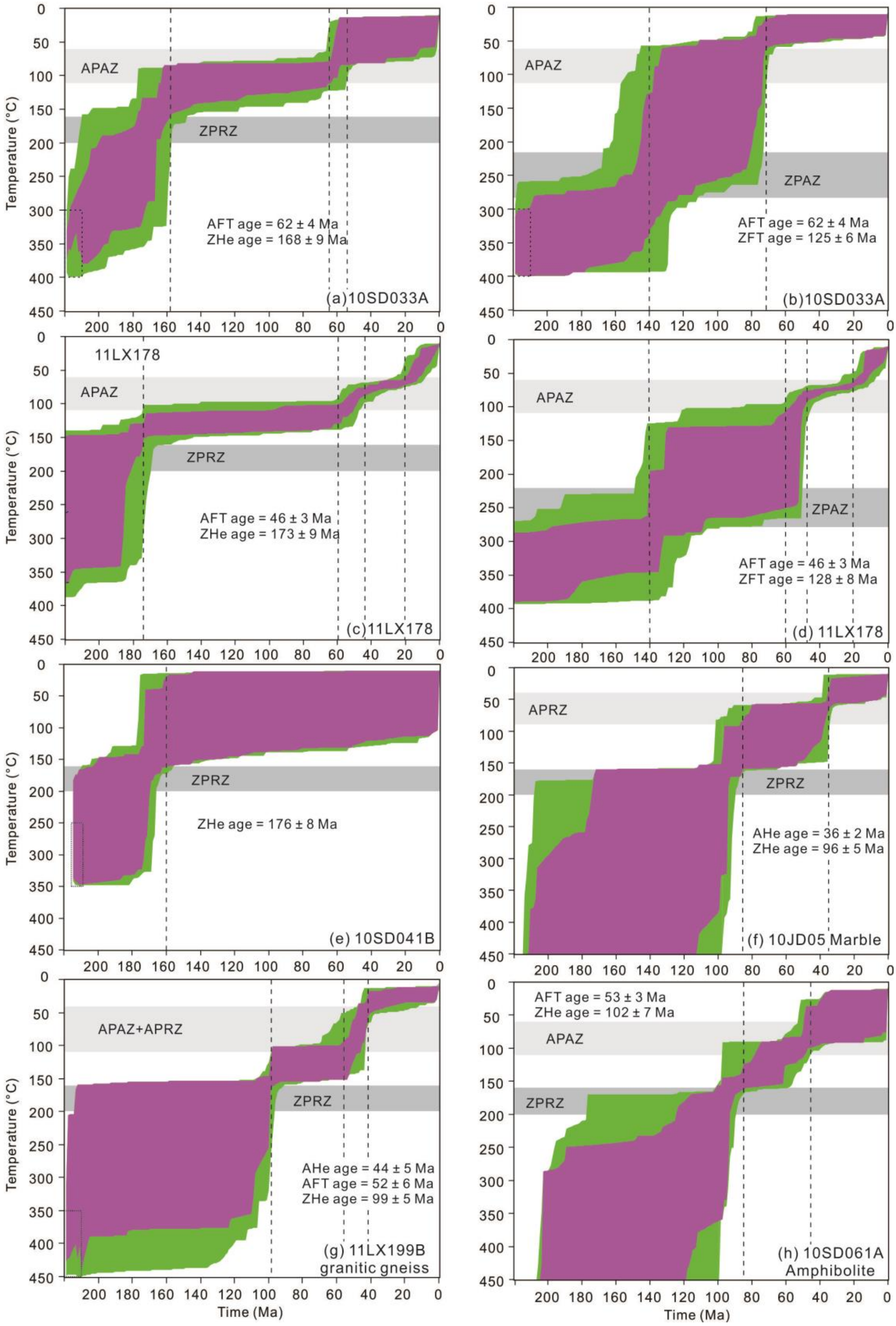
Temperature (°C)
Time (Ma)
APAZ
ZPRZ
AFT age = 62 ± 4 Ma
ZHe age = 168 ± 9 Ma
(a)10SD033A
APAZ
ZPAZ
AFT age = 62 ± 4 Ma
ZFT age = 125 ± 6 Ma
(b)10SD033A
11LX178
APAZ
ZPRZ
AFT age = 46 ± 3 Ma
ZHe age = 173 ± 9 Ma
(c)11LX178
APAZ
ZPAZ
AFT age = 46 ± 3 Ma
ZFT age = 128 ± 8 Ma
(d) 11LX178
ZPRZ
ZHe age = 176 ± 8 Ma
(e) 10SD041B
APRZ
ZPRZ
AHe age = 36 ± 2 Ma
ZHe age = 96 ± 5 Ma
(f) 10JD05 Marble
APAZ+APRZ
ZPRZ
AHe age = 44 ± 5 Ma
AFT age = 52 ± 6 Ma
ZHe age = 99 ± 5 Ma
(g) 11LX199B
granitic gneiss
AFT age = 53 ± 3 Ma
ZHe age = 102 ± 7 Ma
APAZ
ZPRZ
(h) 10SD061A
Amphibolite

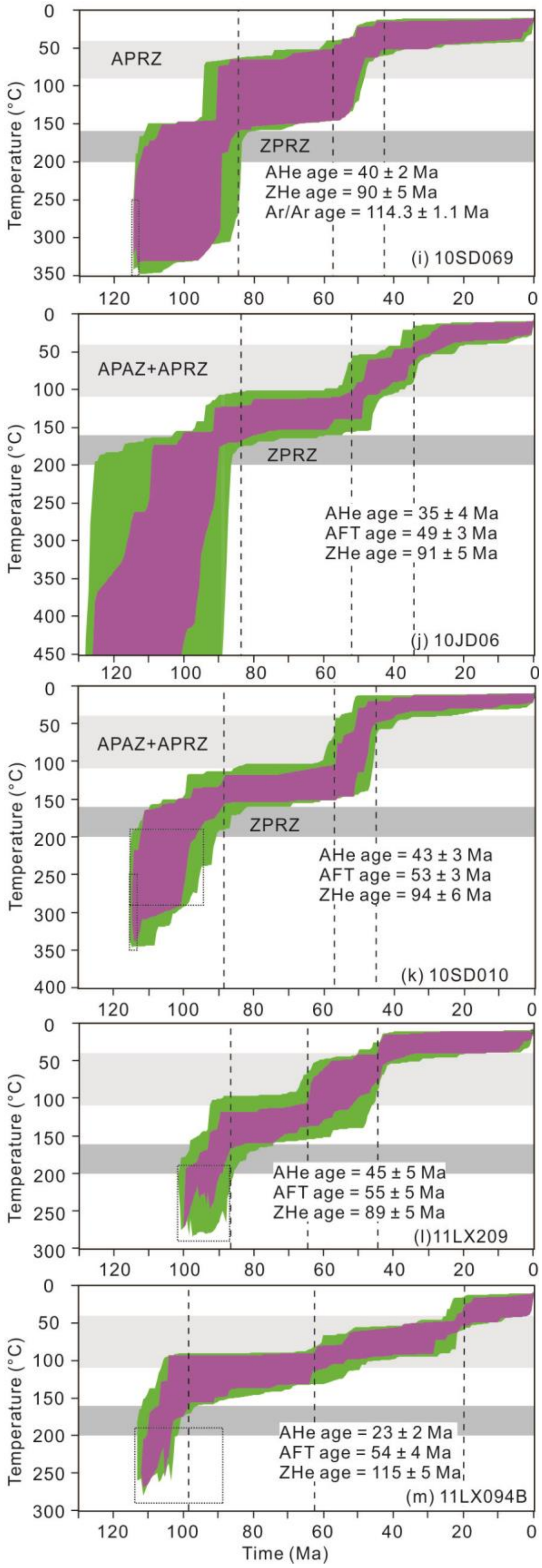

Figure 4.6 Thermal modelling results of thermochronological data in time-temperature diagrams modelled with the HeFTy program. The shaded polygons demonstrate contours of acceptable fit curves (green) and good fit curves (magenta). Dark grey bar: ZHe partial retention zone; light grey bar: apatite fission-track partial annealing zoneAHe partial

retention zone; MTL: mean track length in μm, A “good” result corresponds to the goodness of fit value 0.5 or higher. The dot lines represent dividing lines for different cooling episodes. Note the pre-160 Ma cooling paths in a, c and e are actually not constrained by modelling parameters and less reliable regarding cooling style.

4.5 Interpretation and Discussion

4.5.1 Effect of radiation damage on zircon He diffusion and fission-track annealing

Before presenting the interpretation of our results and discussing their regional implications, we address an apparent discrepancy in two samples (10SD033A and 11LX178B) where the ZFT ages are unexpectedly younger than ZHe ages, as it may have consequences for some of our geological interpretations. We attribute this mismatch to the 'antagonistic' effect of radiation damage on both thermochronologic systems. Radiation damage enhanced He retentivity is relatively well understood in apatite and effective uranium concentration [eU] has been widely utilized as a proxy for radiation damage in apatite (U-Th)/He thermochronometry (Shuster et al., 2006; Flowers et al., 2007). The order of magnitude more abundant parent nuclides in zircon tend to cause stronger radiation damage and He loss (Nasdala et al., 2004). For the ZHe thermochronometer, it was estimated that radiation damage may not significantly decrease He retention in zircon up to doses of 3.5×10^{18} a/g (Reiners et al., 2004). Relatively weaker radiation damage instead increases the He retentivity in zircon. Ketcham et al. (2013) suggest that alpha recoil damage percolated at doses from $2.5–3.1 \times 10^{16}$ α/g. The percolation and further interconnectivity of recoil damage may increase the length or difficulty of pathways that He atoms must transverse to exit crystals, thereby increasing He retentivity and the closure temperature in zircon. At alpha doses between 1.2×10^{16} α/g and 1.4×10^{18} α/g, radiation damage causes He diffusivity to decrease dramatically (by three-four orders of magnitude). Bulk zircon (U-Th)/He closure temperature increases up to 220 ℃ for alpha doses between 10^{16} to 10^{18} α /g and decreases dramatically above this dose because He diffusivity increases by about nine orders of magnitude (Guenthner et al., 2013).

The stability of fission tracks in zircon also depends on radiation damage (Kasuya and Naeser, 1988; Reiners and Brandon, 2006). At geological timescales, alpha radiation damage is retained at temperatures above the ZFT partial annealing zone, as indicated by zircon colour (Garver and Kamp, 2002). Radiation damage by alpha decay appears to cause a decrease in fission-track retentivity. Zircons with significant radiation damage have low annealing temperatures (180 –200 ℃) and thus lower closure temperature compared to fully crystalline zircons with annealing temperatures in excess of ca. 280 – 300 ℃ and thus, a higher closure temperature (Garver et al., 2005). As a consequence, single grain ZFT ages from a single sample may span a wide range showing a negative correlation between U content and ZFT age.

Hereafter, we investigate the possible effect of radiation damage on He diffusion through the proxy of the accumulated alpha dose and on fission-track annealing through uranium concentration. Alpha dose derived from the zircon He dates ranges from 1.8×10^{16} α/g to 3.1×10^{17}α/g (calculated after Guenthner et al. (2013)), lower than 10^{18} α /g. This degree of radiation damage would increase the zircon (U-Th)/He closure temperature and produce older ZHe ages. The positive correlation between radiation dose and ZHe ages in dated samples (e.g. 10SD041B, 10JD05 and 10JD06B in Appendix Figure 4.1b) corroborates the role of radiation damage in increasing He retentivity in zircon.

In addition, radiation damage is also found in many ZFT samples causing a wide range of single grain ages, as indicated by negative correlation between single grain ZFT ages and U concentration (Appendix Figure 4.1c). Due to the contrary effect of radiation damage on ZHe and ZFT systems, one sample can produce unexpectedly older ZHe ages relative to ZFT ages, as seen in samples 11LX178B and 10SD033A.

4.5.2 Thermal history and tectonic implications

Our new data extend the 210–170 Ma cooling previously recorded by K-feldspar $^{40}Ar/^{39}Ar$ data (Chen et al., 1992) and demonstrate that the cooling continued until ca. 160 Ma. However, the question remains as to whether the measured ages reflect a true cooling phase or result from reheating by 160–110 Ma magmatic intrusions (Webb et al., 2006; Hacker et al., 2009). A review and discussion of published results derived from $^{40}Ar/^{39}Ar$ thermochronology (**Figure 4.7**) is presented below, along with the new results, in order to justify the existence of a true cooling event from 210 to 160 Ma. Reconstructing a complete cooling path for the Sulu UHP terrane follows.

The regional pattern of $^{40}Ar/^{39}Ar$ results from UHP rocks conforms to a cooling event during 210–160 Ma in the UHP terrane with Early Cretaceous thermal partial resetting in the northern UHP terrane (Figures 4.7 and 4.8). Results of mica and hornblende $^{40}Ar/^{39}Ar$ analyses from the Sulu UHP belt cluster at 220–195 Ma (Chen et al., 1992; Webb et al., 2006; Hacker et al., 2009) and are generally attributed to deformation at amphibolite-facies conditions (Webb et al., 2006). K-feldspar $^{40}Ar/^{39}Ar$ results usually produce a rugged apparent age spectrum, so the reported maximum and minimum ages are employed here to constrain the time interval of cooling through the 350–150 ℃ temperature range. K-feldspar $^{40}Ar/^{39}Ar$ apparent ages from metamorphic rocks in the southern Sulu UHP terrane range from 212 to157 Ma (older ages induced by excess Ar are excluded) (Chen et al., 1992; Webb et al., 2006; Hacker et al., 2009) (**Figure 4.7**). In addition, K-feldspar and biotite (closure temperature = ~300 ± 50 ℃) from the Upper Triassic syenite yielded identical $^{40}Ar/^{39}Ar$ ages to the zircon U-Pb ages (Yang et al., 2005a), indicating no thermal disturbance to $^{40}Ar/^{40}Ar$ systems since the emplacement of the syenite and extremely fast cooling upon emplacement. Therefore, we interpret these K-feldspar $^{40}Ar/^{39}Ar$ ages representing a simple and straightforward monotonic cooling during 210–160 Ma in the southern UHP terrane.

In contrast, the northern UHP terrane produced a wider spectrum of K-feldspar apparent ages and younger minimum ages (**Figure 4.7**): from 245 to 98 Ma with most steps clustering at 130–98 Ma (Lin et al., 2005a; Hacker et al., 2009; Wang et al., 2014) (see data from Weihai, Yangkou and Haiyangsuo in **Figure 4.7**). This may arise from partial resetting of older ages which may have recorded 210–160 Ma cooling by magmatic reheating up to 350 ℃ in the Early Cretaceous. The 210–160 Ma cooling in the northern UHP terrane is preserved and evidenced by the ZHe age (from 143 ± 8 Ma to 203 ± 11 Ma) of sample 11LX178B (**Figure 4.1** and **Table 4.2**), which locally escaped magmatic reheating. Other ZHe ages (111–87 Ma) from northern UHP rocks represent the timing of cooling through 160 ℃ after the reheating. The Upper Jurassic granite (10JD06B) was likely heated up to 500 ℃ locally as evidenced by the hornblende $^{40}Ar/^{39}Ar$ age of ca. 125 Ma.

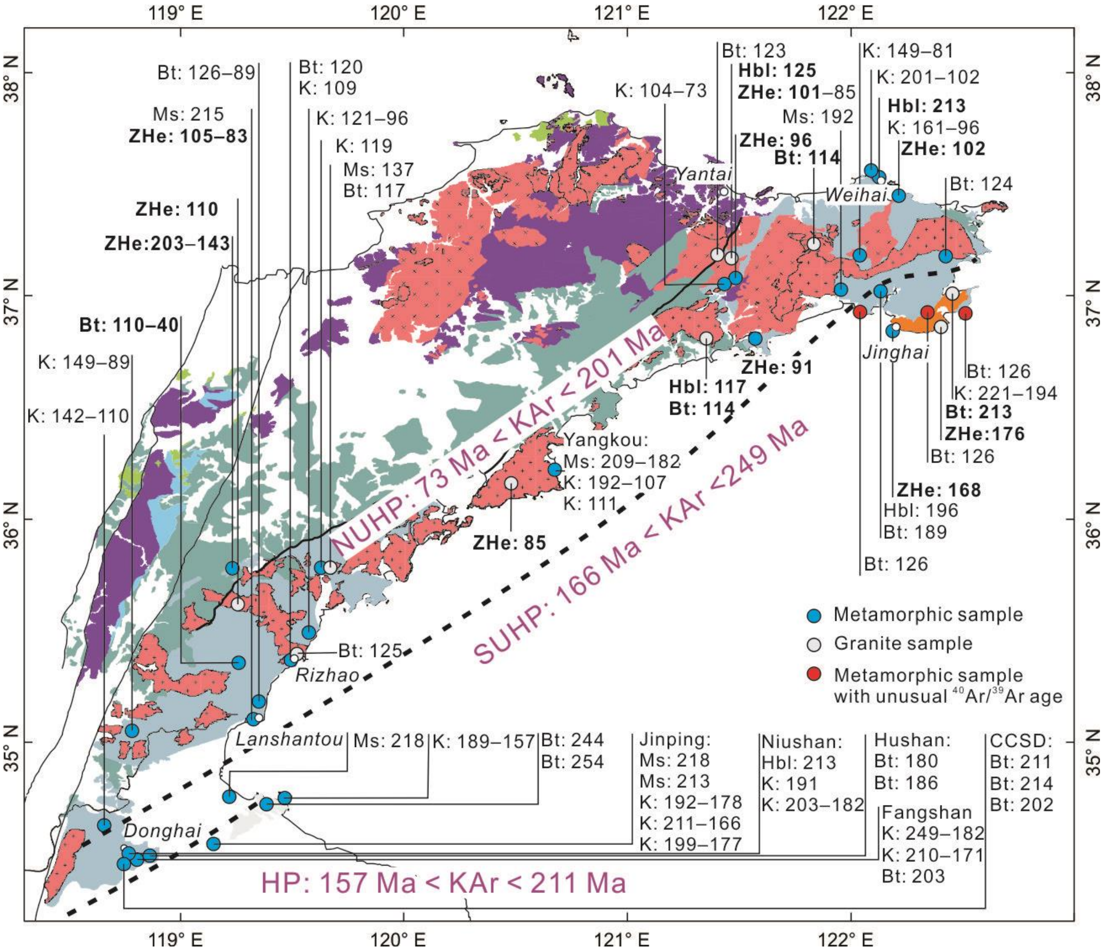

Figure 4.7 Comparison of $^{40}Ar/^{39}Ar$ results and ZHe ages in the Sulu ultrahigh-pressure–high pressure metamorphic terrane. The northern ultrahigh pressure terrane (NUHP) has a wider K-feldspar age spectrum and younger minimum age compared to the southern ultrahigh pressure terrane (SUHP) and high pressure terrane (HP), which indicates partial reheating of NUHP by the Early Cretaceous magmatism. Legend for rocks is the same as **Figure 4.1**. Hbl: Hornblende, Ms: Muscovite, Bt: Biotite, K: K-feldspar, KAr: K-feldspar $^{40}Ar/^{30}Ar$. Dataset for the figure is provided in the Appendix Table 4.7

4.5.3 Thermal history of the UHP terrane

The thermal history specific to each rock type is presented in **Figure 4.6** and **Figure 4.8** with emphasis on the syn- to post-Early Cretaceous history and pre-Early Cretaceous history, respectively. A complete history and tectonic implication is summarized in **Figure 4.9**.

The Sulu UHP rocks appear to have shared the same three-stage thermal history from 250 to 160 Ma (**Figure 4.8**a-c). The 250–235 Ma heating event corresponds to prograde metamorphism during the subduction of the South China Block (Liu et al., 2006b). After peak metamorphism during 235–225 Ma, the UHP rocks rapidly cooled down from 900–700 ℃ to ca. 350 ℃, corresponding to exhumation and retrograde metamorphism from UHP or HP granulite (Wang et al., 1993; Banno et al., 2000; Yao et al., 2000) to amphibolite-facies conditions (Yao et al., 2000; Xu et al., 2006c; Liu et al., 2009a; Zong et al., 2010b) at a rapid rate of~40 ℃/Ma. The third stage of cooling at 210–160 Ma started with the UHP rocks staying in an isothermal status at ~300 ℃ until a rapid cooling during ca. 180–160 Ma (**Figure 4.8**a-c).

However, the northern UHP rocks experienced a cooling event from 125 to 90 Ma following reheating up to 300 ℃ during the Early Cretaceous (**Figure 4.8**c), whereas the southern Sulu UHP rocks do not show the thermal overprinting (**Figure 4.8**a and **Figure 4.9**). The same 125–90 Ma cooling event as recorded by the UHP rocks was also recorded in Late Jurassic–Early Cretaceous granites (**Figure 4.8**d and **Figure 4.9**), indicating that the reheating was related to granitic intrusions. Since ca. 90 Ma, the UHP rocks and granites experienced a uniform thermal history with rapid cooling from 150 to 50 ℃ from ca. 65 to 40 Ma (**Figure 4.9**).

4.5.4 Implication of 210–160 Ma cooling for the NCB-SCB collision model

The 210–160 Ma cooling is of particular importance, representing cooling following amphibolite-facies metamorphism and overlapping in time with top-to-NW transport of the Sulu UHP terrane. It is interpreted to reflect exhumation related to northward thrust-driven uplift. Many kinematic and geochronology data indicate a top-to NW transport of the Sulu orogen throughout the UHP and HP terranes under amphibolite and greenschist facies conditions from 210 to 160 Ma. For example, mylonite shear zones that dip to the southeast in the northern part of the HP terrane suggest a top-to-NW sense of shear under low temperature conditions (Xu et al., 2006c). In the southern part of the HP terrane, NW-directed thrusts and folds are identified as the last generation of compressional deformation in the Zhangbaling region (**Figure 4.1**b) before the Cretaceous extensional deformation (Lin et al., 2005b). A series of imbricate mylonitic shear zones also show a top-to-NW shear sense under amphibolite and greenschist facies conditions in the UHP terrane (**Figure 4.1**d) (Xu et al., 2006c). Hornblende and biotite $^{40}Ar/^{39}Ar$ dating on the SE dipping shear zones yielded deformation ages of 196–189 Ma (Zhang et al., 2007).

The cooling styles of the UHP and HP terrane during 210–160 Ma can be best explained by the crustal detachment model (Li, 1994). As shown in **Figure 4.8**b and

Figure 4.9, the style of 210–160 Ma cooling of the UHP rocks is characterized by thermal stability from 210–180 Ma and rapid cooling from 180–160 Ma.

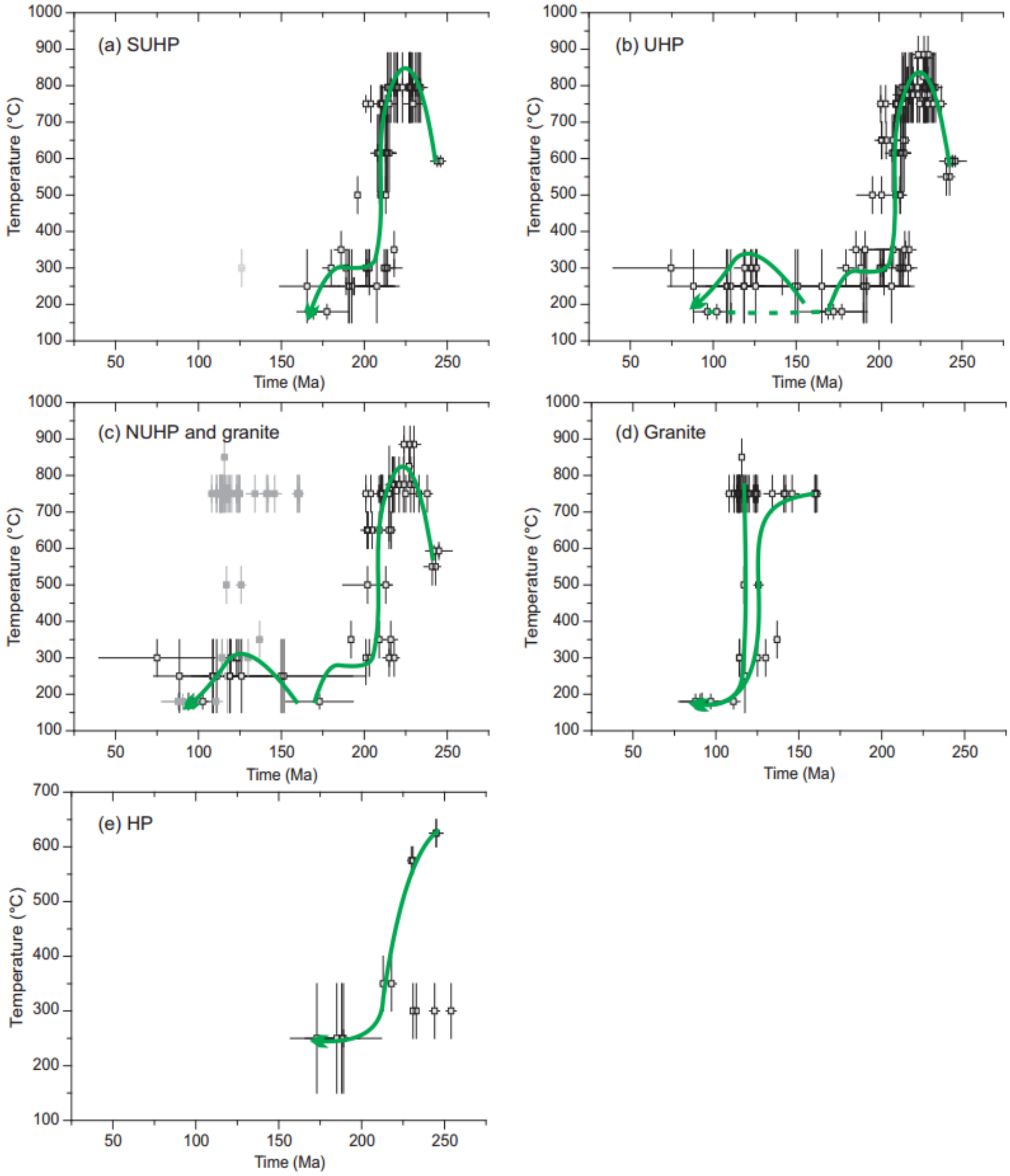

Figure 4.8 Cooling paths for different components of the Sulu ultrahigh pressure-high pressure terrane. The dataset for this figure is provided in Appendix Table 4.7.

Available data for the HP terrane also loosely define an isothermal curve at 210–160 Ma (**Figure 4.8**e). The crustal detachment model (Li, 1994; Li, 1998) proposes that during the collision of the SCB with the NCB, the middle-upper crust of the Sulu terrane were detached from the lower crust and thrust northward (present-day coordinate) along a flat detachment until finally ramping upward along the frontal thrust (**Figure 4.10**a). The predicted cooling paths for the UHP rocks and HP rocks are path ① and ② in Figure 10b, respectively. UHP rocks ① were moved horizontally along a mid-crustal detachment until ca. 180 Ma and then moved upward along the thrust frontal ramp, at which point rock ①, above the ramp, cooled down rapidly. HP rocks ② were also initially in an isothermal state but at a lower temperature compared to the UHP rocks. When the UHP rocks moved upward along the frontal thrust ramp, the HP rocks also moved upward and experienced a somewhat less rapid cooling because of increased distance from the frontal thrust ramp. The predicted paths are consistent with observed cooling paths in **Figure 4.8**b, **Figure 4.8**e and **Figure 4.9**.

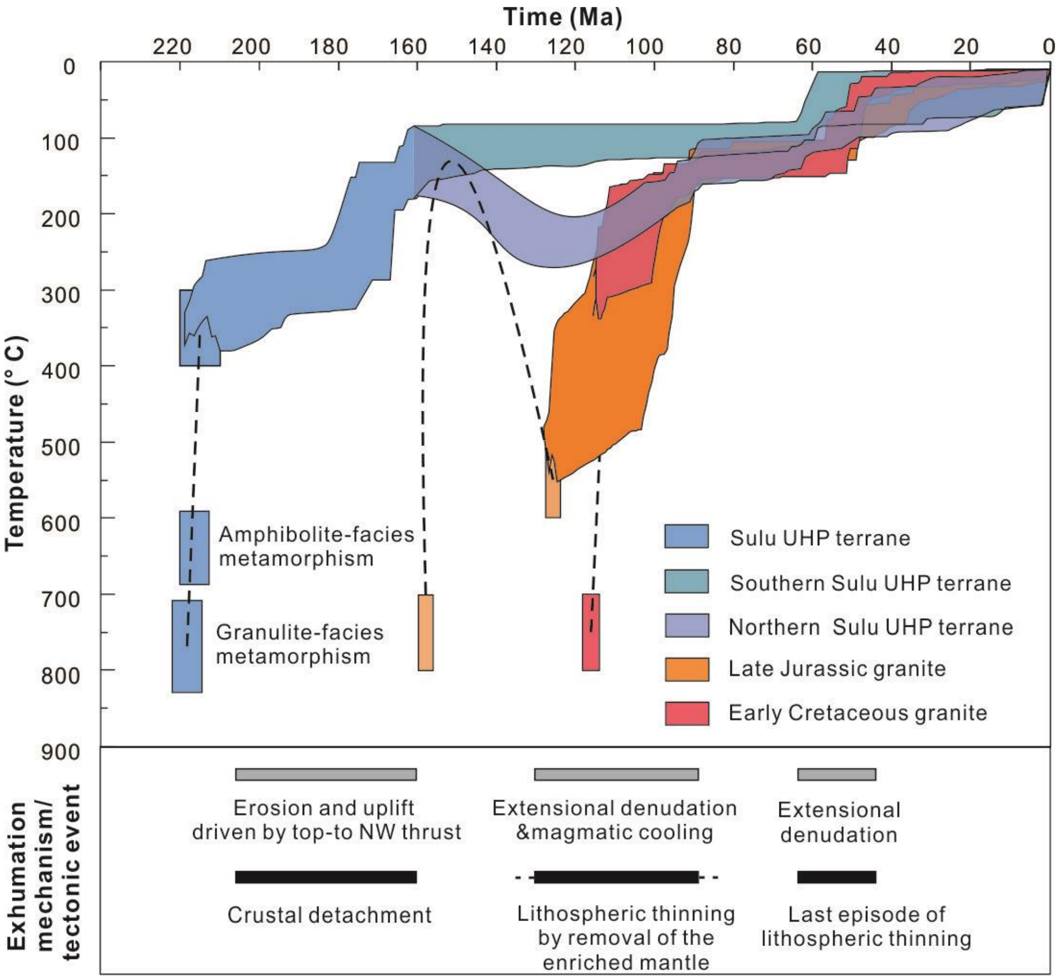

Figure 4.9 Cooling history of major components of the Sulu UHP terrane and related tectonothermal events.

In addition, the kinematics of the Tan-Lu fault also supports northward thrusting of the Sulu orogenic terrane from 210–160 Ma. Muscovite $^{40}Ar/^{39}Ar$ dating of mylonite and microstructure analyses from the Tan-Lu fault showed a sinistral ductile shear displacement at 198–181 Ma (Zhu et al., 2009). The Tan-Lu fault is predicted to participate mainly as a sinistral strike-slip fault, with a possible lateral thrust ramp role, when the Sulu orogenic terrane moved northward as a thrust sheet in the crustal detachment model. Therefore, the available kinematics and geochronology/thermochronology data support the crustal detachment model (Li, 1994) whereas alternative models cannot accommodate the thermochronology and kinematics data.

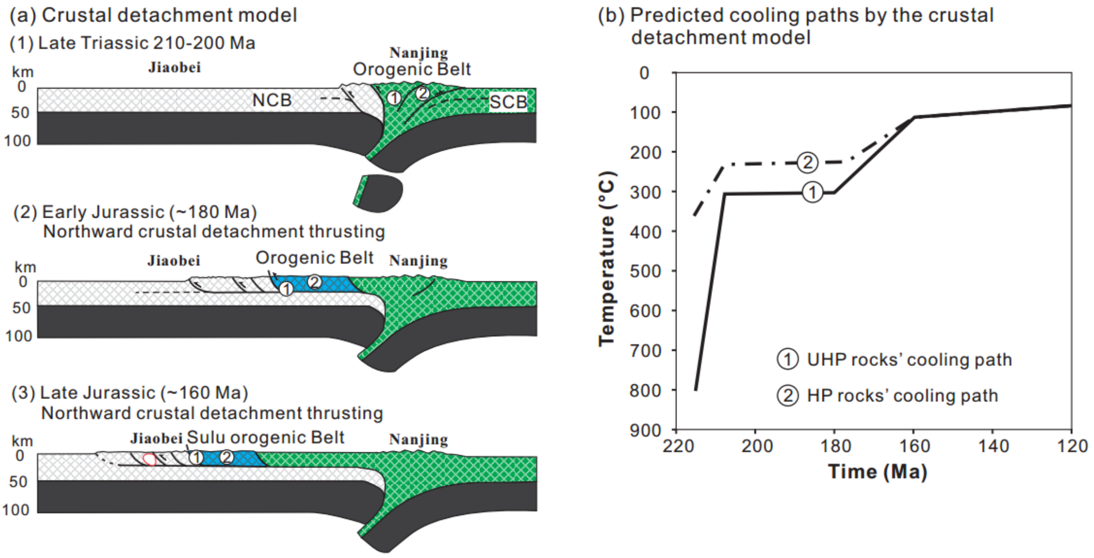

Figure 4.10 Kinematic process (a) of the Sulu UHP-HP terrane predicted by the crustal detachment model and corresponding cooling path (b).

4.5.5 Implication for lithospheric thinning from 125–90 Ma and 65–40 Ma exhumation events

Given the magmatic reheating shown by $^{40}Ar/^{39}Ar$ ages and the younging trend of ZHe ages close to the Wulian-Qingdao-Yantai fault, the 125–90 Ma cooling event is interpreted as a response to coeval magmatic reheating and normal faulting of the WQY fault. The Early Cretaceous magmatic reheating has been shown in the northern Sulu UHP terrane by the $^{40}Ar/^{39}Ar$ ages. The Wulian-Qingdao-Yantai fault was active as a top-to-west detachment fault during the Early Cretaceous (Wallis et al., 1999; Webb et al., 2006; Ni et al., 2013) and controlled Lower Cretaceous deposits in the Jiaolai Basin thickening towards the southeast (Lu and Dai, 1994). ZHe ages increase slightly within the first 70 km southeast of the fault, but an abrupt increase in ZHe ages occurs in the coastal areas (Figure 4.5). This trend is similar to observations in the footwall of the Wasatch Fault in Utah, USA, interpreted to represent normal fault growth and a tilted footwall (Armstrong et al., 2003; Ehlers et al., 2003). Thus, the 125–90 Ma exhumation is partially related to normal faulting of the WQY fault and south-eastward tilting of the Sulu UHP terrane. In contrast, the hanging wall of the Wulian-Qingdao-Yantai fault did not undergo this phase of exhumation and has, therefore, preserved the ZHe record of the previous exhumation (e.g. sample 11LX178B).

In a regional context, the 125–90 Ma event was temporally related to extensional tectonics in eastern North China. Evidence for lithospheric extension during the Early Cretaceous includes widespread metamorphic core complexes (MCC) (**Figure 4.1**b), such as the Southern Liaoning MCC (Lin et al., 2007; Yang et al., 2007; Lin et al., 2011; Wang et al., 2011a), Waziyu (or Yiwulushan) MCC (Lin et al., 2011; Zhang et al., 2012a), and Yunmengshan MMC (Davis et al., 1996; Lin et al., 2011; Wang et al., 2011a) and the bimodal characteristics of widespread Early Cretaceous volcanism (Fan et al., 2001). These phenomena conform to the idea that lithospheric thinning attained a climax in the Early Cretaceous, but it was unclear as to whether lithospheric thinning ceased prior to 100 Ma (Wu et al., 2008; Meng et al., 2014) or continued to the Late Cretaceous-Early Cenozoic (Xu, 2001; Xu et al., 2009b; Kuang et al., 2012c). The 125–90 Ma exhumation terminated synchronously with a change in source of mafic rocks from an ancient enriched lithospheric mantle to varying degrees of participation of the asthenosphere, which is recorded to occur at 100–90 Ma (Xu et al., 2004c; Guo et al., 2005a; Yan et al., 2005; Zhang et al., 2008b; Kuang et al., 2012a; Kuang et al., 2012b; Cai et al., 2013), although localized asthenospheric melting could have occurred as early as 120 Ma (Ma et al., 2014a). Therefore, the episode of exhumation is interpreted to result from removal of the ancient enriched mantle.

4.5.6 65–40 Ma exhumation and tectonic implication

The Sulu UHP terrane was again evidently exhumed between ca. 65 Ma and 40 Ma as recorded by both AFT and AHe data. This event coincided with an episode of rapid deposition in the extensional South Yellow Sea Basin (SYSB in **Figure 4.1**a) where up to 5 km of terrestrial material was deposited from Paleocene to mid-Eocene times (Li, 2010). In contrast, only sparse Cenozoic deposits are found in the Jiaolai Basin and the Sulu UHP terrane. Vitrinite reflectance data also revealed that most of the Jiaolai Basin was subject to denudation since the beginning of the Cenozoic (Lu and Dai, 1994). Hence, the cooling event was associated with uplift and erosion of the Jiaolai Basin and the Sulu UHP terrane at a time of enhanced burial and subsidence in the South Yellow Sea.

The exhumation is concomitant with another episode of lithospheric thinning in the early Cenozoic (Xu, 2001), the onset of which is marked by transition from depleted mantle-derived alkali basalts to tholeiitic basalts during 70–60 Ma in the Jiaodong and Liaodong regions, east of the Tan-Lu fault (Zhao et al., 2001a; Kuang et al., 2012c). The two discrete 125–90 Ma and 65–40 Ma exhumation events thus indicate the episodic nature of lithospheric thinning.

Magma sources for 100–40 Ma basalts in the eastern NCB indicate possible contribution from recycled oceanic crust of subducted Pacific slab (Zhang et al., 2008b; Zhu et al., 2012b). In addition, Cenozoic basins show eastward tectonic migration in eastern China (Suo et al., 2014). The latter stages of lithospheric thining, extension, and crustal exhumaton were, thus, likely related to the roll-back of the old and heavy oceanic slabs in the Western Pacific Ocean (Li et al., 2012c).

4.6 Conclusions

Based on new multi-system thermochronological data, three episodes of exhumation in the Sulu region have been identified to have occurred since 210 Ma.

The Sulu UHP terrane cooled below 160 ℃ from 210 to 160 Ma. This episode of cooling was synchronous with top-to NW thrusting. This stage of cooling and NW-directed transport in the Sulu terrane can be best accounted for by the crustal detachment model.

During ca.125–90 Ma, the northern Sulu UHP terrane underwent rapid cooling (recorded by ZHe data) as a result of post-intrusion cooling as well as normal faulting and tilting. Located in the footwall of Wulian-Yantai-Qingdao fault, the Sulu terrane tilted southward under an extensional regime and the northern section was eroded, whereas the southern section escaped major erosion. This exhumation event corresponded to removal of the ancient enriched mantle.

After stagnation from 90 to 65 Ma, another episode of exhumation from 65 to 40 Ma across the Shandong Peninsula was accompanied by subsidence of peripheral regions that are now submerged in the Yellow Sea.

The two discrete exhumation events and intervening stagnation since the Early Cretaceous demonstrate the episodic nature of lithospheric thinning in eastern

China. Rollback of the West Pacific subduction system likely induced these two episodes of lithospheric thinning and crustal exhumation.

CHAPTER 5 THERMOCHRONOLOGICAL AND STRUCTURAL CONSTRAINTS ON THE CRUSTAL EVOLUTION OF THE JIAOBEI REGION

5.1 Introduction

The Dabie-Sulu orogenic belt in eastern-central China is one of the best preserved ultrahigh-pressure (UHP) belts in the world, where the continental crust of the SCB was subducted to > 100 km depths, overprinted by UHP metamorphism, and finally exhumed to the surface (Zheng et al., 2003). A number of models have been proposed to explain the collision-exhumation processes, including the transform fault model (Okay and Şengör, 1992; Okay et al., 1993), the lithospheric indentation model (Yin and Nie, 1993), the crustal detachment model (Li, 1994; Li, 1998) and the rotational collision model (Zhang, 1997; Gilder et al., 1999; Hacker et al., 2004). Past work in the Dabie-Sulu belt commonly focused on the petrogenesis of the UHP rocks, decoding the timing and P-T conditions of the UHP metamorphism (e.g., Yang et al., 2003b; Zhang et al., 2009b). However, owing to repeated structural and metamorphic overprinting on the UHP rocks, it has been extremely difficult to restore unequivocal kinematic indicators and to constrain the timing of deformation — information crucial for unravelling the kinematics of the continental collision.

Important clues for the tectonic evolution of the orogen can be found in regions adjoining the UHP belt. However, so far very limited work has been carried out outside the UHP or HP metamorphic core of the Dabie-Sulu orogenic belt. The Jiaobei region in the NCB is located immediately to the north of the Sulu UHP belt, and could potentially retain timing and kinematic records of the orogenic processes. The Jiaobei region constitutes the southern segment of the Jiao-Liao-Ji Belt (**Figure 5.1**inset), one of the three major Paleoproterozoic orogenic belts during the assembly of the NCB (Zhao et al., 2005). Multiple episodes of deformation in the region, and loose constraints on time-temperature history, led to contrasting opinions on events affecting the region. For instance, Faure et al. (2001) linked their observed penetrative foliations and folds to the collision and collapse of the Sulu orogen, but Li et al. (2012b) ascribed them to the Paleoproterozoic orogeny. Therefore, a study combining geochronologic and thermochronologic aspects is needed to better interpret the structures observed in the region.

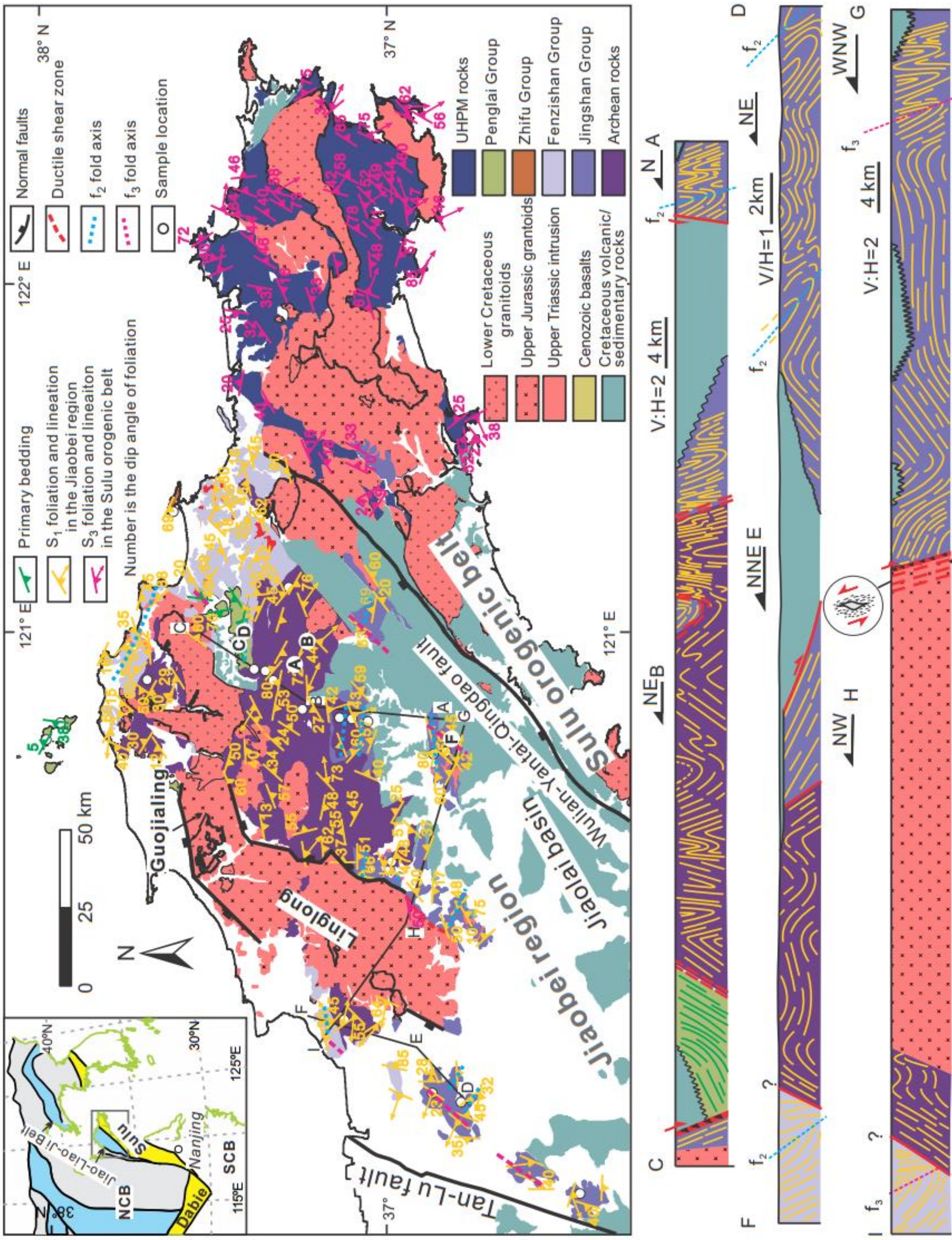

Figure 5.1 Geological map of the Jiaodong Peninsula showing the lithology, structures and sample locations. Three crustal cross sections in the lower panel show the geometry of structures. The DEF cross sections was modified after SBGB (1996). Inset map shows the tectonic location of the study area. Bold letters shaded by white circles represent the location of each figure in Figure 5.2.

This study involves SHRIMP zircon U-Pb, hornblende and mica $^{40}Ar/^{39}Ar$, zircon and apatite fission-track and (U-Th)/He dating on selected samples, as well as a basic structural analysis. These results are then applied to test the various tectonic models related to the Mesozoic continental collision, as well as subsequent tectonic events (including lithospheric thinning) in the region.

5.2 Structural Deformation

The structural pattern of the Jiaobei region is characterized by preferred NNE striking and WNW striking foliation orientation (**Figure 5.1**). Li et al. (2012b) recognised three episodes of deformation in the Jingshan Group and Fenzishan Group: The first (D_1) formed penetrative foliation with top-to NW shear sense, which transposed primary bedding and igneous textures (S_1 foliation in **Figure 5.1**). D_2 deformation was represented by NW-verging asymmetric and recumbent folds (magenta fold axes in **Figure 5.1**), while D_3 deformation was manifested as WNW-trending open to tight folds (blue fold axes in **Figure 5.1**) (Li et al., 2012b). Given that the Jiaobei region was the southern segment of the Jiao-Liao-Ji Belt, Li et al. (2012b) suggested that these structures were developed in the late Paleoproterozoic orogeny. However, previous studies (Faure et al., 2001; Faure et al., 2003a) linked the foliations (yellow foliation in **Figure 5.1**) and NNE-trending folds (magenta fold axes in **Figure 5.1**) to the Mesozoic collision between the SCB and the NCB and the subsequent extension.

Structural analysis of the Penglai Group, which was deposited during the Neoproterzoic or early Paleozoic, can provide a vital clue to the deformation styles associated with the Sulu orogeny. A previous study (Zhu, 1993) reported two episodes of deformation in the Penglai Group with an earlier episode, represented by NW-WNW-trending folds, overprinted by NNE-trending folds. These structures were attributed to the SCB-NCB collision starting from approximately 299 ± 4 Ma based on illite-whole rock Rb-Sr dating (Zhu et al., 1994a; Zhu et al., 1994b).

In this study, we combine new structural data with previously published structural data, as shown in **Figure 5.1** and **Figure 5.2**. (e.g., Zhu, 1993; SBGB, 1996; Faure et al., 2001; Faure et al., 2003a; Li et al., 2012b), and suggest that at least three stages of deformation (D_1, D_2 and D_3) exist in the Jingshan Group, the Fenzishan Group and Archean Complex, but that the Penglai Group underwent two stages of deformation (D_2 and D_3).

Structures designated as D_1 are manifested by ductile deformation, mainly including schistosity, gneissic layering (S_1) and mineral stretching lineations in the Fenzishan and Jingshan groups and Archean metasedimentary and TTG complex. The D_1 deformation also includes rootless intrafolial folds, asymmetrical folds (F_1) (**Figure 5.2**; A and B) and boudinage parallel to the surrounding banded layering (S_1). The boudinage usually consists of mafic amphibolite and granulite in gneiss and quartz/calcite-rich lenses in schist. The strike of the preserved S_1 foliation has two preferred orientations: NE and WNW (**Figure 5.1**). Although the original orientation of the S_1 foliations is obscured by later overprinting deformation events (e.g., D_2 and D_3), the mineral stretching lineations are mainly SE-NW-plunging (**Figure 5.1**), and marked by elongated hornblende grains and stretched quartz. Lattice preferred orientation of quartz from the Archean gneiss shows active basal and prism slip systems indicating moderate deformation temperatures (~350–400 ℃) (Faure et al., 2003a).

D_2 deformation is mainly characterized by WNW-trending, NNE-verging inclined folds (f_2) existing in all the lithological units. In the Penglai Group, this episode of deformation is exhibited as outcrop-scale WNW-trending isoclinal folds and south-verging thrust (Zhu, 1993). Primary bedding (S_0) of the mudstones in the Penglai Group was partly transposed into slaty cleavage (S_2) (**Figure 5.2** C-E).

D_3 deformation is marked by NNE-NE trending cleavages (S_3) and fold hinges (**Figure 5.2** C and D) and kink folds in the Penglai Group. In the Jingshan and Fenzishan groups and in the Archean Complex, D_3 deformation is manifested by a series of NW-verging inclined or overturned folds (f_3) (**Figure 5.2** F) and related axial plane cleavages (S_3). SE-verging thrusts and folds also exist in some outcrops. These structures indicate that D_3 deformation resulted from a NW-SE oriented compression.

In addition to NNE-NE trending folds and thrusts, a ductile shear zone exists along the southeast margin of the Upper Jurassic Linglong pluton **Figure 5.1**). The shear zone consists of granitic mylonites and mica-quartz schists with strongly stretched quartz and K-feldspar. The stretching lineation plunges 115° at 58° on a foliation dipping 130° at 65°. Asymmetrical pressure shadows and S-C fabric indicate a top to NW movement of the hanging wall (SBGB, 1996).

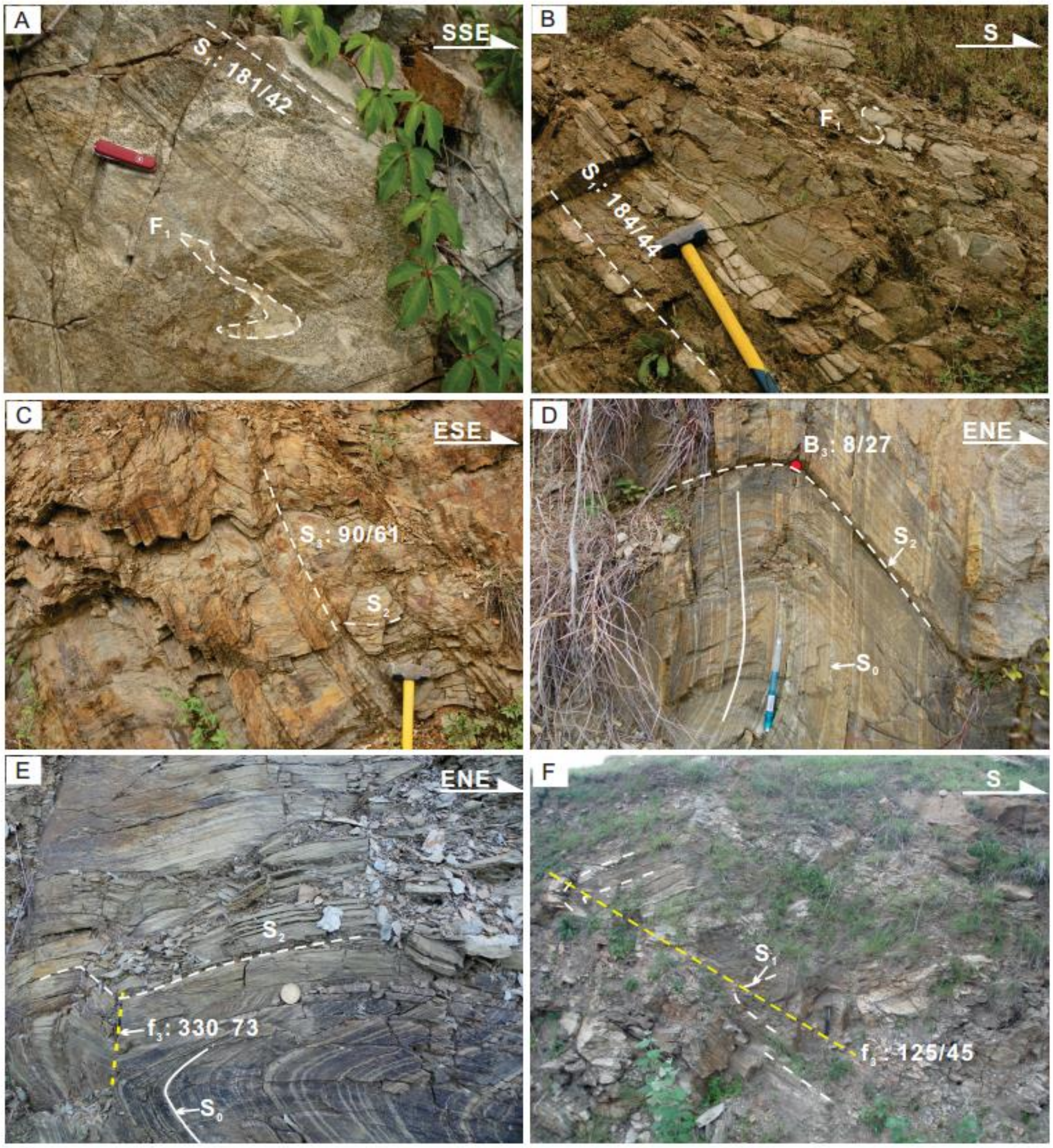

Figure 5.2 Characteristics of D_1, D_2 and D_3 structures in the Jiaobei region. (A) F_1 rootless intrafolial folds in the Archean Complex (GPS: N37°16.012’, E120°53.902’). (B) Intrafolial fold F_1 and gneissic layering S_1 in the Archean Complex (GPS: N37°13.688’, E120°57.938’). (C) Spaced cleavage S_3 cross-cutting S_2 foliation in the Penglai Group (GPS: N37°24.951’, E120°59.875’). (D and E) S_2 Cleavage refolded by NE-striking anticline (B_3) with primary bedding preserved in the Penglai Group (GPS: N37°24.869’, E121°00.417’). (F) S_1 foliation refolded by D_3 deformation with the axial plane foliation (f_2) dipping southeast in the Jingshan Group (36°48.460’, E120°42.046’). Locations of the observations are referred to Figure 5.1.

5.3 Analytical Results

5.3.1 SHRIMP Zircon U-Pb Ages

Seven samples were analysed by SHRIMP zircon U-Pb dating at Curtin University. Sample descriptions can be found in Appendix Table 5.1. The correction for initial common-Pb utilized measured $^{204}Pb/^{206}Pb$ and common-Pb isotopic compositions were determined according to the model of Stacey and Kramers (1975). All data are presented on the concordia diagrams (**Figure 5.3**) and in Appendix Table 5.2.

Twenty analyses on ten zircon grains were performed on granite sample 10SD121. The zircon crystals are transparent, stubby and exhibit core-rim structures without corrosive seams (**Figure 5.3**a). The cores showed well-developed fir-tree sector structure and the rims exhibited nebulous zoning with uniform and low luminescence. These structures can be explained either as crystallisation from melt segregations in the felsic gneisses or as solid zircon growth in the presence of fluids in the mafic granulites (Pidgeon et al., 2000). Due to the granitic compositions of this sample, these structures are interpreted as being formed from melt crystallisation. Paired analyses on rims and cores yielded contrasting Th/U ratios but overall indistinguishable ages (**Figure 5.3**a). Th/U ratios range from 0.68 to 0.83 and 0.05 to 0.07 for cores and rims, respectively, demonstrating compositional changes during crystallisation of individual crystals. All analyses yielded a concordia $^{207}Pb/^{206}Pb$ age of 1837 ± 3 Ma (2σ, n = 20, MSWD = 1.02, P = 0.44), identical to the weighted mean $^{207}Pb/^{206}Pb$ age of 1839 ± 4 Ma (n = 20, MSWD = 1.3, P = 0.19) within analytical error. The granite is considered to have crystallised at 1837 ± 3 Ma.

Most zircon grains from the foliated granite sample 10JD10 are euhedral and show core-rim structures in CL images. Most rims had fuzzy oscillatory zoning with a few displaying clear and sharp oscillatory zoning. Th/U ratios for the fuzzy (grey circles in **Figure 5.3**b) and clear rims (black circles) are 0.032–0.097 and 0.13–0.60, respectively. The $^{206}Pb/^{238}U$ ages for rims with higher Th/U ratios range from 179 ± 4 Ma (1σ) to 154 ± 1 Ma, and from 160 ± 1 Ma to 150 ± 1 Ma for rims with low Th/U ratios. The contrasting ratios may have resulted from differential Pb loss. Thirteen analyses from both types of rims yielded a weighted mean age of 157.9 ± 1.1 Ma (MSWD = 1.7, P = 0.07), which is interpreted as the crystallization age of the granite. The younger ages from fuzzy rims, ranging from 153.3 ± 0.9 Ma to 150 ± 1

Ma, may have resulted from slight lead loss due to deformation after granite emplacement.

Twenty-six spots were analysed on twenty-two zircon grains from foliated granite sample 10SD185. The zircon grains exhibit core-rim structures with rims showing oscillatory zoning and low luminescence. The analyses define a discordia line that intercepts the concordia line at 2507 ± 14 Ma and 171 ± 4 Ma, implying the involvement of Archean crust in the source of the granite. The $^{206}Pb/^{238}U$ ages of the rims range from 181 ± 2 Ma to 161 ± 2 Ma and do not define an age cluster (**Figure 5.3**c). The youngest two grains are considered to represent the crystallization age of the granite. The weighted mean age of these two analyses is 164.7 ± 2.9 Ma.

Thirty-one analyses were performed on seventeen zircon grains from Linglong granite sample 10SD154B. Ten of seventeen analyses on rims yield a weighted mean $^{206}Pb/^{238}U$ age of 157.0 ± 1.3 Ma (MSWD = 1.8, P = 0.063) (**Figure 5.3**d), while the other seven analyses were excluded from the mean age calculation due to high common Pb (Appendix Table 5.2) and unusually low UO/U ratios relative to standard zircons. Reliable ages on the cores range from 235 ± 1 Ma to 190 ± 1 Ma. This sample is interpreted to have crystallised at 157.0 ± 1.3 Ma.

Zircon grains from foliated granite sample 10JD31 are elongated, euhedral and show core-rim structures in CL images. Seventeen analyses on rims ranged from 174 ± 2 Ma to 158 ± 3 Ma and the nine youngest concordant ages yield a weighted mean age of 163.6 ± 1.2 Ma (MSWD = 1.9, P = 0.058) (**Figure 5.3**e). Two analyses were dismissed due to high common Pb abundances (Appendix Table 5.2). This granite was regarded as having crystallised at 163.6 ± 1.2 Ma, in agreement with the crystallization age of 10SD185.

Sample 10JD34 was collected from the Guojialing granodiorite. Zircon grains from the granite sample are elongated and euhedral and most are characterized by oscillatory zoning without cores (**Figure 5.3**f). Twenty analyses out of twenty-three measurements yield a concordia age of 128.7 ± 0.7 Ma (MSWD = 1.3, P = 0.095). The $^{207}Pb/^{206}Pb$ age on one core is 1825 ± 139 Ma. The granite is interpreted as having crystallised at 128.7 ± 0.7 Ma.

10SD128C is a massive medium-grained granite sample collected from the Linglong granite, which intruded the foliated fine-grained granite, 10SD128B. Zircon grains from the non-deformed sample 10SD128C show magmatic growth zonation, and inherited cores are common (**Figure 5.3**G). Forty-five analyses were conducted on thirty-five zircon grains. Apart from three inherited core ages of ca. 207 Ma, 184 Ma and 184 Ma, eleven analyses on cores yield a $^{206}Pb/^{238}U$ age range of ca. 699 Ma to 790 Ma. Eighteen analyses on the rims yield a weighted mean $^{206}Pb/^{238}U$ age of 145. 9 ±0.8 Ma (MSWD = 1.4, P = 0.13) (**Figure 5.3**G). This age represents the crystallisation age of the granite.

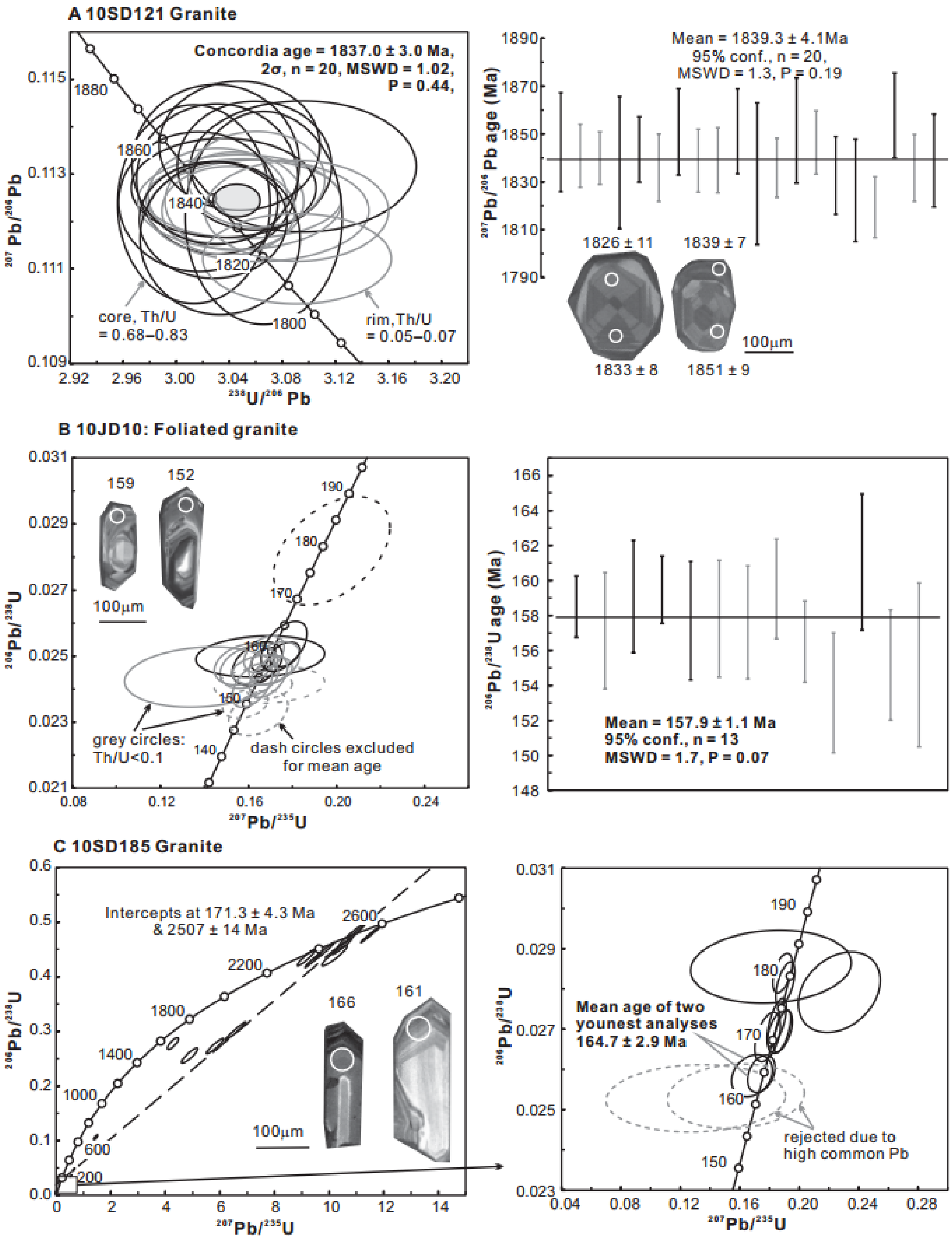

Figure 5.3 SHRIMP U-Pb zircon concordia age plots and cathodoluminescence (CL) images for samples from the Jiaobei region.

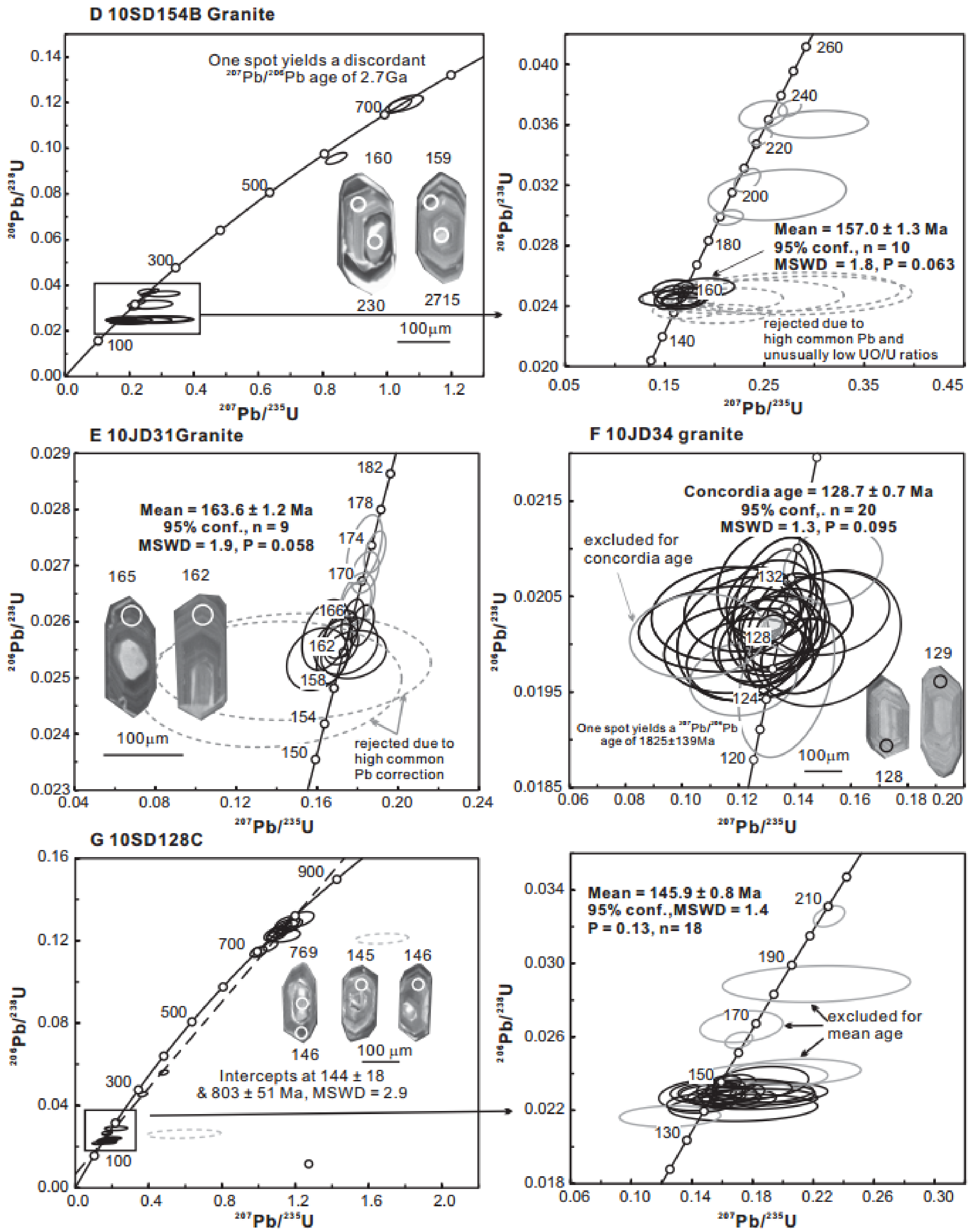

Figure 5.3 continued.

5.3.2 $^{40}Ar/^{39}Ar$ Ages

Fourteen samples were measured for $^{40}Ar/^{39}Ar$ dating. Thirteen of them were degassed by laser heating, with the exception of the multi-grain hornblende from 10SD201 that was degassed in the furnace. The results are presented in **Figure 5.4** and **Appendix Table 5.3**.

10SD134 is a diopside- and phlogopite-bearing marble. Two concordant steps from a single phlogopite grain yielded a plateau age of 1974 ± 13 Ma (MSWD = 0, P

= 1), consisting of 70% released ^{39}Ar (**Figure 5.4**a). Although the plateau consists of only two steps, they are fully concordant and represent more than 70% of the total ^{39}Ar released, giving some confidence that ~1974 Ma represents the approximate closure age of this sample. Biotite from another marble (sample 10SD138) did not yield a plateau age but each step fell within the 1600–1400 Ma age interval (**Figure 5.4**b). A single muscovite crystal from mica schist sample 10JD20 of the Fenzishan Group showed an increasing staircase spectrum in the initial incremental heating and levelled off across the following steps, defining a plateau age of 1834 ± 7 Ma (MSWD = 0.78, P = 0.62) (**Figure 5.4**c) that included 82% of the total ^{39}Ar released. The multi-grain hornblende package from the amphibolite (10SD201), which was heated in the furnace, produced a concordant age spectrum with two slightly younger steps in the middle (**Figure 5.4**d). This excursion may result from local alteration or the occurrence of inclusions in the mineral concentrate. Given that subsequent age steps were not affected, the weighted mean age of the five concordant steps (1833 ± 7 Ma; MSWD = 0.50, P = 0.87) is taken to represent the timing of cooling below the hornblende ^{40}Ar/^{39}Ar closure temperature window (500 ± 50 ℃, Harrison and McDougall, 1981; Harrison, 1982). This age is indistinguishable from the 10JD20 muscovite ^{40}Ar/^{39}Ar age. Two steps from the 10SD148 single-grain hornblende age spectrum comprised about 90% of the ^{39}Ar and yielded a plateau age of 1816 ± 32 Ma (**Figure 5.4**e). Neither analyses on single biotite grains of two samples collected from the Jingshan Group (10SD204 and 11JD006) yielded a plateau age (**Figure 5.4**f and g), but the estimated ages are likely to be late Paleoproterozoic and ca. 900 Ma, respectively. Sample 10SD207 was collected from a greenish diopside marble outcrop from the Jingshan Group, close to a small Mesozoic granite body. Step heating on single muscovite from the sample produced a decreasing staircase spectrum, with the step age dropping from 3733 ± 95 Ma to 425 ± 7 Ma as the temperature increased. This age is interpreted as reflecting a classic case of excess ^{40}Ar (Kelley, 2002b) and thus, the full closure of ^{40}Ar /^{39}Ar system is estimated to be younger than 420 Ma (**Figure 5.4**h). This age is obviously younger than other ^{40}Ar /^{39}Ar ages from the Precambrian rocks.

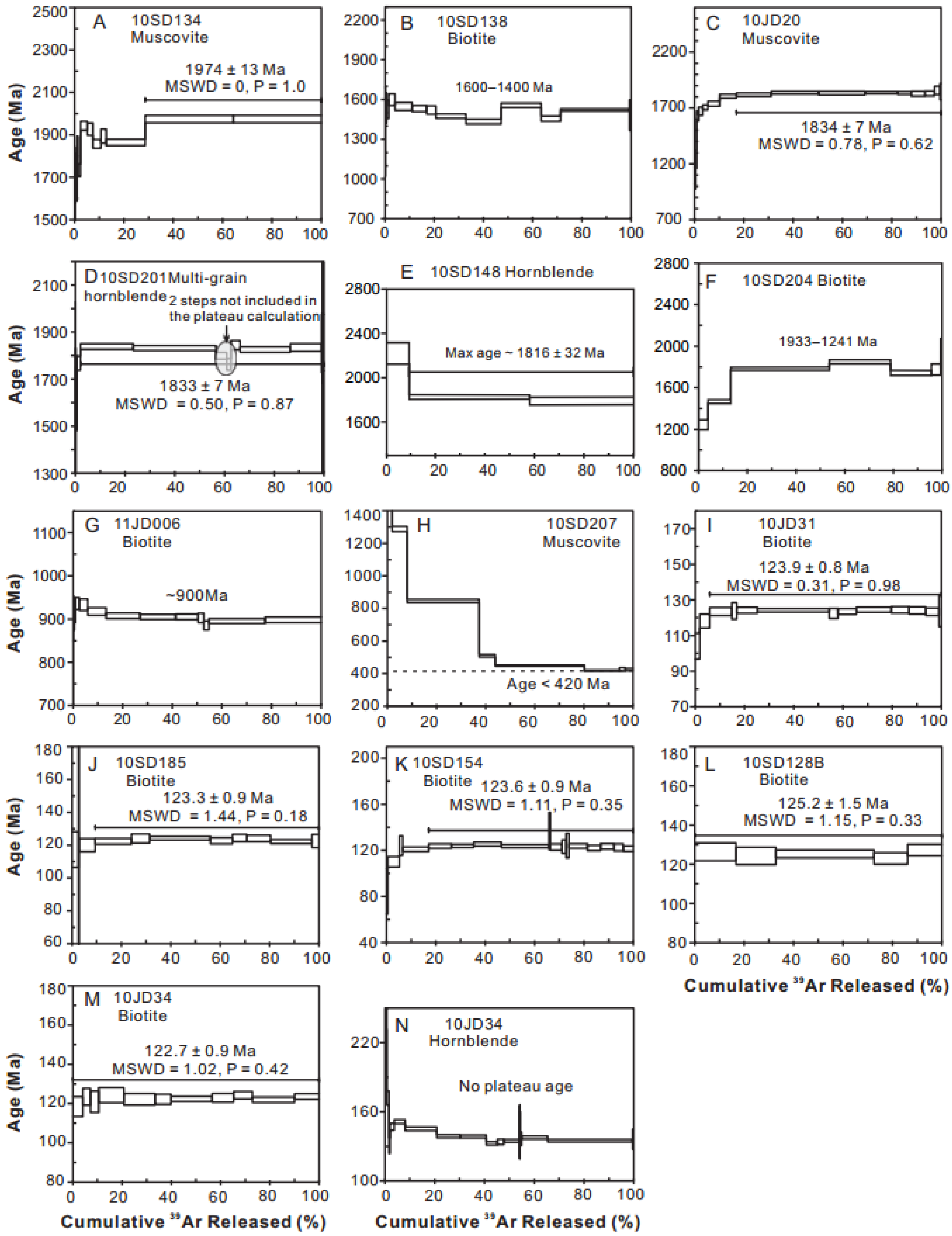

Figure 5.4 $^{40}Ar/^{39}Ar$ age spectrum from the Precambrian basement. Note: 10SD201 was degassed in the furnace.

Single biotite grains from Upper Jurassic granitoid samples 10JD31, 10SD185 and 10SD154 yielded plateau ages of 123.9 ± 0.8 Ma (MSWD = 0.31, P = 0.98), 123.3 ± 0.9 Ma (MSWD = 1.44, P = 0.18) and 123.6 ± 0.9 Ma (MSWD = 1.11, P = 0.35) (**Figure 5.4**I–K), respectively. Step heating on single biotite grains from foliated granite 10SD128B, which was intruded by the massive granite (10SD128C) at 145.9 ± 0.8 Ma, and the Guojialing granodiorite 10JD34, yielded plateau ages of

125.2 ± 1.5 Ma (MSWD = 1.15, P = 0.33) (**Figure 5.4**l) and 122.7 ± 0.9 Ma (MSWD = 1.02, P = 0.42) (**Figure 5.4**m), respectively. One hornblende from granodiorite sample 10JD34 produced step ages from an anomalous age of 5466 Ma to 172 Ma during initial heating, indicating the presence of excess argon (**Figure 5.4**n). This interpretation is supported by the initial $^{40}Ar/^{36}Ar$ ratio of 1492 ± 575, significantly higher than that of atmospheric argon (298.56 ± 0.31, Lee et al., 2006). The subsequent spectrum yielded ages from 151.3 ± 1.8 Ma to 130.5 ± 3.7 Ma without forming a plateau (**Figure 5.4**n). All step ages are older than the granodiorite zircon U-Pb age (128.7 ± 0.7 Ma), testifying to the presence of excess argon in the hornblende crystal and accounting for the lack of plateau. Overall, biotite $^{40}Ar/^{39}Ar$ ages from the Upper Jurassic to Lower Cretaceous granitoids show a concurrent cooling at ~123 Ma below the biotite $^{40}Ar/^{39}Ar$ closure temperature window (300 ± 50 ℃), regardless of their varying crystallisation ages.

5.3.3 Zircon Fission-Track and Zircon (U-Th)/He Data

Zircon fission-track (ZFT) analyses were performed on three samples from pre-collisional rocks, and three samples from Upper Jurassic-Lower Cretaceous granitoids. Each sample passed the chi-square test (P (χ^2) > 12%) (**Error! Reference source not found.**) and can be assumed to comprise a consistent age population. Quartzites from the Penglai group yielded ZFT ages of 205 ± 16 Ma and 191 ± 11 Ma (**Error! Reference source not found.** and **Figure 5.5**), respectively. One gneiss sample (10SD198) from the Precambrian basement yielded a ZFT age of 105 ± 6 Ma. The Upper Jurassic-Lower Cretaceous granitoids (10JD31, 10SD154 and 10JD34) yielded ZFT ages of 121 ± 7 Ma, 122 ± 8 Ma and 114 ± 8 Ma, respectively, recording a post-intrusion cooling event.

Table 5.1 Zircon and apatite fission track results from the Jiaobei region

Sample	# of grains	Rhos	Ns	Rhoi	Ni	Rhod	Nd	P(χ2) (%)	U (ppm)	Central Age (Ma)	± 1 σ	Dpar (μm)	SD	Non-projected MTL	SD	*C-axis projected MTL (μm)	SD
ZIRCON																	
11JD022	30	224.8	1280	78.2	445	11.1	4488	99	258	191	11						
10JD28	25	143.5	681	54.2	257	12.9	4488	91	154	205	16						
10SD198	26	178.7	882	104.2	514	10.1	4488	99	377	105	6						
10JD31	26	163.1	805	104.2	514	12.8	4488	95	298	121	7						
10SD154	25	153.4	728	96.7	459	12.7	4488	99	278	122	8						
10JD34	25	164.2	779	107.9	512	12.6	4488	12	313	114	8						
APATITE																	
11JD006	25	24.6	1204	47.9	2342	7.3	3108	91	86	58	2	2.49	0.52	13.15	1.75	14.38	1.27
10SD112	25	2.3	347	2.4	354	5.6	3108	100	5	85	7	2.26	0.56				
10SD180	25	4.3	459	9.4	1001	6.3	3108	100	23	45	3	1.86	0.25	13.55	1.16	14.48	0.95
10SD204	25	1.8	216	4.2	505	7.2	3108	81	9	48	4	1.68	0.23				
10SD121	25	36.9	687	68.5	1274	6.7	3108	99	129	57	3	2.51	0.5	12.48	1.67	13.88	1.14
10SD132	25	14	567	26.3	1069	6.3	3108	100	58	52	3	2.12	0.33	13.14	1.56	14.35	1.09
10SD128B	25	3.1	335	11.9	1293	12.8	5369	99	12	52	3	4.51	0.87				
10SD198	25	8.2	694	12.7	1067	6.6	3108	86	24	67	4	3.09	0.55				
10JD31	25	3.5	473	13.8	1836	12.6	5369	100	15	51	3	4.37	0.78				
10JD34	25	3.1	426	11.4	1551	12.5	5369	44	12	54	3	2.29	0.47				

Note: # of grains–number of individual grains dated; Rhos and Rhoi–spontaneous and induced track density measured, respectively (tracks/cm^2); Ns and Ni–number of spontaneous and induced tracks counted, respectively; $P(\chi)^2$(%)–chi-square probability, where values greater than 5% are considered to pass this test and represent a single population of ages. Rhod–induced track density in external detector CN2 dosimeter glass (tracks/cm^2) for ZFT and CN5 for AFT; Nd–number of tracks counted in determining Rhod; Dpar–pit diameter parallel to apatite c-axis; MTL–mean length of confined fission track; SD–standard deviation. The zeta value for zircon and apatite is 122.01 ± 1.73, 312.72 ± 3.4, respectively.

Zircon (U-Th)/He (ZHe) ages were obtained for fifteen Precambrian rocks (Appendix Table 5.4). ZHe ages for individual Precambrian rocks range from ~260 Ma to ~95 Ma and exhibit a younging trend toward the arcuate granitoid belt (**Figure 5.5**). Specifically, two Archean granitic gneisses in the inner domain SE of the arcuate belt, yielded ZHe ages of 260 ± 13 Ma (MSWD = 0.33, P = 0.86) and 263 ± 14 Ma (MSWD = 0.46, P = 0.71), respectively. One TTG gneiss had a weighted mean ZHe age of 185 ± 9 Ma (MSWD = 0.62, P = 0.65). Quartzite from the Penglai Group gave a weighted mean ZHe age of 196 ± 9 Ma (MSWD = 0.80, P = 0.52), indistinguishable from its ZFT age (191 ± 11 Ma). Towards the outer domain of the arcuate Upper Jurassic-Lower Cretaceous granitoid belt, one amphibolite from the Jingshan Group in the southwest yielded a weighted mean ZHe age of 164 ± 7 Ma (MSWD = 0.84, P = 0.52). One quartzite from the Penglai Group on the northernmost island of the study area (**Figure 5.5**) displayed a ZHe age of 167 ± 12 Ma (MSWD = 1.06, P = 0.36). The other quartzite yielded dispersed single-grain ZHe ages ranging from 210 ± 11 Ma to 169 ± 10 Ma, with another two grains having younger ages of 144 ± 8 Ma and 147 ± 8 Ma, respectively. In summary, the majority of ZHe ages from the pre-collsional rocks appear to be older than 160 Ma, predating the emplacement of Upper Jurassic granitoids (160–144 Ma), and therefore represent cooling prior to Late Jurassic magmatism. However, other ZHe ages from the Precambrian rocks which are closer to the arcuate belt are clearly younger than, or overlap with, emplacement (160–115 Ma) of the Upper Jurassic-Lower Cretaceous granitoids. These ages include weighted mean ages of 117 ± 6 Ma (MSWD = 0.17, P = 0.92), 115 ± 7 Ma (MSWD = 0.11, P = 0.90), 153 ± 8 Ma (MSWD = 0.15, P = 0.93), 120 ± 5 Ma (MSWD = 0.76, P = 0.58), 118 ± 6 Ma (MSWD = 1.18, P = 0.32) and 94 ± 7 Ma (MSWD = 1.7, P = 0.13) (Appendix Table 5.4 and **Figure 5.5**a). ZHe ages for the remaining two samples (10SD121 and 10SD112) range from 169 ± 10 Ma to 132 ± 8 Ma and from 136 ± 7 Ma to 102 ± 6 Ma, respectively.

Twenty-eight single-grain ZHe ages for the Upper Jurassic–Lower Cretaceous granitoids range from 125 ± 8 Ma to 90 ± 5 Ma, with the exception of one grain yielding a younger ZHe age of 70 ± 4 Ma (Appendix Table 5.4).

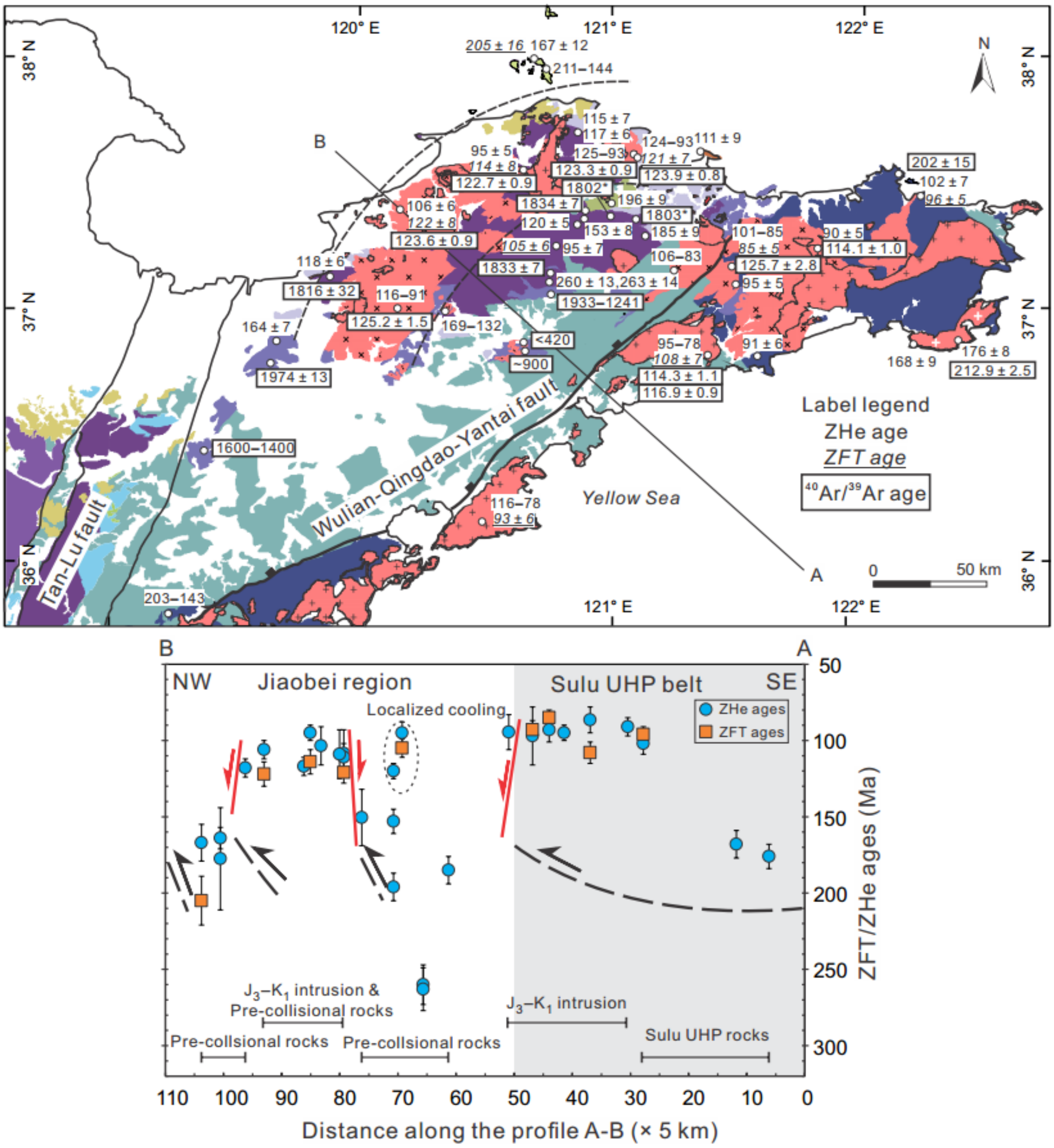

Figure 5.5 (a) New $^{40}Ar/^{39}Ar$ ages, zircon fission track and zircon (U-Th)/He ages for the Jiaodong Peninsula. (b) Time-space exhumation patterns across the Jiaodong Peninsula. Ages were plotted onto the A-B cross section following the curvatures of Upper Jurassic-Lower Cretaceous plutons in the Jiaobei region, whereas ages in the Sulu orogenic belt were plotted directly onto the cross section. Ages in the Sulu orogenic belt were cited from Chapter 4. Two $^{40}Ar/^{39}Ar$ ages with star symbol in the Jiaobei region were after Faure et al. (2003a) and Hacker et al. (2009).

5.3.4 Apatite Fission-Track and Apatite (U-Th)/He Data

Ten apatite fission-track (AFT) ages and six apatite (U-Th)/He (AHe) ages were obtained. The fission-track ages range from 67 ±4 Ma to 45 ±3 Ma, except one sample from the Zhifu Group that yielded an age of 85 ± 7 Ma (**Figure 5.6** and **Error! Reference source not found.**). Dpar values range from 1.68–4.51 μm, indicating a range of annealing kinetics among the dated samples. The mean track length for four Precambrian basement rocks vary within a narrow range of between 13.88 ± 1.09 μm (SD) and 14.48 ± 0.95 μm, suggesting monotonic cooling through the apatite partial annealing zone (110–60 ℃, Wagner et al., 1989.). Four samples (10JD34, 10SD128B, 10JD31 and 10SD185) yielded weighted mean AHe ages from 47 ± 6 Ma to 57 ± 7 Ma (Appendix Table 5.4). The remaining two samples did not yield weighted mean ages and the AHe ages vary from 54 ± 6 Ma to 21 ± 2 Ma (Appendix Table 5.4).

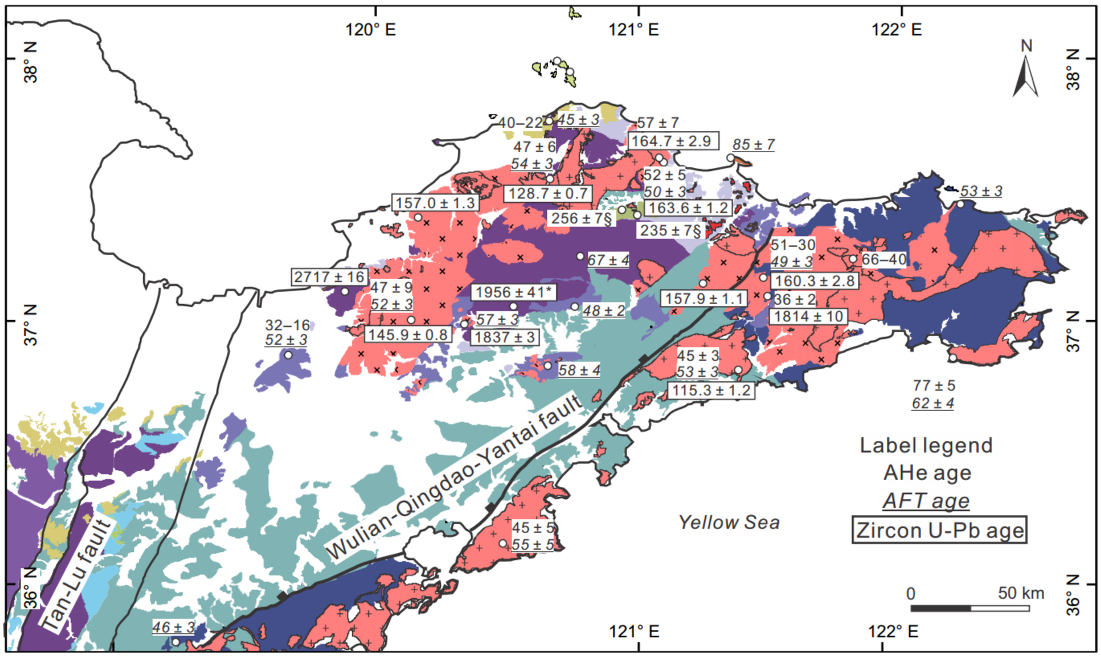

Figure 5.6 Zircon U-Pb, AFT and AHe ages for the Jiaodong Peninsula. AFT and AHe results in the Sulu orogenic belt were adopted from chapter 4. The starred Zircon U-Pb age was cited from Tam et al. (2011). Two ages from the Penglai Group with § signs were originally reported in Zhu et al. (1994b).

5.3.5 Inverse modelling

Inverse modelling of representative samples capable of yielding cooling paths with high time resolution reveals a common cooling event through the apatite PAZ/PRZ over 65–40 Ma for the Upper Jurassic–Lower Cretaceous granite and the Precambrian rocks (**Figure 5.7**). However, the samples revealed different cooling timing through the ZHePRZ, with granite samples by 90 Ma (**Figure 5.7**f-g) and the Precambrian rocks by ca.160 Ma (**Figure 5.7**i-k).

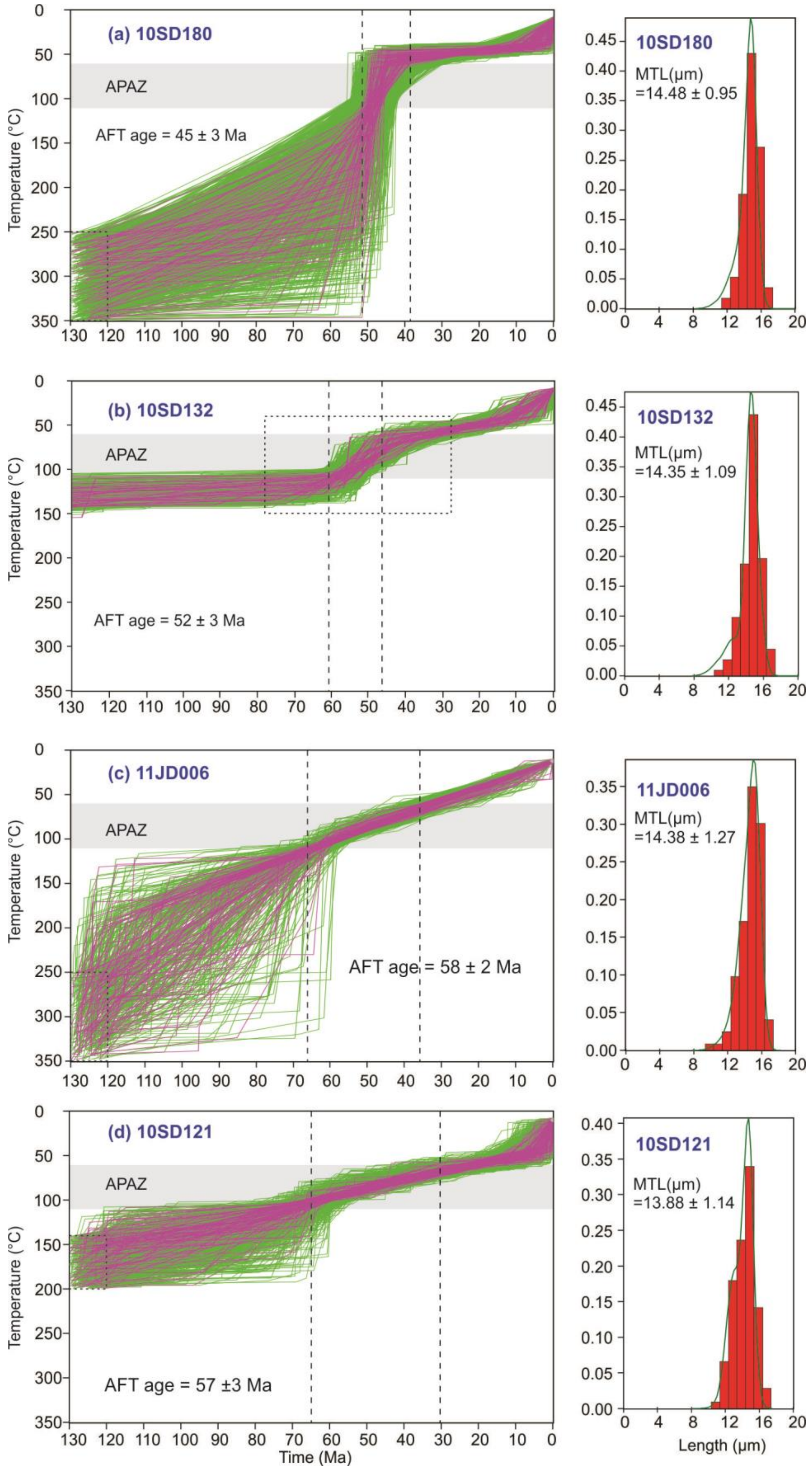
(a) 10SD180
APAZ
AFT age = 45 ± 3 Ma
10SD180
MTL(μm)
=14.48 ± 0.95
(b) 10SD132
APAZ
AFT age = 52 ± 3 Ma
10SD132
MTL(μm)
=14.35 ± 1.09
(c) 11JD006
APAZ
AFT age = 58 ± 2 Ma
11JD006
MTL(μm)
=14.38 ± 1.27
(d) 10SD121
APAZ
AFT age = 57 ±3 Ma
10SD121
MTL(μm)
=13.88 ± 1.14
Temperature (°C)
Time (Ma)
Length (μm)

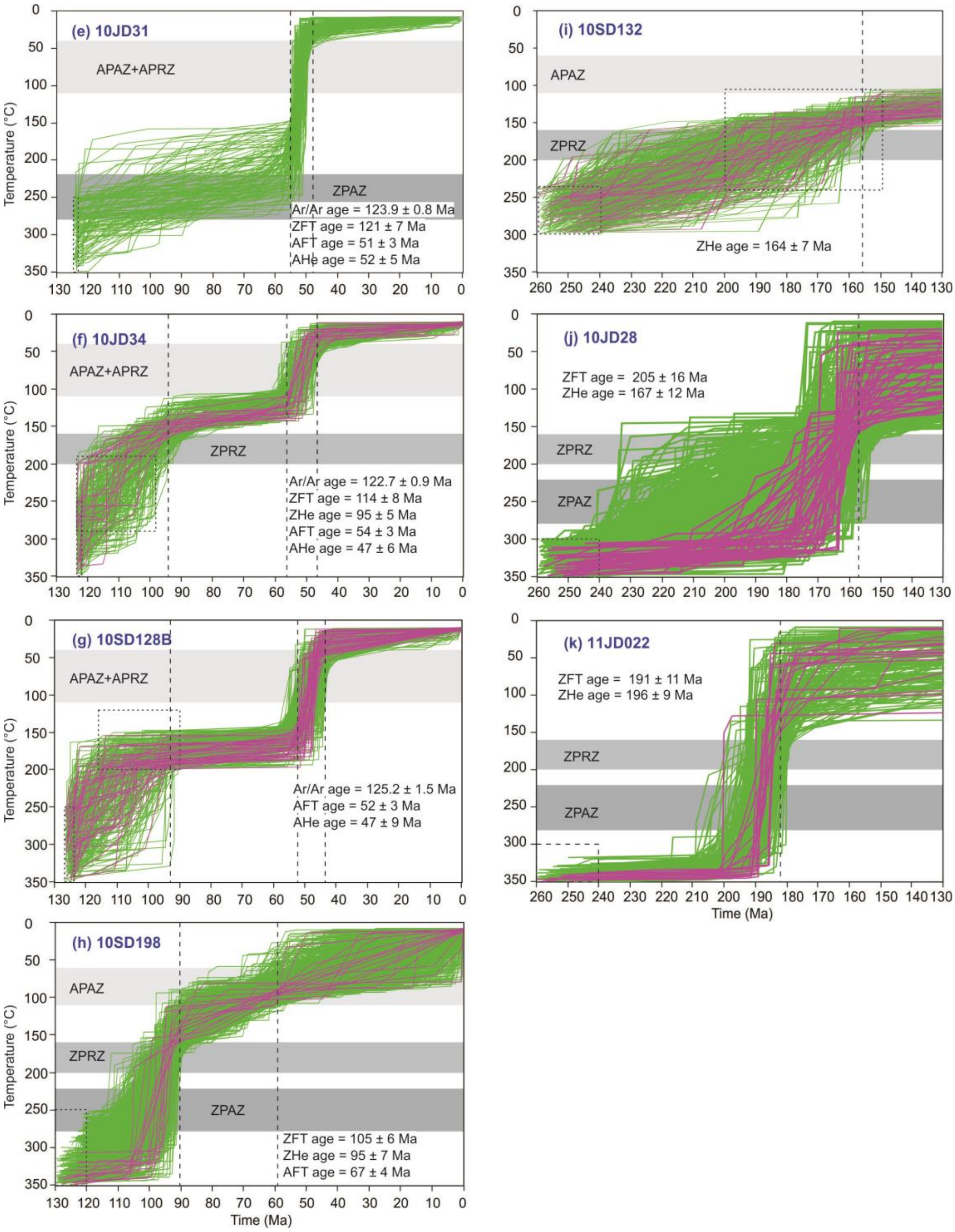

Figure 5.7 Inverse modelling of representative samples from the Jiaobei region. APAZ: apatite partial annealing zone; APRZ: apatite partial retention zone; ZPRZ: zircon partial retention zone; ZPAZ: zircon partial annealing zone. C-projected track length is used for the histogram.

5.4 Discussion

5.4.1 Timing of deformation

A number of zircon U-Pb ages have been obtained that largely reflect the timing of crystallization and metamorphism. Metamorphism related to the late Paleoproterozoic orogenesis in the Jiaobei region is generally considered to have occurred at 1.95–1.8 Ga (Zhou et al., 2008d; Liu et al., 2013a; Peng et al., 2014; Wu et al., 2014). The timing of peak high-pressure metamorphism, which formed under P–T conditions of 780–890 ℃ and 1.31–1.65 GPa (Tam et al., 2012a; Tam et al., 2012b; Liu et al., 2013d), was estimated to be 1900–1860 Ma (Zhou et al., 2008d; Liu et al., 2013d). The medium- to low-pressure granulite–amphibolite facies retrogression occurred mainly at 1860–1800 Ma under P–T conditions of approximately 590–650 ℃ and 0.62–0.82 GPa (Tam et al., 2012a; Tam et al., 2012b; Liu et al., 2013d), probably recording the exhumation of the HP granulites to shallower levels. However, only a few $^{40}Ar/^{39}Ar$ ages were available to constrain the timing of metamorphism/deformation events in the Jiaobei region. Previously obtained hornblende $^{40}Ar/^{39}Ar$ data, obtained by laser step-heating of a single grain from the metagabbro (Faure et al. (2003a), and by furnace heating of hornblende from a mafic lens in the felsic gneiss (Hacker et al. (2009) (see **Figure 5.5** for locations), constrained the timing of high temperature deformation to roughly 1805 Ma. The new phlogopite $^{40}Ar/^{39}Ar$ age of 1974 ± 13 Ma from the marble is consistent with the metamorphic zircon age of 1956 ± 41 Ma obtained on high-pressure mafic granulites (Tam et al., 2011) (see **Figure 5.5** for location) and likely records the incipient stage of collision. The new muscovite and hornblende $^{40}Ar/^{39}Ar$ data presented here from the Fenzishan Group and Archean amphibolite yielded more precise ages and constrains residence of the host rock below 350 ± 50 ℃ (muscovite $^{40}Ar/^{39}Ar$ closure temperature) after 1834 ± 7 Ma. This cooling event not only coincides with post-HP granulite-facies metamorphism, but also the crystallization age of the granite (U-Pb age of 1837 ± 3 Ma, this study) and granitic leucosomes in the mafic/pelitic granulites (Liu et al., 2014a), which reinforces 1860–1800 Ma as the exhumation stage of the HP granulite-facies rocks. The D_1 deformation, which features high to moderate temperature ductile deformation (>350 ℃), is inferred to have been predominantly produced during the late Paleoproterozoic orogeny instead of the Mesozoic SCB-NCB collision, because the

ZHe thermochronology shows that the Archean Complex cooled below 180 ± 20 ℃ by ca. 260 Ma and resided at depths corresponding to temperatures below 300 °C in the Mesozoic.

D_2 and D_3 deformation were previously interpreted to have taken place from 1914 to 1875 Ma (Li et al., 2012b). However, these folds and thrusts were mainly formed at/above mid-crust level and cannot be reconciled with P-T conditions in the late Paleoproterozoic as described above. These two episodes of deformation could have developed due to the SCB-NCB collision in the Mesozoic. This interpretation is consistent with the temperature conditions since ca. 260 Ma and the involvement of the Penglai Group in the deformation. Such low temperature deformation was recorded by the illite K-Ar and ZHe thermochronometers: slates from the Penglai Group yielded illite K-Ar apparent ages as young as 256 ± 7 Ma and an illite-whole rock pair Rb-Sr age of 235 ± 7 Ma, which likely recorded the lower greenschist-facies metamorphism and the first stage of deformation in the Penglai Group (the regional D_2 deformation) characterized by NW- to WNW-trending tight folds and cleavage (Zhu, 1993; Zhu et al., 1994a).

The NNE-trending folds and ductile shear zones with a top to NW sense of shear (D_3 deformation), are parallel to the predominant foliations in the Sulu orogenic belt where stretching lineation indicated a top to NW shear sense (Faure et al., 2003a; Xu et al., 2006c). The similarity of both structural orientation and transport polarity between the Jiaobei region and the Sulu orogenic belt may suggest that these NNE- to NE-trending structures formed in the same stress field. The predominant NE- to SW-trending foliation in the Sulu UHP rocks is considered to have been produced under retrograde amphibolite-facies metamorphism conditions (Faure et al., 2003a; Xu et al., 2006c), constrained to have taken place from 225–208 Ma (Liu and Liou, 2011). These rocks were then exhumed at 180–160 Ma as revealed by their ZHe ages (see Chapter 4). In the Jiaobei region, the ZFT and ZHe ages range from 205 ± 16 Ma to 164 ± 7 Ma, respectively. These temporal relationships and contraints corroborate the structural analysis evidence suggesting that D_3 deformation was associated with the kinematic process of exhumation in the Sulu orogenic belt.

In summary, D_1 deformation is attributed to the late Paleoproterozoic orogeny that formed the Jiao-Liao-Ji Belt, while the latter two episodes of deformation are considered to be related to collision and exhumation processes in the Sulu orogenic belt.

5.4.2 Implication for the South China-North China Collision

5.4.2.1Deformation related to collision and exhumation

Marked by initial sedimentation of the clastic sequence and rapid cooling in the northeast SCB, collision likely started from the Late Permian in the Sulu orogenic belt (Yin and Nie, 1993; Li, 1998). The subducted continental slab generally underwent peak UHP metamorphism at 235–225 Ma (Liu et al., 2006a; Liu et al., 2006b; Liu and Liou, 2011). The UHP metamorphic rocks were then exhumed to crustal levels and overprinted by granulite and amphibolite facies metamorphism *en route* by 208 Ma (Liu and Liou, 2011). Therefore, D_2 deformation, expressed as NW-WNW trending folds and exhumation at ~260 Ma, was likely associated with the incipient continental collision stage before 235 ± 7 Ma (see **Figure 5.5**). The D_3 deformation may relate to subsequent exhumation of the Sulu UHP rocks, which lasted until ~160 Ma (Liu et al., 2014c). The stress field changed to NW-SE oriented compression during the exhumation and produced a series of NNE-trending overturned folds with the axial surface dominantly dipping southeast. Backthrusting also developed.

5.4.2.2 Westward propagation of thrusting-related exhumation

A comprehensive view of the exhumation across the Sulu orogenic belt and the Jiaobei region can be provided by comparing all ZHe ages across the region. ZHe ages from the Sulu UHP rocks which escaped from subsequent magmatic reheating, ranged from 180 to 160 Ma, younger than the ages from basement rocks SE of the Upper Jurassic-Lower Cretaceous granitoid belt (205–176 Ma) (**Figure 5.5**). This probably suggests an active thrust fault between the Sulu orogenic belt and the Jiaobei region at 180–160 Ma. Although post-orogenic erosion could lead to an increase in ZHe ages from the orogenic core to its flank (Reiners et al., 2003), this process cannot unequivocally explain age relationships in this study area because the ZHe ages become younger (179–155 Ma), instead of older, further northwest of the inner domain (**Figure 5.5**). Therefore, we consider that tectonic exhumation by thrusting was the dominant factor controlling ZHe ages across the Jiaodong Peninsula. Thrusting may result in burial of the footwall, as well as creation of topography and relief in the hanging wall with concomitant erosion. Thus, initiation of rapid cooling in the hanging wall typically reflects the youngest thrust movement (Metcalf et al., 2009; Fitzgerald et al., 2010). ZHe ages of 179–155 Ma in the outer domain and those of 205–176 Ma in the inner domain record the minimum ages of thrusting. It is noteworthy that younger ZHe ages in the outer domain reflect the later initiation of thrusting toward the northwest during continued deformation.

5.4.2.3 Crustal detachment model

Several models have been proposed for the collision between the SCB and the NCB. The indentation model suggested a promontory in the north margin of the South China block with initiation of collision with the North China block in the Late Permian (Yin and Nie, 1993). The problem with this model is that orthogonally oriented structures cannot be accounted for by continuous, uni-directional indentation of the SCB. In addition, a pulse of rapid exhumation, predominantly in the Jurassic rather than the Triassic, is also difficult to accommodate by the indentation model, which limits intense thrusting and inferred exhumation primarily to the Triassic (Yin and Nie, 1993). The transform-fault model requires that the NCB was subducted underneath the SCB in the Sulu orogenic belt (Okay and Şengör, 1992; Okay et al., 1993), contrary to the present-day finding that UHP rocks have an affinity with the SCB. The rotational collision model (Zhang, 1997) faces the same challenge as the indentation model.

On the other hand, the change of stress field between the collision and exhumation stages in the Sulu orogenic belt is consistent with the prediction of the crustal detachment model (Li, 1994), which explicitly accommodated the change of structural orientation during the transcrustal exhumation of the Sulu UHP rocks, and also explains the style of exhumation in the Jiaobei region as revealed by ZFT and ZHe thermochronology. The kinematic processes, integrated with thermochronologic data from the Jiaobei region, are described below according to the crustal detachment model (Li, 1994; Li, 1998). During the progressively deeper subduction of the SCB, the Jiaobei region was under N-S compression and produced WNW trending folds (D_2 deformation) from south to north (**Figure 5.8**a). Local exhumation related to this deformation was recorded by ZHe ages of ca. 260 Ma, but this episode of deformation was not so intense as to exhume most of the Jiaobei region to ZHe sensitive temperatures. Following the UHP-HP exhumation to the base of the crust, underthrusting of the upper crust of the SCB pushed the UHP-HP rocks northwest, and caused the upper crust of the North China block to detach from its lower crust (**Figure 5.8**b). The UHP-HP rocks and the upper crust in the Jiaobei region were pushed northward above the NCB lower crust and mantle, driven by continued convergence. As a result, the majority of the present-day exposed rocks in the Jiaobei region were deformed by the D_3 deformation, pushed upward and cooled through ZHe temperature window of 180 ± 20 ℃ (Reiners et al., 2004) at ca. 205–176 Ma in the east and at ca. 179–155 Ma in the west. Upper Jurassic granites (e.g., samples 10SD185, 10JD31, 10JD10, 10SD154) were emplaced during late stage thrusting and exhumation. A top-to-northwest ductile thrust was developed along the southeast margin of the Upper Jurassic Linglong granite. Neoproterozoic U-Pb ages of inherited zircons in the ~146 Ma undeformed granite may imply that materials originally located in the Sulu orogenic belt were also transported by means of the weak detachment zone to be emplaced in the Linglong pluton. The younger $^{40}Ar/^{39}Ar$ ages (~900 Ma and <420 Ma) from the Jingshan Group may have resulted either from a weak Paleozoic event or from magmatic reheating in the Mesozoic.

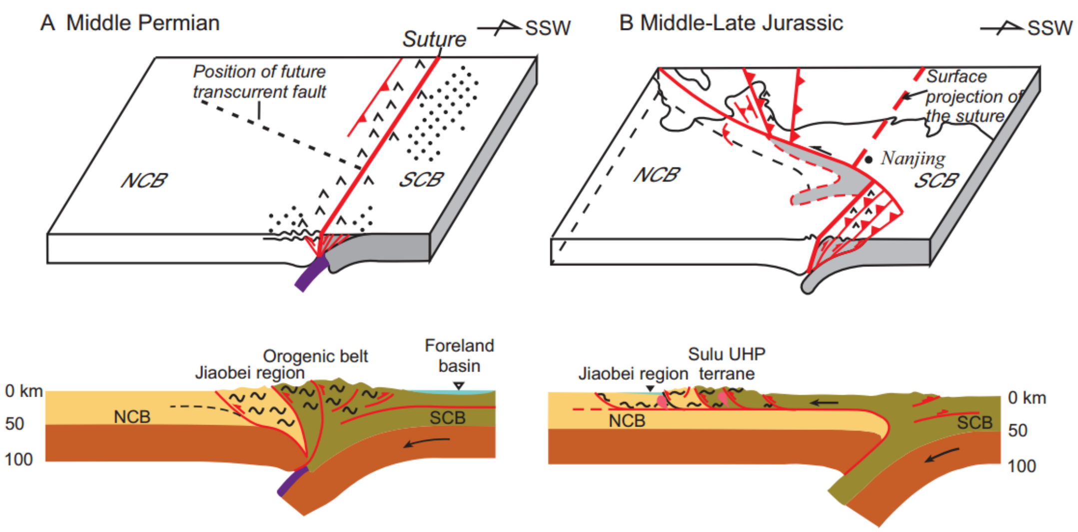

Figure 5.8 Schematic map and lithospheric cross sections showing the kinematic process for the Mesozoic collision between South China and North China blocks, modified after Li (1994) and Li (1998).

The ZFT age of 205 ± 16 Ma from the Penglai group likely represents the timing of earlier cooling through a higher temperature of 230 ± 50 ℃ (Tagami and Shimada, 1996; Brandon et al., 1998). It remains ambiguous as to whether deformation could have continued until 153 ± 8 Ma (ZHe), because this age could reflect the Late Jurassic to Early Cretaceous magmatic reheating. This thermal reheating also potentially renders the significance of the ZFT/ZHe ages from 143 ± 8 Ma to 95 ± 7 Ma as ambiguous, as they may have recorded either cooling following the magmatic reheating, or extensional erosion during that time.

5.4.3 Extensional Tectonics and Implication for Lithospheric Thinning

Biotite $^{40}Ar/^{39}Ar$ ages from the Upper Jurassic–Lower Cretaceous granitoids recorded their concurrent cooling below 300 ± 50 ℃ at 125–122 Ma. The exhumation of the Upper Jurassic–Lower Cretaceous granitoids was most likely caused by extensional denudation of the footwall of normal faults. For example, the arcuate Upper Jurassic–Lower Cretaceous granitoid belt is bordered by an east-southeast dipping fault with top-to SE ductile shear in the east margin of the Linglong pluton and a north-dipping normal fault with top to NW shear in the north of the Guojialing pluton (Charles et al., 2011). The southern segment of the former fault was originally a ductile thrust along the southeast margin of the Linglong pluton in the Late Jurassic and was reactivated as a normal fault in the Cretaceous. Synkinematic white mica on the brittle plane of this fault yielded $^{40}Ar/^{39}Ar$ ages of 130–126 Ma (Charles et al., 2013). The faulting was accompanied by gold mineralization in the footwall, as confirmed by $^{40}Ar/^{39}Ar$ geochronology on hydrothermal sericite and muscovite from a gold deposit along the fault (Yang et al., 2014a). The latter fault is a juvenile normal fault, cutting the Guojialing pluton. The Upper Jurassic–Lower Cretaceous granitoids exhumed like a horst between the two faults and cooled below 300 ± 50 ℃ at 130–122 Ma. Further insight into the subsequent exhumation of the Upper Jurassic–Lower Cretaceous granitoids can be gained from the ZFT and ZHe ages which are sensitive to lower temperatures. The cluster of ZFT and ZHe ages between 125 ± 8 Ma and 90 ± 5 Ma indicates that this exhumation lasted until ~90 Ma, mainly as a result of normal faulting. Thus, the $^{40}Ar/^{39}Ar$ ages and ZHe ages, along with ZFT ages, defined the duration exhumation as ~130 Ma to ~90 Ma.

This knowledge of exhumation, coupled with features of igneous magmatism, can help elucidate the process of lithospheric thinning. It is commonly recognised that the eastern NCB has undergone widespread lithospheric thinning with removal of up to 120 km of lithospheric root since the Mesozoic (Menzies et al., 1993; Griffin et al., 1998; Xu, 2001). This exhumation appears to have commenced with a simultaneous 132–120 Ma “giant igneous event” in eastern China (Wu et al., 2005) and terminated when the enriched lithospheric mantle was largely removed in the Jiaodong Peninsula, as evidenced by associated mafic magmatism that shows a transition from an ancient lithospheric mantle isotopic signature to a young asthenospheric mantle isotopic signature from 100–90 Ma (**Figure 5.9**). The 40-million-year duration of removal of ancient lithospheric mantle indicates that this episode of lithospheric thinning likely resulted from small convective instabilities developing over a range of tens of million years, in contrast to large drips that should appear as catastrophic events in the geologic record.

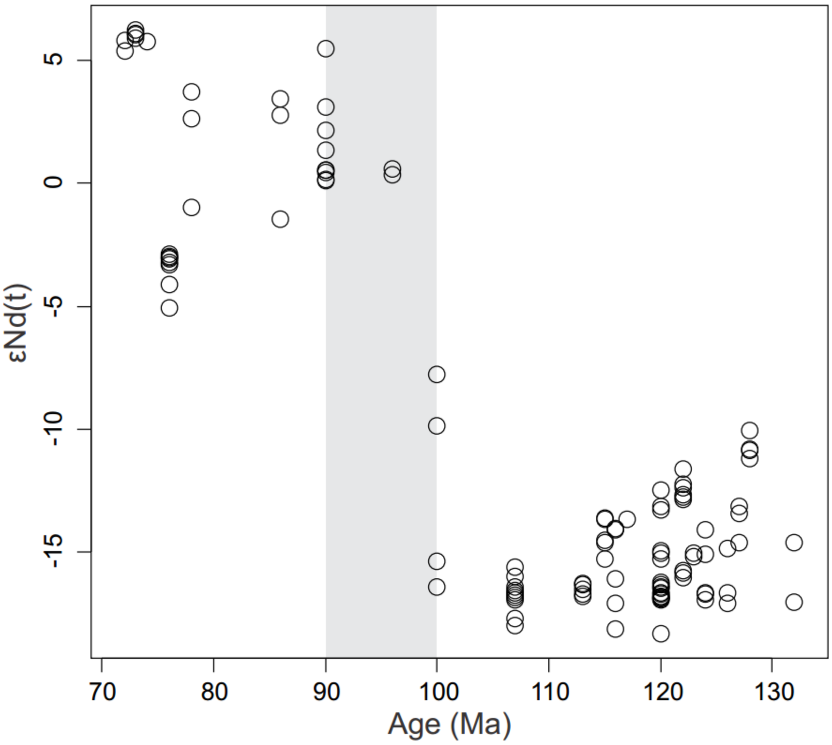

Figure 5.9 Whole rock εNd(t) versus ages for Cretaceous mafic rocks in the Jiaodong Peninsula. Data sources are: Guo et al. (2004), Yang et al. (2004), Guo et al. (2005a), Yan et al. (2005), Zhang et al. (2008b), Liu et al. (2009b),Kuang et al. (2012a), Kuang et al. (2012b), Cai et al. (2013), and Ma et al. (2014b).

Removal of a relatively cold and dense lower lithosphere can cause surface uplift of crustal rocks (Bird, 1979; Foster and John, 1999) and a regional surface uplift is predicted as a line of evidence for delamination (Ducea, 2011). The temporal change in the source of basaltic magmas, along with crustal exhumation, as recorded by the thermochronological data, however, is insufficient to fingerprint delamination, as extension alone, for example, can produce the same results (Ducea, 2011). Strictly speaking, surface uplift cannot equate with rock exhumation (England and Molnar, 1990).

AFT and AHe ages (**Figure 5.6** and **Figure 5.7**) indicate that the region only exhumed to near surface after 65–40 Ma, not immediately after the 100–90 Ma event. Therefore, there appear to be two episodes of exhumation in the region. This, along with the change of isotopic signature of mafic magmatism at 100–90 Ma, does not support a catastrophic delamination of the lithospheric mantle either at ~130 Ma or at 100–90 Ma. In addition, the two episodes of exhumation temporally coincide with two stages of lithospheric thinning in the Early Cretaceous and early Cenozoic in eastern North China (Xu, 2001; Xu et al., 2004b). The thermochronological data, therefore, provide additional support for episodic lithospheric thinning.

5.5 Conclusions

Multiple chronometric techniques have been performed on samples from the Jiaobei region, north of the Sulu orogenic belt. This approach, along with the structural studies, has revealed the nature and timing of deformation, and exhumation pertaining to the collision between the South and North China blocks. The following conclusions can be drawn:

(1) Hornblende and muscovite $^{40}Ar/^{39}Ar$ ages from the Meso-Neoarchean Complex and the Paleoproterozoic Fenzishan Group indicate that these rocks had cooled to 350 ± 50 ℃ by 1834 ± 7 Ma and below 180 ± 20 ℃ by as early as 260 Ma. The penetrative foliation and lineation widely observed in the region were, therefore, mainly produced during the late Paleoproterozoic orogeny of the Jiao-Liao-Ji Belt.

(2) NW-trending and NNE-trending folds were sequentially superimposed on these foliations in the Precambrian rocks. New ZHe ages constrain the ages of the D_2 deformation to be between ~260 Ma and ~235 Ma, overlapping with subduction and peak metamorphism of the continental protolith of the Sulu UHP rocks. D_3 deformation appears to be related to the exhumation processes of the UHP rock in the Sulu UHP belt. ZHe ages decrease from 196 ± 9 Ma to 164 ± 7 Ma towards northwest, showing an outward propagation of exhumation from the Sulu UHP belt. The timing and pattern of deformation and exhumation can be best accounted for by the crustal detachment model, whereas other models cannot accommodate the change of structural orientation, and some of the cooling pattens.

(3) $^{40}Ar/^{39}Ar$, ZFT and ZHe ages of the Upper Jurassic-Lower Cretaceous plutons reveal an episode of exhumation at ~130–90 Ma, coinciding with the initiation of the 130–120 Ma “giant igneous event” and the removal of the enriched

lithospheric mantle by 100–90 Ma. A second episode of exhumation occurred during 65–40 Ma. The two episodes of exhumation may be associated with episodic lithospheric thinning since the Early Cretaceous.

CHAPTER 6 THERMOCHRONOLOGY OF THE LUXI REGION

6.1 Introduction

The eastern NCB has undergone multiple episodes of reactivation during the Phanerozoic after the formation of a coherent NCB in the Paleoproterozoic (Zhao et al., 2005). One of the tectonic events was lithospheric thinning from a thickness of about 200 km during the Ordovician to 60–80 km in the Cenozoic (Menzies et al., 1993; Griffin et al., 1998; Xu, 2001). Previous studies have focused mainly on the geochronology, geochemistry and petrology of Mesozoic igneous rocks in the region (Zhang and Sun, 2002; Zhang et al., 2002; Yang et al., 2004; Yang et al., 2005b; Liu et al., 2008b; Xu et al., 2008; Yang et al., 2012a; Zhao et al., 2013) and generated several competing hypotheses for the mechanisms controlling lithospheric thinning (Xu, 2001; Gao et al., 2004; Xu et al., 2006a; Zheng et al., 2007; Xu et al., 2013). All these studies underscore the fact that the enriched lithospheric mantle was significantly removed in the Early Cretaceous (Zhang et al., 2003a; Wang et al., 2007a; Zheng et al., 2007), and accompanied by widespread and contemporaneous extensional tectonics (Ren et al., 2002; Yang et al., 2007; Lin et al., 2011; Zhang et al., 2012a; Liu et al., 2013c). Nonetheless, whether the lithospheric thinning continued during the Cenozoic is still debated and poorly constrained (Xu, 2001; Wu et al., 2008; Kuang et al., 2012c; Li et al., 2014). In addition, in the early Mesozoic, closure of Paleo-Asian Ocean along the northern margin of the NCB, and the collision between the North China and the South China blocks along the southern margin resulted in intraplate crustal shortening in the NCB (Zhao et al., 2000; Davis et al., 2001; Li et al., 2009). These extensional and compressional events have induced repeated episodes of erosion and burial in the interior of the NCB as recorded by sequences of Phanerozoic sedimentary strata interspersed with unconformities.

In this study, multiple thermochronologic systems were applied to the Luxi region (which means western Shandong Province), in order to better constrain the timing and magnitude of denudation and burial episodes. Incorporation of our thermochronologic data with available geologic constraints allows new insights into the timing and magnitude of crustal shortening and lithospheric thinning.

6.2 Sampling

Archean basement rocks and siltstone-sandstone rocks from Neoproterozoic to Jurassic strata were collected in order to elucidate the tempo-spatial framework of the thermal history. No samples were collected from Cambrian–Middle Ordovician strata as they predominantly consist of limestone. The locations and detailed information of samples are shown in **Figure 6.1** and **Error! Reference source not found.**.

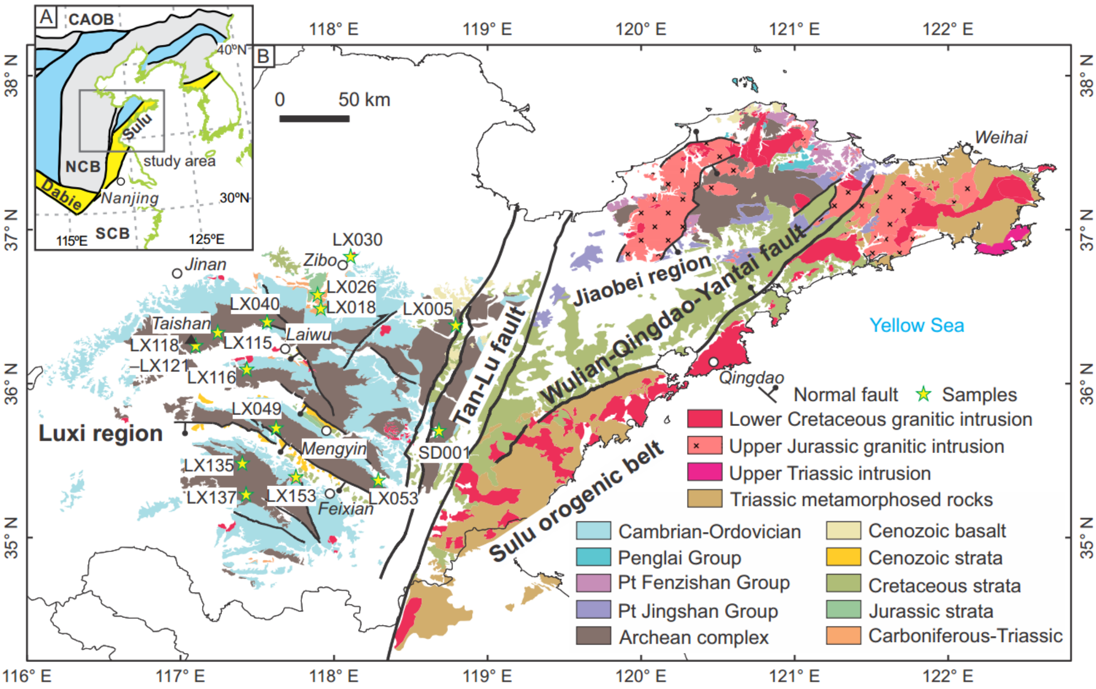

Figure 6.1 Geolological map of the Luxi region and locations of samples collected during this study. The first two letters of sample codes are not shown in the figure for a succinct view. Pt = Proterozoic.

6.3 Results

6.3.1 Zircon fission-track and (U-Th)/He data

Three ZFT ages and thirteen ZHe ages were obtained. The majority of samples show a substantial dispersion (>20%) of single grain ZHe ages, and inverted relationship between ZFT and ZHe ages (Appendix Table 6.1 and Appendix Table 6.2). For instance, TTG gneiss sample 11LX049A yielded a ZFT age of 442 ±37 Ma

(Figure 6.2), whereas ZHe ages range from 738 ± 40 Ma to 484 ± 26 Ma (Appendix Table 6.2). Although apparently older than the central ZFT age, these ZHe ages fall within the single grain ZFT age range, possibly resulting from a secular residence in the temperature range of 250–160 ℃. Sandstone sample 11LX153 from the basal Tongjiazhuang Formation of Neoproterozoic Tumen Group yielded a ZFT central age of 309 ± 24 Ma (Figure 6.2), that is significantly younger than the highly dispersed single-grain ZHe ages (1136 ± 61 Ma to 681 ± 36 Ma). Both the ZFT and ZHe ages are no older than the depositional age. A sandstone sample from the Triassic Fenghuangshan Formation in the Zibo Basin (11LX026A) yielded a central ZFT age of 173 ± 10 Ma (**Figure 6.2**) with ZHe ages ranging from 250 ± 13 Ma to 111 ± 6 Ma.

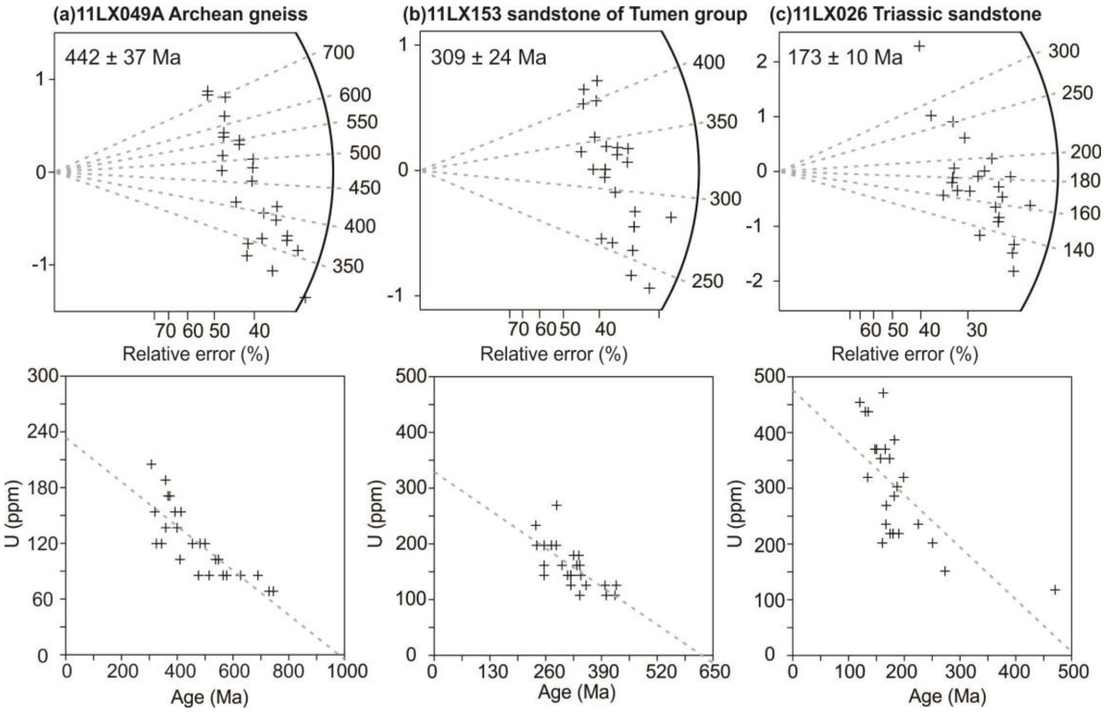

Figure 6.2 Radial plots of ZFT data (upper panels) and correlation between single-grain age and U concentration (lower panels).

Sample 10SD001C from the Archean basement in the Yishui area yielded a weighted mean ZHe age of 118 ± 5 Ma (MSWD = 0.25, P = 0.94). Syenite 11LX053A from the Tongshi intrusive complex (emplaced at ~180 Ma; Lan et al., 2012) yielded a weighted mean age of 139 ± 10 Ma (MSWD = 1.7, P = 0.14). Precambrian sample 11LX120 from Taishan mountain had a weighted mean age of 127 ± 14 Ma (MSWD = 2.6, P = 0.03). Sample 11LX005 from an Archean gneiss yielded a weighted mean ZHe age of 34.3 ± 3.3 Ma (MSWD = 2.1, P = 0.8).

The other thirty-six analyses from the remaining samples did not yield individual weighted mean ages and were plotted by DensityPlotter (Vermeesch, 2012) to visualize the age distribution and capture the major peaks. Four peaks were identified at ~217, ~136, ~82 and ~42 Ma, respectively (**Figure 6.3**).

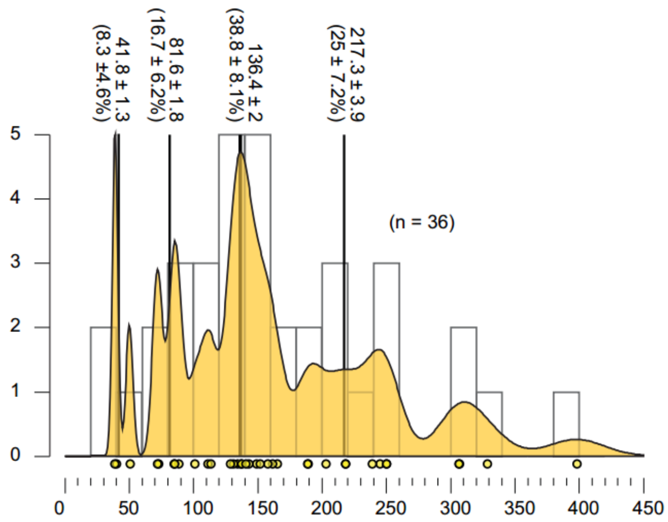

Figure 6.3 Histogram of ZHe ages from samples where no weighted mean age was calculated.

6.3.2 Apatite fission-track and (U-Th)/He data

Eight of nine samples analysed by apatite fission-track dating form a loose cluster of 60 ± 5 Ma to 40 ± 4 Ma (Appendix Table 6.1 and Figure 6.4). In particular, sample 11LX137 from a non-deformed diorite yielded an AFT age of 53.8 ± 2.6 Ma and a mean track length of 14.8 ± 0.8 μm (n = 119). In contrast, sample 11LX030 from the Lower Cretaceous diorite yielded an older AFT age of 85 ± 6 Ma and mean track length of 15.1 ± 1.0 μm, suggesting a rapid cooling through the AFT partial annealing zone (110–60 ℃, Wagner et al., 1989). Dpar values range from 1.67 to 2.96 μm, showing relatively diverse annealing kinetics (Appendix Table 6.1) (Carlson et al., 1999; Barbarand et al., 2003).

Weighted mean AHe ages for samples 10SD001C, 11LX018 and 11LX030 are 36 ± 8 Ma, 40 ± 10 Ma and 37 ± 4 Ma, respectively and are all younger than their corresponding AFT age. Sample 11LX116A yielded an older AHe age of 61 ± 6 Ma than the AFT age of 50 ± 4 Ma. Single-grain AHe ages for other samples are scattered between 96 Ma and 40 Ma. This dispersion likely arises from the abundant fluid inclusions present in most Archean apatites, which have contained excess He and resulted in the older AHe age for 11LX116A. These AHe ages are therefore considered to have no geological significance.

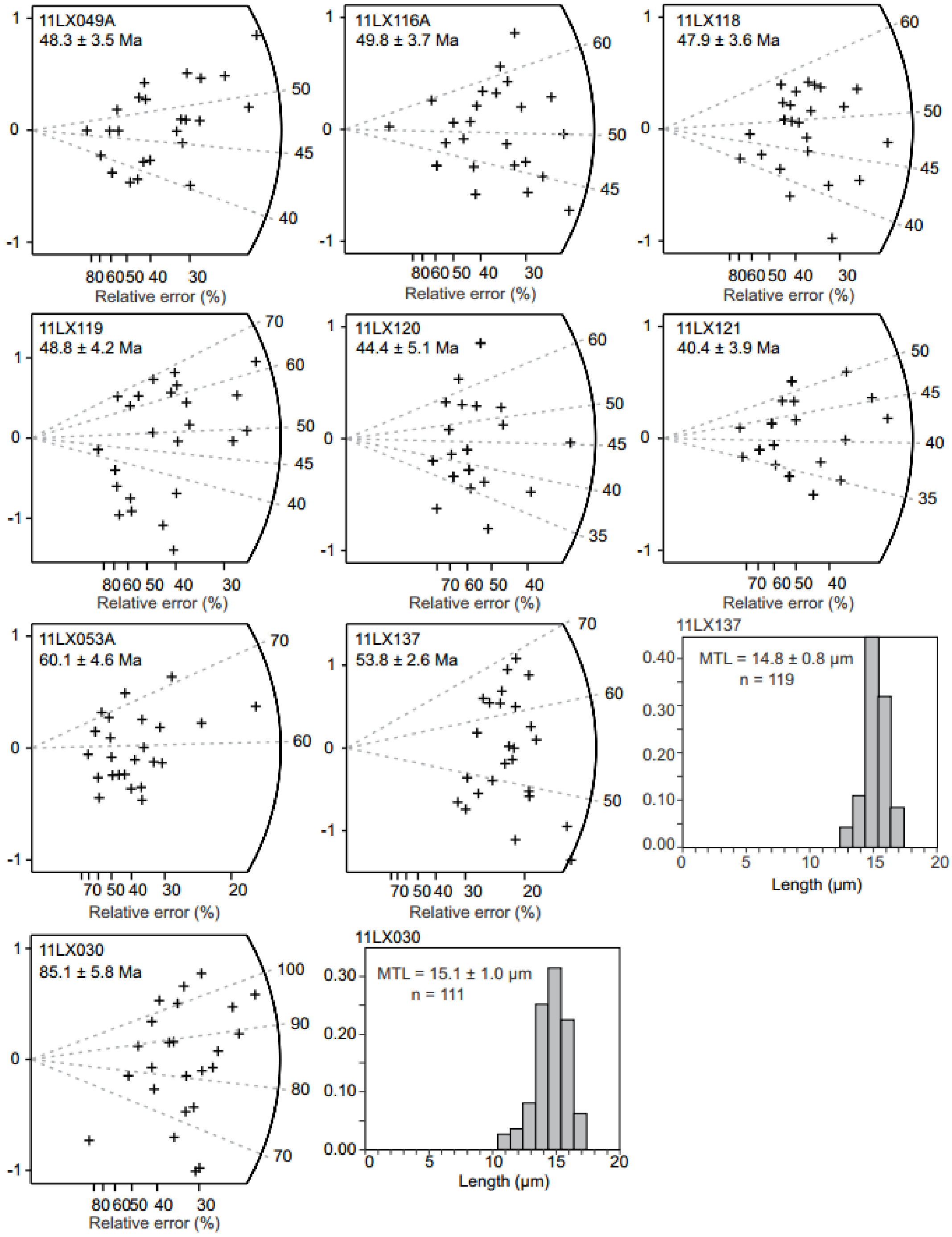

Figure 6.4 Radial plots of AFT results. The large relative error arises from low U abundance in the apatite.

Table 6.1 Summary of thermochronology data in the Jiaodong region in the study

Sample No.	Latitude	Logitude	Elevation (m)	Rock type	ZFT ± σ (Ma)	ZHe ± σ (Ma)	AFT ± σ (Ma)	AHe ± σ (Ma)
10SD001C*	35° 41.890'N	118° 41.305'E	142	Granulite		118 ± 5		35 ± 8
11LX005	36° 22.394'N	118° 47.596'E	186	Gneiss		29–37		
11LX018	36° 29.575'N	117° 54.832'E	348	Carboniferous siltstone		134–328		40 ± 10
11LX026	36° 35.057'N	117° 53.917'E	133	Triassic sandstone	173 ± 10	111–250		
11LX030*	36° 48.994'N	118° 05.863'E	108	Lower Cretaceous diorite			85 ± 6	37 ± 4
11LX040	36° 24.143'N	117° 34.251'E	293	Undeformed granite				63–96
11LX049A	35° 43.851'N	117° 37.298'E	212	TTG gneiss	442 ± 37	484–738	48 ± 4	50–85
11LX053A*	35° 23.239'N	117° 45.763'E	134	Middle Jurassic Tongshi intrusive complex		139 ± 10	60 ± 5	40–97
11LX115	36° 19.594'N	117° 14.916'E	220	Amphibolite		88–188		60 ± 11
11LX118	36° 15.482'N	117° 06.091'E	1508	Granitic gneiss			48 ± 4	
11LX119	36° 15.195'N	117° 05.993'E	1268	Amphibolite			49 ± 4	
11LX120*	36° 15.067'N	117° 06.104'E	1156	Archean granite		127 ± 14	44 ± 5	
11LX121	36° 14.748'N	117° 06.341'E	982	TTG gneiss		84–149	40 ± 4	
11LX116A*	36° 05.822'N	117° 26.074'E	227	Mylonite		137–398	50 ± 4	61 ± 6
11LX135	35° 28.523'N	117° 22.687'E	233	Undeformed granite		38–152		
11LX137*	35° 17.224'N	117° 25.955'E	270	Undeformed dirotite (K?)		72–250	54 ± 3	
11LX153	35° 22.601'N	118° 16.688'E	137	Neoproterozoic sandstone	309 ± 24	681–1136		

- Samples modelled by HeFTy

6.4 Interpretation and Discussion

The dispersion of single grain fission-track and (U-Th)/He ages can be significantly magnified in a partial annealing/partial retention zones or in slow cooling settings depending on chemical composition, the presence of inclusions, grain size, radiation damage, or zonation of parent nuclides (Hendriks and Redfield, 2005; Fitzgerald et al., 2006; Kohn et al., 2009; Flowers and Kelley, 2011; Brown et al., 2013; Fitzgerald, 2013). The large dispersion of zircon (U-Th)/He ages for samples from the Luxi region, together with the inverted or overlapping relationship between the (U-Th)/He age and corresponding ZFT age, may imply a complex or slow cooling history for the region since the Silurian. In particular, a Silurian ZFT age for sample 11LX049A and Carboniferous ZFT age for sample 11LX153 is in accord with up to 140 million years of denudation from the Late Ordovician to early Carboniferous, which is manifested as an absence of strata of this age in the region, and a transition from shallow sea carbonate association to parallic association (Wang, 1985). The older ZHe ages, relative to the ZFT age, for sample 11LX153 probably resulted from partial resetting of the inherited ZHe ages of detrital zircons. The low eU concentration (8–21 ppm) of this sample reflects low radiation damage and low diffusivity of He, which allows detrital zircons to retain inherited He and yield older ZHe ages (Guenthner et al., 2014).

6.4.1 Implication for a weak crustal shortening in the early Mesozoic

Structural analysis revealed that NE-NNE trending folds and WNW trending thrusts and folds in the Luxi region, and other regions such as Taihang Mountain to the west and Bohai Bay Basin and Western Hills to the north, may have developed from the Triassic to the Late Jurassic (Qi et al., 2004; Li et al., 2005; Wang and Li, 2008; Wang et al., 2011b). The WNW-trending folds are characterised by open to gentle folds, whereas NNE-trending folds are manifested as Jura-type folds in the Luxi region (Li et al., 2005). The Cambrian-Ordovician strata are mostly sub-horizontal with dips < 30°, indicating a weak regional deformation. Detachment structures were found to have developed along the unconformity between the Cambrian strata and the Archean basement, with the slip direction orientated parallel to the rotation direction of fault blocks during subsequent extension (Lü et al., 1990; Li et al., 2007a). The timing of the detachment is poorly constrained. The detachment formed in the Cretaceous may be a result of block tilting and accompanying gravity instability (Li et al., 2007a). This detachment layer could have operated as a thrust detachment under regional compression during the Triassic–Late Jurassic deformation, based on the observation that small thrusts developed the Cambrian strata have a thrusting polarity opposite to the dip direction of strata. The upper structural layer above the detachment was gently folded, whereas the underlying Archean rocks were little disrupted by thrusting and folding. This is supported by the ZHe age component of 240–160 Ma from Archean samples 11LX115 and 11LX116A, and from Carboniferous sample 11LX018 and Triassic sample 11LX026 in the upper structural layer. Specifically, the wide ZHe age range of 400–130 Ma for sample 11LX116A, and that of 190–90 Ma for sample 11LX115, implies a longstanding residence in the ZHe partial retention zone (180 ± 20 ℃, equivalent to ~8–10 km) and slow cooling at the time interval defined by each ZHe age ranges. After excluding ZHe ages which are likely partially reset, inherited ZHe ages from 11LX018 and 11LX026, ZHe ages range from 245 Ma to 135 Ma for 11LX018 and from 190 to 110 Ma for 11LX026, also indicating slow cooling during the Triassic–Late Jurassic period.

The ZHe age (37–29 Ma) of sample 11LX005 is remarkably younger than the ZHe and AFT ages of other samples, which may have resulted from partial resetting by an adjacent basalt eruption in the Neogene.

In summary, correlating ZHe ages with structural information allows us to suggest that a weak crustal shortening event occurred in the Luxi region from the Triassic to the Late Jurassic. The driving force for this deformation may be south-north collision along the northern and southern margins of the North China block (Davis et al., 2001; Li et al., 2005; Li et al., 2009), or the up to 400 km northward displacement of the Sulu orogenic belt along the Tan-Lu fault (Li, 1994; Li, 1998; Qi et al., 2004).

6.4.2 Implication for two episodes of lithospheric thinning

Inverse modelling of paired ZHe and AFT/AHe ages (samples 10SD001C, 11LX120 and10SD053A) suggests one episode of cooling through the ZPRZ occurred prior to 110 Ma or ca. 130 Ma and another through the APAZ/APRZ after 60 Ma (Figure **6.5**). The duration for the Cenozoic cooling is not well constrained by the three samples, but is restricted to 60–40 Ma by samples 11LX137 and

11LX116A. Modelling results of these samples show both relatively slow and rapid paths for the first episode of cooling. However, the relatively rapid cooling path for the two episodes is suggested based on the following evidence. The Early Cretaceous cooling event is relatively rapid compared to the Triassic–Late Jurassic cooling event, because more samples (e.g., 10SD001C, 11LX053A, 11LX120) yielded relatively well reproducible ZHe ages rather than dispersed age spectra. A rapid cooling in the early Cenozoic (60–40 Ma) is indicated by modelling results of samples 11LX137 and 11LX116A (AFT age = 53.8 ± 2.6 Ma) (Figure **6.5**e–f) and supported by the weighted mean AHe ages of 11LX001C (35 ± 8 Ma), 11LX018 (40 ± 10 Ma), 11lX030 (37 ± 4 Ma), 11LX115 (60 ± 11 Ma). It is also noteworthy that Early Cretaceous intrusive sample 11LX030 in the northern margin of the study area underwent a rapid cooling at 90 Ma (Figure **6.5**d) or a slow cooling over ca. 90–60 Ma. The rapid cooling path is preferred given the long track length (15.1 ± 1.0 μm).

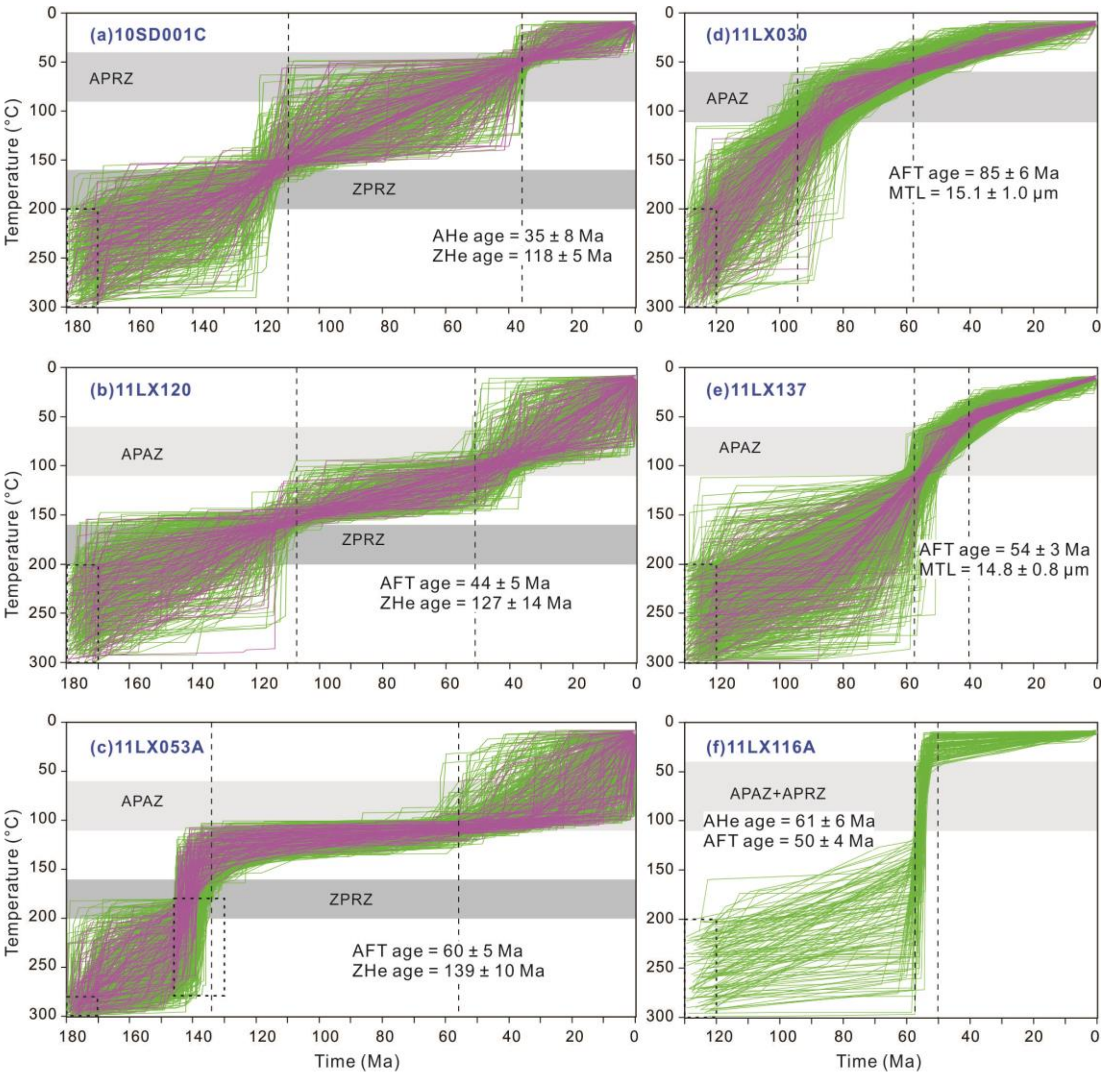

Figure 6.5 Inverse modelling results for representative samples with pairwise ages and those with track length data. Ages shown in each panel were used to constrain cooling paths that can reproduce the measured results. Note: all the high temerpature constraints were drawn artificially in order to reveal the cooling through ZPRZ. The constraint box for 11LX053A around 140 Ma comes from the ZFT age reported in Guo (2014). AHe age for 11LX030 is not used because it failed to yield cooling paths when it is incorporated into the modelling.

The development of southwest-dipping normal faults in the region not only controlled the distribution of the Lower Cretaceous and Lower Cenozoic strata, but also likely caused the erosion of the footwall, thereby inducing the two episodes of exhumation. Although regional extension itself could generate the normal faulting (Ren et al., 2002), contemporaneous change of mantle sources for accompanied mafic rocks in the Early Cretaceous implies that normal faulting and exhumation is geodynamically linked to deep mantle process — lithospheric thinning. Mafic rocks with strongly negative εNd(t) signatures intruded/extruded in the region west of the Tan-Lu fault from ~140 Ma to 110 Ma, indicating an episode of melting of an enriched lithospheric mantle in the Early Cretaceous (Zhang et al., 2003a; Xu et al., 2006a; Liu et al., 2008a; Liu et al., 2008b; Xu et al., 2012; Yang et al., 2012a; Yang et al., 2012d). The mafic magmatism temporally matches the timing of exhumation in the Luxi region, which suggests possible coupling between mantle process and crustal events.

The early Cenozoic (60–40 Ma) exhumation, which took place in the Jiaodong Peninsula as well, was a result of a regional extension represented by normal faulting and development of rift basins in surrounding regions (Allen et al., 1998; Ren et al., 2002; Feng et al., 2010; Qi and Yang, 2010). Concomitant eruption of asthenosphere-derived basalts demonstrates that this extension event represents the second episode of lithospheric thinning. In addition, characteristics of the early Cenozoic basalts also suggested that lithospheric thinning was ongoing in the Bohai Bay basin north of the Luxi region (Xu, 2001; Xu et al., 2004b; Li et al., 2014). However, lower Cenozoic basalts and sedimentary rocks are sparse in both the Luxi region and the Jiaodong Peninsula, but Neogene basalts in the Luxi region reflect a deeper magma source in comparison to the lower Eocene basalts in the Bohai Bay basin (Zeng et al., 2010; Zeng et al., 2011; Li et al., 2014), indicating a lithospheric thickening process from the Neogene (Li et al., 2014). Heat flow peaked in the Paleogene (Hu et al., 2001; Qiu et al., 2014) and the basin evolved from rifting to post-rifting subsidence since the Neogene (Allen et al., 1998; Qi and Yang, 2010), supporting the occurrence of lithospheric thinning in the early Cenozoic and thickening since the Neogene. The Luxi region and the Jiaodong Peninsula were not at the centre of extension and subsidence in the early Cenozoic. Consequently, these regions were relatively weakly extended, and were eroded to shed sediments to surrounding basins as topographic highs.

In summary, thermochronology and geological constraints support two episodes of lithospheric thinning: one in the Early Cretaceous and the other in the early Cenozoic. In comparison, the Cretaceous cooling through the ZPRZ in the Luxi region finished by 110 Ma, 20 Ma earlier than the Jiaodong region (by 90 Ma).

6.5 Conclusions

Application of zircon and apatite fission-track and (U-Th)/He methods to the Luxi region revealed a comprehensive denudation history during the Phanerozoic. ZFT ages of 442–309 Ma, coupled with an absence of Upper Odovician–Lower Carboniferous strata, testify to a slow-rate denudation of up to 140 million years duration. Crustal shortening during the Triassic–Late Jurassic was weak and did not exhume the Archean basement above the depth of ZHe partial annealing zone (180 ± 20 ℃, ~8–10 km), leading to the ZHe ages from those samples spreading from 250 Ma to 160 Ma. The Luxi region was exhumed to a depth shallower than 8–10 km by the Early Cretaceous, and to < 3 km in early Cenozoic. The latter two episodes of exhumation were likely related to episodic lithospheric thinning.

CHAPTER 7 PETROGENESIS OF LATE MESOZOIC ADAKITE-LIKE GRANITOIDS IN THE JIAOBEI REGION, EASTERN NORTH CHINA

7.1 Introduction

Granitic magmas are generally considered to be sourced from the continental crust or the mantle through partial melting, fractional crystallization and magma mixing. They may therefore exhibit features related to the composition and physical conditions (e.g. temperature, pressure, redox condition and water content) of the source region and the thickness of the crust. Petrological and chemical studies of granitic rocks can therefore help to decipher the tectonic setting of a region at the time of the magma formation (Pearce, 1996).

Two episodes of granitic magmatism took place in the Jiaobei region during the Late Jurassic (160–145 Ma) and the Early Cretaceous (130–110 Ma) (Wang et al., 1998; Guo et al., 2005c; Zhang et al., 2010a; Yang et al., 2012c). Geochemically, most of the Late Jurassic and Early Cretaceous granitoids have high Ba and Sr contents, high Sr/Y and La/Yb ratios and positive Eu anomaly. They are different from leucogranites in the Himalaya, characterized by low Ba and Sr contents, negative Eu anomaly and low Sr/Y (< 20) (Zhang et al., 2004b; Guo and Wilson, 2012). Together with high initial $^{87}Sr/^{86}Sr$ ratios, and strongly negative εNd(t) and zircon εHf(t) values, the Upper Jurassic granites are interpreted to have been derived from partial melting of a thickened crust with garnet in the residue (Hou et al., 2007; Yang et al., 2012c; Ma et al., 2013). Emplacement of the Lower Cretaceous granodiorite was accompanied by contemporaneous mafic dykes and volcanic rocks. The proposed petrogenetic models include: (1) mixing between mantle-derived mafic and crustal-derived felsic magmas accompanied by fractional crystallization (Qian et al., 2003; Chen et al., 2007); and (2) dehydration melting of earlier underplated mafic rocks in the lower crust (Yang et al., 2003a; Wang et al., 2006).

In this study, new geochronologic and geochemical data is presented for the Jurassic-Cretaceous granitoids and mafic enclaves found within, and both the source and petrogenesis of these granitoids is investigated. The data and interpretation furnish new constraints on the tectono-thermal evolution of the Sulu orogenic belt and the Jiaobei region during the Late Mesozoic.

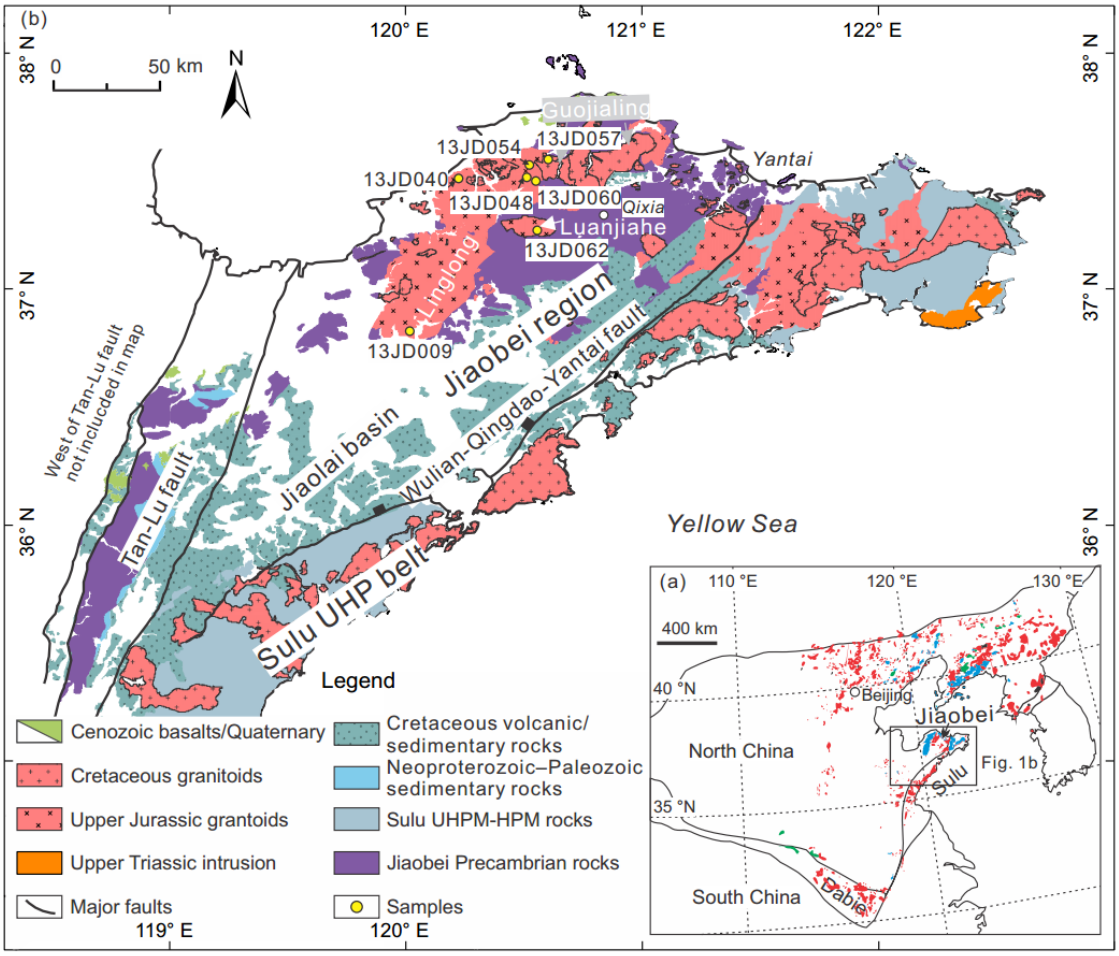

Figure 7.1 Sketch map of North China (a) and geological map of the Jiaobei region (b) showing distribution of Mesozoic magmatic rocks. Symbols in Figure. 1a: red intrusions (Early Cretaceous), blue granitoids (Jurassic), green intrusions (Triassic). This figure 1a is modified after Sun and Yang (2013).

7.2 Sampling and petrology

Detailed sample locations for granitoids and mafic rocks from the Linglong, Luanjiahe and Guojialing granites are shown in **Figure 7.1**b and listed in Appendix Table 7.1.

The Linglong granite mainly consists of medium- to fine-grained monzogranite, with locally developed gneissic textures (e.g., **Figure 7.2**a, e and g). Alkali feldspar from the granite commonly contains considerable barium (**Figure 7.2**b, d, f and h). Accessory minerals include allanite, titanite, apatite, zircon and Fe oxides (**Figure 7.2**b, d and f). The magnetic susceptibilities of the Linglong granite samples are 0.06×10^{-3} SI for 13JD009B, 4.8−5.2 $\times10^{-3}$ SI for samples 13JD054B and 13JD048B, and 12.2 $\times10^{-3}$ SI for 13JD040I (magnetite-series to ilmenite-series) (Ishihara et al., 2000), respectively (Appendix Table 7.1). Mafic enclaves are rare in the Linglong granite. Mafic enclave sample 13JD054D contains hornblende, biotite, feldspar, quartz, and accessory minerals allanite, apatite and titanite (**Figure 7.2**c and d). Magnetic susceptibility of the enclave is 0.3 $\times10^{-3}$ SI (Appendix Table 7.1), which is lower than its host granite by an order of magnitude.

The Luanjiahe granite comprises non-foliated and coarse-grained monzogranite (**Figure 7.2**i). Sample 13JD062B consists of plagioclase, quartz, microcline, biotite, epidote, apatite, titanite, zircon and Fe oxides (**Figure 7.2**j). Plagioclase exhibits reverse concentric zoning with rims relatively richer in An (**Figure 7.2**j). Magnetic susceptibility values for the Luanjiahe granite average 0.3×10^{-3} SI (ilmenite-series) (Appendix Table 7.1).

The Guojialing granodiorite is characterized by medium- to coarse-grained porphyritic granodiorite with alkali feldspar as the phenocryst (**Figure 7.2**k). The mineral composition includes quartz, feldspar, amphibolite, biotite, titanite, apatite and Fe oxides. Mafic microgranular enclaves (MMEs) are common in the Guojialing pluton. MME sample 13JD057D consists of feldspar, amphibole, biotite, quartz and titanite (**Figure 7.2**n) and has higher modes of hornblende, biotite, apatite and titanite than the host granodiorite13JD057A. Magnetic susceptibility values for the Guojialing granodiorite and its mafic enclaves are 2.2×10^{-3} SI and 0.3 $\times10^{-3}$ SI, respectively (Appendix Table 7.1).

There are many mafic dykes contemporaneous with the Guojialing granodiorite. Samples 13JD040A and 13JD040B were collected from a mafic intrusion in the Linglong granite. They consist of amphibole, plagioclase, biotite, alkali feldspar and quartz with accessory minerals such as allanite and titanite (**Figure 7.2**o and p). Magnetic susceptibility for the mafic dyke is 0.4–1.1×10^{-3} SI (Appendix Table 7.1).

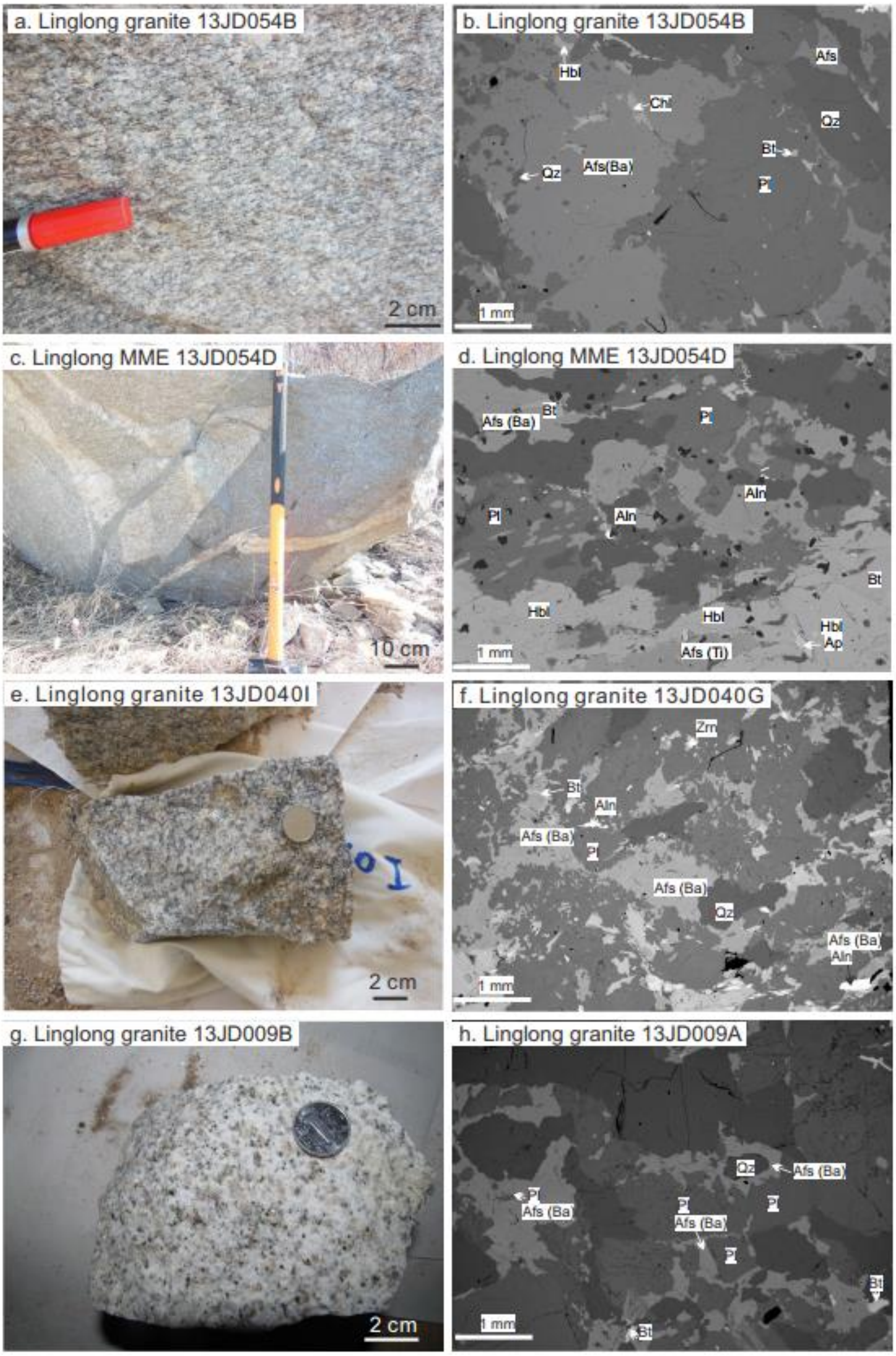

Figure 7.2 Field, hand specimen and SEM microphotographs of the Mesozoic rocks from the Jiaobei region. All microphotographs were taken using Hitachi TM3030 Tabletop Microscope integrated with SwiftEDS3000 at Curtin University (Accelerating voltage = 15kV, Filament current = 1850 mA). Mineral abbreviations: Afs (Ba): alkali feldspar rich in

barium, Aln: allanite, Ap: apatite, Bt: biotite, Chl: chlorite, Hbl: hornblende, Pl: plagioclase, Qz: quartz, Ttn: titanite, Zrn: zircon.

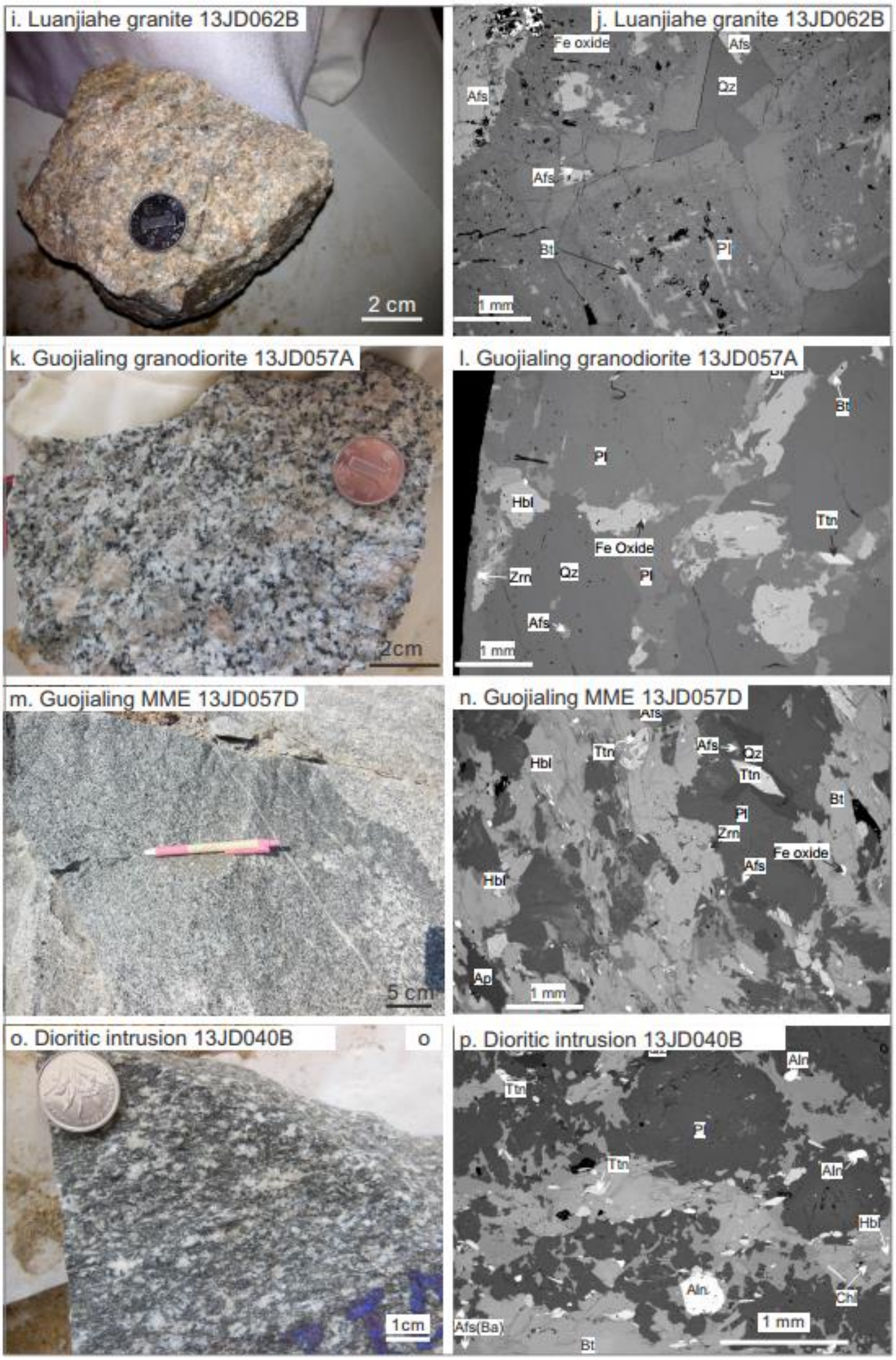

Figure 7.2 (continued)

7.3 Results

7.3.1 Zircon U-Pb ages and Hf isotopes

7.3.1.1 Linglong granite

Six samples including 13JD009B, 13JD040I, 13JD048B, 13JD060A, 13JD054B and 13JD054D from the Linglong granite were dated using the LA-ICP-MS zircon U-Pb method, and details of data are presented in Appendix Table 7.2. The majority of the zircons from the Linglong granite are prismatic, transparent or light brown, and range from 200 to 400 μm in length. Most zircon crystals show clear core-rim structures, where the cores are usually mantled by rims with oscillatory zoning (**Figure 7.3**a-f).

Thirty-five spots were analysed on twenty-four zircon grains from sample 13JD054B. Sixteen analyses on the rims yield a weighted mean $^{206}Pb/^{238}U$ age of 155 ± 3 Ma (n = 16, MSWD = 3.9) (**Figure 7.4**a), which is regarded as the crystallization age of the granite. High MSWD values were also reported by other studies (e.g.,Yang et al., 2012c; Ma et al., 2013), likely reflecting prolonged crystallization process. Three analyses on rims yielded concordant $^{206}Pb/^{238}U$ ages of 167 ± 13Ma–173 ± 12 Ma and one yielded a younger age of 137 ± 11 Ma. These were rejected from the calculation of mean age. Six analyses of the cores gave concordant ages from 221 ± 7 Ma to 237 ± 8 Ma, suggesting a contribution from materials with affinity to the Sulu orogenic belt. Other discordant results yielded an upper intercept age at 2673 ± 85 Ma, consistent with the emplacement of Archean igneous rocks in the region. Twenty-eight Hf isotopic analyses were obtained. For zircons with a crystallization age determined, εHf(t) values of −28.9 to −18.4 were obtained (n = 16) (**Figure 7.5**) (Appendix Table 7.3). The six Late Triassic inherited cores have εHf(t) values ranging from −21.6 to −14.5.

Thirty-three U-Pb analyses were conducted on twenty-six zircons from sample 13JD054D. Twenty-three concordant U-Pb analyses yielded a weighted mean $^{206}Pb/^{238}U$ age of 154 ± 4 Ma (n = 23, MSWD = 6.7) (**Figure 7.4**b). Three analyses on two grains were not concordant and yielded Precambrian ages. εHf(t) values from the concordant zircons ranged from −27.0 to −18.3 (**Figure 7.5**).

Sixteen analyses on magmatic zircon rims from samples 13JD009B yielded a concordant $^{206}Pb/^{238}U$ age of 157 ± 2 Ma (n = 17, MSWD = 2.9) (**Figure 7.4**c), which is taken as the crystallization age of the granite. Four spots on the rims gave younger ages, which may have resulted from Pb loss due to high U content (> 2000 ppm). Inherited zircon cores from the sample yielded four groups of concordant ages: 188–214 Ma ($^{206}Pb/^{238}U$ age), 690–768 Ma ($^{206}Pb/^{238}U$ age), 1.85Ga ($^{207}Pb/^{206}Pb$ age), and 2.3–2.4Ga ($^{207}Pb/^{206}Pb$ age). The Late Triassic and Neoproterzoic inherited zircons reflect signatures of the Sulu orogenic belt, whereas the Paleoproterzoic and Archean cores are likely inherited zircons from the basement of the NCB.

Forty analyses were conducted on thirty-one zircon grains from sample 13JD060A and twenty-two concordant ages yield a weighted mean $^{206}Pb/^{238}U$ age of 155 ± 2 Ma (n = 22, MSWD = 1.9) (**Figure 7.4**d). Four concordant analyses on the cores yielded $^{206}Pb/^{238}U$ ages ranging from 212 ± 7 Ma to 238 ±30 Ma. Other ages from zircon cores are discordant and are not considered further.

Thirty-two analyses were conducted on twenty-three zircon grains from sample 13JD040I. Fourteen analyses on rims yielded a weighted mean $^{206}Pb/^{238}U$ age of 154 ± 2 Ma (n = 12, MSWD = 1.5). The discordia line defines an upper intercept at 2468 ± 63 Ma, and two inherited zircons yield similar concordant $^{207}Pb/^{206}Pb$ ages of 2452 ± 45 Ma and 2511 ± 40 Ma, respectively (**Figure 7.4**e). Other concordant $^{206}Pb/^{238}U$ ages from zircon cores include 174 ± 9 Ma, 191 ± 6 Ma, 231 ± 10 Ma, 283 ± 12 Ma, 638 ± 31 Ma and 1778 ± 57 Ma (Appendix Table 7.2). There are also four concordant ages from zircon rims: 170 ± 7 Ma, 169 ± 7 Ma, 190 ± 9 Ma and 206 ± 6 Ma, and these outliers were excluded from the mean age calculation. However, these ages may reflect earlier thermal events. For zircons yielding crystallization ages (154 ± 2 Ma), εHf(t) values ranging from −23.5 to −20.3 were obtained (**Figure 7.5**).

Thirty-five analyses were conducted on twenty-eight zircon grains for sample 13JD048B. Twenty-nine concordant analyses yielded a weighted mean age of 148.7 ± 0.9 Ma (n = 29, MSWD = 1.3) (**Figure 7.4**f), which is interpreted as the crystallization age of the granite. One analysis on an inherited zircon gave a discordant Mesoproterozoic age.

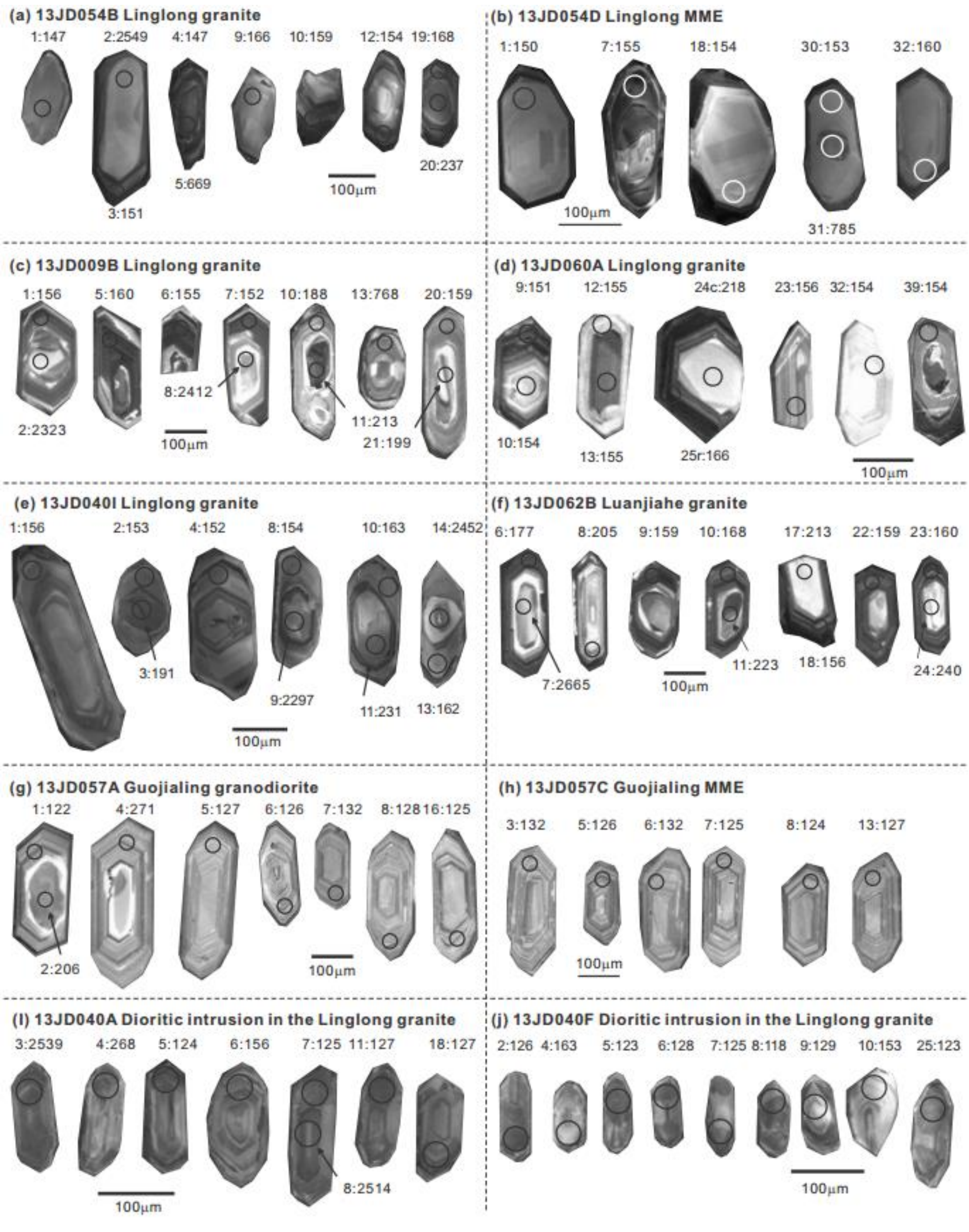

Figure 7.3 Representative zircon CL images from dated samples. Spot numbers and $^{206}Pb/^{238}U$ ages are shown with analysed spots

7.3.1.2 Luanjiahe granite

Zircon grains from 13JD062B show core-rim structures and rims with oscillatory zoning are generally darker than cores on CL images (**Figure 7.3**f). Thirty-eight spots were analysed on twenty-eight grains. The result mainly comprises three populations. Thirteen youngest concordant ages from the magmatic rims yield a weighted mean $^{206}Pb/^{238}U$ age of 159 ± 1 Ma (**Figure 7.4**g), which represents the crystallization age of the granite. The ~220 Ma population, derived from analyses on zircon cores (bright and unzoned on CL images), was likely formed during the Sulu ultrahigh pressure metamorphism. The ~180 Ma population comes from spots that cut across rims and cores, and thus likely represents mixed ages with no geological meaning. Of the remaining four discordant analyses, two spots yielded $^{207}Pb/^{206}Pb$ ages of ~2.5 Ga, implying possible involvement of Archean rocks.

7.3.1.3 Guojialing granodiorite

Zircon grains from sample 13JD057A are mostly euhedral, transparent or light brown. In comparison to the Linglong and Luangjiahe granites, most zircons from the Guojialing granodiorite showed oscillatory zoning without inherited cores (**Figure 7.3**g). Fifteen out of eighteen analyses yield a weighted mean $^{206}Pb/^{238}U$ age of 127 ± 1 Ma (n = 15, MSWD = 1.2), which defines the emplacement age of the granite (**Figure 7.4**h). Three out of six analyses on the rare cores have concordant $^{206}Pb/^{238}U$ ages at 206 ± 7 Ma (spot 2), 151 ± 4 Ma (spot 23) and 228 ± 8 Ma (spot 24), respectively. The other analyses are discordant with a poorly defined upper intercept at 2269 ± 46 Ma. For zircons of concordant crystallisation age, εHf(t) values range from −15.0 to −11.3 (**Figure 7.5**). εHf(t) values for two concordant inherited zircons are −28.5 (spot 23) and −16.9 (spot 24), respectively.

Thirty-four analyses were conducted on twenty-eight zircons from mafic enclave sample 13JD057C. Zircon grains have the same morphology and internal structure as those from 13JD057A (**Figure 7.3**g–h). Except for the youngest age of 107 ± 4Ma, twenty-seven analyses yielded a concordia age of 127 ± 1 Ma (**Figure 7.4**i). Inherited zircons yielded discordant Precambrian ages (**Figure 7.4**i). εHf(t) values for the dated magmatic zircons range from −14.9 to −9.6, with the exception of one zircon that had a εHf(t) value of −20.5 (**Figure 7.5**).

7.3.1.4 Early Cretaceous dioritic intrusion

Zircon crystals from samples 13JD040A and 13JD040F were transparent and 100–200 μm in length. Zircon grains from 13JD040A show weakly oscillatory zoning while those from 13JD040F are dominantly sector-zoned zircons showing oscillatory zoning (**Figure 7.3**i–j).

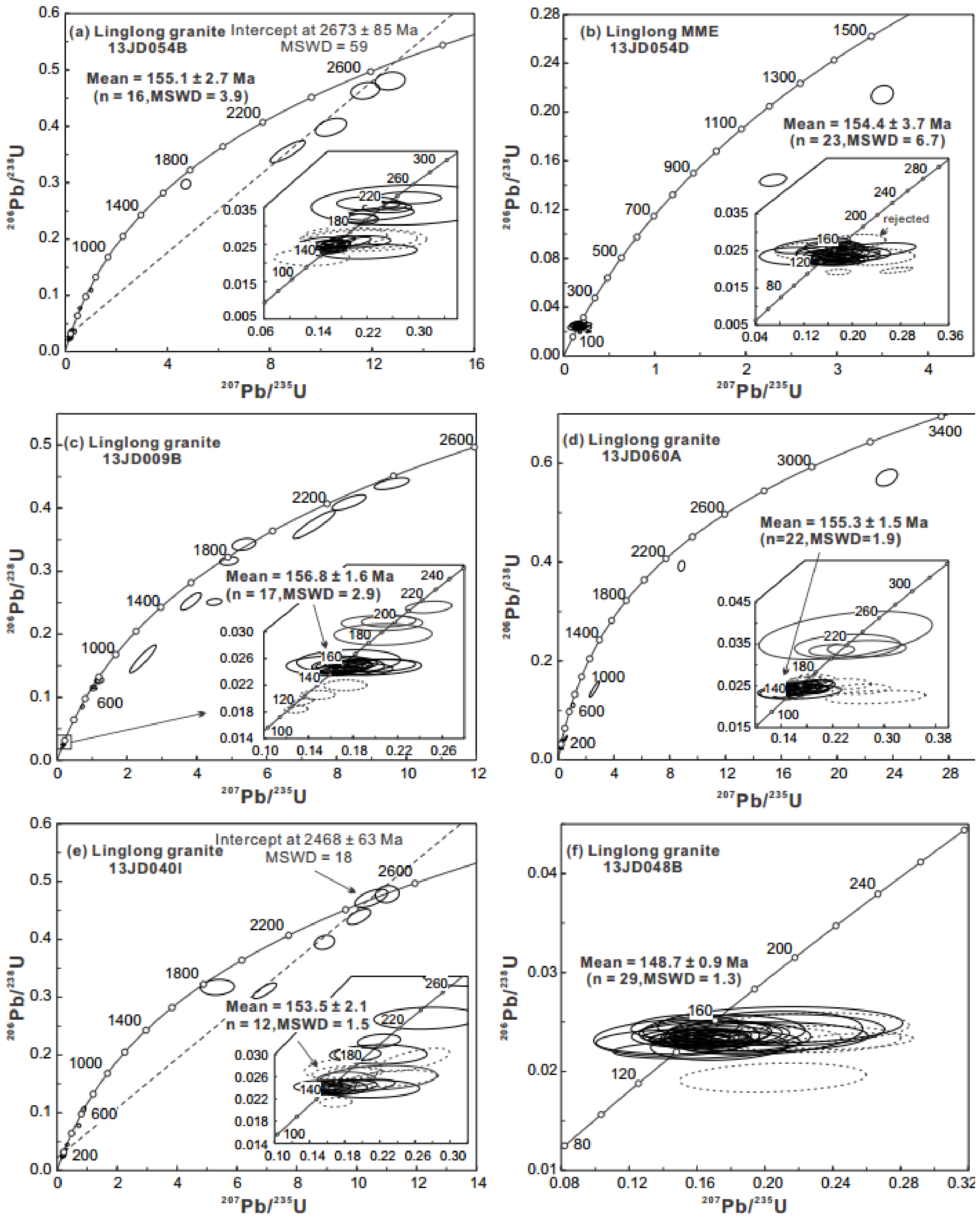

Figure 7.4 Zircon LA-ICP-MS U-Pb results. The dash circles refer to analyses excluded for calculation of weighted mean $^{206}Pb/^{238}U$ age.

Fifteen zircons from 13JD040A yielded a weighted mean $^{206}Pb/^{238}U$ age of 123 ± 2 Ma (n = 15, MSWD = 1.8) (**Figure 7.4**j). Four spots gave older concordant Mesozoic ages of 248 ± 21 Ma, 133 ± 6 Ma, 145 ± 13 Ma and 156 ± 6 Ma. Two analyses on inherited cores yielded concordant $^{207}Pb/^{206}Pb$ ages of 2539 ± 55 Ma and 1440 ± 310 Ma. εHf(t) values from most zircons with concordant ages range from −21.9 to −15.3; however, three grains had εHf(t) values vary from −47.4 to −37.3

(**Figure 7.5**). εHf(t) values for three older Mesozoic zircons are −17.2 (248 Ma), −17.0 (133 Ma) and −44.7 (145 Ma), respectively.

Thirty-two analyses were conducted on thirty-two zircons from sample 13JD040F. Twenty of the spots yielded a weighted mean $^{206}Pb/^{238}U$ age of 122 ± 3 Ma (n = 20, MSWD = 4), indistinguishable from that of sample 13JD040A within 2SE (**Figure 7.4**k). The εHf(t) values ranged from −22.9 to −18.2. Four analyses yielded older concordant ages between 132 ± 5 Ma and 187 ± 13 Ma. Their εHf(t) values ranged from −42.4 to −15.9 (**Figure 7.5**).

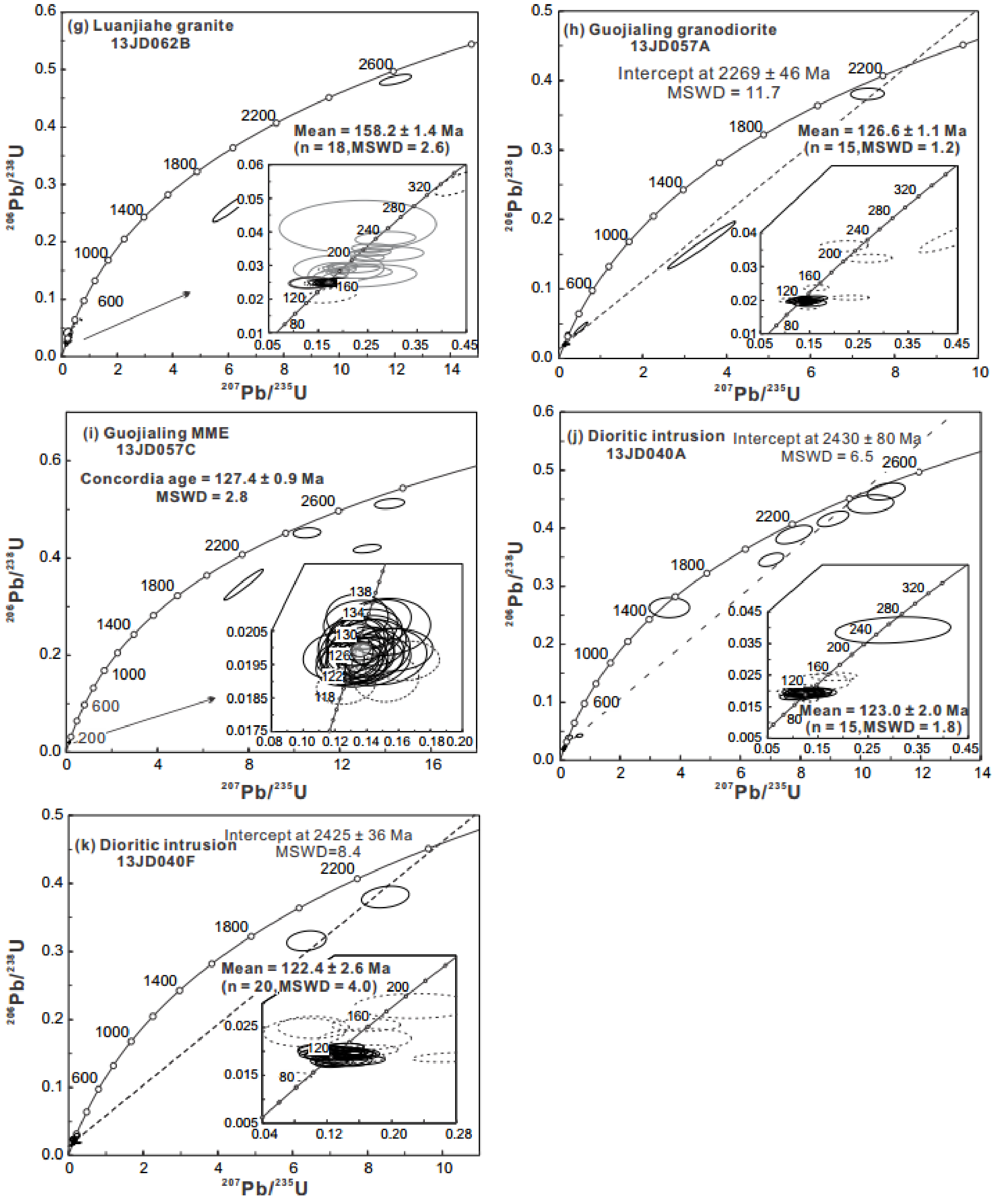

Figure 7.4 (continued).

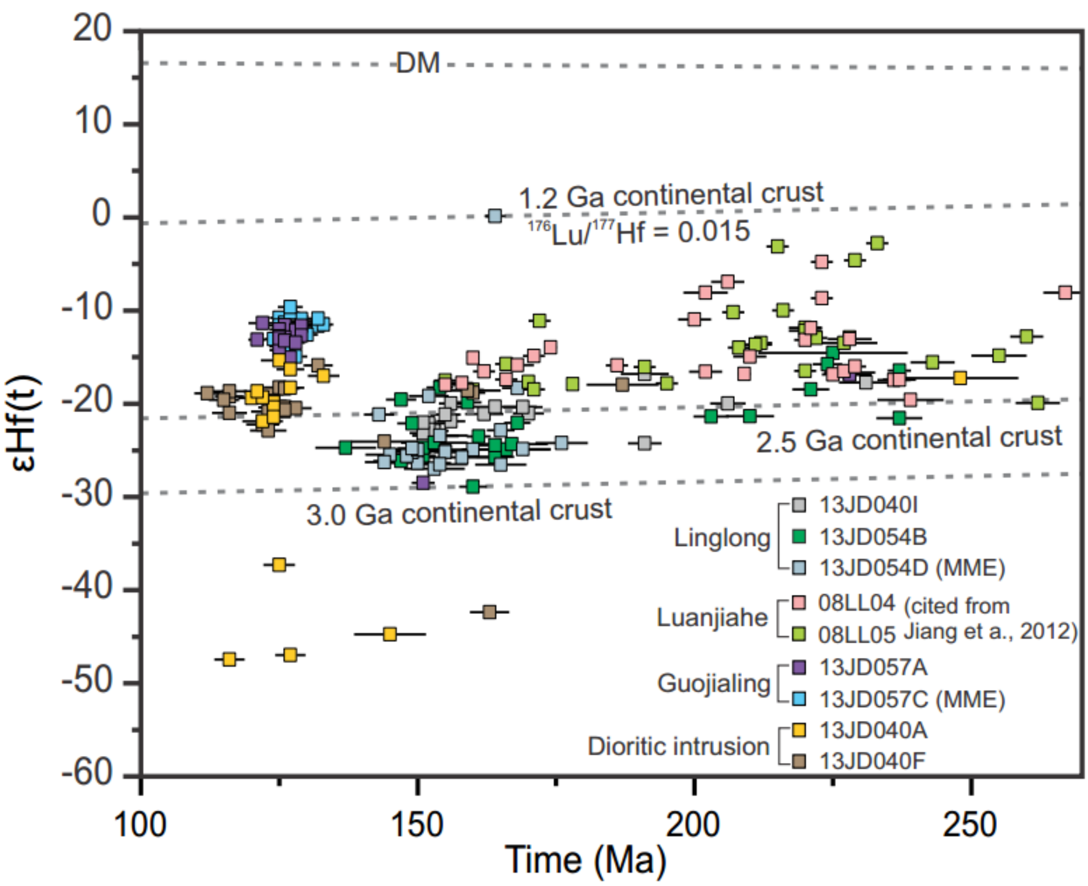

Figure **7.5** Diagram of Hf isotopic evolution in zircons from the Linglong granite, Luanjiahe granite, Guojialing granodiorite and Early Cretaceous dioritic intrusion. The Hf isotopic data for the Luanjiahe granite were cited from Jiang et al. (2012).

7.3.2 Major and trace elements

The whole-rock major and trace element data are listed in Appendix Table 7.4. Samples from the Linglong and Luanjiahe granites have SiO_2 contents from 67.7–75.5 wt. %. They have moderate FeOt/(FeOt + MgO) ratios and straddle the ferroan and magnesian boundary (**Figure 7.6**a). They are all weakly peraluminous with A/CNK ratios ranging from 1.02 to 1.08, except for sample 13JD062B (A/CNK = 1.20) from the Luanjie granite (**Figure 7.6**b). In contrast, the enclaves (13JD054D and 13JD054E) from the Linglong granite are magnesian with SiO_2 contents of 64.1–69.4 wt. % and low $FeO_t/(FeO_t + MgO)$ ratios of ~ 0.58. They are classified as alkali-calcic and calc-alkalic (**Figure 7.6**c).

The Linglong granite and their enclaves are more enriched in LREE (La/Yb = 12.2–86.1) than the Luanjiahe granite (La/Yb = 8.6–9.2) and display more significant HREE fractionation than the Luanjiahe granite, as indicated by their Gd/Yb ratios of 1.2–5.1 and < 1, respectively. Both granites are high Ba-Sr granites (**Figure 7.6**d), although the Linglong granite has higher concentrations of Ba (1505–2809 ppm) and Sr (530–1544 ppm) than the Luanjiahe granite (Ba = 937–1040 ppm and Sr = 251–294 ppm). In addition, the Linglong granite has higher average Zr concentrations (24–150 ppm) than the Luanjiahe granite (66–72 ppm) (Appendix Table 7.4).

Samples from the Guojialing granodiorite are metaluminous and magnesian with low FeOt/(FeOt + MgO) ratios of ~ 0.60 (**Figure 7.6**a). The granodiorite and associated MMEs are both enriched in LREE with La/Yb ratios of 27.4–46.6, and show similar HREE fractionation with Gd/Yb ratios of 3.2–3.5. However, the Guojialing granodiorite has higher Ba (845–1786 ppm) and Sr (848–952 ppm) and lower Zr (113–137 ppm) contents than associated MMEs (Ba; 577–533 ppm, Sr: 411–605 ppm, Zr: 340–350 ppm) (Appendix Table 7.4).

The Cretaceous dioritic intrusion has the highest Ba and Sr concentrations and most heavy REE fractionation. Zr contents range from 179 to 355 ppm (Appendix Table 7.4).

To compare the trace element patterns among the different granites, the whole-rock trace element results were normalized to the global average upper continental crust (UCC) (Rudnick and Gao, 2003) in order from large ion lithophile elements, rare earth elements, high field strength elements and transition metal elements (Zhu et al., 2014). The most conspicuous feature of the dataset is that all the Linglong (except for sample 13JD009) samples show similar patterns: Ba, Sr, LREE, Eu, Zr and Hf are relatively enriched but Th and U are relatively depleted. Sample 13JD009A-D has a flat REE pattern (**Figure 7.7**a). Compared with host granites, the MME sample 13JD054D-E shows parallel but higher trace element patterns for most elements with slightly lower concentrations of Ba, Pb, Zr, Hf, Nb and Ta (**Figure 7.7**a). In comparison, the Luanjiahe granite is enriched in Rb, Ba, HREE and Eu, but is relatively depleted in U, Th, LREE, Zr and Hf (**Figure 7.7**a).

The Guojialing granodiorite shows the same pattern as the majority of the Linglong granite samples, including a Cu depletion. Compared with host granodiorites, MMEs (13JD057C-D) show a parallel pattern but with higher concentrations of Th, U, REEs and transitional metals (**Figure 7.7**b). The MME is relatively depleted in Ba, Sr and Pb.

The dioritic intrusion (13JD40A-F) also shows the same trace element patterns as the Guojialing granodiorites but is more enriched in LREE, Ba and Sr (**Figure 7.7**b).

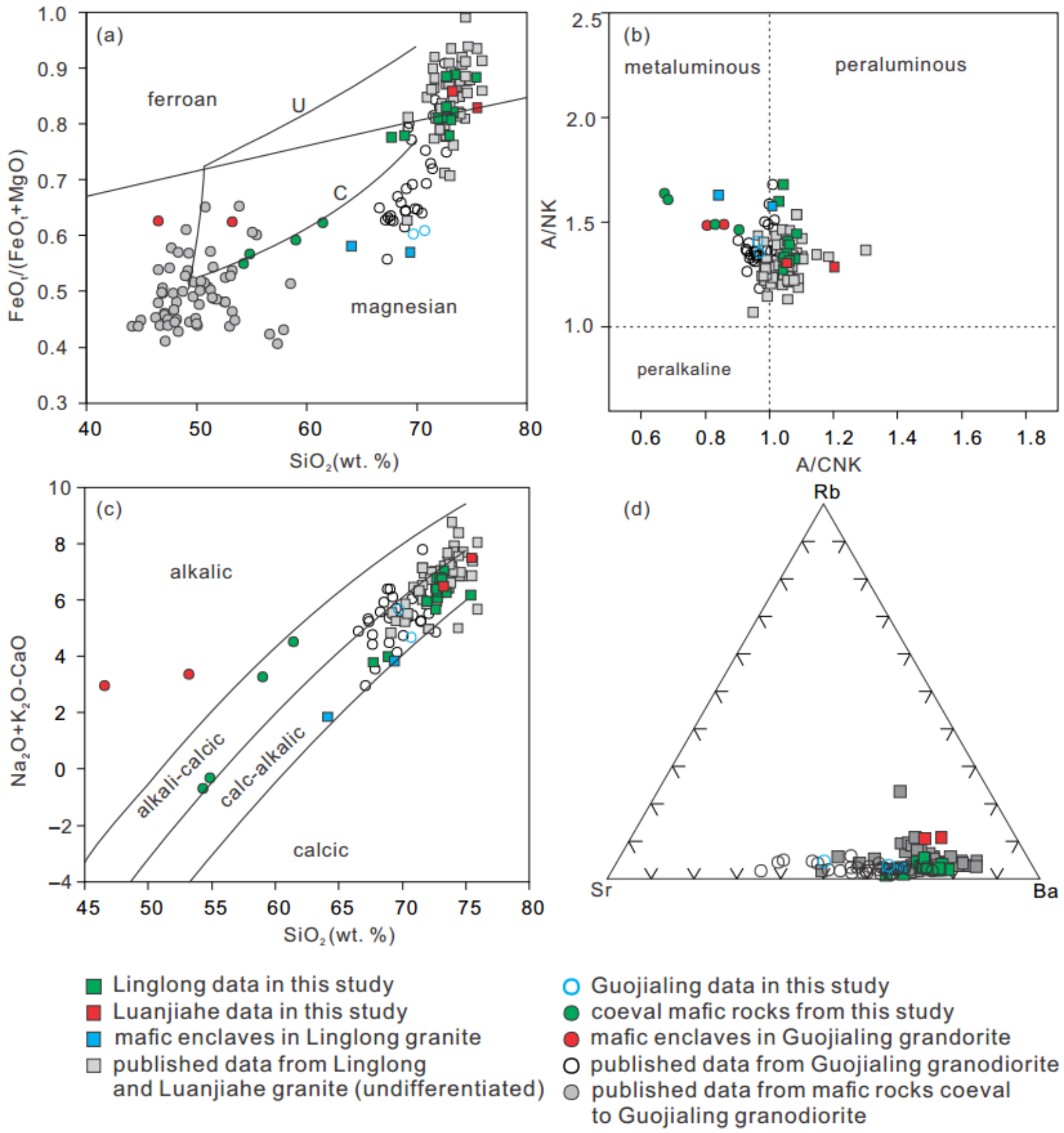

Figure 7.6 Whole rock geochemical plots for the samples in the study and from the literature. (a): $FeO_t/(FeO_t+MgO)$ versus SiO_2, after Osborn (1979) and Frost et al. (2001), U = Northeast Umnak Island, Aleutian Islands, C = Cascades, western United States; (b): Molar $Al_2O_3/(Na_2O+K_2O)$ versus $Al_2O_3/(CaO+Na_2O+K_2O)$; (c): Na_2O+K_2O-Cao versus SiO_2, after Frost et al. (2001); d: Sr-Rb-Ba plot, after Tarney and Jones (1994). Data quoted in the plot include Hou et al. (2007),Zhang et al. (2010a), Jiang et al. (2012), Yang et al. (2012c), and Ma et al. (2013) for Linglong and Luanjiahe granites and Guojialing granodiorite; Guo et al. (2004), Yang et al. (2004), Liu et al. (2009b), Kuang et al. (2012b) and Ma et al. (2014b) for coeval mafic rocks to the Guojialing granodiorite in the Jiaobei region.

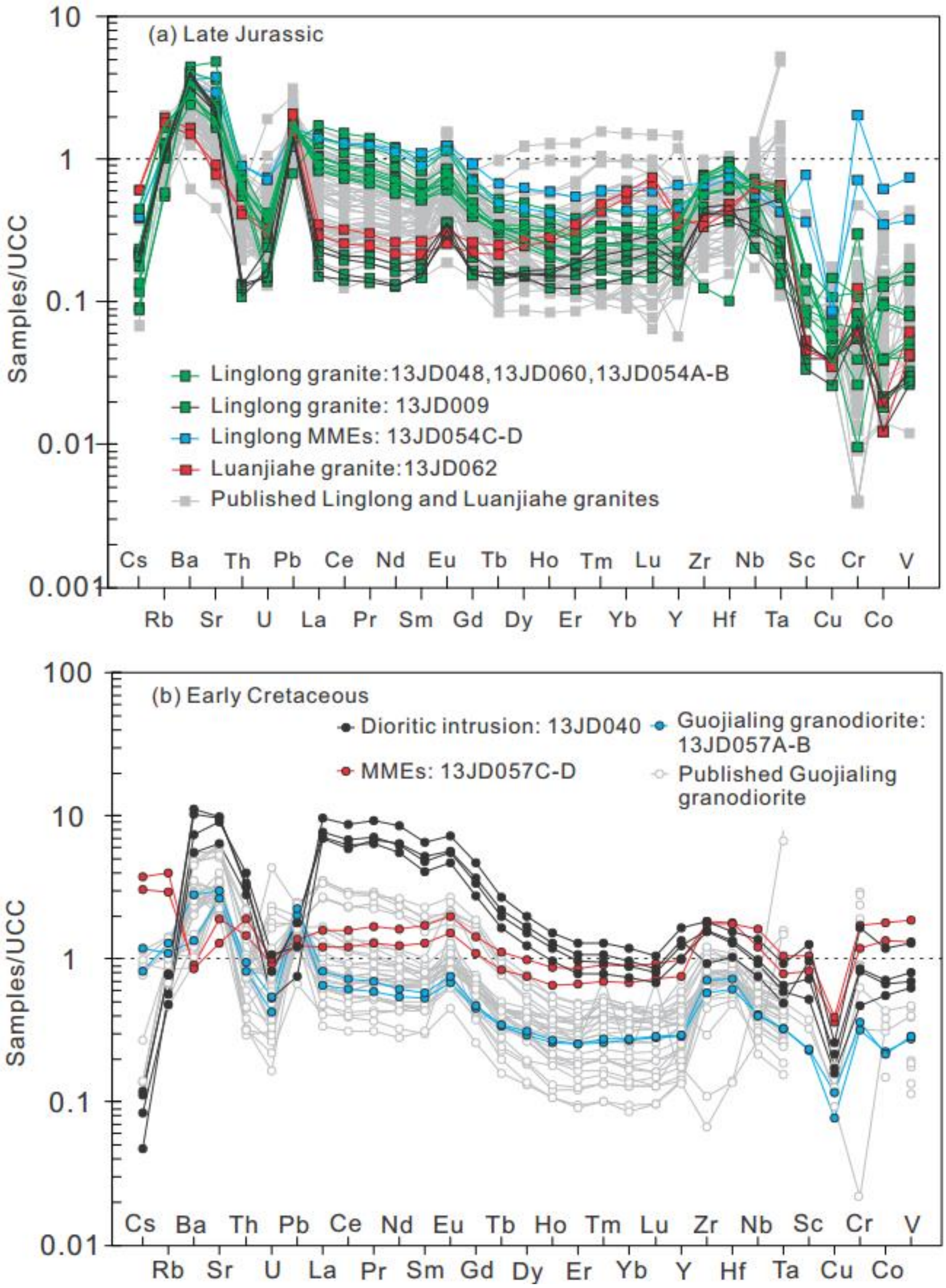

Figure 7.7 Trace element patterns of the Mesozoic magmatic rocks normalized to the global average continental upper crust (Rudnick and Gao, 2003). Data quoted in the plot include Hou et al. (2007), Zhang et al. (2010a), Jiang et al. (2012), Yang et al. (2012c), and Ma et al. (2013) for Linglong and Luanjiahe granites and Guojialing granodiorite; Guo et al. (2004), Yang et al. (2004), Liu et al. (2009b), Kuang et al. (2012b) and Ma et al. (2014b) for coeval mafic rocks to the Guojialing granodiorite in the Jiaobei region.

7.4 Discussion

7.4.1 Petrogenisis of Linglong granites and Luanjiahe granites

7.4.1.1 Sr-Nd-Hf isotopic constraints on the sources

The Linglong granite has high initial $^{87}Sr/^{86}Sr$ ratios that range from 0.708336 to 0.712514 and strongly negative εNd(t) values that range from −21.6 to−17.7 (**Figure 7.8**). Their two stage model ages (T_{DM2}) range from 2.3 to 2.6 Ga, indicating that the Late Jurassic granitic magma dominantly originated from partial melting of the Neoarchean continental crust in the North China Block (Hou et al., 2007). The same range of εHf(t) values (−27.2 to −18.3) in the MME sample (13JD054D) and its host granite (13JD054B) indicates their cogenetic relationship and predominant Neoarchean source (T_{DM2} = 2.9–2.4 Ga). Nonetheless, these εHf(t) values are much higher than those from the regional Neoarchean TTG rocks at 160 Ma [εHf(160 Ma) = −58 to −42] (cacluated from Wu, 2014; Wu et al., 2014). This indicates that other sources must have been involved in the formation of the Late Jurassic magma. Furthermore, the Linglong granite contains a number of inherited zircons with Neoproterozoic and Triassic ages, implying that materials with affinity to the Sulu orogenic belt may be involved in the formation of the Late Jurassic granites in addition to the local Archean crust of the North China block (Yang et al., 2012c; Ma et al., 2013). Furthermore, there is no obvious correlation between SiO_2, εNd(t) and initial$^{87}Sr/^{86}Sr$ for the Upper Jurassic granitoids, suggesting a heterogeneous sources rather than crustal contamination (Yang et al., 2012c).

Compared to most samples from the Linglong granite, those from the Luanjiahe granite have higher but less variable εHf(t) values (−11.6 to −18.6) and εNd(t) values (−17.55 to −17.68) (Jiang et al., 2012; Yang et al., 2012c) (**Figure 7.5** and **Figure 7.8**), indicating that they were generated from a younger and relatively homogeneous source. Because the Luangjiahe granite contains inherited zircons with predominantly Triassic and Neoproterozoic ages, it is inferred that the younger source is likely similar to materials in the Sulu orogenic belt.

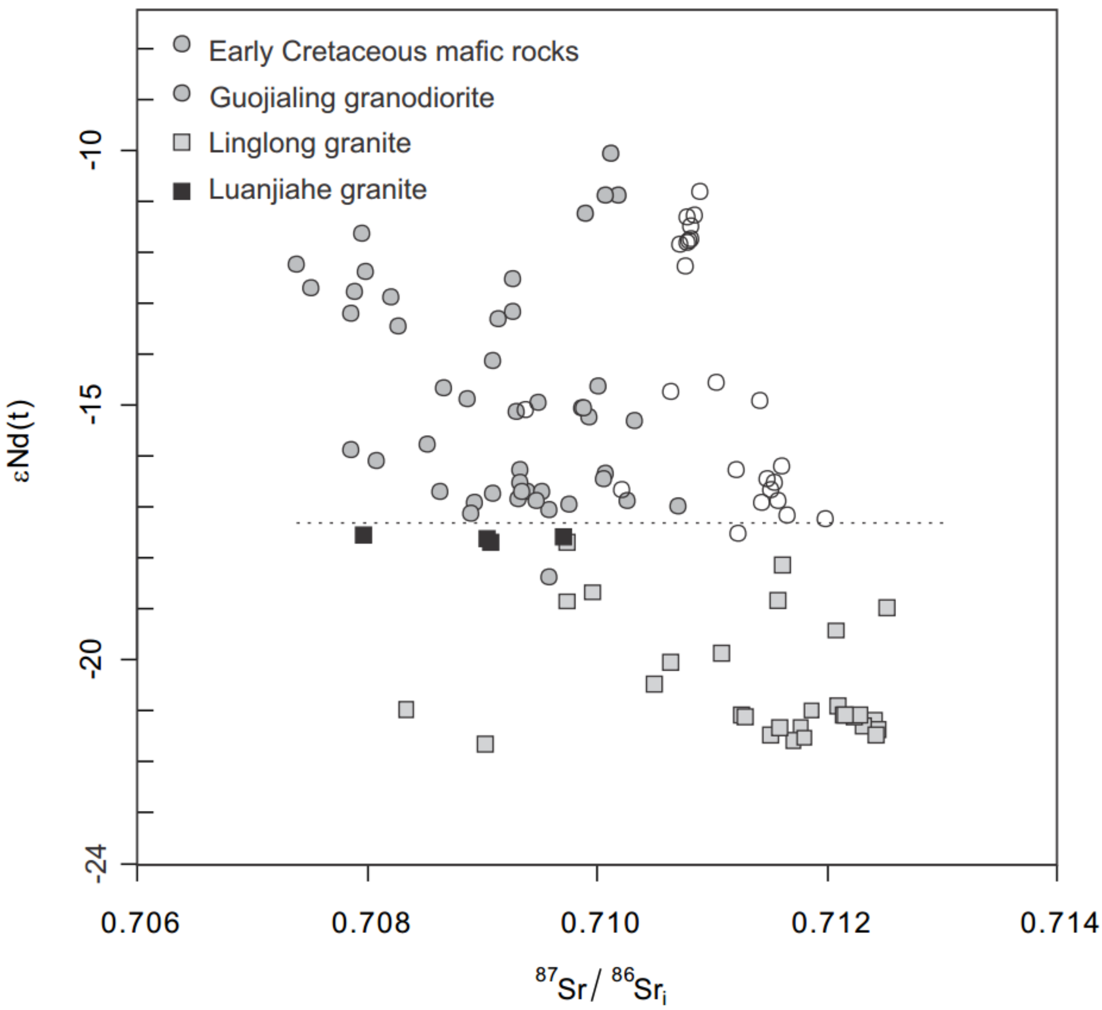

Figure 7.8 εNd(t) versus initial $^{87}Sr/^{86}Sr$ diagram plotted with published data. Data quoted in the plot include Hou et al. (2007),Zhang et al. (2010a), Jiang et al. (2012), Yang et al. (2012c), and Ma et al. (2013) for Linglong and Luanjiahe granites and Guojialing granodiorite; Guo et al. (2004), Yang et al. (2004), Liu et al. (2009b), Kuang et al. (2012b) and Ma et al. (2014b) for coeval mafic rocks to the Guojialing granodiorite in the Jiaobei region.

7.4.1.2 REE fractionation by hornblende, allanite and titanite

The Linglong granite is characterized by various REE patterns, which were probably caused by hornblende and allanite fractionation. The MME samples (13JD054D and E) have identical Dy/Yb ratios and lower La/Sm ratios in comparison to the host granites (13JD054A-C) (**Figure 7.9**), implying fractionation of hornblende rather than garnet (Richards and Kerrich, 2007). For granitic rocks, plagioclase, alkali feldspar, biotite, epidote and apatite each contain approximately 1% or less REE, with the exception of Eu, which can be up to 7% in plagioclase (Gromet and Silver, 1983). A large fraction of REE resides in hornblende and the accessory phases such as titanite and allanite (Bea, 1996). In particular, allanite is strongly enriched in LREE (Gromet and Silver, 1983) and its fractionation thus lowers LREE/HREE ratios of residual melt. Various degrees of allanite fractionation during melting and/or fractionation resulted in the different REE slopes of the Linglong granite. The Luanjiahe granite is notably depleted in LREE, which can be also attributed to fractionation of allanite (Miller and Mittlefehldt, 1982).

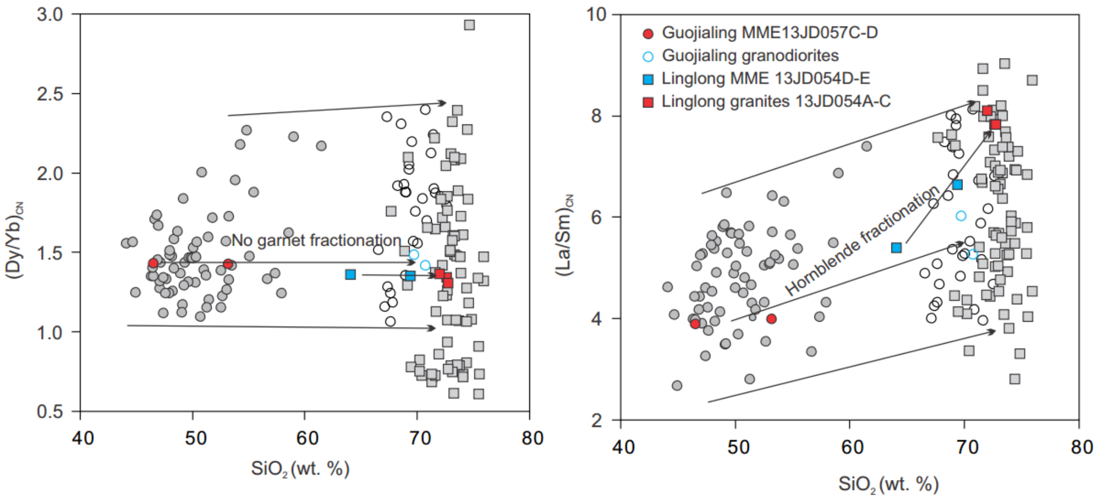

Figure 7.9 Cl chondrite-normalized $(Dy/Yb)_{CN}$ and $(La/Sm)_{CN}$ ratios versus SiO_2 for mafic rocks and granitoids. Normalization values are from Sun and McDonough (1989).

7.4.1.3 Water-present partial melting of biotite-rich gneiss and/or lower continental crust?

Water, even in small amounts, plays an important role in magma generation. For example, the granitic solidus can be depressed by as much as 400 ℃ by the addition of water (Whitney, 1988), and water can control the degree of melting.

The initial magma temperatures of the Jiaobei granitoids were estimated by zircon saturation geothermometry (Watson and Harrison, 1983). Temperature estimations for the Linglong granites range from 645 to 780 ℃ (Appendix Table 7.4). The presence of abundant inherited zircons also suggests relatively low melt temperatures. The temperature range is far below the temperature required for dehydration melting of lower crustal amphibolite (>925 ℃) (Rushmer, 1991), indicating that the Linglong granite was not derived from hornblende dehydration. Instead, the enrichment of Sr and Eu reflects the high solubility of plagioclase under such low temperatures, which therefore requires addition of external water (Housh and Luhr, 1991; Richards and Kerrich, 2007; Richards, 2011). Abundant hornblende is present in mafic enclave sample 13JD054D, either as a residual or an early fractionated mineral, indicating high water contents during partial melting/fractionation. Therefore, water-fluxed melting is the melting mechanism for the Linglong granite.

By comparing major elements and mineral assemblages between samples and experimental results, the pressure and possible source rocks for the generation of magma of the Linglong granites can be constrained. Experimental investigations of metapelite (biotite+ plagioclase + quartz ± aluminosilicate) with 4 wt.% water at 10 kbar reveal that the melting reactions produce garnet + amphibole + melt (Gardien et al., 2000). Since the Linglong granite has a low magma temperature (< 800 ℃), the pressure condition for water-present melting of biotite gneiss is estimated to be 10–15 kbar according to the experimental results. In addition, geochemical features of melts produced by water-present melting of the lower continental crustal at 10–12.5 kbar and 800–900 ℃, 15 kbar and 800 ℃ resemble those of the Linglong granite (Qian and Hermann, 2013). Therefore, it is inferred that the magma of the Linglong granites derived from water-present partial melting of biotite-rich gneiss and/or lower continental crust at 10–15 kbar.

Zircon saturation temperatures for the Luanjiahe granite are estimated at 716−737 °C (Appendix Table 7.4). The Luanjiahe granite is, therefore, interpreted to have derived from partial melting of a different source under similar temperature-pressure-water conditions.

7.4.2 Petrogenesis of Guojialing granodiorite

7.4.2.1 Sr-Nd-Hf isotopic constraints on melt sources

Compared with the Linglong and Luanjiahe granites, the Guojialing granodiorite has higher εNd(t) values (–17.5 to – 10.7) (**Figure 7.8**), which overlap with the values of coeval mafic rocks, implying the involvement of mantle-derived materials. Furthermore, the Guojialing grandiorite has a high Mg#, similar ranges of εNd(t) and subparallel trace element patterns to coeval mafic rocks (e.g., MMEs in the study) (**Figure 7.7**b), implying that the Guojialing granodiorite is cogenetic with coeval mafic rocks. There appears to be a link between mafic enclave samples (13JD057C and D) and host granodiorites (13JD057A-B) as they have overlapping εHf(t) values (**Figure 7.5**). The mafic rocks have been interpreted to have been sourced from an enriched mantle (Yang et al., 2004; Guo et al., 2006; Liu et al., 2009b; Ma et al., 2014b). Therefore, the Guojialing granodiorite likely also originated from an enriched mantle source, with some crustal assimilation as evidenced by higher initial $^{87}Sr/^{86}Sr$ isotope ratios compared with coeval mafic rocks (**Figure 7.8**). Inherited Neoarchean and Paleoproterozoic zircons preserved in the Guojialing granodiorite also indicate the participation of ancient crustal materials. The mismatch of εHf(t) values between the dioritic intrusion and the Guojialing granodiorite reported in this study simply hints that there is no genetic link between them. This agrees well with the supposition that the Guojialing granodiorite (13JD057A and-B) evolved from mafic magma, forming its MMEs (13JD057C and -D). Therefore, from a regional perspective, the genetic link between mafic rocks and the Guojialing granodiorite holds. Variable Hf and Nd isotopic ratios of the Guojialing granodiorite were inherited from the parent mafic magma derived from the isotopic heterogeneity of the lithospheric mantle source (Zhang et al., 2004a).

7.4.2.2 Fractional crystallisation of enriched mantle-derived magma

The Guojialing granodiorite (13JD057A-B) possesses the same $(Dy/Yb)_{CN}$ ratios and higher $(La/Sm)_{CN}$ ratios compared to the enclosed MMEs (13JD057C-D) (**Figure 7.9**), which indicates the dominant control of hornblende fractionation during magma evolution (Richards and Kerrich, 2007). This genetic link may also apply to the Guojialing granodiorite bodies and coeval mafic dykes in the Jiaobei region. An important difference between the Guojialing granodiorite and coeval mafic rocks is that their trace element contents decreased during magma evolution. This may arise from titanite and apatite fractionation in addition to hornblende fractionation. Because titanite and apatite generally have up to two orders of magnitude higher abundances of REEs than granodioritic magma (Gromet and Silver, 1983; Stern and Hanson, 1991), separation of titanite and apatite could have lowered the REE contents in the residual magma. Separation of either monazite or allanite from magma can also decrease LREE contents in the residual magma (Miller and Mittlefehldt, 1982), nonetheless, contribution of these two minerals is likely less significant than titanite and apatite separation given that the latter are rare in the Guojialing granodiorite.

7.4.3 Tectonic implications

The discovery of coesite and diamond in the Dabie-Sulu ultra-high pressure belt suggest that the continental crust was once subducted to mantle depths, possibly up to 200 km or greater (Ye et al., 2000a). This event may have significantly modified the chemical composition of the NCB lithospheric mantle as revealed by mantle xenoliths and Early Cretaceous mafic magmas (Jahn et al., 1999; Yang et al., 2012a; Zhao et al., 2013). However, the impact of this continental collision on the overriding continental crust is yet to be clearly recognized, especially in the region east of Tan-Lu fault. The Linglong granites, as the largest Late Jurassic pluton in Shandong Peninsula, are expected to bear critical implications for crustal process during the South China-North China continental collision

7.4.3.1 A crustal detachment model for origin of Upper Jurassic granites

Crustal anatexis, without the addition of water, requires anomalously high temperature and therefore a source of heat, or decompression of heated rocks during crustal thinning (Thompson, 1999). Processes such as crustal thickening, lithospheric mantle thinning and underplating of mafic magma can drive the geotherm towards higher temperature to produce partial melting. During continental collision (for example, the collision between North China and South China in the Mesozoic), temperature in the middle to lower crust will increase during thermal relaxation several tens of million years after crustal thickening (England and Thompson, 1984; England and Thompson, 1986; Clark et al., 2011). The absence of contemporaneous Jurassic mafic rocks in the Jiaobei region implies that there was no significant convective heat from the mantle at that time. Therefore, crustal thickening was the main mechanism for providing high temperature to produce crustal melting. In addition, the results of this work indicate that the melting temperatures for the Linglong granite were relatively low (645 to 780 ℃; Appendix Table 7.4), and water flux may be a more important trigger for the crustal melting. As there is little pore fluid in the lower continental crust (Yardley, 1986), the question then becomes, where did the external water came from?

At low temperatures (<750 ℃) and moderate to high crustal pressures, the production of sufficient melt to enable melt drainage, requires an influx of aqueous fluid along structurally controlled pathways or recycling of fluid via migration of melt and exsolution during crystallization (Brown, 2013). Recycling of fluid is unlikely here because no mafic magma existed to release water during its crystallization. Alternatively, aqueous fluid may be introduced to the continental crust along structurally controlled pathways, for example, through crustal-scale structures such as shear zones (Reichardt and Weinberg, 2012b; Reichardt and Weinberg, 2012a).

In addition to the heat and water conditions, the generation of the Linglong granite also appears to have involved materials from the South China block, as indicated by the exotic Neoproterozoic and Late Triassic inherited zircons.

The source, heat and water requirements for the generation of the Linglong granites can best be accommodated by the crustal detachment model (Li, 1994; Li, 1998) (**Figure 7.10**). In this model, during the Triassic to the Middle Jurassic collision between the North and South China blocks, the ultrahigh pressure metamorphic rocks were firstly exhumed rapidly to the crustal level (**Figure 7.10**a). The upper crust of the South China block along the proto-Sulu orogenic belt then started to detach from the lower crust after ca. 210 Ma, and thrust northward for > 400 km over the lower crust of the North China block along a crustal detachment zone at > 20 km depth (**Figure 7.10**b-c). The continental crust in the Jiaobei region was thus thickened by thrust duplication, folding and pure-share shortening. The thrusting and crustal thickening likely reached the present-day position of the Linglong granite by ca. 160 Ma, as the collision-induced convergent deformation was about to terminate (Li, 1998). Heat generated in the thickened continental crust, plus water released from the detachment shear zone and thrust faults, likely induced partial melting of the Jiaobei Archean basement, possibly mixed with minor partial melts from the Sulu orogenic belt (migrated along the crustal detachment plane?), and formed the Linglong and Luanjiahe granites.

As an alternative collision mechanism, the indentation model could also produce a thickened continental crust, and thus provide the heat for continental crust to melt; however, it could not easily explain the source for the external water that is required to generate the melting, or the origin for the South China-like source materials.

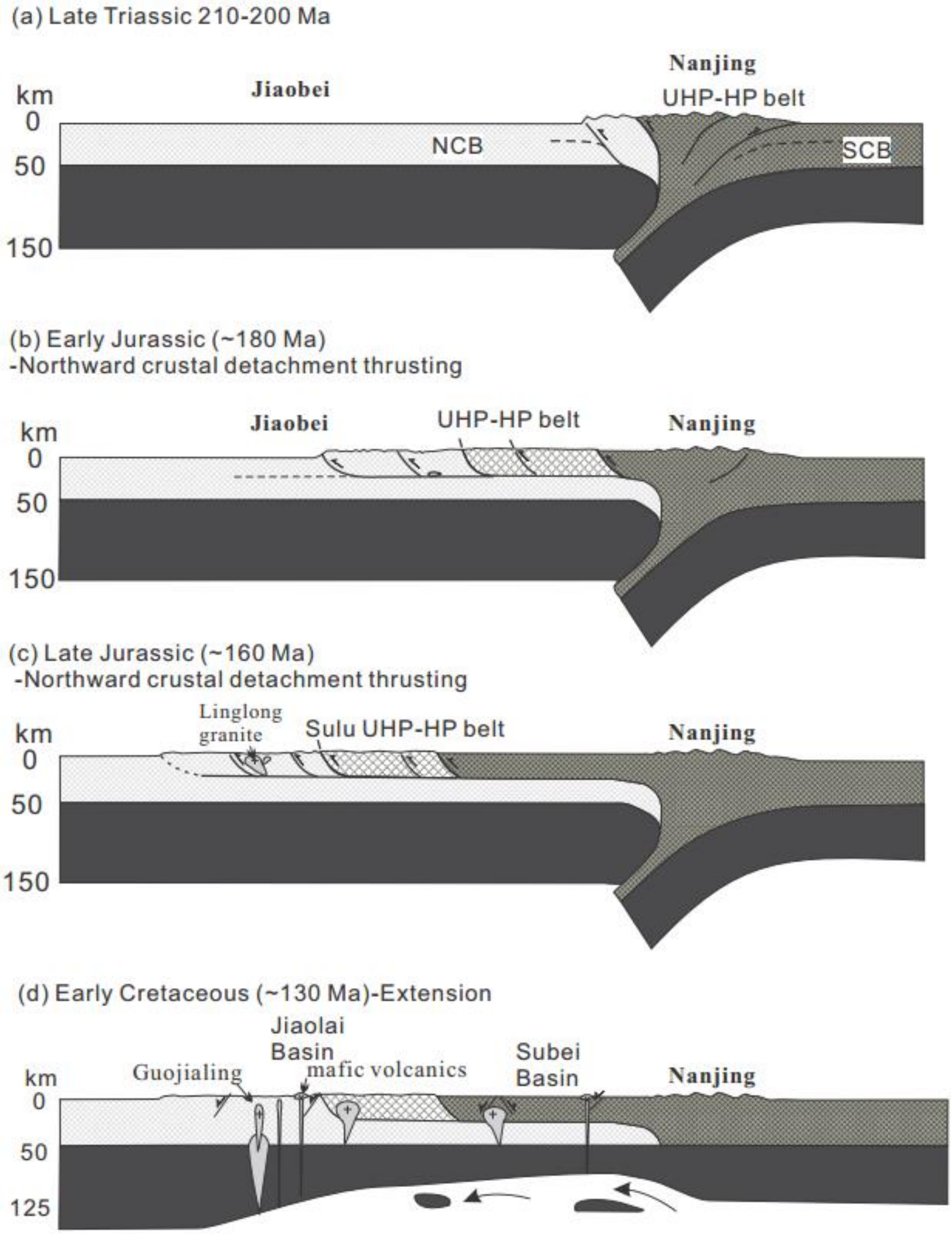

Figure 7.10 Tectonic model for the geneses of Late Jurassic Linglong and Luanjiahe granites and Guojialing graondiorites, modified after Li (1998).

7.4.3.2 Thinning of lithospheric mantle in the Early Cretaceous

It has been well documented that the widespread mafic intrusive or eruptive rocks in both the Jiaobei region and much of eastern China during the Early Cretaceous originated from melting of an enriched continental lithospheric mantle (Guo et al., 2004; Yang et al., 2004; Liu et al., 2009b; Zhang et al., 2012b; Zhao et al., 2013; Ma et al., 2014b). As shown in this study, the Guojialing granidiorite in the Jiaobei region was also derived from the melting of the enriched continental lithospheric mantle (**Figure 7.10**d). This demonstrates a thinned continental lithospheric mantle by that time. Formation of the Jiaolai rift basin demonstrates that the crust was also extended. However, it remains unclear whether the continental crust was thicker or thinner than the normal continental crust at that time. Useful insight can be gained by examining the FeO-MgO-SiO_2 relationship of the Guojialing granodiorite. In the FeOt/(FeOt+MgO)-SiO_2 plot, both the Guojialing granodiorite and coeval mafic rocks are magnesian and exhibit a monotonously and continuous increasing trend (**Figure 7.6**a). This trend indicates that the fractionation took place at a high pressure, high oxygen fugacity and high water content where magnetite precipitates continuously during fractional crystallisation, whereas in a thinner crust, FeOt/(FeOt+MgO) ratios tend to increase dramatically at low silica content (Osborn, 1979; Sisson and Grove, 1993; Frost et al., 2001; Chiaradia, 2014). Average Fe_2O_3t and Cu contents for mafic rocks with 4–6 wt% MgO are 6.81% ± 1.08% (n = 8) and 35 ppm, respectively. Based on Chiaradia (2014, Figure 2), such magmas should be accompanied by a ~35 km continental crust. This thickness is similar to the present thickness (about 33 km) of continental crust (Jia et al., 2014), indicating that the thickened crust, if it had existed, was already thinned by ca. 130–120 Ma.

7.5 Conclusion

The Linglong and Luanjiahe granites intruded the North China block in the Jiaobei region at 158–148 Ma. The presence of a large number of inherited zircons, especially Neoproterozoic and Late Triassic populations that are representative of the South China block, implies that part of the sources are possibly from the Sulu orogenic belt, in addition to the Archean lower crust of the North China block. A petrogenetic analysis shows that the granites originated from water-fluxed partial melting of complex sources and underwent fractionation of hornblende, titanite and allanite, which caused variation of REE patterns. The generation of the Upper Jurassic granites may be associated with northward thrusting of the Sulu orogenic melt along a mid-crust detachment from the Late Triassic to the Late Jurassic, and water released from the detachment zone triggered partial melting of the crustal materials.

The Guojialing granodiorite and enclosed MMEs crystallised simultaneously at 127 Ma. They have indistinguishable εHf(t) values (−15.0 to −9.6) and parallel REE patterns. These features suggest that they were cogenetic and sourced from an enriched mantle, with crystallization differentiation and some crustal contamination. Titanite, apatite and hornblende fractionations caused the decrease of REE contents from mafic magma to felsic magma. The thickness of the continental crust at 130–120 Ma in the Jiaobei region is estimated to be ca. 35 km, indicating that both the lithospheric mantle and the crust had probably been attenuated in the Early Cretaceous.

CHAPTER 8 SYNTHESIS

8.1 Introduction

Tectonic models for Mesozoic SCB and NCB collision and models for lithospheric thinning will be discussed, based on new results from this study and a review of observations from the literature. Specifically, the indentation model, the crustal detachment model and the rotational collision model will be discussed, whereas, the transform fault model is not considered, because the southward subduction polarity in the Sulu orogenic belt that it requires, is not supported by geological observations. Models under discussion for lithospheric thinning include delamination (detachment and sinking of the lower crust and underlying lithospheric mantle), and thermo-chemical erosion.

8.2 Collision between the SCB and NCB

8.2.1 Exhumation of the Sulu UHP rocks and in the Jiaobei region

Thermochronology studies using zircon fission-track and zircon (U-Th)/He methods (Chapter 4 and Chapter 5) reveal contrasting exhumation processes in the Sulu UHP belt and in the Jiaobei region. Exhumation of the Sulu UHP rocks took place from 180–160 Ma (**Figure 8.1**) which resulted in cooling below 200–160 ℃ whereas in the Jiaobei region, cooling resulted from secular and spatially diachronous exhumation. Exhumation and cooling of the Jiaobei region to below 200–160 ℃ occurred predominantly between 205 Ma to 160 Ma, and showed a temporal variation with increased distance from the Sulu orogenic belt (**Figure 8.1**), with the earlier exhumation occurred proximal to the Sulu UHP belt. Overall, this exhumation pattern likely reflected kinematics of crustal thickening in the Jiaodong Peninsula. Earlier exhumation at ca. 260 Ma in the Jiaobei region may represent localised cooling and erosion induced by crustal shortening at the beginning of continental collision between the SCB and NCB. The next stage of exhumation in the Jiaobei region (from ~205 Ma), may represent the start of crustal thickening after the UHP rocks in the Sulu belt were exhumed to middle crust levels. Concomitant erosion accompanied thrusting and induced the exhumation. Exhumation of the Sulu

UHP rocks did not commence until 180–160 Ma, which may indicate that the UHP rocks first travelled along the horizontal detachment fault of the thrusting system at 205–180 Ma, and only during 180–160 Ma was the UHP belt driven upward along a thrust ramp. The earlier onset of exhumation at in the Jiaobei region, relative to the Sulu UHP rocks, implies that the Jiaobei region was experiencing crustal shortening and resultant cooling when the Sulu UHP rocks were transported horizontally along the detachment. Exhumation propagated towards the northwest in the Jiaobei region, after the UHP rocks were pushed upward along the thrust ramp during 180–160 Ma. Exhumation in the Luxi region (Chapter 6) was weak during the Triassic-Late Jurassic, indicating that crustal exhumation during the SCB-NCB collision was not as severe as in the region east of the Tan-Lu fault.

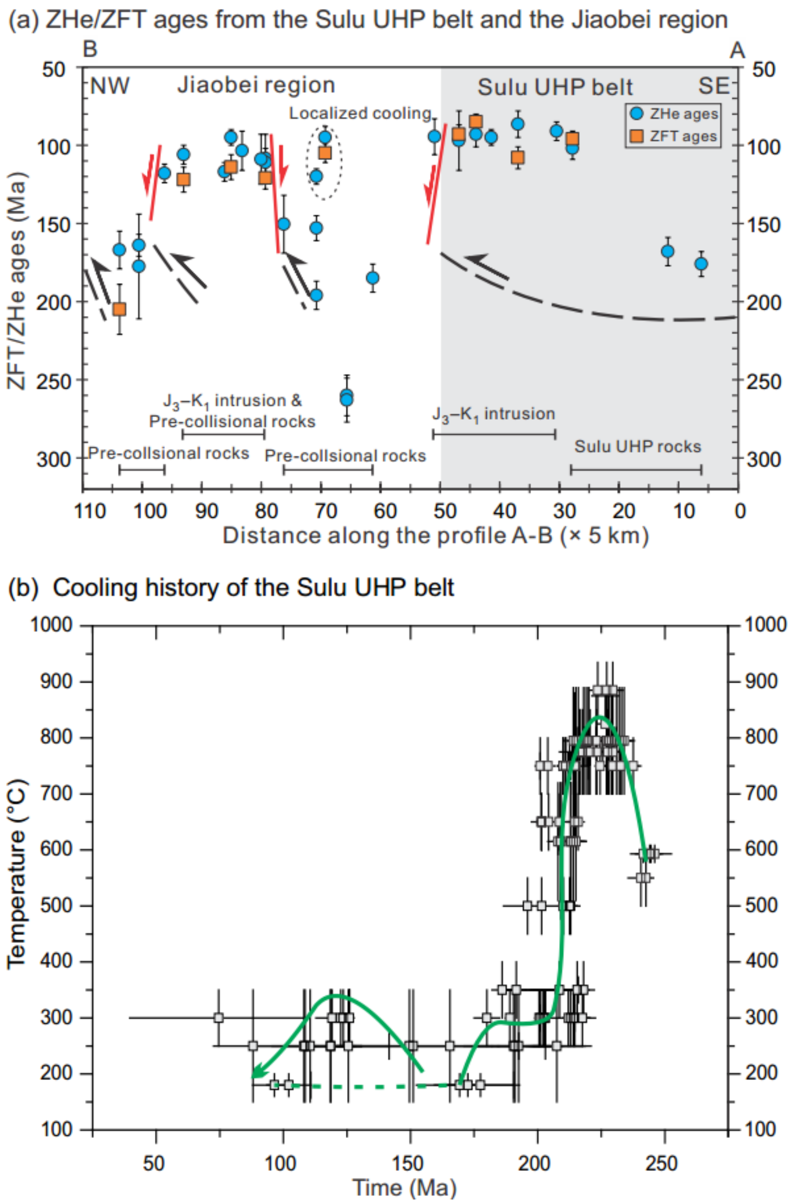

Figure 8.1 (a) zircon fission-track and (U-Th)/He ages across the Sulu orogenic belt and the Jiaobei region. (b) Cooling history of the Sulu UHP rocks constrained by ages obtained by zircon U-Pb, 40Ar/39Ar of mica, hornblende and feldspar, and zircon (U-Th)/He methods.

This exhumation pattern, together with structural deformation in the Sulu UHP belt and the Jiaobei region (**Figure 4.1** and **Figure 5.1**), is consistent with the crustal detachment model as shown in **Figure 8.2**. The Sulu UHP-HP rocks were originally located in Nanjing as an eastern extension of the Dabie orogenic belt, and pre-collision rocks now in the Jiaobei region were situated immediately north of the original location of the UHP-HP rocks. Northward translocation of the UHP-HP rocks along a crustal detachment since 210–200 Ma, induced shortening and folding of the rocks now in the eastern part of the Jiaobei region, whilst the UHP-HP rocks were rigid enough to escape internal folding and exhumation. Continuous shortening drove the UHP-HP rocks, to their present location and they were exhumed along the thrust ramp at 180–160 Ma.

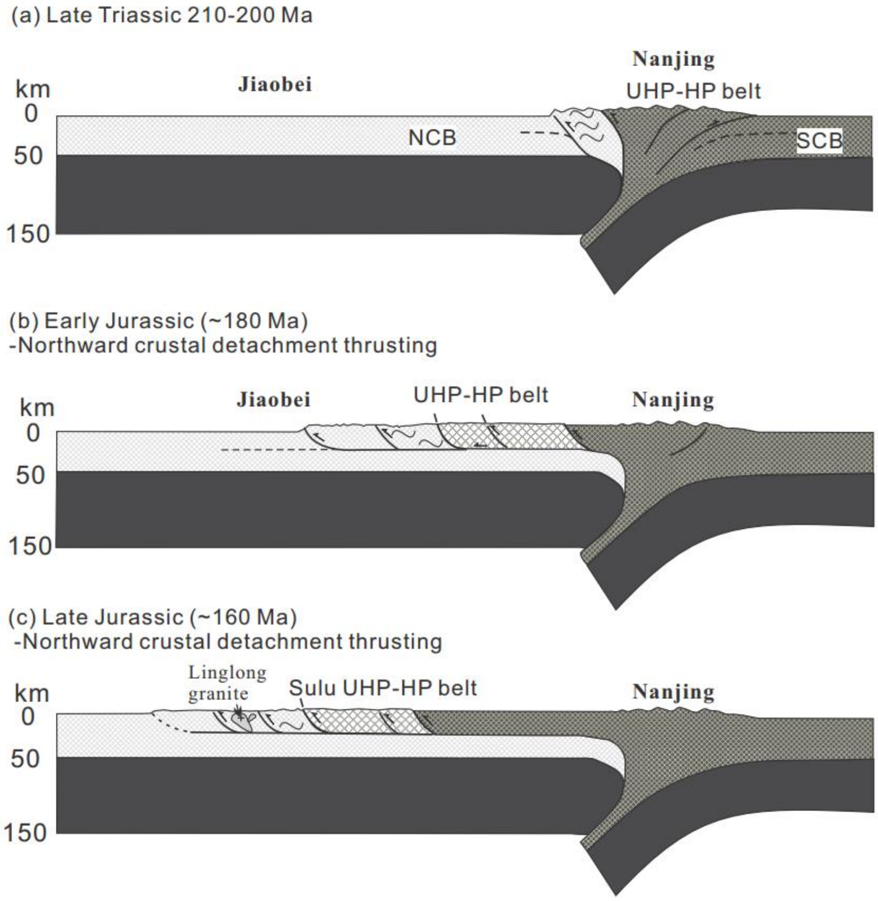

Figure 8.2 The crustal detachment model after Li (1998) which could explain exhumation process of the Sulu UHP rocks and the Jiaobei region.

The lithospheric indentation model (Yin and Nie, 1993) predicted that 550 km of crustal shortening could have been accommodated by the eastern NCB east of the Tan-Lu fault during the latest Early Permian and possibly into the Early Jurassic. Accordingly, exhumation of the Jiaobei region and the Sulu UHP rocks would be associated with an intense shortening and exhumation should have predominantly happened in the Triassic. This, however, is not consistent with the 205–160 Ma exhumation ages obtained for the Jiaobei region. More importantly, this model cannot explain the differential exhumation between the Jiaobei region and the Sulu UHP belt at 205–160 Ma. The rotational collision model (e.g., Zhang, 1997) postulated an *in situ* collision along the Sulu orogenic belt and the Tan-Lu fault from the Early Permian to the Middle Jurassic. This model can accommodate exhumation of ~205– 160 Ma in the Jiaobei region, but it is difficult to explain the absence of exhumation at ~205–180 Ma in the Sulu UHP rocks since the Jiaobei region was exhumed under the same tectonic regime.

8.2.2 Formation of the Tan-Lu fault

The Tan-Lu fault is predicted to have played different roles in different tectonic models proposed for the SCB-NCB collision. The lithospheric indentation model requires a syn-collisional strike slip movement of this fault (cutting the entire lithosphere of the NCB) from the Early Permian to the Middle Jurassic (Yin and Nie, 1993). The rotational collision model predicts it as a suture zone during the same time interval (Zhang, 1997). In contrast, the crustal detachment model (Li, 1994) emphasises a sinistral strike-slip displacement during the Late Triassic to the Middle Jurassic, and mainly at the upper crustal levels. A compilation of age data along the Tan-Lu fault may help to test these models. Table 8.1 shows the $^{40}Ar/^{39}Ar$ ages of gneiss and mylonite in/around the fault zone. Three main groups of ages have been revealed: 221–181 Ma, ~160 Ma and 140–110 Ma (**Figure 8.3**). The youngest age group was interpreted to represent cooling ages of the sinistral movement of this fault in the Early Cretaceous (Zhu et al., 2005). The two older age groups likely represent cooling associated with both the exhumation of the UHP rocks, and/or sinistral shearing along the Tan-Lu fault (Wang, 2006; Zhu et al., 2009). The timing and anti-clockwise displacement of the Tan-Lu fault from 221 to 160 Ma imply a northward translocation of the Sulu UHP belt, which agrees with the prediction of the crustal detachment model. Although these data cannot preclude possible cooling in the

Early-Middle Triassic, they are not readily explained by the indentation model, especially sinistral shearing at ~160 Ma. The rotational collisional model does not predict strike-slip movement of the Tan-Lu fault during the collision, nor could it explain sinistral movement at ~160 Ma.

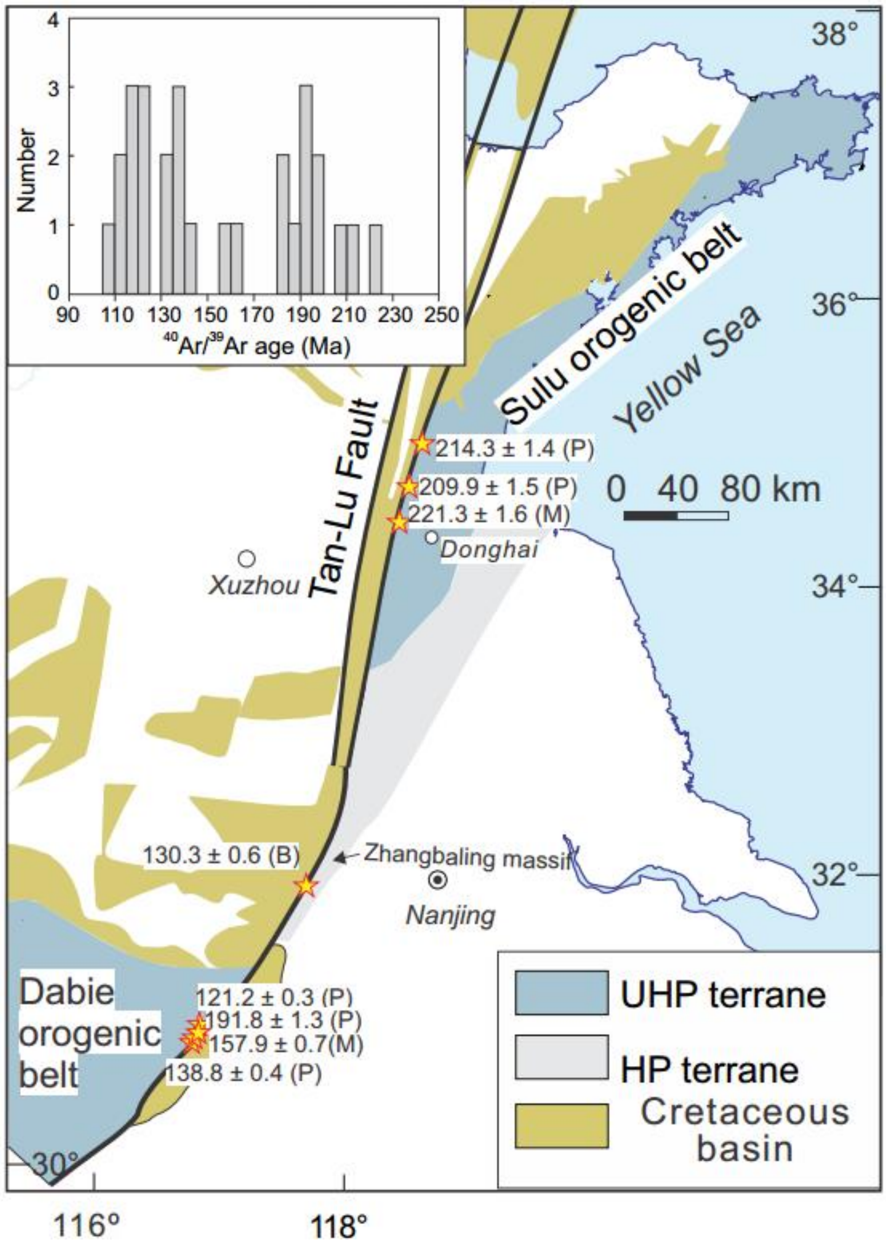

Figure 8.3 Representative $^{40}Ar/^{39}Ar$ results for three well studied segments (Dabie, Zhangbaling and Sulu) within the Tan-Lu fault zone, modified after Zhu et al. (2010). The full dataset is presented in Table 8.1. For brevity, not all results are shown in the figure. Letters in parenthesis represent minerals analysed by $^{40}Ar/^{39}Ar$ dating; phengite (P), biotite (B), muscovite (M).

Table 8.1 Published $^{40}Ar/^{39}Ar$ ages from the Tan-Lu fault

Sample	Latitude	Longitude	Segment of the Tan-Lu fault	Rock type	Dating method	Age (Ma)	References
DB20	30° 58.505'N	116°49.634'E	Dabie	Gneissic granite	$^{40}Ar/^{39}Ar$ Muscovite	161.5 ±0.8	Wang (2006)
DB26	30° 58.503'N	116°49.662'E	Dabie	Gneissic granite	$^{40}Ar/^{39}Ar$ Muscovite	157.9 ±0.7	
T15-5	30°58.435' N	116°49.662'E	Dabie	Protomylonite	$^{40}Ar/^{39}Ar$ Phengite	138.8 ±0.4	Zhu et al. (2005)
T41-2	30°59.388' N	116°48.483'E	Dabie	Mylonite	$^{40}Ar/^{39}Ar$ Phengite	121.2 ±0.3	
T15-1	30°59.820' N	116°51.000'E	Dabie	Protomylonite	$^{40}Ar/^{39}Ar$ Biotite	110.7 ±0.2	
T19-5	30°59.388' N	116°51.317'E	Dabie	Mylonite	$^{40}Ar/^{39}Ar$ Biotite	117.6 ±0.2	
T19-8	30°59.388' N	116°51.317'E	Dabie	Mylonite	$^{40}Ar/^{39}Ar$ Biotite	109.8 ±0.2	
T19-10	30°59.388' N	116°51.317'E	Dabie	Mylonite	$^{40}Ar/^{39}Ar$ Biotite	119.7 ±0.4	
T19-11	30°59.388' N	116°51.317'E	Dabie	Protomylonite	$^{40}Ar/^{39}Ar$ Biotite	111.9 ±0.2	
N13	31°54.595' N	117°40.563'E	Zhangbaling	Mylonite	$^{40}Ar/^{39}Ar$ Biotite	130.3 ±0.6	
N14	31°54.595' N	117°40.563'E	Zhangbaling	Mylonite	$^{40}Ar/^{39}Ar$ Biotite	134.1 ±0.6	
N15	31°53.892' N	117°40.860'E	Zhangbaling	Mylonite	$^{40}Ar/^{39}Ar$ Biotite	118.7 ±0.5	
N17	31°52.205' N	117°39.250'E	Zhangbaling	Mylonite	$^{40}Ar/^{39}Ar$ Biotite	135.6 ±0.6	
N21	31°50.878' N	117°38.908'E	Zhangbaling	Protomylonite	$^{40}Ar/^{39}Ar$ Biotite	124.8 ±0.7	
N22	31°50.878' N	117°38.908'E	Zhangbaling	Protomylonite	$^{40}Ar/^{39}Ar$ Biotite	124.9 ±0.4	
N47	31°49.110' N	117°38.480'E	Zhangbaling	Protomylonite	$^{40}Ar/^{39}Ar$ Biotite	137.2 ±0.8	
N14	31°54.595' N	117°40.563'E	Zhangbaling	Mylonite	$^{40}Ar/^{39}Ar$ Hornblende	143.3 ±2.4	
N18	31°51.485' N	117°38.937'E	Zhangbaling	Mylonite	$^{40}Ar/^{39}Ar$ Hornblende	190.5 ±2.3	
TL1	30°58.605'N	116°49.797'E	Dabie	Mylonite	$^{40}Ar/^{39}Ar$ Phengite	191.8 ±1.3	Zhu et al. (2009)
TL2	30°59.260'N	116°51.038'E	Dabie	Mylonite	$^{40}Ar/^{39}Ar$ Phengite	196.6 ±1.3	
TL3	30°59.388'N	116°51.155'E	Dabie	Mylonite	$^{40}Ar/^{39}Ar$ Phengite	189.1 ±1.3	
TL4	30°59.530'N	116°51.273'E	Dabie	Mylonite	$^{40}Ar/^{39}Ar$ Phengite	197.7 ±1.4	
TL5	30°59.820'N	116°51.000'E	Dabie	Mylonite	$^{40}Ar/^{39}Ar$ Phengite	190.9 ±1.2	
T28-12	30°58.435'N	116°49.662'E	Dabie	Mylonite	$^{40}Ar/^{39}Ar$ Phengite	181.4 ±0.5	
T28-13	30°58.435'N	116°49.662'E	Dabie	Mylonite	$^{40}Ar/^{39}Ar$ Phengite	181.6 ±0.8	
X19	34°30.138'N	118°27.430'E	Sulu	Ultramylonite	$^{40}Ar/^{39}Ar$ Muscovite	221.3 ±1.6	
X42	34°42.533'N	118°30.463'E	Sulu	Ultramylonite	$^{40}Ar/^{39}Ar$ Phengite	209.9 ±1.5	

X57-4	34°57.693'N	118°36.047'E	Sulu	Ultramylonite	$^{40}Ar/^{39}Ar$ Phengite	214.3 ± 1.4

8.2.3 Crustal melting

Crustal melting in a thickened continental crust likely occurs due to elevated temperatures resulting from the radiogenic heat generated by U, Th and K (England and Thompson, 1986; Clark et al., 2011). The Linglong granite, emplaced in the Late Jurassic without coeval mafic intrusions, is inferred to have derived from water-flux partial melting of a thickened continental crust (Chapter 7). Neoproterozoic and Triassic ages of the inherited zircons in the granite suggests the involvement of South China and/or Dabie-Sulu orogenic belt-sourced materials in the formation of the Linglong and coeval Luanjiahe granites. Possible mechanisms for this are currently under investigation. The crustal detachment model can best explain the water source (fluids traveling along the detachment fault) that caused the water-flux partial melting during the mid-Jurassic.

8.3 Mesozoic–Cenozoic lithospheric thinning

An array of mechanisms has been invoked to explain how lithospheric thinning occurred, however, there is no widely accepted explanation. A review of well-documented observations is given below, which is then used to further test the various mechanisms.

8.3.1 A thickened continental crust in the early to mid-Mesozoic

Evidence for a thickened continental crust was provided by xenoliths of eclogite and garnet clinopyroxenite in Early Cretaceous high-Mg adakitic intrusions in Xuzhou (**Figure 8.3**). The xenoliths underwent eclogite-facies metamorphism at pressures > 1.5 GPa at ca. 220 Ma (Xu et al., 2006b). Some xenoliths contain Late Archean to early Paleoproterozoic (2.3–2.6Ga) inherited zircons and lack Neoproterozoic zircons, suggesting involvement of a protolith of the North China continental crust (Xu et al., 2006b). The timing of the eclogite-facies metamorphism agrees with the ages of high-pressure retrograde metamorphism in the Dabie-Sulu orogenic belt, implying that the continental crust of the NCB was likely thickened by the Mesozoic collision with the SCB. Due to the higher density of the eclogite in the lower continental crust relative to the underlying mantle, this eclogitised continental crustal may eventually founder, together with the underlying lithospheric mantle, into the asthenosphere.

8.3.2 Metasomatised lithospheric mantle

A recent study of high Mg basalts derived from the lithospheric mantle in the Luxi region estimated that the original lithospheric mantle contained > 1000 ppm water, almost an order of magnitude higher than that in the stable Kaapvaal cratonic mantle in South Africa (~120 ppm by weight) (Xia et al., 2013). The hydrated lithospheric mantle could have resulted from peripheral subduction and collision (Niu, 2005; Windley et al., 2010). The high water content of the lithospheric mantle will not only significantly reduce viscosity (Li et al., 2008), thereby facilitating its participation in mantle convection (Niu, 2005; Xia et al., 2013), but can also lower the temperature of the mantle solidus (Xu et al., 2009b). Mantle xenoliths in Meosozoic–Cenozoic mafic rocks in the margin and interior of the eastern NCB and in the Dabie-Sulu orogenic belt, demonstrate multiple stages of metasomatic overprinting of the lithospheric mantle (Chen and Zhou, 2005; Zhao et al., 2007; Xu et al., 2008; Zhang et al., 2009a; Liu et al., 2010; Yang et al., 2012b; Xu et al., 2013; Zheng et al., 2014). Delamination of the eclogitised crust of the NCB (Gao et al., 2004; Gao et al., 2008) and subduction of the SCB (Yang et al., 2012a; Guo et al., 2013) were proposed to have metasomatised the remaining lithospheric mantle of the North China block. This interaction could convert peridotite into olivine-free pyroxenite (Sobolev et al., 2007).

8.3.3 Temporal variations in the Cretaceous magmatic composition

Subsequent melting of the hybridised mantle, consisting of refractory Archean peridotitic mantle and olivine-free pyroxenite, could have produced the Early Cretaceous mafic and high-Mg andesitic rocks (Gao et al., 2008; Xu et al., 2008; Gao et al., 2009; Liu et al., 2009b). A shift from enriched to depleted mantle source for mafic magmas can indicate the removal of such a hybridized mantle. A wealth of data is available to identify this transition. The shift from an enriched to a depleted mantle source occurred at 100–90 Ma in the region east of the Tan-Lu fault, and at 110–100 Ma in the region west of the Tan-Lu fault (chapter 5); after which, the mafic magma became alkali, had OIB-type trace element patterns and positive $\varepsilon Nd(t)$ (Xu, 2001; Zhang et al., 2003a; Xu et al., 2004c; Yan et al., 2005; Liu et al., 2008c; Zhang et al., 2008b; Kuang et al., 2012a; Cai et al., 2013; Meng et al., 2014). Before the transition, the mafic magma was largely characterised by calc-alkaline series signatures, with negative Nb-Ta anomalies and strongly negative εNd(t) values, indicative of derivation from an enriched lithospheric mantle, (e.g., Zhang et al., 2002; Guo et al., 2004; Yang et al., 2004; Guo et al., 2005a; Liu et al., 2008c; Liu et al., 2009b; Kuang et al., 2012b; Yang et al., 2012a; Cai et al., 2013; Meng et al., 2014).

8.3.4 Extension and subsidence since the Cretaceous

It is commonly believed that Mesozoic lithospheric thinning in the NCB occurred to the east of Taihang Mountain, across which, topography, crustal and lithospheric thickness and gravity anomalies all change considerably (Xu, 2007; Chen et al., 2009; Chen et al., 2014; Jia et al., 2014). Present topography shows an up to 2000 m elevation contrast between the two sides. Paleogeography shows that such a topographic contrast did not exist until the late Early Cretaceous, when regions east of the Taihang moutnain started to subside and deposit sediments in rift basins/grabens (**Figure 8.4**) (Wang, 1985; Ren et al., 2002; Xu, 2007; Qi and Yang, 2010). This may indicate that the crust subsided, instead of uplifted, when the enriched lithospheric mantle melted.

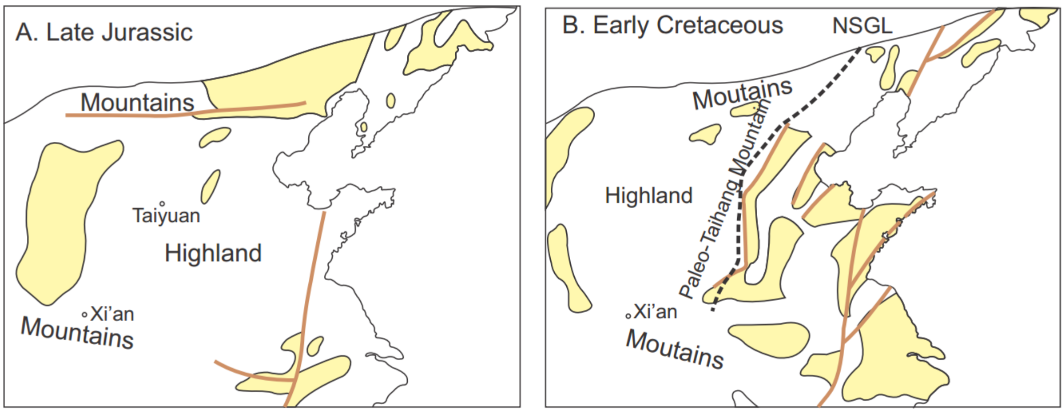

Figure 8.4 Paleogeography of the eastern NCB from the Late Jurassic to the Early Cretaceous (after Wang (1985).NSGL — North-South Gravity lineament.

Along with formation of the NE-NNE-oriented extensional basins/grabens, several metamorphic core complexes (MCCs) (Figure 4.1b), such as the Southern Liaoning MCC, Waziyu (or Yiwulushan) MCC, and Yunmengshan MMC, have been found to form in the Early Cretaceous. Fabric data of these MCCs and normal faults show that the principal extension direction for the Early Cretaceous was approximately NW-SE oriented (Zhang et al., 2003d; Zhu et al., 2012a and references therein).

8.3.5 Lithospheric thickening during mid- to late Cenozoic

Basalts erupted in the Cenozoic are characterised by OIB-type trace element features and depleted isotopic compositions (Xu, 2001; Zeng et al., 2010; Li et al., 2014). OIBs erupted on a thicker lithosphere have geochemical characteristics consistent with a lower extent and higher pressure partial melting of the asthenosphere, whereas those erupted on thin lithosphere exhibit features indicating a higher extent and lower pressure of melting (Niu et al., 2011). Alkali basalts are usually produced by small degree of partial melting of peridotite at high pressure (> 3.0 GPa) while tholeiitic basalts are derived from larger degree of melting at lower pressure (1.5–2.5 GPa). Therefore, alkali basalts generally are produced under a thicker lithosphere, whereas tholeiitic basalts are produced under a thinner lithosphere. A shift from alkali basalts to tholeiitic basalts might, therefore, be indicative of lithospheric thinning and the reverse trend likely implies lithospheric thickening (Xu, 2001; Xu et al., 2004b; Xu et al., 2009b). On the basis of this logic, Xu et al. (2004b) suggested a lithospheric thickening process during the mid- to late Cenozoic. A recent study on the Cenozoic basalts in the Bohai Bay basin suggested that the lithospheric thinning was on-going during the Eocene based on the presence of rising Dy/Yb ratios in the Miocene (Li et al., 2014). This lithospheric thickening is consistent with the Cenozoic evolution of the Bohai Bay basin from a rift basin to a sag basin since the Miocene (Hu et al., 2001).

8.3.6 Two episodes of exhumation

Thermochronology studies (Chapters 4–6) revealed two episodes of exhumation at ca.140–90 Ma and 65–40 Ma as a result of extensional erosion in the upper crust. A reconstruction of thermal history of the Bohai Bay basin showed that the basin experienced two heat flow peaks: one in the late Early Cretaceous and the other in the Middle to Late Paleogene (Hu et al., 2001; Qiu et al., 2014). These two lines of observations, together with evidence for basaltic eruptions, argue for two episodes of lithospheric thinning in the region.

8.3.7 Implication for the mechanism of lithospheric thinning

Based on the multiple disciplinary evidence described above, possible processes of the lithospheric thinning are discussed below.

Proponents for the delamination model suggest that melting of the delaminated eclogites could have metasomatised the asthenospheric/lithospheric mantle, and partial melting of the metasomatised mantle then formed the Early Cretaceous mafic rocks. The onset of mafic magmatism occurred at ca. 145Ma. Therefore, delamination must have occurred prior to that time. However, there are a number of observations that argue against such a delamination model. First, full delamination of the denser lithospheric root could be followed by lithospheric rebound and surface uplift (Krystopowicz and Currie, 2013). However, this contradicts the regional subsidence that started from the Early Cretaceous. Second, the delamination model cannot explain how two episodes of lithospheric thinning happened at the same place. If delamination of the lower crust had primarily occurred no later than the Early Cretaceous, there is no self-sustaining mechanism to induce the second lithospheric thinning in the early Cenozoic at the same place without introducing other factors, such as extension linked to the subduction of the Pacific plate. Third, the delamination model predicts a juvenile lithospheric mantle at present. However, Re-Os analysis of peridotitic xenoliths from Pliocene and quaternary basalts, and petrology and geochemistry of mantle xenoliths from the latest Late Cretaceous, show that relict Archean lithospheric mantle still existed in the already thinned regions (Ying et al., 2006; Zheng et al., 2009; Liu et al., 2014b). Therefore, full delamination is an unlikely mechanism for lithospheric thinning.

On the other hand, a thermo-chemical-erosion mechanism could have been involved given that the metasomatised lithospheric mantle can facilitate thermal erosion. Progressive and slow erosion of the enriched lithospheric mantle can accommodate the regional subsidence from the Cretaceous. It is also compatible with other observations. Nonetheless, as the bulk lower crust of the NCB has an intermediate composition, in contrast to global mafic lower crust (Gao et al., 1998), it was argued that the thermo-chemical erosion mechanism would was unlikely because such a mechanism would only impact on the subcontinental lithospheric mantle but not the composition of the crust (Wu et al., 2008). However, such an argument may not be valid as it is uncertain if the composition of the lower crust for the NCB can be linked to lithospheric thinning.

For this mechanism to work, regional extension due to the subduction of the Izanagi/Pacific plate along the eastern margin of Asia is required. This is supported by available data. For example, the nearly NW-SE-oriented extension direction for the Early Cretaceous suggests that this extension was likely associated with the subduction of the Izanagi/Pacific plate. In addition, magma sources for the 90–40 Ma basalts in the eastern NCB suggest possible contributions from recycled oceanic crust of subducted Pacific slab (Zhang et al., 2008b; Zhu et al., 2012b; Guo, 2013; Xu, 2014). Therefore, the two stages of lithospheric thinning, extension, and crustal exhumaton were, in the first instance, likely related to the roll-back of the old and heavy oceanic slabs in the Western Pacific Ocean (Li et al., 2012c). The two episodes of widespread extension across eastern North China suggest that roll-back of the oceanic slab along the eastern margin of Asia may have taken place twice, first during the Early Cretaceous and again during the Paleocene..

8.4 Conclusions

8.4.1 Implications for Mesozoic continental collision

Geo- and thermochronology results illustrate that the Sulu UHP rocks experienced crustal exhumation from 180–160 Ma. The Jiaobei region, to the north of this high grade metamorphic core, was influenced by the collision between the SCB and the NCB and exhumed at ~260 Ma and 205–160 Ma. The crustal detachment model can best explain the exhumation history of the Jiaobei region and the Sulu UHP rocks. Available timing and sinistral shearing of the Tan-Lu fault also agree well with this model. Late Jurassic melts in the Jiaobei region likely resulted from water-flux partial melting of a thickened continental crust. The different exhumation patterns between the Jiaobei region and the Sulu UHP rocks contradict those predicted by the indentation model and the rotational collision model. Age data for the sinistral shearing of the Tan-Lu fault also contradicts these models, so do the genesis of the Upper Jurassic granites in the Jiaobei region.

8.4.2 Implications for lithospheric thinning

Geo- and thermochronology results also reveal two episodes of extensional exhumation at 140–90 Ma and 65–40 Ma, respectively, and hint at an episodic nature of lithospheric thinning. This finding does not support a full delamination of the lower crust and lithospheric mantle prior to the generation of the mafic rocks in the Early Cretaceous as such a model predicts subsequent regional uplift, rather than the observed topographic subsidence. The thermo-chemical erosion mechanism, accompanied by regional extension, can account for the subsidence as well as the two episodes of exhumation. Extension due to roll-back of the subducting Western Pacific oceanic slab provided the first order control on the lithospheric thinning.

REFERENCES

Allen, M.B., Macdonald, D.I.M., Xun, Z., Vincent, S.J., Brouet-Menzies, C., 1998. Early Cenozoic two-phase extension and late Cenozoic thermal subsidence and inversion of the Bohai Basin, northern China. Marine and Petroleum Geology, 14(7-8): 951-972.

Ames, L., Gaozhi, Z., Baocheng, X., 1996. Geochronology and isotopic character of ultrahigh-pressure metamorphism with implications for collision of the Sino-Korean and Yangtze cratons, central China. Tectonics, 15(2): 472-489.

Armstrong, P.A., Ehlers, T.A., Chapman, D.S., Farley, K.A., Kamp, P.J.J., 2003. Exhumation of the central Wasatch Mountains, Utah: 1. Patterns and timing of exhumation deduced from low-temperature thermochronology data. Journal of Geophysical Research: Solid Earth, 108(B3): 2172.

Banno, S., Enami, M., Hirajima, T., Ishiwatari, A., Wang, Q.C., 2000. Decompression P–T path of coesite eclogite to granulite from Weihai, eastern China. Lithos, 52(1–4): 97-108.

Barbarand, J., Carter, A., Wood, I., Hurford, T., 2003. Compositional and structural control of fission-track annealing in apatite. Chemical Geology, 198(1–2): 107-137.

Bea, F., 1996. Residence of REE, Y, Th and U in granites and crustal protoliths: Implications for the chemistry of crustal melts. Journal of Petrology, 37(3): 521-552.

Bird, P., 1979. Continental delamination and the Colorado Plateau. Journal of Geophysical Research: Solid Earth, 84(B13): 7561-7571.

Black, L.P. et al., 2004. Improved $^{206}Pb/^{238}U$ microprobe geochronology by the monitoring of a trace-element-related matrix effect: SHRIMP, ID-TIMS, ELA-ICP-MS and oxygen isotope documentation for a series of zircon standards. Chemical Geology, 205(1-2): 115-140.

Blichert-Toft, J., Albarède, F., 1997. The Lu-Hf isotope geochemistry of chondrites and the evolution of the mantle-crust system. Earth and Planetary Science Letters, 148(1–2): 243-258.

Brandon, M.T., Roden-Tice, M.K., Garver, J.I., 1998. Late Cenozoic exhumation of the Cascadia accretionary wedge in the Olympic Mountains, northwest Washington State. Geological Society of America Bulletin, 110(8): 985-1009.

Brown, M., 2013. Granite: From genesis to emplacement. Geological Society of America Bulletin, 125(7-8): 1079-1113.

Brown, R.W. et al., 2013. Natural age dispersion arising from the analysis of broken crystals. Part I: Theoretical basis and implications for the apatite (U-Th)/He thermochronometer. Geochimica et Cosmochimica Acta, 122: 478-497.

Burtner, R.L., Nigrini, A., Donelick, R.A., 1994. Thermochronology of Lower Cretaceous Source Rocks in the Idaho-Wyoming Thrust Belt. AAPG Bulletin, 78(10): 1613-1636.

Cai, Y.-C. et al., 2013. Evolution of the lithospheric mantle beneath the southeastern North China Craton: Constraints from mafic dikes in the Jiaobei terrain. Gondwana Research, 24(2): 601-621.

Carlson, W.D., Donelick, R.A., Ketcham, R.A., 1999. Variability of apatite fission-track annealing kinetics: I. Experimental results. American Mineralogist, 84(9): 1213-1223.

Charles, N. et al., 2011. Metamorphic Core Complexes vs. synkinematic plutons in continental extension setting: Insights from key structures (Shandong Province, eastern China). Journal of Asian Earth Sciences, 40(1): 261-278.

Charles, N. et al., 2013. Timing, duration and role of magmatism in wide rift systems: Insights from the Jiaodong Peninsula (China, East Asia). Gondwana Research, 24(1): 412-428.

Chen, B., Zhai, M.-G., Tian, W., 2007. Origin of the Mesozoic magmatism in the North China Craton: constraints from petrological and geochemical data. Geological Society, London, Special Publications, 280(1): 131-151.

Chen, J.F. et al., 2003. U-Pb zircon ages for a collision-related K-rich complex at Shidao in the Sulu ultrahigh pressure terrane, China. Geochemical Journal, 37: 35-46.

Chen, L.-H., Zhou, X.-H., 2005. Subduction-related metasomatism in the thinning lithosphere: Evidence from a composite dunite-orthopyroxenite xenolith entrained in Mesozoic Laiwu high-Mg diorite, North China Craton. Geochemistry, Geophysics, Geosystems, 6(6): Q06008.

Chen, L., Cheng, C., Wei, Z.G., 2009. Seismic evidence for significant lateral variations in lithospheric thickness beneath the central and western North China Craton. Earth and Planetary Science Letters, 286(1-2): 171-183.

Chen, L. et al., 2014. Presence of an intralithospheric discontinuity in the central and western North China Craton: Implications for destruction of the craton. Geology, 42(3): 223-226.

Chen, W. et al., 1992. The cooling history of melange zone in north Jiangsu-South Shandong region: evidence from multiple diffusion domain ^{40}Ar-^{39}Ar thermal geochornology. Acta Petrologica Sinica (in Chinese with English abstract), 8(1): 1-17.

Chen, Y.-X., Zheng, Y.-F., Hu, Z., 2013. Synexhumation anatexis of ultrahigh-pressure metamorphic rocks: Petrological evidence from granitic gneiss in the Sulu orogen. Lithos, 156–159: 69-96.

Chiaradia, M., 2014. Copper enrichment in arc magmas controlled by overriding plate thickness. Nature Geoscience, 7(1): 43-46.

Chu, H., Lu, S., Wang, H., Xiang, Z., Liu, H., 2011. U-Pb age secptrum of detrital zircons from the Fuzikuang Formatioin, Penglai Group in Changdao, Shandong Province. Acta Petrologica Sinica, 27(4): 1017-1028.

Chu, Z.-Y. et al., 2009. Temporal Evolution of the Lithospheric Mantle beneath the Eastern North China Craton. Journal of Petrology, 50(10): 1857-1898.

Clark, C., Fitzsimons, I.C.W., Healy, D., Harley, S.L., 2011. How does the continental crust get really hot? Elements, 7(4): 235-240.

Danišík, M., Kuhlemann, J., Dunkl, I., Székely, B., Frisch, W., 2007. Burial and exhumation of Corsica (France) in the light of fission track data. Tectonics, 26(1): TC1001.

Danišík, M., Štěpančíková, P., Evans, N.J., 2012. Constraining long-term denudation and faulting history in intraplate regions by multisystem thermochronology: An example of the Sudetic Marginal Fault (Bohemian Massif, central Europe). Tectonics, 31(2): TC2003.

Davis, G.A. et al., 1996. Mesozoic deformation and plutonism in the Yunmeng Shan: A Chinese metamorphic core complex north of Beijing, China. In: Yin, A., Harrison, T.A. (Editors). The tectonic evolution of Asia. Cambridge University Press, New York, pp. 253-280.

Davis, G.A. et al., 2001. Mesozoic tectonic evolution of the Yanshan fold and thrust belt, with emphasis on Hebei and Liaoning provinces, northern China. Geological Society of America Memoirs, 194: 171-197.

De Bievre, P., Taylor, P.D.P., 1993. IUPAC recommended isotopic abundances. International Journal of Mass Spectrometry and Ion Physics, 123: 149.

De Laeter, J.R., Kennedy, A.K., 1998. A double focusing mass spectrometer for geochronology. International Journal of Mass Spectrometry, 178(1–2): 43-50.

Deng, J. et al., 2007. A possible model for the lithospheric thinning of North China Craton: Evidence from the Yanshanian (Jura-Cretaceous) magmatism and tectonism. Lithos, 96(1–2): 22-35.

Dodson, M.H., 1973. Closure temperature in cooling geochronological and petrological systems. Contributions to Mineralogy and Petrology, 40(3): 259-274.

Donelick, R.A., Ketcham, R.A., Carlson, W.D., 1999. Variability of apatite fission-track annealing kinetics: II. Crystallographic orientation effects. American Mineralogist, 84(9): 1224-1234.

Donelick, R.A., O'Sullivan, P.B., Ketcham, R.A., 2005. Apatite fission-track analysis. Reviews in Mineralogy and Geochemistry, 58(1): 49-94.

Dong, S. et al., 2004. Crustal structure of the southern Dabie ultrahigh-pressure orogen and Yangtze foreland from deep seismic reflection profiling. Terra Nova, 16(6): 319-324.

Du, L., Zhuang, Y., Yang, C., Wan, Y., Wang, X., 2005. SHRIMP U-Pb zircon chronology of fine-grained amphibolite in the Mengjiatun area, western Shandong. Acta Geoscientica Sinica, 26(5): 429-434.

Ducea, M.N., 2011. Fingerprinting orogenic delamination. Geology, 39(2): 191-192.

Dumitru, T.A., 2000. Fission-track geochronology. In: Noller, J.S., Sowers, J.M., Lettis, W.R. (Eds.), Quaternary Geochronology: Methods and Applications. American Geophysical Union, pp. 131-155.

Dunkl, I., 2002. Trackkey: a Windows program for calculation and graphical presentation of fission track data. Computers & Geosciences, 28(1): 3-12.

Ehlers, T.A., Willett, S.D., Armstrong, P.A., Chapman, D.S., 2003. Exhumation of the central Wasatch Mountains, Utah: 2. Thermokinematic model of exhumation, erosion, and thermochronometer interpretation. Journal of Geophysical Research: Solid Earth, 108(B3): 2173.

Elkins-Tanton, L.T., 2007. Continental magmatism, volatile recycling, and a heterogeneous mantle caused by lithospheric gravitational instabilities. Journal of Geophysical Research: Solid Earth, 112(B3): B03405.

England, P., Molnar, P., 1990. Surface uplift, uplift of rocks, and exhumation of rocks. Geology, 18(12): 1173-1177.

England, P.C., Thompson, A.B., 1984. Pressure-Temperature-Time Paths of Regional Metamorphism I. Heat Transfer during the Evolution of Regions of Thickened Continental Crust. Journal of Petrology, 25(4): 894-928.

England, P.C., Thompson, A., 1986. Some thermal and tectonic models for crustal melting in continental collision zones. Collision Tectonics, 19. Geological Society, London, Special Publications, 83-94 pp.

Evans, N.J., Byrne, J.P., Keegan, J.T., Dotter, L.E., 2005. Determination of Uranium and Thorium in zircon, apatite, and fluorite: Application to laser (U-Th)/He thermochronology. Journal of Analytical Chemistry, 60(12): 1159-1165.

Fan, W.M. et al., 2000. On and off the North China Craton: Where is the Archaean keel? Journal of Petrology, 41(7): 933-950.

Fan, W.M., Guo, F., Wang, Y.J., Lin, G., Zhang, M., 2001. Post-orogenic bimodal volcanism along the Sulu orogenic belt in Eastern China. Physics and Chemistry of the Earth, Part A: Solid Earth and Geodesy, 26(9-10): 733-746.

Farley, K.A., Wolf, R.A., Silver, L.T., 1996. The effects of long alpha-stopping distances on (U-Th)/He ages. Geochimica et Cosmochimica Acta, 60(21): 4223-4229.

Farley, K.A., 2000. Helium diffusion from apatite: General behavior as illustrated by Durango fluorapatite. Journal of Geophysical Research: Solid Earth, 105(B2): 2903-2914.

Farley, K.A., 2002. (U-Th)/He Dating: Techniques, Calibrations, and Applications. Reviews in Mineralogy and Geochemistry, 47(1): 819-844.

Farley, K.A., Stockli, D.F., 2002. (U-Th)/He Dating of Phosphates: Apatite, Monazite, and Xenotime. Reviews in Mineralogy and Geochemistry, 48(1): 559-577.

Faure, M., Lin, W., Le Breton, N., 2001. Where is the North China-South China block boundary in eastern China? Geology, 29(2): 119-122.

Faure, M. et al., 2003a. Exhumation tectonics of the ultrahigh-pressure metamorphic rocks in the Qinling orogen in east China: New petrological-structural-radiometric insights from the Shandong Peninsula. Tectonics, 22(3): 1018.

Faure, M. et al., 2003b. Continental subduction and exhumation of UHP rocks. Structural and geochronological insights from the Dabieshan (East China). Lithos, 70(3-4): 213-241.

Feng, Y., ZHou, H., Ren, J., Zheng, H., Miao, S., 2010. Paleogene sequence stratigraphy in the east of the Bohai Bay Basin and its response to structural movement. Science China Earth Sciences, 40(10): 1356-1376.

Fitzgerald, P.G., Baldwin, S.L., Webb, L.E., O'Sullivan, P.B., 2006. Interpretation of (U–Th)/He single grain ages from slowly cooled crustal terranes: A case study from the Transantarctic Mountains of southern Victoria Land. Chemical Geology, 225(1–2): 91-120.

Fitzgerald, P.G., Metcalf, J.R., Baldwin, S., Muñoz, J., 2010. Thermal and exhumation histories of the footwall and hanging wall of the Gavarnie thrust, West-Central Pyrenees: Implications for thrusting. AGU Fall Meeting Abstracts, 1: 2015.

Fitzgerald, P.G., 2013. Concept of the exhumed partial annealing (retention) zone in thermochronology: An appraisal. AGU Fall Meeting Abstracts, 1: 2724.

Fleischer, R.R.L., Price, P.B., Walker, R.M., 1975. Nuclear Tracks in Solids: Principles and Applications. University of California Press.

Flowers, R.M., Shuster, D.L., Wernicke, B.P., Farley, K.A., 2007. Radiation damage control on apatite (U-Th)/He dates from the Grand Canyon region, Colorado Plateau. Geology, 35(5): 447-450.

Flowers, R.M., Kelley, S.A., 2011. Interpreting data dispersion and “inverted” dates in apatite (U–Th)/He and fission-track datasets: An example from the US midcontinent. Geochimica et Cosmochimica Acta, 75(18): 5169-5186.

Foster, D.A., John, B.E., 1999. Quantifying tectonic exhumation in an extensional orogen with thermochronology: examples from the southern Basin and Range Province. Geological Society, London, Special Publications, 154(1): 343-364.

Frost, B.R. et al., 2001. A Geochemical Classification for Granitic Rocks. Journal of Petrology, 42(11): 2033-2048.

Gallagher, K., Brown, R., Johnson, C., 1998. Fission track analysis and its applications to geological problems. Annual Review of Earth and Planetary Sciences, 26: 519-572.

Gao, S. et al., 1998. How mafic is the lower continental crust? Earth and Planetary Science Letters, 161(1–4): 101-117.

Gao, S., Rudnick, R.L., Carlson, R.W., McDonough, W.F., Liu, Y.-S., 2002. Re–Os evidence for replacement of ancient mantle lithosphere beneath the North China craton. Earth and Planetary Science Letters, 198(3–4): 307-322.

Gao, S. et al., 2004. Recycling lower continental crust in the North China craton. Nature, 432(7019): 892-897.

Gao, S. et al., 2008. Recycling deep cratonic lithosphere and generation of intraplate magmatism in the North China Craton. Earth and Planetary Science Letters, 270(1–2): 41-53.

Gao, S., Zhang, J.F., Xu, W.L., Liu, Y.S., 2009. Delamination and destruction of the North China Craton. Chinese Science Bulletin, 54(19): 3367-3378.

Gardien, V., Thompson, A.B., Ulmer, P., 2000. Melting of biotite + plagioclase + quartz gneisses: the role of H2O in the stability of amphibole. Journal of Petrology, 41(5): 651-666.

Garver, J.I., Kamp, P.J.J., 2002. Integration of zircon color and zircon fission-track zonation patterns in orogenic belts: application to the Southern Alps, New Zealand. Tectonophysics, 349(1–4): 203-219.

Garver, J.I., Reiners, P.W., Walker, L.J., Ramage, J.M., Perry, S.E., 2005. Implications for timing of andean uplift from thermal resetting of radiation‐damaged zircon in the Cordillera Huayhuash, Northern Peru. The Journal of Geology, 113(2): 117-138.

Gilder, S.A. et al., 1999. Tectonic evolution of the Tancheng-Lujiang (Tan-Lu) fault via Middle Triassic to Early Cenozoic paleomagnetic data. Journal of Geophysical Research: Solid Earth, 104(B7): 15365-15390.

Gleadow, A.J.W., 1981. Fission-track dating methods: What are the real alternatives? Nuclear Tracks, 5(1–2): 3-14.

Gleadow, A.J.W., Duddy, I.R., Green, P.F., Hegarty, K.A., 1986a. Fission track lengths in the apatite annealing zone and the interpretation of mixed ages. Earth and Planetary Science Letters, 78(2–3): 245-254.

Gleadow, A.J.W., Duddy, I.R., Green, P.F., Lovering, J.F., 1986b. Confined fission track lengths in apatite: a diagnostic tool for thermal history analysis. Contributions to Mineralogy and Petrology, 94(4): 405-415.

Gleadow, A.J.W., Belton, D.X., Kohn, B.P., Brown, R.W., 2002. Fission track dating of phosphate minerals and the thermochronology of apatite. Reviews in Mineralogy and Geochemistry, 48(1): 579-630.

Goss, S.C., Wilde, S.A., Wu, F., Yang, J., 2010. The age, isotopic signature and significance of the youngest Mesozoic granitoids in the Jiaodong Terrane, Shandong Province, North China Craton. Lithos, 120(3-4): 309-326.

Griffin, W.L., Andi, Z., O'Reilly, S.Y., Ryan, C.G., 1998. Phanerozoic evolution of the lithosphere beneath the Sino-Korean craton. In: Martin, J.F., Chung, S.-L., Lo, C.-H., Lee, T.-Y. (Eds.), Mantle Dynamics and Plate Interactions in East Asia. Geodyn. Ser. AGU, Washington, DC, pp. 107-126.

Griffin, W.L. et al., 2000. The Hf isotope composition of cratonic mantle: LAM-MC-ICPMS analysis of zircon megacrysts in kimberlites. Geochimica et Cosmochimica Acta, 64(1): 133-147.

Grimmer, J.C. et al., 2003. When did the ultrahigh-pressure rocks reach the surface? A $^{207}Pb/^{206}Pb$ zircon, $^{40}Ar/^{39}Ar$ white mica, Si-in-white mica, single-grain provenance study of Dabie Shan synorogenic foreland sediments. Chemical Geology, 197(1-4): 87-110.

Gromet, L.P., Silver, L.T., 1983. Rare earth element distributions among minerals in a granodiorite and their petrogenetic implications. Geochimica et Cosmochimica Acta, 47(5): 925-939.

Guenthner, W.R., Reiners, P.W., Ketcham, R.A., Nasdala, L., Giester, G., 2013. Helium diffusion in natural zircon: Radiation damage, anisotropy, and the interpretation of zircon (U-Th)/He thermochronology. American Journal of Science, 313(3): 145-198.

Guenthner, W.R., Reiners, P.W., DeCelles, P.G., Kendall, J., 2014. Sevier belt exhumation in central Utah constrained from complex zircon (U-Th)/He data sets: Radiation damage and He inheritance effects on partially reset detrital zircons. Geological Society of America Bulletin.

Guo, F., Fan, W., Wang, Y., Zhang, M., 2004. Origin of early Cretaceous calc-alkaline lamprophyres from the Sulu orogen in eastern China: implications for enrichment processes beneath continental collisional belt. Lithos, 78(3): 291-305.

Guo, F., Fan, W., Wang, Y., Li, C., 2005a. Petrogenesis and tectonic implications of Early Cretaceous high-K calc-alkaline volcanic rocks in the Laiyang Basin of the Sulu Belt, eastern China. Island Arc, 14(2): 69-90.

Guo, F., Fan, W., Li, C., 2006. Geochemistry of late Mesozoic adakites from the Sulu belt, eastern China: magma genesis and implications for crustal recycling beneath continental collisional orogens. Geological Magazine, 143(1): 1-13.

Guo, F., 2013. The modification of the lithospheric mantle beneath the North China Craton by subducted continental and oceanic crust: Oxygen isotopic records of olivine. Acta Petrologica et Mineralogica, 32(5): 593-603.

Guo, J., Chen, F., Zhang, X., Siebel, W., Zhai, M., 2005b. Evolution of syn- to post-collisional magmatism from north Sulu UHP belt, eastern China: Zircon U-Pb geochronology. Acta Petrologica Sinica, 21(4): 1281-1301.

Guo, J., Chen, F., Zhang, X., Siebel, W., Zhai, M., 2005c. Evolution of syn-to post-collisional magmatism from north Sulu UHP belt, eastern China: zircon U-Pb geochronology. Acta Petrologica Sinica, 21(4): 1281-1301.

Guo, J., Guo, F., Yan Wang, C., Li, C., 2013. Crustal recycling processes in generating the early Cretaceous Fangcheng basalts, North China Craton: New constraints from mineral chemistry, oxygen isotopes of olivine and whole-rock geochemistry. Lithos, 170–171: 1-16.

Guo, P., 2014. Geodynamic setting of Mesozoic gold metallogy in the Western Shandong Province, China University of Geosciences (Beijing), Beijing, 216 pp.

Guo, Z., Wilson, M., 2012. The Himalayan leucogranites: Constraints on the nature of their crustal source region and geodynamic setting. Gondwana Research, 22(2): 360-376.

Hacker, B.R., Ratschbacher, L., Liou, J.G., 2004. Subduction, collision and exhumation in the ultrahigh-pressure Qinling-Dabie orogen. Geological Society, London, Special Publications, 226(1): 157-175.

Hacker, B.R., Wallis, S.R., McWilliams, M.O., Gans, P.B., 2009. $^{40}Ar/^{39}Ar$ Constraints on the tectonic history and architecture of the ultrahigh-pressure Sulu orogen. Journal of Metamorphic Geology, 27(9): 827-844.

Hames, W.E., Bowring, S.A., 1994. An empirical evaluation of the argon diffusion geometry in muscovite. Earth and Planetary Science Letters, 124(1–4): 161-169.

Harrison, M.T., 1982. Diffusion of ^{40}Ar in hornblende. Contributions to Mineralogy and Petrology, 78(3): 324-331.

Harrison, T.M., McDougall, I., 1981. Excess ^{40}Ar in metamorphic rocks from Broken Hill, New South Wales: implications for $^{40}Ar/^{39}Ar$ age spectra and the thermal history of the region. Earth and Planetary Science Letters, 55(1): 123-149.

Harrison, T.M., Duncan, I., McDougall, I., 1985. Diffusion of ^{40}Ar in biotite: Temperature, pressure and compositional effects. Geochimica et Cosmochimica Acta, 49(11): 2461-2468.

He, H. et al., 2011. New $^{40}Ar/^{39}Ar$ dating results from the Shanwang Basin, eastern China: Constraints on the age of the Shanwang Formation and associated biota. Physics of the Earth and Planetary Interiors, 187(1–2): 66-75.

Hendriks, B.W.H., Redfield, T.F., 2005. Apatite fission track and (U-Th)/He data from Fennoscandia: An example of underestimation of fission track annealing in apatite. Earth and Planetary Science Letters, 236(1–2): 443-458.

Hou, G., Liu, Y., Li, J., 2006. Evidence for ~1.8 Ga extension of the Eastern Block of the North China Craton from SHRIMP U–Pb dating of mafic dyke swarms in Shandong Province. Journal of Asian Earth Sciences, 27(4): 392-401.

Hou, M.-L., Jiang, Y.-H., Jiang, S.-Y., Ling, H.-F., Zhao, K.-D., 2007. Contrasting origins of late Mesozoic adakitic granitoids from the northwestern Jiaodong Peninsula, east China: implications for crustal thickening to delamination. Geological Magazine, 144(4): 619-631.

Housh, T.B., Luhr, J.F., 1991. Plagioclase-melt equilibria in hydrous systems. American Mineralogist, 76(3-4): 477-492.

Hu, S., O'Sullivan, P.B., Raza, A., Kohn, B.P., 2001. Thermal history and tectonic subsidence of the Bohai Basin, northern China: a Cenozoic rifted and local pull-apart basin. Physics of the Earth and Planetary Interiors, 126(3–4): 221-235.

Huang, J. et al., 2006. Melting of subducted continent: Element and isotopic evidence for a genetic relationship between Neoproterozoic and Mesozoic granitoids in the Sulu orogen. Chemical Geology, 229(4): 227-256.

Hurford, A.J., Green, P.F., 1983. The zeta-age calibration of Fission-Track dating. Isotope Geoscience, 1(4): 285-317.

Ishihara, S., Hashimoto, M., Machida, M., 2000. Magnetite/Ilmenite–series Classification and Magnetic Susceptibility of the Mesozoic-Cenozoic Batholiths in Peru. Resource Geology, 50(2): 123-129.

Jahn, B.-M., Wu, F.-Y., Lo, C.-H., Tsai, C.-H., 1999. Crust–mantle interaction induced by deep subduction of the continental crust: geochemical and Sr–Nd isotopic evidence from post-collisional mafic–ultramafic intrusions of the northern Dabie complex, central China. Chemical Geology, 157(1–2): 119-146.

Jahn, B.-M., Liu, D., Wan, Y., Song, B., Wu, J., 2008. Archean crustal evolution of the Jiaodong Peninsula, China, as revealed by zircon SHRIMP geochronology, elemental and Nd-isotope geochemistry. American Journal of Science, 308(3): 232-269.

Ji, Z., Zhao, H., 1992. New evidence for the age of the Penglai Group in Ludong. Journal of Stratigraphy, 16(3): 237-239.

Jia, S. et al., 2014. Crustal structure and tectonic study of North China Craton from a long deep seismic sounding profile. Tectonophysics, 627: 48-56.

Jiang, N., Chen, J., Guo, J., Chang, G., 2012. In situ zircon U-Pb, oxygen and hafnium isotopic compositions of Jurassic granites from the North China craton: Evidence for Triassic subduction of continental crust and subsequent metamorphism-related ^{18}O depletion. Lithos, 142–143: 84-94.

Kasuya, M., Naeser, C.W., 1988. The effect of α-damage on fission-track annealing in zircon. Nuclear Tracks and Radiation Measurements, 14(4): 477-480.

Kelley, S., 2002a. K-Ar and Ar-Ar Dating. Reviews in Mineralogy and Geochemistry, 47(1): 785-818.

Kelley, S., 2002b. Excess argon in K–Ar and Ar–Ar geochronology. Chemical Geology, 188(1–2): 1-22.

Ketcham, R.A., 2005. Forward and inverse modeling of low-temperature thermochronometry data. Reviews in Mineralogy and Geochemistry, 58(1): 275-314.

Ketcham, R.A., Carter, A., Donelick, R.A., Barbarand, J., Hurford, A.J., 2007a. Improved modeling of fission-track annealing in apatite. American Mineralogist, 92(5-6): 799-810.

Ketcham, R.A., Carter, A., Donelick, R.A., Barbarand, J., Hurford, A.J., 2007b. Improved measurement of fission-track annealing in apatite using c-axis projection. American Mineralogist, 92(5-6): 789-798.

Ketcham, R.A., Guenthner, W.R., Reiners, P.W., 2013. Geometric analysis of radiation damage connectivity in zircon, and its implications for helium diffusion. American Mineralogist, 98(2-3): 350-360.

Kohn, B.P. et al., 2009. A reappraisal of low-temperature thermochronology of the eastern Fennoscandia Shield and radiation-enhanced apatite fission-track annealing. Geological Society, London, Special Publications, 324(1): 193-216.

Koppers, A.A.P., 2002. ArArCALC—software for $^{40}Ar/^{39}Ar$ age calculations. Computers & Geosciences, 28(5): 605-619.

Kravchinsky, V.A., Cogné, J.-P., Harbert, W.P., Kuzmin, M.I., 2002. Evolution of the Mongol-Okhotsk Ocean as constrained by new palaeomagnetic data from the Mongol-Okhotsk suture zone, Siberia. Geophysical Journal International, 148(1): 34-57.

Krystopowicz, N.J., Currie, C.A., 2013. Crustal eclogitization and lithosphere delamination in orogens. Earth and Planetary Science Letters, 361: 195-207.

Kuang, Y., Pang, C., Hong, L., Zhong, Y., Xu, Y., 2012a. Geochronology and geochemistry of the Late Cretaceous basalts in the Jiaolai Basin: Constrains on lithospheric thinning and accretion beneath North China Craton. Geotectonica et Metallogenia, 36(4): 559-571.

Kuang, Y. et al., 2012b. ^{40}Ar-^{39}Ar geochronology and geochemistry of mafic rocks from Qingshan Group, Jiaodong area: Implication for the destruction of the North China Craton. Acta Petrologica Sinica, 28(4): 1073-1091.

Kuang, Y.S. et al., 2012c. Petrogenetic evaluation of the Laohutai basalts from North China Craton: Melting of a two-component source during lithospheric thinning in the late Cretaceous–early Cenozoic. Lithos, 154: 68-82.

Lan, T.-G. et al., 2012. Early Jurassic high-K calc-alkaline and shoshonitic rocks from the Tongshi intrusive complex, eastern North China Craton: Implication for crust–mantle interaction and post-collisional magmatism. Lithos, 140–141: 183-199.

Lee, J.-Y. et al., 2006. A redetermination of the isotopic abundances of atmospheric Ar. Geochimica et Cosmochimica Acta, 70(17): 4507-4512.

Leech, M.L., Webb, L.E., 2013. Is the HP–UHP Hong'an–Dabie–Sulu orogen a piercing point for offset on the Tan–Lu fault? Journal of Asian Earth Sciences, 63: 112-129.

Li, H.-Y., Xu, Y.-G., Liu, Y.-M., Huang, X.-L., He, B., 2013. Detrital zircons reveal no Jurassic plateau in the eastern North China Craton. Gondwana Research, 24(2): 622-634.

Li, H.-Y., Huang, X.-L., Guo, H., 2014. Geochemistry of Cenozoic basalts from the Bohai Bay Basin: Implications for a heterogeneous mantle source and lithospheric evolution beneath the eastern North China Craton. Lithos, 196-197: 54-66.

Li, L., Zhang, J., Zhong, D., Wang, X., 2007a. Main characteristics of the decollement structures along the Cambrian/Archean unconformity surface in westeran Shandong. Chinese Journal of Geology, 42(2): 335-352.

Li, N., 2010. Research on structural evolution and sedimentary facies in North Depression of South Yellow Sea Basin. PhD Thesis, Ocean University of China, Qingdao, China, 112 pp.

Li, S. et al., 2005. Mesozoic structure and its tectonic setting in the western Shandong block. Acta Geologica Sinica, 79(4): 487-197.

Li, S. et al., 2009. Triassic folding and thrusting in the Eastern Block of the North China Craton and the Dabie-Sulu orogen and its geodynamics. Acta Petrologica Sinica, 25(9): 2031-2049.

Li, S. et al., 2011. Thermochronological constraints on two-stage extrusion of HP/UHP terranes in the Dabie–Sulu orogen, east-central China. Tectonophysics, 504(1–4): 25-42.

Li, S. et al., 2012a. Mesozoic basins in eastern China and their bearing on the deconstruction of the North China Craton. Journal of Asian Earth Sciences, 47: 64-79.

Li, S. et al., 2012b. Paleoproterozoic structural evolution of the southern segment of the Jiao-Liao-Ji Belt, North China Craton. Precambrian Research, 200–203: 59-73.

Li, X.-H., Li, Z.-X., Zhou, H., Liu, Y., Kinny, P.D., 2002. U-Pb zircon geochronology, geochemistry and Nd isotopic study of Neoproterozoic bimodal volcanic rocks in the Kangdian Rift of South China: implications for the initial rifting of Rodinia. Precambrian Research, 113(1-2): 135-154.

Li, X.-H. et al., 2007b. South China provenance of the lower-grade Penglai Group north of the Sulu UHP orogenic belt, eastern China: Evidence from detrital zircon ages and Nd-Hf isotopic composition Geochemical Journal, 41: 29-45.

Li, Z.-X. et al., 2012c. Magmatic switch-on and switch-off along the South China continental margin since the Permian: Transition from an Andean-type to a Western Pacific-type plate boundary. Tectonophysics, 532–535: 271-290.

Li, Z.-X.A., Lee, C.-T.A., Peslier, A.H., Lenardic, A., Mackwell, S.J., 2008. Water contents in mantle xenoliths from the Colorado Plateau and vicinity: Implications for the mantle rheology and hydration-induced thinning of continental lithosphere. Journal of Geophysical Research: Solid Earth, 113(B9): B09210.

Li, Z.X., 1994. Collision between the North and South China Blocks - A crustal-detachment model for suturing in the region east of the Tanlu fault. Geology, 22(8): 739-742.

Li, Z.X., 1998. Tectonic history of the major East Asian lithospheric blocks since the mid-Proterozoic: a synthesis In: Martin, F.J.F., Sun-Lin Chung, Ching-Hua Lo, and Tung-Yi Lee (Editor), Mantle dynamics and plate interactions in East Asia. Geodynamics Series American Geophysical Union, Washington, DC, pp. 221-243.

Lin, L.-H., Wang, P.-L., Lo, C.-H., Tsai, C.-H., Jahn, B.-M., 2005a. ^{40}Ar-^{39}Ar thermochronological constraints on the exhumation of ultrahigh-pressure metamorphic rocks in the Sulu terrane of Eastern China. International Geology Review, 47(8): 872-886.

Lin, W., Faure, M., Wang, Q., Monié, P., Panis, D., 2005b. Triassic polyphase deformation in the Feidong-Zhangbaling Massif (eastern China) and its place in the collision between the North China and South China blocks. Journal of Asian Earth Sciences, 25(1): 121-136.

Lin, W., Faure, M., Monié, P., Wang, Q.-C., 2007. Polyphase Mesozoic tectonics in the eastern part of the North China Block: insights from the eastern Liaoning Peninsula massif (NE China). Geological Society, London, Special Publications, 280(1): 153-169.

Lin, W., Shi, Y., Wang, Q., 2009. Exhumation tectonics of the HP-UHP orogenic belt in Eastern China: New structural-petrological insights from the Tongcheng massif, Eastern Dabieshan. Lithos, 109(3-4): 285-303.

Lin, W. et al., 2011. Cooling paths of the NE China crust during the Mesozoic extensional tectonics: Example from the south-Liaodong peninsula metamorphic core complex. Journal of Asian Earth Sciences, 42(5): 1048-1065.

Ling, W.-L. et al., 2009. Contrasting geochemistry of the Cretaceous volcanic suites in Shandong province and its implications for the Mesozoic lower crust delamination in the eastern North China craton. Lithos, 113(3-4): 640-658.

Liou, J.G. et al., 1996. Metamorphism and tectonics of high-pressure and ultra-high-pressure belt in the Dabie-Sulu region,China. In: Harrison, A.Y.a.M. (Editor), The tectonic evolution of Asia. Cambridge University Press, Cambridge.

Liu, D., Jian, P., Kröner, A., Xu, S., 2006a. Dating of prograde metamorphic events deciphered from episodic zircon growth in rocks of the Dabie-Sulu UHP complex, China. Earth and Planetary Science Letters, 250(3-4): 650-666.

Liu, D.Y., Nutman, A.P., Compston, W., Wu, J.S., Shen, Q.H., 1992. Remnants of ≥3800 Ma crust in the Chinese part of the Sino-Korean craton. Geology, 20(4): 339-342.

Liu, F., Zhang, Z., Katayama, I., Xu, Z., Maruyama, S., 2003. Ultrahigh-pressure metamorphic records hidden in zircons from amphibolites in Sulu Terrane, eastern China. Island Arc, 12(3): 256-267.

Liu, F., Liou, J.G., Xu, Z., 2005. U-Pb SHRIMP ages recorded in the coesite-bearing zircon domains of paragneisses in the southwestern Sulu terrane, eastern China: New interpretation. American Mineralogist, 90(5-6): 790-800.

Liu, F., A., G., P. T., R., Xue, H., Ye, J., 2007. Zoned zircon from eclogite lenses in marbles from the Dabie-Sulu UHP terrane, China: A clear record of ultra-deep subduction and fast exhumation. Acta Geologica Sinica - English Edition, 81(2): 204-225.

Liu, F. et al., 2014a. U–Pb dating of zircons from granitic leucosomes in migmatites of the Jiaobei Terrane, southwestern Jiao–Liao–Ji Belt, North China Craton: Constraints on the timing and nature of partial melting. Precambrian Research, 245: 80-99.

Liu, F.L., Gerdes, A., Liou, J.G., Xue, H.M., Liang, F.H., 2006b. SHRIMP U-Pb zircon dating from Sulu-Dabie dolomitic marble, eastern China: constraints on prograde, ultrahigh-pressure and retrograde metamorphic ages. Journal of Metamorphic Geology, 24(7): 569-589.

Liu, F.L., Gerdes, A., Xue, H.M., 2009a. Differential subduction and exhumation of crustal slices in the Sulu HP-UHP metamorphic terrane: insights from mineral inclusions, trace elements, U-Pb and Lu-Hf isotope analyses of zircon in orthogneiss. Journal of Metamorphic Geology, 27(9): 805-825.

Liu, F.L., Liou, J.G., 2011. Zircon as the best mineral for P-T-time history of UHP metamorphism: A review on mineral inclusions and U-Pb SHRIMP ages of zircons from the Dabie-Sulu UHP rocks. Journal of Asian Earth Sciences, 40(1): 1-39.

Liu, F.L., Robinson, P.T., Liu, P.H., 2012. Multiple partial melting events in the Sulu UHP terrane: zircon U–Pb dating of granitic leucosomes within amphibolite and gneiss. Journal of Metamorphic Geology, 30(8): 887-906.

Liu, J. et al., 2013a. The growth, reworking and metamorphism of early Precambrian crust in the Jiaobei terrane, the North China Craton: Constraints from U–Th–Pb and Lu–Hf isotopic systematics, and REE concentrations of zircon from Archean granitoid gneisses. Precambrian Research, 224: 287-303.

Liu, J. et al., 2013b. U–Pb dating and Hf isotope study of detrital zircons from the Zhifu Group, Jiaobei Terrane, North China Craton: Provenance and implications for Precambrian crustal growth and recycling. Precambrian Research, 235: 230-250.

Liu, J. et al., 2013c. The Liaonan/Wanfu metamorphic core complexes in the Liaodong Peninsula: Two stages of exhumation and constraints on the destruction of the North China Craton. Tectonics, 32(5): 1121-1141.

Liu, J. et al., 2014b. Big insights from tiny peridotites: Evidence for persistence of Precambrian lithosphere beneath the eastern North China Craton. Tectonophysics, In press.

Liu, L.-P. et al., 2014c. Thermochronology of the Sulu ultrahigh-pressure metamorphic terrane: implications for continental collision and lithospheric thinning. Tectonics.

Liu, P. et al., 2013d. Petrogenesis, P–T–t path, and tectonic significance of high-pressure mafic granulites from the Jiaobei terrane, North China Craton. Precambrian Research, 233: 237-258.

Liu, S. et al., 2008a. K-Ar ages and geochemical plus Sr-Nd isotopic compositions of adakitic volcanic rocks, western Shandong Province, eastern China: Foundering of the lower continental crust. International Geology Review, 50(8): 763-779.

Liu, S. et al., 2008b. Zircon U-Pb geochronology and major, trace elemental and Sr-Nd-Pb isotopic geochemistry of mafic dykes in western Shandong Province, east China: Constrains on their petrogenesis and geodynamic significance. Chemical Geology, 255(3-4): 329-345.

Liu, S. et al., 2009b. Petrogenesis of Late Mesozoic mafic dykes in the Jiaodong Peninsula, eastern North China Craton and implications for the foundering of lower crust. Lithos, 113(3-4): 621-639.

Liu, S.S., Weber, U., Glasmacher, U.A., Xu, Z.Q., Wagner, G.A., 2009c. Fission track analysis and thermotectonic history of the main borehole of the Chinese Continental Scientific Drilling project. Tectonophysics, 475(2): 318-326.

Liu, Y. et al., 2010. Continental and oceanic crust recycling-induced melt–peridotite interactions in the Trans-North China Orogen: U–Pb dating, Hf isotopes and trace elements in zircons from mantle xenoliths. Journal of Petrology, 51(1-2): 537-571.

Liu, Y.S., Gao, S., Kelemen, P.B., Xu, W.L., 2008c. Recycled crust controls contrasting source compositions of Mesozoic and Cenozoic basalts in the North China Craton. Geochimica et Cosmochimica Acta, 72(9): 2349-2376.

Lu, K., Dai, J., 1994. Formation and evolution of Jiaolai Basin. China University of Petroleum Press, Dongying, China, 174 pp.

Lü, P., Zhang, M., Zhu, X., 1990. Discovery of sliding structures on the plane of unconformity between the lower Paleozoic and the Taishan group in the vicinity of Taishan mountains. Geological Review, 36(5): 473-478.

Ludwig, K.R., 2012. Users manual for Isoplot 3.75: A geochronological toolkit for Microsoft Excel. Berkeley Geochronology Center Special Publication, Berkeley, No.5: 1-77.

Luo, D., Chen, L.-H., Zeng, G., 2009. Gensis of intra-continental strongly alkaline volcanic rocks: a case study of Dashan nephelinites in Wudi, Shandong Province. Acta Petrologica Sinica, 25(2): 311-319.

Ma, L. et al., 2013. Multiple sources for the origin of Late Jurassic Linglong adakitic granite in the Shandong Peninsula, eastern China: Zircon U-Pb geochronological, geochemical and Sr-Nd-Hf isotopic evidence. Lithos, 162–163: 251-263.

Ma, L. et al., 2014a. Lithospheric and asthenospheric sources of lamprophyres in the Jiaodong Peninsula: A consequence of rapid lithospheric thinning beneath the North China Craton? Geochimica et Cosmochimica Acta, 124: 250-271.

Ma, L. et al., 2014b. Geochemistry of Early Cretaceous calc-alkaline lamprophyres in the Jiaodong Peninsula: Implication for lithospheric evolution of the eastern North China Craton. Gondwana Research, 25(2): 859-872.

Maruyama, S., 1997. Pacific-type orogeny revisited: Miyashiro-type orogeny proposed. Island Arc, 6(1): 91-120.

McDougall, I., Harrison, T.M., 1999. Geochronology and thermochronology by the $^{40}Ar/^{39}Ar$ method. Oxford University Press, New York, 269 pp.

McDowell, F.W., McIntosh, W.C., Farley, K.A., 2005. A precise $^{40}Ar–^{39}Ar$ reference age for the Durango apatite (U–Th)/He and fission-track dating standard. Chemical Geology, 214(3-4): 249-263.

Meng, F., Gao, S., Niu, Y., Liu, Y., Wang, X., 2014. Mesozoic–Cenozoic mantle evolution beneath the North China Craton: A new perspective from Hf–Nd isotopes of basalts. Gondwana Research.

Meng, Q.-R., Li, S.-Y., Li, R.-W., 2007. Mesozoic evolution of the Hefei basin in eastern China: Sedimentary response to deformations in the adjacent Dabieshan and along the Tanlu fault. Geological Society of America Bulletin, 119(7-8): 897-916.

Menzies, M.A., Fan, W., Zhang, M., 1993. Palaeozoic and Cenozoic lithoprobes and the loss of >120 km of Archaean lithosphere, Sino-Korean craton, China. Geological Society, London, Special Publications, 76(1): 71-81.

Menzies, M.A., Xu, Y., 1998. Geodynamics of the North China Craton, Mantle Dynamics and Plate Interactions in East Asia. American Geophysical Union, pp. 155-165.

Metcalf, J.R., Fitzgerald, P.G., Baldwin, S.L., Muñoz, J.-A., 2009. Thermochronology of a convergent orogen: Constraints on the timing of thrust faulting and subsequent exhumation of the Maladeta Pluton in the Central Pyrenean Axial Zone. Earth and Planetary Science Letters, 287(3–4): 488-503.

Miller, C.F., Mittlefehldt, D.W., 1982. Depletion of light rare-earth elements in felsic magmas. Geology, 10(3): 129-133.

Nasdala, L. et al., 2004. Incomplete retention of radiation damage in zircon from Sri Lanka. American Mineralogist, 89(1): 219-231.

Ni, J. et al., 2013. The Wulian metamorphic core complex: A newly discovered metamorphic core complex along the Sulu orogenic belt, eastern China. Journal of Earth Science, 24(3): 297-313.

Niu, Y., 2005. Generation and evolution of basaltic magmas: Some basic concepts and a new view on the origin of Mesozoic-Cenozoic basaltic volcanism in eastern China. Journal of China University of Geosciences, 11(1): 9-46.

Niu, Y., Wilson, M., Humphreys, E.R., O'Hara, M.J., 2011. The Origin of Intra-plate Ocean Island Basalts (OIB): the Lid Effect and its Geodynamic Implications. Journal of Petrology, 52(7-8): 1443-1468.

Okay, A.I., Şengör, A.M.C., 1992. Evidence for intracontinental thrust-related exhumation of the ultra-high-pressure rocks in China. Geology, 20(5): 411-414.

Okay, A.I., Şengör, A.M.C., Satir, M., 1993. Tectonics of an ultrahigh-pressure metamorphic terrane: The Dabie Shan/Tongbai Shan Orogen, China. Tectonics, 12(6): 1320-1334.

Osborn, E.F., 1979. The reaction principle, The evolution of the igneous rocks. Princeton University Press, Princeton, pp. 133-169.

Paton, C. et al., 2010. Improved laser ablation U-Pb zircon geochronology through robust downhole fractionation correction. Geochemistry, Geophysics, Geosystems, 11(3): Q0AA06.

Paton, C., Hellstrom, J., Paul, B., Woodhead, J., Hergt, J., 2011. Iolite: Freeware for the visualisation and processing of mass spectrometric data. Journal of Analytical Atomic Spectrometry, 26(12): 2508-2518.

Pearce, J.A., 1996. Sources and settings of granitic rocks. Episodes, 19(4): 120-125.

Pearson, N.J., Griffin, W.L., O’Reilly, S.Y., 2008. Mass fractionation correction in laser ablation-multiple collector ICP-MS: implications for overlap corrections and precise and accurate in situ isotope ratio measurement. In: Sylvester, P. (Editor), Laser-Ablation-ICP-MS in the Earth Sciences: Current Practices and Outstanding Issues. Mineralogical Association of Canada, Vancouver, pp. 93–116.

Peng, P. et al., 2014. Spatial distribution of ~1950–1800 Ma metamorphic events in the North China Craton: Implications for tectonic subdivision of the craton. Lithos, 202–203: 250-266.

Peng, T., Wilde, S.A., Fan, W., Peng, B., 2013a. Neoarchean siliceous high-Mg basalt (SHMB) from the Taishan granite–greenstone terrane, Eastern North China Craton: Petrogenesis and tectonic implications. Precambrian Research, 228: 233-249.

Peng, T., Wilde, S.A., Fan, W., Peng, B., 2013b. Late Neoarchean potassic high Ba–Sr granites in the Taishan granite–greenstone terrane: Petrogenesis and implications for continental crustal evolution. Chemical Geology, 344: 23-41.

Peng, T.P., Wilde, S.A., Fan, W.M., Peng, B.X., Mao, Y.S., 2013c. Mesoproterozoic high Fe-Ti mafic magmatism in western Shandong, North China Craton: Petrogenesis and implications for the final breakup of the Columbia supercontinent. Precambrian Research, 235: 190-207.

Pidgeon, R.T., Nemchin, A.A., Kinny, P.D., 2000. Fir-tree and nebulously zoned zircons from granulite facies rocks: evidence for zircon growth and interaction with metamorphic fluids, Journal of Conference Abstracts, pp. 798.

Price, P., Walker, R., 1962. Chemical etching of charged - particle tracks in solids. Journal of applied physics, 33(12): 3407-3412.

Qi, J., Yang, Q., Lu, K., Zhou, J., Wang, Z., 2004. Geologic map of sub-outcrop and its implied information of tectogenesis in Bohai Bay basin province. Earth Science Frontiers, 11(3): 299-307.

Qi, J., Yang, Q., 2010. Cenozoic structural deformation and dynamic processes of the Bohai Bay basin province, China. Marine and Petroleum Geology, 27(4): 757-771.

Qian, Q., Chung, S.-L., Lee, T.-Y., Wen, D.-J., 2003. Mesozoic high-Ba–Sr granitoids from North China: geochemical characteristics and geological implications. Terra Nova, 15(4): 272-278.

Qian, Q., Hermann, J., 2013. Partial melting of lower crust at 10–15 kbar: constraints on adakite and TTG formation. Contributions to Mineralogy and Petrology, 165(6): 1195-1224.

Qiu, J., Xu, X., Lo, C.H., 2001. ^{40}Ar/^{39}Ar dating and source tracing on K-rich volcanics and lamprorite in the western Shandong Province. Chinese Science Bulletin, 46(18): 1500-1508.

Qiu, N., Zuo, Y., Chang, J., Li, W., 2014. Geothermal evidence of Meso-Cenozoic lithosphere thinning in the Jiyang sub-basin, Bohai Bay Basin, eastern North China Craton. Gondwana Research, 26(3–4): 1079-1092.

Ratschbacher, L. et al., 2000. Exhumation of the ultrahigh-pressure continental crust in east central China: Cretaceous and Cenozoic unroofing and the Tan-Lu fault. Journal of Geophysical Research: Solid Earth, 105(B6): 13303-13338.

Reichardt, H., Weinberg, R.F., 2012a. The dike swarm of the Karakoram shear zone, Ladakh, NW India: Linking granite source to batholith. Geological Society of America Bulletin, 124(1-2): 89-103.

Reichardt, H., Weinberg, R.F., 2012b. Hornblende chemistry in meta- and diatexites and its retention in the source of leucogranites: an example from the Karakoram Shear Zone, NW India. Journal of Petrology, 53(6): 1287-1318.

Reiners, P.W. et al., 2003. Post-orogenic evolution of the Dabie Shan, eastern China, from (U-Th)/He and fission-track thermochronology. American Journal of Science, 303(6): 489-518.

Reiners, P.W., Spell, T.L., Nicolescu, S., Zanetti, K.A., 2004. Zircon (U-Th)/He thermochronometry: He diffusion and comparisons with $^{40}Ar/^{39}Ar$ dating. Geochimica et Cosmochimica Acta, 68(8): 1857-1887.

Reiners, P.W., 2005. Zircon (U-Th)/He Thermochronometry. Reviews in Mineralogy and Geochemistry, 58(1): 151-179.

Reiners, P.W., Brandon, M.T., 2006. Using thermochronology to understand orogenic erosion. Annual Review of Earth and Planetary Sciences, 34(1): 419-466.

Ren, J., Tamaki, K., Li, S., Junxia, Z., 2002. Late Mesozoic and Cenozoic rifting and its dynamic setting in Eastern China and adjacent areas. Tectonophysics, 344(3-4): 175-205.

Renne, P.R., Mundil, R., Balco, G., Min, K., Ludwig, K.R., 2010. Joint determination of ^{40}K decay constants and $^{40}Ar*/^{40}K$ for the Fish Canyon sanidine standard, and improved accuracy for $^{40}Ar/^{39}Ar$ geochronology. Geochimica et Cosmochimica Acta, 74(18): 5349-5367.

Renne, P.R., Balco, G., Ludwig, K.R., Mundil, R., Min, K., 2011. Response to the comment by W.H. Schwarz et al. on "Joint determination of ^{40}K decay constants and $^{40}Ar*/^{40}K$ for the Fish Canyon sanidine standard, and improved accuracy for $^{40}Ar/^{39}Ar$ geochronology" by P.R. Renne et al. (2010). Geochimica et Cosmochimica Acta, 75(17): 5097-5100.

Richards, J.P., Kerrich, R., 2007. Special Paper: Adakite-Like Rocks: Their Diverse Origins and Questionable Role in Metallogenesis. Economic Geology, 102(4): 537-576.

Richards, J.P., 2011. High Sr/Y Arc Magmas and Porphyry Cu ± Mo ± Au Deposits: Just Add Water. Economic Geology, 106(7): 1075-1081.

Rudnick, R., Gao, S., 2003. Composition of the continental crust. Treatise on geochemistry, 3, 1-64 pp.

Rushmer, T., 1991. Partial melting of two amphibolites: contrasting experimental results under fluid-absent conditions. Contributions to Mineralogy and Petrology, 107(1): 41-59.

SBGB, 1996. Laiyang-Weifang-Xiyou geological survey report (1:200000).

Shuster, D.L., Flowers, R.M., Farley, K.A., 2006. The influence of natural radiation damage on helium diffusion kinetics in apatite. Earth and Planetary Science Letters, 249(3–4): 148-161.

Siebel, W., Danišík, M., Chen, F., 2009. From emplacement to unroofing: thermal history of the Jiazishan gabbro, Sulu UHP terrane, China. Mineralogy and Petrology, 96(3): 163-175.

Sisson, T.W., Grove, T.L., 1993. Experimental investigations of the role of H2O in calc-alkaline differentiation and subduction zone magmatism. Contributions to Mineralogy and Petrology, 113(2): 143-166.

Sláma, J. et al., 2008. Plešovice zircon — A new natural reference material for U-Pb and Hf isotopic microanalysis. Chemical Geology, 249(1–2): 1-35.

Sobolev, A.V. et al., 2007. The amount of recycled crust in sources of mantle-derived melts. Science, 316(5823): 412-417.

Söderlund, U., Patchett, P.J., Vervoort, J.D., Isachsen, C.E., 2004. The ^{176}Lu decay constant determined by Lu-Hf and U-Pb isotope systematics of Precambrian mafic intrusions. Earth and Planetary Science Letters, 219(3–4): 311-324.

Stacey, J.S., Kramers, J.D., 1975. Approximation of terrestrial lead isotope evolution by a two-stage model. Earth and Planetary Science Letters, 26(2): 207-221.

Stern, R.A., Hanson, G.N., 1991. Archean High-Mg Granodiorite: A Derivative of Light Rare Earth Element-enriched Monzodiorite of Mantle Origin. Journal of Petrology, 32(1): 201-238.

Stern, R.A., 2001. A new isotopic and trace-element standard for the ion microprobe: Preliminary thermal ionisation mass spectrometry (TIMS) U-Pb and electron-microprobe data: Radiogenic Age and Isotope Studies, Geological Survey of Canada.

Sun, J., Yang, J., 2013. Mesozoic magmatism related to dectratonizatoin of the north china craton. Acta Petrologica et Mineralogica, 32(5): 577-592.

Sun, S.-s., McDonough, W.F., 1989. Chemical and isotopic systematics of oceanic basalts: implications for mantle composition and processes. Geological Society, London, Special Publications, 42(1): 313-345.

Suo, S., Zhong, Z., Zhou, H., You, Z., Zhang, L., 2009. Meso- and micro-structures of foliated eclogites in Dabie-Sulu UHP belt and implications for the earliest stages of exhumation of UHP metamorphic rocks: An example from Taohang, southeastern Shandong, China. Journal of Earth Science, 20(4): 649-658.

Suo, Y., Li, S., Dai, L., Liu, X., Zhou, L., 2012. Cenozoic tectonic migration and basin evolutioin in East Asia and its continental margins. Acta Petrologica Sinica, 28(8): 2602-2618.

Suo, Y. et al., 2014. Cenozoic tectonic jumping and implications for hydrocarbon accumulation in basins in the East Asia Continental Margin. Journal of Asian Earth Sciences, 88: 28-40.

Tagami, T., Shimada, C., 1996. Natural long-term annealing of the zircon fission track system around a granitic pluton. Journal of Geophysical Research: Solid Earth, 101(B4): 8245-8255.

Tagami, T., 2005. Zircon Fission-Track Thermochronology and Applications to Fault Studies. Reviews in Mineralogy and Geochemistry, 58(1): 95-122.

Tam, P.Y. et al., 2011. Timing of metamorphism in the Paleoproterozoic Jiao-Liao-Ji Belt: New SHRIMP U-Pb zircon dating of granulites, gneisses and marbles of the Jiaobei massif in the North China Craton. Gondwana Research, 19(1): 150-162.

Tam, P.Y. et al., 2012a. Petrology and metamorphic P–T path of high-pressure mafic granulites from the Jiaobei massif in the Jiao-Liao-Ji Belt, North China Craton. Lithos, 155(0): 94-109.

Tam, P.Y. et al., 2012b. Metamorphic P–T path and implications of high-pressure pelitic granulites from the Jiaobei massif in the Jiao-Liao-Ji Belt, North China Craton. Gondwana Research, 22(1): 104-117.

Tang, J., Zheng, Y.F., Wu, Y.B., Gong, B., Liu, X., 2007. Geochronology and geochemistry of metamorphic rocks in the Jiaobei terrane: Constraints on its tectonic affinity in the Sulu orogen. Precambrian Research, 152(1-2): 48-82.

Tang, J. et al., 2008. Zircon U-Pb age and geochemical constraints on the tectonic affinity of the Jiaodong terrane in the Sulu orogen, China. Precambrian Research, 161(3-4): 389-418.

Tarney, J., Jones, C.E., 1994. Trace element geochemistry of orogenic igneous rocks and crustal growth models. Journal of the Geological Society, 151(5): 855-868.

Thompson, A.B., 1999. Some time-space relationships for crustal melting and granitic intrusion at various depths. Geological Society, London, Special Publications, 168(1): 7-25.

Tomurtogoo, O., Windley, B.F., Kröner, A., Badarch, G., Liu, D.Y., 2005. Zircon age and occurrence of the Adaatsag ophiolite and Muron shear zone, central Mongolia:

constraints on the evolution of the Mongol–Okhotsk ocean, suture and orogen. Journal of the Geological Society, 162(1): 125-134.

Vermeesch, P., 2012. On the visualisation of detrital age distributions. Chemical Geology, 312–313(0): 190-194.

Wagner, G.A., Gleadow, A.J.W., Fitzgerald, P.G., 1989. The significance of the partial annealing zone in apatite fission-track analysis: Projected track length measurements and uplift chronology of the transantarctic mountains. Chemical Geology, 79(4): 295-305.

Wallis, S., Enami, M., Banno, S., 1999. The Sulu UHP Terrane: A Review of the Petrology and Structural Geology. International Geology Review, 41(10): 906-920.

Wan, Y. et al., 2006. SHRIMP U-Pb zircon geochronology of Palaeoproterozoic metasedimentary rocks in the North China Craton: Evidence for a major Late Palaeoproterozoic tectonothermal event. Precambrian Research, 149(3–4): 249-271.

Wan, Y. et al., 2010. Juvenile magmatism and crustal recycling at the end of the Neoarchean in Western Shandong Province, North China Craton: Evidence from SHRIMP zircon dating. American Journal of Science, 310(10): 1503-1552.

Wan, Y. et al., 2011. ~2.7 Ga juvenile crust formation in the North China Craton (Taishan-Xintai area, western Shandong Province): Further evidence of an understated event from U–Pb dating and Hf isotopic composition of zircon. Precambrian Research, 186(1–4): 169-180.

Wan, Y. et al., 2012. Redefinition of depositional ages of Neoarchean supracrustal rocks in western Shandong Province, China: SHRIMP U–Pb zircon dating. Gondwana Research, 21(4): 768-784.

Wang, F., Gao, S., Niu, B., Zhang, H., 2007a. Geochemistry of Dabeigou Basalt in Chengde Basin, Hebei Province and Constraints on Lithospheric Mantle Thinning of North China Craton. Earth Science Frontiers, 14(2): 98-108.

Wang, F. et al., 2014. $^{40}Ar/^{39}Ar$ geochronology of the North China and Yangtze Cratons: New constraints on Mesozoic cooling and cratonic destruction under East Asia. Journal of Geophysical Research: Solid Earth, 119(4): 3700-3721.

Wang, H., 1985. Atlas of the paleogeography of China. Catographic Publishing House, Beijing, 281 pp.

Wang, L.G. et al., 1998. Constraints on crustal evolution and gold metallogeny in the Northwestern Jiaodong Peninsula, China, from SHRIMP U-Pb zircon studies of granitoids. Ore Geology Reviews, 13(1-5): 275-291.

Wang, Q. et al., 1993. Coesite-bearing granulite retrograded from eclogite in Weihai, eastern China. European Journal of Mineralogy, 5(1): 141-152.

Wang, T. et al., 2011a. Pattern and kinematic polarity of late Mesozoic extension in continental NE Asia: Perspectives from metamorphic core complexes. Tectonics, 30(6): TC6007.

Wang, W. et al., 2010. Formation age of the Neoarchaen Jining Group (banded iron formation) in the western Shandong Province: Constraints from SHRIMP zircon U-Pb dating. Acta Petrologica Sinica, 26(4): 1175-1181.

Wang, W. et al., 2013. Geochemistry of ∼2.7 Ga basalts from Taishan area: Constraints on the evolution of early Neoarchean granite-greenstone belt in western Shandong Province, China. Precambrian Research, 224: 94-109.

Wang, X.-C., Liu, Y.-S., Liu, X.-M., 2006. Mesozoic adakites in the Lingqiu Basin of the central North China Craton: Partial melting of underplated basaltic lower crust. Geochemical Journal, 40(5): 447-461.

Wang, Y., 2006. The onset of the Tan–Lu fault movement in eastern China: constraints from zircon (SHRIMP) and $^{40}Ar/^{39}Ar$ dating. Terra Nova, 18(6): 423-431.

Wang, Y. et al., 2007b. LA-ICP-MS U–Pb zircon geochronology and geochemistry of Paleoproterozoic mafic dykes from western Shandong Province: Implications for back-arc basin magmatism in the Eastern Block, North China Craton. Precambrian Research, 154(1–2): 107-124.

Wang, Y., Li, H., 2008. Initial formation and mesozoic tectonic exhumation of an intracontinental tectonic belt of the northern part of the Taihang mountain belt, eastern Asia. The Journal of Geology, 116(2): 155-172.

Wang, Y., Zhou, L., Li, J., 2011b. Intracontinental superimposed tectonics—A case study in the Western Hills of Beijing, eastern China. Geological Society of America Bulletin, 123(5-6): 1033-1055.

Watson, E.B., Harrison, T.M., 1983. Zircon saturation revisited: temperature and composition effects in a variety of crustal magma types. Earth and Planetary Science Letters, 64(2): 295-304.

Webb, L.E., Leech, M.L., Yang, T.N., 2006. $^{40}Ar/^{39}Ar$ thermochronology of the Sulu terrane: Late Triassic exhumation of high- and ultrahigh-pressure rocks and implications for Mesozoic tectonics in East Asia. Geological Society of America Special Papers, 403: 77-92.

Whitney, J.A., 1988. The origin of granite: The role and source of water in the evolution of granitic magmas. Geological Society of America Bulletin, 100(12): 1886-1897.

Wiedenbeck, M. et al., 1995. Three natural zircon standards for U-Th-Pb, Lu-Hf, trace element and REE analyses. Geostandards Newsletter, 19(1): 1-23.

Wilde, S.A., Zhao, G., Sun, M., 2002. Development of the North China craton during the late Archaean and its final amalgamation at 1.8 Ga: Some speculations on its position within a global Palaeoproterozoic supercontinent. Gondwana Research, 5(1): 85-94.

Windley, B.F., Alexeiev, D., Xiao, W., Kröner, A., Badarch, G., 2007. Tectonic models for accretion of the Central Asian Orogenic Belt. Journal of the Geological Society, 164(1): 31-47.

Windley, B.F., Maruyama, S., Xiao, W.J., 2010. Delamination/thinning of sub-continental lithospheric mantle under Eastern China: The role of water and multiple subduction. American Journal of Science, 310(10): 1250-1293.

Wolf, R.A., Farley, K.A., Kass, D.M., 1998. Modeling of the temperature sensitivity of the apatite (U–Th)/He thermochronometer. Chemical Geology, 148(1–2): 105-114.

Woodhead, J.D., Hergt, J.M., 2005. A Preliminary Appraisal of Seven Natural Zircon Reference Materials for In Situ Hf Isotope Determination. Geostandards and Geoanalytical Research, 29(2): 183-195.

Wu, C.-L. et al., 2006a. Geometry and kinematics of tectonic evolution in northern part of Sulu orogenic belt. Earth Science-Journal of China University of Geosciences, 31(6): 817-829.

Wu, F.-Y., Walker, R.J., Ren, X.-w., Sun, D.-y., Zhou, X.-h., 2003. Osmium isotopic constraints on the age of lithospheric mantle beneath northeastern China. Chemical Geology, 196(1–4): 107-129.

Wu, F.-Y., Lin, J.-Q., Wilde, S.A., Zhang, X.O., Yang, J.-H., 2005. Nature and significance of the Early Cretaceous giant igneous event in eastern China. Earth and Planetary Science Letters, 233(1-2): 103-119.

Wu, F.-Y. et al., 2007. The Heilongjiang Group: A Jurassic accretionary complex in the Jiamusi Massif at the western Pacific margin of northeastern China. Island Arc, 16(1): 156-172.

Wu, F.Y., Walker, R.J., Yang, Y.H., Yuan, H.L., Yang, J.H., 2006b. The chemical-temporal evolution of lithospheric mantle underlying the North China Craton. Geochimica et Cosmochimica Acta, 70(19): 5013-5034.

Wu, F.Y., Xu, Y.G., Gao, S., Zheng, J.P., 2008. Lithospheric thinning and destruction of the North China Craton. Acta Petrologica Sinica, 24: 1145-1174.

Wu, M., 2014. Ages, geochemistry and metamorphism of the Neoarchean basement in Shandong Province: implications for evolution of the Eastern block, North China Craton Hongkong University, Hongkong.

Wu, M. et al., 2014. Zircon U-Pb geochronology and Hf isotopes of major lithologies from the Jiaodong Terrane: Implications for the crustal evolution of the Eastern Block of the North China Craton. Lithos, 190-191: 71-84.

Xia, Q.-K. et al., 2013. High water content in Mesozoic primitive basalts of the North China Craton and implications on the destruction of cratonic mantle lithosphere. Earth and Planetary Science Letters, 361: 85-97.

Xiao, W., Windley, B.F., Hao, J., Zhai, M., 2003. Accretion leading to collision and the Permian Solonker suture, Inner Mongolia, China: Termination of the central Asian orogenic belt. Tectonics, 22(6): 1069.

Xu, W.-L., Wang, Q.-H., Wang, D.-Y., Guo, J.-H., Pei, F.-P., 2006a. Mesozoic adakitic rocks from the Xuzhou–Suzhou area, eastern China: Evidence for partial melting of delaminated lower continental crust. Journal of Asian Earth Sciences, 27(2): 230-240.

Xu, W.-L. et al., 2013. Destruction of the North China Craton: Delamination or thermal/chemical erosion? Mineral chemistry and oxygen isotope insights from websterite xenoliths. Gondwana Research, 23(1): 119-129.

Xu, W., Gao, S., Wang, Q., Wang, D., Liu, Y., 2006b. Mesozoic crustal thickening of the eastern North China craton: Evidence from eclogite xenoliths and petrologic implications. Geology, 34(9): 721-724.

Xu, W. et al., 2008. Interaction of adakitic melt-peridotite: Implications for the high-Mg# signature of Mesozoic adakitic rocks in the eastern North China Craton. Earth and Planetary Science Letters, 265(1–2): 123-137.

Xu, W.L., Gao, S., Yang, D.B., Pei, F.P., Wang, Q.H., 2009a. Geochemistry of eclogite xenoliths in Mesozoic adakitic rocks from Xuzhou-Suzhou area in central China and their tectonic implications. Lithos, 107(3-4): 269-280.

Xu, Y.-G. et al., 2004a. Crust-mantle interaction during the tectono-thermal reactivation of the North China Craton: constraints from SHRIMP zircon U–Pb chronology and geochemistry of Mesozoic plutons from western Shandong. Contributions to Mineralogy and Petrology, 147(6): 750-767.

Xu, Y.-G., 2007. Diachronous lithospheric thinning of the North China Craton and formation of the Daxin'anling-Taihangshan gravity lineament. Lithos, 96(1-2): 281-298.

Xu, Y.-G., 2014. Recycled oceanic crust in the source of 90–40Ma basalts in North and Northeast China: Evidence, provenance and significance. Geochimica et Cosmochimica Acta, 143: 49-67.

Xu, Y., Li, H., Pang, C., He, B., 2009b. On the timing and duration of the destruction of the North China Craton. Chinese Science Bulletin, 54(19): 3379-3396.

Xu, Y.G., 2001. Thermo-tectonic destruction of the Archaean lithospheric keel beneath the Sino-Korean craton in china: evidence, timing and mechanism. Physics and Chemistry of the Earth, Part A: Solid Earth and Geodesy, 26(9-10): 747-757.

Xu, Y.G., Chung, S.L., Ma, J., Shi, L., 2004b. Contrasting Cenozoic Lithospheric Evolution and Architecture in the Western and Eastern Sino - Korean Craton: Constraints from

Geochemistry of Basalts and Mantle Xenoliths. The Journal of Geology, 112(5): 593-605.

Xu, Y.G. et al., 2004c. Crust-mantle interaction during the tectono-thermal reactivation of the North China Craton: constraints from SHRIMP zircon U–Pb chronology and geochemistry of Mesozoic plutons from western Shandong. Contributions to Mineralogy and Petrology, 147(6): 750-767.

Xu, Z. et al., 2006c. Polyphase subduction and exhumation of the Sulu high-pressure–ultrahigh-pressure metamorphic terrane. Geological Society of America Special Papers, 403: 93-113.

Xu, Z., Zhao, Z.-F., Zheng, Y.-F., 2012. Slab–mantle interaction for thinning of cratonic lithospheric mantle in North China: Geochemical evidence from Cenozoic continental basalts in central Shandong. Lithos, 146–147: 202-217.

Yan, J. et al., 2005. Studies on petrology and geochemistry of the Late Cretaceous basalt and mantle-derived xenolith from eastern Shandong. Acta Petrologica Sinica, 21(1): 14.

Yan, S., Wang, G., Shao, Z., Meng, X., 1996. Extensional tectonic model of crsutal elevation in western Shandong. Acta Geologica Sinica, 70(1): 1-11.

Yang, D.-B., Xu, W.-L., Pei, F.-P., Yang, C.-H., Wang, Q.-H., 2012a. Spatial extent of the influence of the deeply subducted South China Block on the southeastern North China Block: Constraints from Sr–Nd–Pb isotopes in Mesozoic mafic igneous rocks. Lithos, 136–139: 246-260.

Yang, D.-B., Xu, W.-L., Xu, Y.-G., Pei, F.-P., Wang, F., 2013. Provenance of sediments from Mesozoic basins in western Shandong: Implications for the evolution of the eastern North China Block. Journal of Asian Earth Sciences, 76: 12-29.

Yang, D., Xu, W., Gao, S., Xu, Y., Pei, F., 2012b. Repeated modification of lithospheric mantle in the eastern North China Craton: Constraints from SHRIMP zircon U-Pb dating of dunite xenoliths in western Shandong. Chinese Science Bulletin, 57(6): 651-659.

Yang, J.-H., Chung, S.-L., Zhai, M.-G., Zhou, X.-H., 2004. Geochemical and Sr-Nd-Pb isotopic compositions of mafic dikes from the Jiaodong Peninsula, China: evidence for vein-plus-peridotite melting in the lithospheric mantle. Lithos, 73(3-4): 145-160.

Yang, J.-H. et al., 2005a. Petrogenesis of post-orogenic syenites in the Sulu Orogenic Belt, East China: geochronological, geochemical and Nd-Sr isotopic evidence. Chemical Geology, 214(1-2): 99-125.

Yang, J.-H. et al., 2005b. Petrogenesis of Early Cretaceous intrusions in the Sulu ultrahigh-pressure orogenic belt, east China and their relationship to lithospheric thinning. Chemical Geology, 222(3-4): 200-231.

Yang, J.-H. et al., 2007. Rapid exhumation and cooling of the Liaonan metamorphic core complex: Inferences from 40Ar/39Ar thermochronology and implications for Late Mesozoic extension in the eastern North China Craton. Geological Society of America Bulletin, 119(11-12): 1405-1414.

Yang, J.-H. et al., 2010. Diachronous decratonization of the Sino-Korean craton: Geochemistry of mantle xenoliths from North Korea. Geology, 38(9): 799-802.

Yang, J.H., Chu, M.F., Liu, W., Zhai, M.G., 2003a. Geochemistry and petrogenesis of Guojialing granodiorites from the northwestern Jiaodong Peninsula, eastern China. Acta Petrologica Sinica, 19(4): 692-700.

Yang, J.S. et al., 2003b. SHRIMP U-Pb dating of coesite-bearing zircon from the ultrahigh-pressure metamorphic rocks, Sulu terrane, east China. Journal of Metamorphic Geology, 21(6): 551-560.

Yang, K.-F. et al., 2012c. Reactivation of the Archean lower crust: Implications for zircon geochronology, elemental and Sr–Nd–Hf isotopic geochemistry of late Mesozoic granitoids from northwestern Jiaodong Terrane, the North China Craton. Lithos, 146–147: 112-127.

Yang, L.-Q. et al., 2014a. $^{40}Ar/^{39}Ar$ geochronological constraints on the formation of the Dayingezhuang gold deposit: New implications for timing and duration of hydrothermal activity in the Jiaodong gold province, China. Gondwana Research, 25(4): 1469-1483.

Yang, Q.-L., Zhao, Z.-F., Zheng, Y.-F., 2012d. Modification of subcontinental lithospheric mantle above continental subduction zone: Constraints from geochemistry of Mesozoic gabbroic rocks in southeastern North China. Lithos, 146–147: 164-182.

Yang, Q., Santosh, M., Shen, J., Li, S., 2014b. Juvenile vs. recycled crust in NE China: Zircon U–Pb geochronology, Hf isotope and an integrated model for Mesozoic gold mineralization in the Jiaodong Peninsula. Gondwana Research, 25(4): 1445-1468.

Yang, W., 2002. Geophysical profiling across the Sulu ultra-high-pressure metamorphic belt, eastern China. Tectonophysics, 354(3-4): 277-288.

Yao, Y., Ye, K., Liu, J., Cong, B., Wang, Q., 2000. A transitional eclogite- to high pressure granulite-facies overprint on coesite–eclogite at Taohang in the Sulu ultrahigh-pressure terrane, Eastern China. Lithos, 52(1–4): 109-120.

Yardley, B.W.D., 1986. Earth science: Is there water in the deep continental crust? Nature, 323(6084): 111-111.

Ye, K., Cong, B., Ye, D., 2000a. The possible subduction of continental material to depths greater than 200 km. Nature, 407(6805): 734-736.

Ye, K. et al., 2000b. Large areal extent of ultrahigh-pressure metamorphism in the Sulu ultrahigh-pressure terrane of East China: new implications from coesite and omphacite inclusions in zircon of granitic gneiss. Lithos, 52(1–4): 157-164.

Yin, A., Nie, S., 1993. An indentation model for the North and South China collision and the development of the Tan-Lu and Honam Fault Systems, eastern Asia. Tectonics, 12(4): 801-813.

Yin, A., Nie, S., 1996. A Phanerozoic palinspastic reconstruction of China and its neighboring regions. In: Harrison, A.Y.a.M. (Editor), The tectonic evolution of Asia. Cambridge University Press, Cambridge.

Ying, J., Zhang, H., Kita, N., Morishita, Y., Shimoda, G., 2006. Nature and evolution of Late Cretaceous lithospheric mantle beneath the eastern North China Craton: Constraints from petrology and geochemistry of peridotitic xenoliths from Jünan, Shandong Province, China. Earth and Planetary Science Letters, 244(3–4): 622-638.

Zaun, P.E., Wagner, G.A., 1985. Fission-track stability in zircons under geological conditions. Nuclear Tracks and Radiation Measurements, 10(3): 303-307.

Zeng, G., Chen, L.-H., Xu, X.-S., Jiang, S.-Y., Hofmann, A.W., 2010. Carbonated mantle sources for Cenozoic intra-plate alkaline basalts in Shandong, North China. Chemical Geology, 273(1-2): 35-45.

Zeng, G., Chen, L.-H., Hofmann, A.W., Jiang, S.-Y., Xu, X.-S., 2011. Crust recycling in the sources of two parallel volcanic chains in Shandong, North China. Earth and Planetary Science Letters, 302(3-4): 359-368.

Zhai, M., Liu, W., 1998. The boundary between Sino-Korea Craton and Yangtze Craton and its extension to the Korean Peninsula. Journal of the Petrological Society of Korea, 7(1): 15-26.

Zhai, M. et al., 2000. Sm–Nd geochronology and petrography of garnet pyroxene granulites in the northern Sulu region of China and their geotectonic implication. Lithos, 52(1–4): 23-33.

Zhai, M.G., Santosh, M., 2011. The early Precambrian odyssey of the North China Craton: A synoptic overview. Gondwana Research, 20(1): 6-25.

Zhang, B., Zhu, G., Jiang, D., Li, C., Chen, Y., 2012a. Evolution of the Yiwulushan metamorphic core complex from distributed to localized deformation and its tectonic implications. Tectonics, 31(4): TC4018.

Zhang, H.-F., Sun, M., 2002. Geochemistry of Mesozoic basalts and mafic dikes, southeastern North China Craton, and tectonic implications. International Geology Review, 44(4): 370-382.

Zhang, H.-F. et al., 2002. Mesozoic lithosphere destruction beneath the North China Craton: evidence from major-, trace-element and Sr-Nd-Pb isotope studies of Fangcheng basalts. Contributions to Mineralogy and Petrology, 144(2): 241-254.

Zhang, H.-F. et al., 2003a. Secular evolution of the lithosphere beneath the eastern North China Craton: evidence from Mesozoic basalts and high-Mg andesites. Geochimica et Cosmochimica Acta, 67(22): 4373-4387.

Zhang, H.-F. et al., 2004a. Highly heterogeneous Late Mesozoic lithospheric mantle beneath the North China Craton: evidence from Sr-Nd-Pb isotopic systematics of mafic igneous rocks. Geological Magazine, 141(1): 55-62.

Zhang, H.-F. et al., 2008a. Evolution of subcontinental lithospheric mantle beneath eastern China: Re–Os isotopic evidence from mantle xenoliths in Paleozoic kimberlites and Mesozoic basalts. Contributions to Mineralogy and Petrology, 155(3): 271-293.

Zhang, H.-F., Goldstein, S.L., Zhou, X.-H., Sun, M., Cai, Y., 2009a. Comprehensive refertilization of lithospheric mantle beneath the North China Craton: further Os–Sr–Nd isotopic constraints. Journal of the Geological Society, 166(2): 249-259.

Zhang, H. et al., 2004b. Causes and consequences of protracted melting of the mid-crust exposed in the North Himalayan antiform. Earth and Planetary Science Letters, 228(1–2): 195-212.

Zhang, H., Hou, Q., Cao, D., 2007. Tectono-chronologic constraints on a Mesozoic slip and thrust belt in the eastern Jiaodong Peninsula. Science in China Series D: Earth Sciences, 50(1): 25-32.

Zhang, J., Zhang, H.-f., Ying, J.-f., Tang, Y.-j., Niu, L.-f., 2008b. Contribution of subducted Pacific slab to Late Cretaceous mafic magmatism in Qingdao region, China: A petrological record. Island Arc, 17(2): 231-241.

Zhang, J., Zhao, Z.-F., Zheng, Y.-F., Dai, M., 2010a. Postcollisional magmatism: Geochemical constraints on the petrogenesis of Mesozoic granitoids in the Sulu orogen, China. Lithos, 119(3-4): 512-536.

Zhang, J., Zhao, Z.-F., Zheng, Y.-F., Liu, X., Xie, L., 2012b. Zircon Hf-O isotope and whole-rock geochemical constraints on origin of postcollisional mafic to felsic dykes in the Sulu orogen. Lithos, 136–139: 225-245.

Zhang, K.J., 1997. North and South China collision along the eastern and southern North China margins. Tectonophysics, 270(1-2): 145-156.

Zhang, R.Y., Liou, J.G., Yang, J.S., Ye, K., 2003b. Ultrahigh-pressure metamorphism in the forbidden zone: the Xugou garnet peridotite, Sulu terrane, eastern China. Journal of Metamorphic Geology, 21(6): 539-550.

Zhang, R.Y., Liou, J.G., Ernst, W.G., 2009b. The Dabie-Sulu continental collision zone: A comprehensive review. Gondwana Research, 16(1): 1-26.

Zhang, R.Y. et al., 2010b. Origin and tectonic implication of an UHP metamorphic mafic-ultramafic complex from the Sulu UHP terrane, eastern China: Evidence from petrological and geochemical studies of CCSD-Main Hole core samples. Chemical Geology, 276(1-2): 69-87.

Zhang, S.-B., Tang, J., Zheng, Y.-F., 2014. Contrasting Lu–Hf isotopes in zircon from Precambrian metamorphic rocks in the Jiaodong Peninsula: Constraints on the tectonic suture between North China and South China. Precambrian Research, 245: 29-50.

Zhang, X.O. et al., 2003c. Geology and timing of mineralization at the Cangshang gold deposit, north-western Jiaodong Peninsula, China. Mineralium Deposita, 38(2): 141-153.

Zhang, Y., Dong, S., Shi, W., 2003d. Cretaceous deformation history of the middle Tan-Lu fault zone in Shandong Province, eastern China. Tectonophysics, 363(3–4): 243-258.

Zhao, G., Han, Z., Luan, G., Xing, G., Chen, Z., 2001a. Geochemistry of basaltic rocks in Laoshan Mountain area. Geological Journal of China Universities, 7(4): 435-443.

Zhao, G., Wilde, S.A., Cawood, P.A., Sun, M., 2001b. Archean blocks and their boundaries in the North China Craton: lithological, geochemical, structural and P–T path constraints and tectonic evolution. Precambrian Research, 107(1–2): 45-73.

Zhao, G., Sun, M., Wilde, S.A., Sanzhong, L., 2005. Late Archean to Paleoproterozoic evolution of the North China Craton: key issues revisited. Precambrian Research, 136(2): 177-202.

Zhao, G., Li, S., Sun, M., Wilde, S.A., 2011. Assembly, accretion, and break-up of the Palaeo-Mesoproterozoic Columbia supercontinent: record in the North China Craton revisited. International Geology Review, 53(11-12): 1331-1356.

Zhao, R., Liou, J.G., Tsujimori, T., Zhang, R.Y., 2007. Petrology and U-Pb SHRIMP geochronology of a garnet peridotite, Sulu UHP terrane, east-central China. International Geology Review, 49(8): 732-752.

Zhao, X., Coe, R.S., 1987. Palaeomagnetic constraints on the collision and rotation of North and South China. Nature, 327(6118): 141-144.

Zhao, Z.-F. et al., 2012. Syn-exhumation magmatism during continental collision: Evidence from alkaline intrusives of Triassic age in the Sulu orogen. Chemical Geology, 328: 70-88.

Zhao, Z.-F., Dai, L.-Q., Zheng, Y.-F., 2013. Postcollisional mafic igneous rocks record crust-mantle interaction during continental deep subduction. Scientific Reports, 3: 3413.

Zhao, Z., Yang, S., Zhou, J., Zhu, G., Chen, H., 2000. Comprehensive explanation of Geology and Geophysics of orverthrust belt in Hefei Basin and initial study of its tectonic attribute. Journal of Chengdu Universtiy of Technology, 27(2): 151-157.

Zheng, J.P. et al., 2007. Mechanism and timing of lithospheric modification and replacement beneath the eastern North China Craton: Peridotitic xenoliths from the 100 Ma Fuxin basalts and a regional synthesis. Geochimica et Cosmochimica Acta, 71(21): 5203-5225.

Zheng, J.P. et al., 2009. Age and composition of granulite and pyroxenite xenoliths in Hannuoba basalts reflect Paleogene underplating beneath the North China Craton. Chemical Geology, 264(1–4): 266-280.

Zheng, J.P. et al., 2014. Linking continental deep subduction with destruction of a cratonic margin: strongly reworked North China SCLM intruded in the Triassic Sulu UHP belt. Contributions to Mineralogy and Petrology, 168(1): 1028.

Zheng, Y.-F., Fu, B., Gong, B., Li, L., 2003. Stable isotope geochemistry of ultrahigh pressure metamorphic rocks from the Dabie-Sulu orogen in China: implications for geodynamics and fluid regime. Earth-Science Reviews, 62(1-2): 105-161.

Zheng, Y.-F. et al., 2004. Zircon U-Pb and oxygen isotope evidence for a large-scale 18O depletion event in igneous rocks during the Neoproterozoic. Geochimica et Cosmochimica Acta, 68(20): 4145-4165.

Zheng, Y.-F., Xia, Q.-X., Chen, R.-X., Gao, X.-Y., 2011. Partial melting, fluid supercriticality and element mobility in ultrahigh-pressure metamorphic rocks during continental collision. Earth-Science Reviews, 107(3–4): 342-374.

Zheng, Y.-F., Zhang, L., McClelland, W.C., Cuthbert, S., 2012. Processes in continental collision zones: Preface. Lithos, 136–139: 1-9.

Zheng, Y.F., Gong, B., Zhao, Z.F., Wu, Y.B., Chen, F.K., 2008. Zircon U-Pb age and O isotope evidence for Neoproterozoic low-18O magmatism during supercontinental rifting in South China: Implications for the snowball earth event. American Journal of Science, 308(4): 484-516.

Zhou, J.-B. et al., 2008a. SHRIMP U-Pb zircon dating of the Wulian complex: Defining the boundary between the North and South China Cratons in the Sulu Orogenic Belt, China. Precambrian Research, 162(3-4): 559-576.

Zhou, J.-B. et al., 2008b. SHRIMP U-Pb zircon dating of the Neoproterozoic Penglai Group and Archean gneisses from the Jiaobei Terrane, North China, and their tectonic implications. Precambrian Research, 160(3-4): 323-340.

Zhou, J.-B. et al., 2008c. Detrital zircon U–Pb dating of low-grade metamorphic rocks in the Sulu UHP belt: evidence for overthrusting of the North China Craton onto the South China Craton during continental subduction. Journal of the Geological Society, 165(1): 423-433.

Zhou, J., Zheng, Y., Wu, Y., 2003. Zircon U-Pb ages for Wulian granites in northwest Sulu and their tectonic implications. Chinese Science Bulletin, 48(4): 379-384.

Zhou, X., Zhao, G., Wei, C., Geng, Y., Sun, M., 2008d. EPMA U-Th-Pb monazite and SHRIMP U-Pb zircon geochronology of high-pressure pelitic granulites in the Jiaobei massif of the North China Craton. American Journal of Science, 308(3): 328-350.

Zhu, G., 1993. Geotectonic implications of the deformation and metamorphism of the Penglai Group of the Jiaobei region, China. Geotectonica et Metallogenia, 17(3): 259-270.

Zhu, G. et al., 1994a. Isotopic constraints on the Palaeozoic evolution of the Shandong Peninsula, N.E. China. Journal of Southeast Asian Earth Sciences, 9(3): 241-248.

Zhu, G., Xu, J., Fitches, W.R., Fletcher, C.J.N., 1994b. Isotropic ages of the Penglai Group in the Jiaobei belt and their geotectonoic implication. Acta Geologica Sinica, 68(2): 158-172.

Zhu, G. et al., 2005. $^{40}Ar/^{39}Ar$ dating of strike-slip motion on the Tan-Lu fault zone, East China. Journal of Structural Geology, 27(8): 1379-1398.

Zhu, G. et al., 2009. Syn-collisional transform faulting of the Tan-Lu fault zone, East China. International Journal of Earth Sciences, 98(1): 135-155.

Zhu, G., Niu, M., Xie, C., Wang, Y., 2010. Sinistral to normal faulting along the Tan - Lu Fault Zone: Evidence for geodynamic switching of the east China continental margin. The Journal of Geology, 118(3): 277-293.

Zhu, G., Jiang, D., Zhang, B., Chen, Y., 2012a. Destruction of the eastern North China Craton in a backarc setting: Evidence from crustal deformation kinematics. Gondwana Research, 22(1): 86-103.

Zhu, K.-Y., Li, Z.-X., Xu, X.-S., Wilde, S.A., 2014. A Mesozoic Andean-type orogenic cycle in southeastern China as recorded by granitoid evolution. American Journal of Science, 314(1): 187-234.

Zhu, R. et al., 2012b. Destruction of the North China Craton. Science China Earth Sciences, 55(10): 1565-1587.

Zong, K. et al., 2010a. In situ U-Pb dating and trace element analysis of zircons in thin sections of eclogite: Refining constraints on the ultra high-pressure metamorphism of the Sulu terrane, China. Chemical Geology, 269(3-4): 237-251.

Zong, K. et al., 2010b. Melting-induced fluid flow during exhumation of gneisses of the Sulu ultrahigh-pressure terrane. Lithos, 120(3–4): 490-510.

APPENDICES

Appendix Table 4.1 SHRIMP zircon U-Pb results for samples from the Sulu UHP belt

Spot	U (ppm)	Th (ppm)	Th/U	$^{206}Pb_c$ (%)	Corrected isotope ratios						Isotope age (Ma)			
					$^{207}Pb/^{206}Pb$	1σ (%)	$^{207}Pb/^{235}U$	1σ (%)	$^{206}Pb/^{238}U$	1σ (%)	$^{207}Pb/^{235}U$	1σ	$^{206}Pb/^{238}U$	1σ
10SD033A, Granitic gneiss														
1	202	123	0.63	1.25	0.0663	3.29	1.07	3.4	0.1166	0.9	737	18	711	6
2	218	182	0.86	-0.19	0.0686	1.63	1.16	1.9	0.1232	0.9	784	10	749	6
3	285	296	1.07	0.08	0.0648	1.23	1.11	1.5	0.1243	0.8	758	8	755	6
4R	1104	74	0.07	0.2	0.0536	1.61	0.27	1.8	0.0368	0.8	244	4	233	2
4C	203	150	0.76	0.16	0.0623	1.81	1.05	2	0.1219	0.9	727	11	741	6
5	322	214	0.69	0.02	0.0638	1.14	1.08	1.4	0.1229	0.8	744	7	747	6
6	877	68	0.08	0.1	0.0504	1.68	0.24	1.8	0.0349	0.6	220	4	221	1
6C	238	218	0.95	0.07	0.0644	1.44	1.08	1.7	0.122	0.9	745	9	742	6
7	223	209	0.97	0.17	0.0644	2.37	1.12	2.5	0.126	0.9	763	14	765	6
8	207	165	0.83	0.04	0.0642	1.43	1.09	1.7	0.1227	0.9	747	9	746	6
9	251	185	0.76	0.07	0.0657	1.38	1.15	1.6	0.1265	0.9	775	9	768	6
10	289	297	1.06	0.11	0.0654	1.32	1.15	1.5	0.1276	0.8	778	8	774	6
11R	685	44	0.07	-0.21	0.0571	1.75	0.35	1.9	0.0442	0.7	303	5	279	2
11C	356	211	0.61	0.02	0.0652	1.13	1.01	1.4	0.1124	0.8	709	7	687	5
12	378	531	1.45	-0.04	0.0648	1.01	1.13	1.3	0.127	0.8	770	7	771	5
13	223	179	0.83	0.07	0.0659	1.41	1.13	1.7	0.1245	0.9	768	9	756	6
14	278	191	0.71	0.06	0.0638	1.34	1.01	1.6	0.1144	0.8	707	8	698	5

15C	261	224	0.88	0.04	0.0657	1.38	0.98	1.6	0.1084	0.9	695	8	664	5
15R	1412	103	0.08	0.17	0.057	1.20	0.38	1.6	0.0485	1.1	328	5	305	3
16C	245	255	1.07	0.16	0.0634	1.58	1.09	1.8	0.1244	0.9	747	10	756	6
17C	391	293	0.77	0.13	0.0634	1.32	0.94	1.5	0.1076	0.8	674	8	659	5
17R	1074	24	0.02	0.21	0.0494	1.74	0.24	1.8	0.0355	0.6	220	4	225	1
18	973	20	0.02	0.16	0.0506	1.78	0.25	1.9	0.0358	0.6	226	4	227	1
19	250	323	1.33	0.06	0.0656	1.34	1.14	1.6	0.1256	0.9	771	9	763	6
20	316	303	0.99	0	0.065	1.05	1.11	1.3	0.1234	0.8	757	7	750	6
21	356	177	0.52	0.4	0.0648	1.73	0.62	2.1	0.0698	1.2	492	8	435	5
22	1671	32	0.02	-0.02	0.0504	1.03	0.25	1.2	0.0365	0.6	230	2	231	1
23	954	18	0.02	0.09	0.0503	1.59	0.25	1.7	0.0357	0.6	224	3	226	1
23C	283	251	0.92	0.06	0.0646	1.37	1.12	1.6	0.1261	0.8	764	9	766	6
24	272	233	0.89	0.03	0.0646	2.59	0.91	2.7	0.1027	0.8	659	13	630	5
25	456	230	0.52	0.06	0.0647	1.05	1.12	1.3	0.1254	0.7	763	7	762	5
10JD06B, Granite														
01R	153	35	0.24	0.44	0.0513	5.74	0.18	5.9	0.0256	1.3	169	9	163	2
02R	294	31	0.11	1.26	0.0429	7.66	0.14	7.9	0.0245	1.8	137	10	156	3
03R	101	16	0.16	4.46	0.0211	50.0	0.07	50	0.0249	2.2	70.9	34	159	3
04R	140	14	0.11	0.26	0.0562	6.11	0.19	6.4	0.0246	1.9	177	10	157	3
05R	435	3	0.01	0.67	0.0453	4.19	0.16	4.4	0.0264	1.3	155	6	168	2
06R	379	44	0.12	0	0.0512	2.00	0.17	2.3	0.0247	1.1	163	3	157	2
07R	688	135	0.2	0.11	0.0526	1.87	0.18	2.1	0.0247	1	167	3	157	2
07C	54	38	0.73	4.41	0.0184	67.0	0.09	67.3	0.0345	2.2	85	55	218	5
08R	723	160	0.23	0.54	0.0471	3.05	0.17	3.2	0.0255	1	155	5	162	2
09R	378	49	0.13	0.92	0.0444	5.78	0.15	5.9	0.0253	1.1	146	8	161	2
10R	538	109	0.21	0	0.0519	1.60	0.18	1.9	0.0251	1	168	3	160	2
11R	676	145	0.22	0.72	0.0444	3.75	0.16	4	0.0256	1.3	148	5	163	2

12R	354	61	0.18	1.97	0.037	11.0	0.13	11.5	0.025	1.3	122	13	159	2
12C	229	162	0.73	0.27	0.0637	1.60	1.03	3.1	0.1171	2.7	718	16	714	18
13R	252	33	0.14	1.18	0.0438	7.83	0.15	8	0.0249	1.4	142	11	159	2
14R	236	28	0.12	0.68	0.0473	5.77	0.16	5.9	0.025	1.2	154	8	159	2
10SD010, Granite														
1	339	282	0.86	0.66	0.0469	6.56	0.12	6.7	0.0181	1.4	112	7	116	2
2	463	375	0.84	0.22	0.0484	3.66	0.12	3.9	0.0178	1.3	114	4	114	1
3	284	394	1.43	-0.41	0.0555	5.20	0.14	5.4	0.0182	1.4	132	7	116	2
4	342	236	0.71	0.93	0.0433	8.67	0.11	8.8	0.0179	1.4	103	9	115	2
4C	1341	1470	1.13	1.04	0.0524	3.68	0.13	3.9	0.0183	1.4	126	5	117	2
5	292	458	1.62	-0.22	0.0546	4.59	0.14	4.9	0.0183	1.6	131	6	117	2
6	250	429	1.78	1.32	0.0365	14.0	0.09	14.3	0.0185	1.5	90.3	12	118	2
7	459	648	1.46	0.14	0.0477	3.85	0.12	4.1	0.0181	1.3	114	4	116	1
8	318	386	1.25	-0.73	0.0535	6.18	0.13	6.3	0.0177	1.4	124	7	113	2
9	163	202	1.28	3.18	0.0235	44.0	0.05	44.3	0.017	1.9	54.3	23	109	2
10	500	407	0.84	0.39	0.0456	4.93	0.12	5.2	0.0183	1.6	111	5	117	2
11	276	517	1.94	0.84	0.0461	8.36	0.11	8.5	0.0175	1.4	107	9	112	2
12	412	1136	2.85	6.28	0.0052	196	0.01	196.5	0.0122	2	8.8	17	78.3	2
13	653	573	0.91	1.3	0.0373	10.0	0.09	10.3	0.0184	1.3	91.8	9	118	2
14	356	348	1.01	0.83	0.0444	7.67	0.11	7.8	0.0176	1.4	104	8	112	2
15	141	296	2.17	0.42	0.047	12.0	0.12	11.7	0.0182	2	113	13	116	2
16	486	408	0.87	0.37	0.0469	4.59	0.12	4.8	0.0179	1.3	111	5	114	1
17	240	224	0.96	1.31	0.0433	12.0	0.11	12.2	0.0184	2	106	12	117	2
					Corrected isotope ratios						Isotope age (Ma)			
Spot	**U (ppm)**	**Th (ppm)**	**Th/U**	**$^{206}Pb_c$ (%)**	**$^{207}Pb/^{206}Pb$**	**1σ (%)**	**$^{207}Pb/^{235}U$**	**1σ (%)**	**$^{206}Pb/^{238}U$**	**1σ (%)**	**$^{207}Pb/^{206}Pb$**	**1σ**	**$^{206}Pb/^{238}U$**	**1σ**
10JD05, Marble														

1.1	94	53	0.58	0.44	0.1093	1.46	4.81	1.9	0.3194	1.3	1788	27	1787	20
2.1	187	150	0.83	0.29	0.1101	0.84	4.99	1.3	0.3289	0.9	1801	15	1833	15
3.1	623	201	0.33	0.17	0.1107	0.47	4.68	1.1	0.3066	1.0	1811	9	1724	15
4	412	352	0.88	0.11	0.1123	0.47	5.08	0.9	0.3280	0.7	1838	9	1829	12
5.1	165	135	0.85	0.22	0.1118	0.85	4.86	1.3	0.3154	1.0	1829	15	1767	15
6.1	171	81	0.49	0.19	0.1126	0.83	4.56	1.3	0.2939	1.0	1842	15	1661	14
7.1	472	288	0.63	0.13	0.1113	0.52	4.92	1.4	0.3204	1.3	1820	9	1792	21
8.1	102	58	0.59	0.71	0.1061	1.46	4.55	1.9	0.3110	1.2	1733	27	1746	18
9.1	141	124	0.90	0.50	0.1102	1.14	5.09	1.6	0.3353	1.1	1802	21	1864	17
10.1	160	131	0.84	0.62	0.1077	1.95	4.93	2.2	0.3324	1.1	1760	36	1850	17
11.1	302	227	0.77	0.37	0.1100	0.81	4.87	1.9	0.3215	1.7	1799	15	1797	26
12.1	173	95	0.57	0.38	0.1109	1.54	5.13	2.4	0.3356	1.8	1814	28	1865	29
13.1	155	109	0.73	0.74	0.1057	1.47	4.36	1.8	0.2990	1.1	1726	27	1686	16
14.1	131	125	0.99	0.42	0.1096	1.11	5.09	1.6	0.3369	1.1	1792	20	1872	18
15.1	262	14	0.06	4.15	0.0166	49	0.05	49.2	0.0229	1.7			146	2
15.2	285	15	0.05	1.69	0.0389	13	0.12	13.3	0.0232	1.0	-423	347	148	2
16.1	135	70	0.53	0.62	0.1063	1.59	4.20	2.0	0.2866	1.2	1736	29	1625	18
17.1	216	162	0.78	0.17	0.1124	0.80	5.22	1.2	0.3367	0.9	1838	15	1871	15
18.1	887	196	0.23	0.12	0.1103	0.36	4.60	0.7	0.3022	0.6	1804	7	1702	10
19.1	156	60	0.40	0.41	0.1096	1.05	4.87	1.5	0.3225	1.0	1793	19	1802	16

Appendix Table 4.2 $^{40}Ar/^{39}Ar$ results for granites and metamorphic rocks in the Sulu UHP belt

N	Power (W)	^{40}Ar Volt	σ %	^{39}Ar Volt	σ%	^{38}Ar Volt	σ %	^{37}Ar Volt	σ %	^{36}Ar Volt	σ %	% $^{40}Ar^*$	% $^{39}Ar_k$	Age (Ma)	± 2σ (Ma)
Sample: 10JD06B, Horblende,Irradiation disk: I15t40h , J:0.00345700 ±0.00000484, Mass Spec: MAP 215-50, MDF: 1.006309 ±0.003522															
1	56.5	0.10850	0.21	0.00520	0.9	0.00011	9.7	0.01153	4.1	8.563E-06	52.5	98.56	36.63	125.6	3.8
2	56.7	0.06716	0.24	0.00319	1.0	0.00008	8.9	0.00752	5.6	1.543E-06	337.6	100.25	22.46	126.7	6.2
3	57.1	0.07457	0.24	0.00366	1.0	0.00009	5.1	0.00808	6.3	1.137E-05	54.1	96.49	25.75	122.9	6.4
4	57.3	0.04723	0.29	0.00215	1.2	0.00006	8.3	0.00482	7.9	-4.016E-06	155.5	103.52	15.15	131.9	10.5
Sample: 10SD010, Hornblende,Irradiation disk: I12t25h , J:0.00881500 ±0.00002204, Mass Spec: MAP 215-50, MDF: 1.006127±0.0038															
1	63.0	0.09405	0.34	0.00021	14.2	0.00017	5.5	0.00155	202.7	2.298E-04	5.5	27.21	0.02	1303.7	383.2
2	64.0	0.02930	0.97	0.00023	14.2	0.00006	11.2	0.00438	72.2	8.436E-05	13.9	15.32	0.02	295.0	435.6
3	65.0	0.04474	0.62	0.00073	4.6	0.00009	8.5	0.00750	43.3	1.330E-04	9.2	12.69	0.05	120.2	150.9
4	66.0	0.04424	0.34	0.00128	1.9	0.00007	11.2	0.01042	12.4	1.206E-04	9.1	20.62	0.09	110.4	77.3
5	67.0	0.05010	0.32	0.00108	1.7	0.00006	12.6	0.01696	8.9	1.346E-04	8.2	22.63	0.08	160.8	89.5
6	68.2	0.13244	0.15	0.00327	1.0	0.00015	6.6	0.03040	8.0	3.439E-04	3.3	24.40	0.23	151.3	30.8
7	69.2	0.14049	0.15	0.00699	0.7	0.00018	6.0	0.01874	10.0	3.014E-04	4.9	37.07	0.50	114.9	19.1
8	70.2	0.13910	0.12	0.00831	0.6	0.00019	4.1	0.01619	14.0	2.470E-04	3.6	47.97	0.59	123.4	9.7
9	71.0	0.17553	0.18	0.01216	0.6	0.00025	5.6	0.03170	8.5	2.567E-04	5.2	57.86	0.87	128.2	9.8
10	71.8	1.11633	0.06	0.10853	0.4	0.00316	1.6	0.84906	4.6	1.182E-03	2.5	74.80	7.69	118.9	2.8
11	71.9	0.72487	0.12	0.08090	0.5	0.00227	1.6	0.61754	4.6	5.278E-04	3.8	85.44	5.73	118.3	2.7
12	72.0	0.59430	0.08	0.06745	0.4	0.00190	1.7	0.51596	4.7	4.071E-04	3.3	86.87	4.78	118.3	2.3
13	72.2	0.65564	0.06	0.07430	0.4	0.00215	2.1	0.60170	4.7	4.914E-04	3.9	85.36	5.27	116.5	2.7
14	72.4	1.53621	0.06	0.17489	0.4	0.00516	1.3	1.49489	4.6	1.171E-03	2.3	85.45	12.39	116.2	2.0
15	72.6	0.40982	0.04	0.04963	0.5	0.00143	2.7	0.40798	4.7	2.417E-04	4.7	90.79	3.52	116.0	2.6
16	73.0	1.05412	0.05	0.12720	0.4	0.00376	1.1	1.07257	4.6	6.304E-04	2.6	90.73	9.01	116.3	1.8
17	80.0	0.03408	0.25	0.00397	0.9	0.00008	6.4	0.02899	9.5	1.878E-05	43.4	90.71	0.28	120.4	18.6
18	80.5	0.34343	0.11	0.04246	0.4	0.00122	1.9	0.35485	4.7	1.930E-04	8.2	91.94	3.01	115.1	3.6
19	81.3	1.80115	0.05	0.21877	0.4	0.00638	1.1	1.87823	4.6	1.040E-03	2.8	91.56	15.50	116.6	1.8

20	82.0	3.47780	0.04	0.42895	0.4	0.01244	0.9	3.70668	4.6	1.888E-03	2.5	92.78	30.39	116.4	1.7
Sample: 10SD010, Biotite,Irradiation disk: I12t25h , J:0.00881500 ± 0.00002204, Mass Spec: MAP 215-50, MDF: 1.006228± 0.003723															
1	55.5	0.00325	1.65	0.00034	2.2	0.00000	235.9	0.00015	386.3	7.835E-06	61.9	28.43	0.21	42.5	131.7
2	55.9	0.00843	0.99	0.00076	3.0	0.00001	31.7	0.00109	54.2	1.786E-05	23.9	37.81	0.47	65.8	52.0
3	56.6	0.14958	0.17	0.01918	0.6	0.00026	4.4	0.00042	139.6	2.047E-05	28.8	95.93	11.97	115.1	3.1
4	56.8	0.17456	0.12	0.02288	0.5	0.00033	2.3	0.00018	228.3	7.021E-06	66.0	98.80	14.28	115.9	2.2
5	57.0	0.15938	0.14	0.02131	0.6	0.00029	4.0	0.00012	398.9	3.156E-06	175.3	99.41	13.30	114.4	2.7
6	57.4	0.23477	0.13	0.03144	0.5	0.00043	3.4	0.00024	227.5	4.065E-06	168.4	99.48	19.62	114.3	2.2
7	57.5	0.10875	0.12	0.01449	0.8	0.00021	6.2	-0.00049	111.0	3.917E-06	135.0	98.88	9.05	114.2	3.7
8	57.9	0.18366	0.15	0.02466	0.6	0.00036	4.3	0.00011	516.8	9.334E-06	47.1	98.48	15.39	112.9	2.1
9	58.4	0.06386	0.33	0.00865	0.8	0.00011	3.9	-0.00024	260.8	7.484E-07	653.9	99.61	5.40	113.2	5.4
10	58.6	0.08447	0.19	0.01139	0.7	0.00015	5.4	0.00012	418.9	1.487E-07	2915	99.95	7.11	114.1	3.8
11	58.6	0.03762	0.42	0.00513	1.0	0.00006	9.9	-0.00010	628.6	5.264E-06	95.2	95.79	3.20	108.3	9.0
Sample: 10SD069, Biotite,Irradiation disk: I12t25h , J:0.00881500 ± 0.00002204, Mass Spec: MAP 215-50, MDF: 1.006228± 0.003723															
1	56.1	0.14407	0.21	0.01496	0.5	0.00023	2.9	0.00050	153.7	1.136E-04	6.9	76.48	8.51	113.3	4.8
2	56.3	0.14684	0.12	0.01834	0.5	0.00025	3.2	0.00018	377.9	4.065E-05	15.4	91.74	10.43	113.1	3.2
3	56.5	0.19502	0.30	0.02554	0.5	0.00036	4.1	0.00098	70.3	1.915E-05	28.5	97.10	14.52	114.1	2.3
4	56.9	0.15333	0.16	0.02012	0.6	0.00030	3.1	-0.00064	131.7	8.950E-06	70.1	98.22	11.44	115.1	3.1
5	57.1	0.27034	0.12	0.03589	0.4	0.00051	3.6	0.00047	167.0	1.315E-05	36.0	98.56	20.41	114.2	1.5
6	57.3	0.21869	0.29	0.02894	0.5	0.00043	1.6	0.00153	57.2	1.282E-05	31.0	98.30	16.45	114.3	1.8
7	58.2	0.11481	0.21	0.01531	0.5	0.00021	2.7	-0.00029	267.4	2.721E-06	228.1	99.26	8.71	114.5	3.8
8	59.0	0.12446	0.09	0.01678	0.6	0.00025	4.8	-0.00069	119.9	2.081E-06	241.0	99.45	9.54	113.5	2.9
Sample 11LX199B, Muscovite, Irradiation disk: I15t40h , J: 0.00341900 ± 0.00000615, Mass Spec: MAP 215-50, MDF: 1.006253 ± 0.003119															
1	56.3	4.38013	0.02	0.01031	0.5	0.00272	1.6	-0.00019	44.0	1.347E-02	1.3	8.190	5.313	202.6	58.0
2	56.5	2.09638	0.03	0.03277	0.4	0.00099	1.7	-0.00019	46.2	2.965E-03	2.1	57.767	16.893	214.4	6.6
3	56.7	1.73537	0.04	0.04171	0.4	0.00066	3.0	-0.00002	321.5	6.814E-04	2.9	88.275	21.503	213.2	2.2
4	56.9	1.29102	0.07	0.03446	0.3	0.00046	2.7	-0.00002	484.8	3.448E-05	17.4	99.201	17.768	215.5	1.5
5	57.1	1.18148	0.05	0.03127	0.5	0.00040	1.7	0.00004	207.6	1.291E-05	47.9	99.672	16.123	218.2	2.0
6	57.3	0.93079	0.08	0.02424	0.4	0.00033	3.5	-0.00009	103.1	4.668E-06	136.0	99.848	12.498	221.9	2.1
7	57.5	0.17938	0.14	0.00472	1.0	0.00007	9.1	-0.00012	72.3	-5.074E-06	107.6	100.837	2.434	221.9	5.8
8	57.8	0.05633	0.26	0.00150	1.6	0.00002	27.2	-0.00012	64.2	1.493E-06	453.3	99.189	0.773	216.1	16.2

9	58.0	0.05053	0.31	0.00133	2.1	0.00001	29.4	-0.00003	244.4	-1.892E-06	330.3	101.110	0.687	221.9	17.7
10	58.3	0.14575	0.22	0.00394	1.1	0.00005	9.5	0.00001	1560.1	-8.379E-07	757.6	100.170	2.031	215.0	6.9
11	58.7	0.07036	0.29	0.00183	1.4	0.00003	23.0	0.00000	4953.2	4.609E-07	1527.1	99.803	0.944	222.1	13.8
12	59.1	0.03571	0.41	0.00090	2.3	0.00002	25.6	0.00002	555.3	1.166E-05	54.9	90.258	0.463	208.6	25.1
13	59.6	0.05450	0.29	0.00143	1.2	0.00002	29.6	-0.00008	125.6	-5.024E-07	1341.8	100.261	0.738	221.0	16.2
14	60.1	0.08602	0.29	0.00230	1.2	0.00003	16.9	-0.00007	122.8	5.362E-06	125.3	98.130	1.186	213.0	10.7
15	61.0	0.04720	0.37	0.00126	2.2	0.00002	25.9	-0.00006	151.9	-3.281E-06	197.2	102.063	0.647	222.1	19.3
Sample 11LX196, Biotite package, Irradiation disk: I15t40h, J: 0.00341900 ±0.000006, Mass Spec: MAP 215-50, MDF: 1.006302 ±0.003421															
1	62.0	0.29267	0.14	0.00932	0.6	0.00027	4.2	-0.00049	603.6	7.224E-04	2.8	26.287	1.689	50.3	7.9
2	64.0	0.87351	0.06	0.02789	0.4	0.00079	2.1	-0.00106	259.4	2.044E-03	2.0	30.115	5.057	57.4	5.4
3	66.0	1.15164	0.06	0.03429	0.5	0.00092	1.4	-0.00177	187.2	2.475E-03	1.7	35.816	6.217	72.9	4.5
4	67.0	0.72815	0.07	0.02165	0.4	0.00058	3.0	-0.00084	356.3	1.512E-03	1.6	38.003	3.925	77.3	4.1
5	68.0	1.06001	0.04	0.03086	0.4	0.00080	3.0	0.00118	263.7	2.149E-03	1.7	39.466	5.594	81.9	4.2
6	68.5	0.68976	0.07	0.02056	0.4	0.00052	2.6	-0.00234	125.3	1.306E-03	1.9	43.431	3.729	87.9	4.2
7	69.0	0.63178	0.06	0.01879	0.6	0.00047	3.6	-0.00081	358.7	1.230E-03	2.5	41.846	3.406	85.0	5.9
8	69.5	1.32881	0.06	0.03754	0.5	0.00103	1.7	-0.00010	2940.6	2.652E-03	1.9	40.421	6.806	86.4	4.7
9	70.0	1.22180	0.04	0.03437	0.4	0.00095	2.0	-0.00279	100.1	2.451E-03	2.4	40.093	6.231	86.0	6.2
10	70.5	1.54686	0.05	0.04526	0.5	0.00120	1.5	0.00001	62244	3.001E-03	1.5	42.077	8.206	86.8	3.6
11	71.0	2.29135	0.07	0.07049	0.4	0.00177	1.7	0.00024	1255.8	4.204E-03	1.8	45.221	12.779	88.7	3.9
12	71.5	4.36280	0.03	0.14006	0.4	0.00323	0.8	0.00147	222.6	7.402E-03	1.7	49.349	25.394	92.6	3.3
13	72.0	1.56243	0.09	0.05446	0.6	0.00117	1.5	0.00025	1095.5	2.226E-03	1.6	57.456	9.873	99.1	2.6
14	80.0	0.15913	0.19	0.00525	0.6	0.00011	6.3	-0.00003	8927.9	2.530E-04	4.2	52.531	0.952	95.8	7.2
15	82.0	0.04828	0.61	0.00078	3.0	0.00003	20.8	-0.00102	265.0	1.078E-04	11.3	33.160	0.142	122.5	54.4
Sample 10SD062B, Hornblende package, Irradiation disk: I15t40h, J: 0.00357500 ±0.00000501, Mass Spec: MAP 215-50, MDF: 1.006254 ±0.003019															
1	80.0	0.01842	0.56	0.00050	2.8	0.00000	256.6	0.00000	535.4	8.664E-06	159.6	85.956	7.711	193.9	96.5
2	80.5	0.02336	0.67	0.00066	3.2	0.00001	113.7	0.00001	256.9	4.417E-06	319.7	94.356	10.246	202.6	74.4
3	81.0	0.03584	0.69	0.00099	2.4	0.00001	61.5	0.00001	147.8	1.051E-05	137.4	91.247	15.288	201.5	51.2
4	81.5	0.06850	0.32	0.00188	1.8	0.00003	25.5	0.00005	50.5	2.697E-05	53.2	88.248	29.033	196.4	27.3
5	82.0	0.09025	0.24	0.00245	1.2	0.00003	23.9	0.00004	61.5	2.640E-05	53.6	91.268	37.722	205.5	20.4

Appendix Table 4.3 ZFT ages for samples in the Sulu UHP belt

Sample	N	ρ_s	N_s	ρ_i	N_i	ρ_d	N_d	P (χ2)(%)	Uran.	U rel %	Central Age (Ma)	±σ
11LX178B	25	233.720	1109	113.172	537	10.265	4488	27	402.4	24	128	8
11LX199B	38	86.641	888	64.883	665	10.176	4488	100	290.2	42	82	5
11LX209	25	156.440	772	106.590	526	10.445	4488	99	373.0	26	93	6
10JD06B	28	206.232	1096	143.008	760	9.727	4488	90	536.6	21	85	4
11LX094B	25	80.643	750	52.472	488	10.893	4488	100	174.8	29	101	6
10SD061A	25	241.517	1146	150.053	712	9.817	4488	66	557.9	20	96	5
10SD010	25	148.334	732	105.171	519	12.596	4488	100	311.1	26	108	7
10SD033A	50	180.506	1713	111.064	1054	12.775	4488	80	317.3	20	125	6

N= nubmer of dated apatite grains; ρs(ρi) = spontaneous (induced) track densities (× 10^5 tracks/cm^2); N_s (N_i) = number of counted spontaneous (induced) tracks; ρd = track density of dosimeter (× 10^5 tracks/cm^2); Nd = number of tracks counted on dosimeter; P(χ2) = probability of obtaining chi-square value for N degree of freedom; Uran. = U concentration (ppm); U rel = relative error of U concentration. Glass dosimeter CN-1 is used for zircon samples and the zeta value is 122.01 ± 1.73 (Operator: Martin Danišík).

Appendix Table 4.4 Zircon (U-Th)/He data for samples in the Sulu UHP belt

Sample ID	^{232}Th (ng)	±σ (%)	^{238}U (ng)	±σ (%)	^{147}Sm (ng)	±σ (%)	eU ppm	He (ncc)	±σ (%)	TAU (%)	Th/U	Ft	Raw age (Ma)	±1σ (Ma)	Cor. age (Ma)	±1σ (Ma)	Rs	Alpha dose α/g
10SD41B	0.718	1.4	0.935	1.8	0.003	35.1	94	17.3	1.2	2.0	0.76	0.64	127.7	2.5	199	11	36.2	2.8E+17
10SD41B	0.719	1.4	0.725	1.9	0.005	8.8	51	13.0	1.2	1.9	0.98	0.69	118.1	2.3	172	9	41.7	1.5E+17
10SD41B	2.257	1.4	1.921	1.8	0.012	4.5	59	41.9	1.2	1.9	1.17	0.77	138.8	2.6	180	10	56.7	1.8E+17
10SD41B	1.300	1.4	1.080	1.8	0.005	8.6	34	21.6	1.2	1.9	1.19	0.77	126.9	2.4	165	9	56.7	8.3E+16
10SD41B	3.237	1.4	1.566	1.9	0.022	3.3	65	37.1	1.2	1.8	2.05	0.76	129.8	2.3	171	9	55.0	1.6E+17
Mean age ±2SE (Ma), MSWD = 1.7, P = 0.14															**176**	**8**		
10SD33A	0.217	3.7	1.572	2.8	n/a	n/a	777	22.2	2.5	3.7	0.14	0.72	111.1	4.1	155	10	44.7	1.9E+17
10SD33A	0.456	3.8	1.325	2.8	n/a	n/a	842	21.8	2.5	3.6	0.35	0.69	123.9	4.5	180	11	40.9	2.4E+17
10SD33A	0.359	3.7	1.897	2.7	n/a	n/a	763	29.8	2.5	3.6	0.19	0.73	122.1	4.4	167	10	47.6	2.1E+17
10SD33A	0.684	3.7	2.140	2.7	n/a	n/a	1087	36.0	2.5	3.6	0.33	0.72	127.3	4.6	177	11	45.3	3.1E+17
10SD33A	0.753	3.7	1.630	2.8	n/a	n/a	563	27.9	2.5	3.6	0.47	0.75	125.6	4.5	168	10	51.2	1.6E+17
Mean ±2SE (Ma), MSWD = 0.93, P = 0.45															**168**	**9**		
10SD010	2.353	3.7	1.759	2.8	n/a	n/a	1051	19.2	2.5	3.4	1.36	0.72	68.0	2.3	95	6	46.3	1.6E+17
10SD010	5.871	3.7	4.897	2.8	n/a	n/a	2241	55.9	2.5	3.4	1.22	0.77	72.7	2.5	94	6	57.0	2.4E+17
10SD010	2.400	3.7	1.872	2.8	n/a	n/a	1624	16.6	2.5	3.4	1.31	0.72	55.9	1.9	78	5	46.8	1.3E+17
10SD010	2.323	3.7	1.353	2.8	n/a	n/a	1224	15.5	2.5	3.4	1.75	0.71	66.9	2.3	94	6	46.4	1.2E+17
10SD010	1.180	3.7	1.004	2.9	n/a	n/a	1360	8.2	1.4	2.7	1.20	0.67	52.7	1.4	78	4	40.3	1.0E+17
11LX209	1.454	4.0	1.878	2.9	0.010	23.9	919	18.2	1.2	2.8	0.77	0.78	67.0	1.9	86	5	58.5	8.2E+16

11LX209	2.026	4.0	1.448	2.9	0.008	19.4	574	16.1	1.2	2.7	1.39	0.79	68.6	1.8	87	5	63.1	6.0E+16
11LX209	0.934	4.0	0.703	2.9	0.000	14.3	403	6.6	1.2	2.7	1.32	0.74	58.2	1.6	78	4	51.5	3.7E+16
11LX209	1.156	4.0	0.963	2.9	0.010	26.8	726	10.7	1.2	2.7	1.19	0.79	70.8	1.9	89	5	63.3	3.8E+16
11LX209	1.777	4.0	1.277	2.9	0.001	22.8	945	18.1	1.2	2.7	1.38	0.77	87.1	2.3	113	6	57.8	8.5E+16
Mean (of former four ages) ± 2SE (Ma), MSWD = 1.08, P = 0.36															**85**	**5**		
10SD069	0.749	3.7	2.605	2.8	n/a	n/a	756	21.6	2.5	3.7	0.29	0.76	63.6	2.3	84	5	52.1	1.1E+17
10SD069	0.559	3.7	1.237	2.8	n/a	n/a	643	10.4	2.5	3.6	0.46	0.69	62.2	2.2	90	6	41.3	9.0E+16
10SD069	0.966	3.7	4.431	2.9	n/a	n/a	1927	38.0	2.5	3.7	0.22	0.70	66.6	2.5	95	6	42.1	2.9E+17
10SD069	1.148	3.6	1.875	2.8	n/a	n/a	957	17.1	2.5	3.6	0.62	0.69	65.2	2.3	94	6	41.6	1.4E+17
10SD069	1.057	3.6	1.438	2.8	n/a	n/a	761	12.4	2.5	3.5	0.75	0.68	60.1	2.1	88	5	40.7	1.0E+17
Mean ± 2SE (Ma), MSWD = 0.70, P = 0.59															**90**	**5**		
10JD05	1.370	3.7	2.098	2.7	n/a	n/a	523	22.3	2.5	3.5	0.67	0.78	75.4	2.6	97	6	57.5	8.9E+16
10JD05	1.266	3.7	2.187	2.7	n/a	n/a	386	21.8	2.5	3.5	0.59	0.79	71.5	2.5	91	6	60.5	6.2E+16
10JD05	1.051	3.7	2.349	2.7	n/a	n/a	561	23.4	2.5	3.6	0.46	0.78	73.7	2.6	95	6	57.2	9.3E+16
10JD05	0.748	3.7	1.546	2.7	n/a	n/a	698	15.8	2.5	3.5	0.49	0.71	75.0	2.6	105	6	44.7	1.2E+17
10JD05	0.682	3.7	1.471	2.7	n/a	n/a	411	14.8	2.5	3.5	0.47	0.77	74.3	2.6	96	6	56.7	6.9E+16
Mean ± 2SE (Ma), MSWD = 0.74, P = 0.57															**96**	**5**		
10JD06B	0.383	4.0	3.357	2.9	0.002	27.8	439	29.7	1.2	3.1	0.11	0.83	70.4	2.2	85	5	73.5	5.4E+16
10JD06B	0.775	4.0	3.071	2.9	0.011	15.0	576	32.8	1.2	3.0	0.25	0.83	82.2	2.5	99	6	75.3	5.8E+16
10JD06B	0.402	4.0	3.038	2.9	0.005	30.2	357	26.2	1.2	3.1	0.13	0.86	68.5	2.1	80	5	89.2	2.7E+16
10JD06B	0.374	4.0	2.715	2.9	0.005	20.4	463	25.8	1.2	3.1	0.14	0.83	75.1	2.3	91	5	72.7	5.2E+16
10JD06B	0.501	4.0	3.363	3.0	0.008	26.3	696	34.4	1.2	3.1	0.15	0.79	80.6	2.5	101	6	61.6	9.6E+16
Mean (of former four ages)± 2SE (Ma), MSWD = 2.4, P = 0.065															**88**	**5**		
10SD061A	0.646	4.0	4.302	2.9	0.005	37.6	1454	40.9	1.2	3.1	0.15	0.81	75.1	2.3	93	5	65.1	1.2E+17
10SD061A	1.272	4.0	1.441	2.9	0.004	33.6	1585	16.1	1.2	2.8	0.88	0.70	75.8	2.1	108	6	43.3	1.6E+17

10SD061A	0.322	4.0	2.205	3.0	0.005	39.1	1701	21.2	1.2	3.1	0.14	0.72	76.1	2.4	106	6	44.6	2.0E+17
Mean ±2SE (Ma), MSWD = 2, P = 0.13															**102**	**7**		
11LX199B	0.219	1.5	0.197	1.9	0.002	13.9	15	1.8	1.3	2.0	1.10	0.69	57.8	1.1	83	4	42.8	2.0E+16
11LX199B	0.234	1.5	0.154	1.9	0.003	12.0	14	1.7	1.3	1.9	1.51	0.68	67.4	1.3	99	5	41.6	2.0E+16
11LX199B	0.126	1.5	0.139	1.9	0.001	16.0	12	1.4	1.3	2.1	0.90	0.69	67.3	1.4	98	5	41.4	1.8E+16
11LX199B	0.187	1.5	0.231	1.9	0.004	26.4	12	2.2	1.3	2.0	0.81	0.73	66.8	1.4	91	5	48.4	1.8E+16
11LX199B	0.435	1.4	0.328	1.9	0.002	13.7	26	3.9	1.3	1.9	1.32	0.70	73.2	1.4	105	6	43.6	4.1E+16
11LX199B	0.401	1.4	0.206	1.9	0.008	5.5	16	2.7	1.3	1.9	1.94	0.70	74.0	1.4	105	6	44.7	2.8E+16
Mean (of former four ages) ±2SE (Ma), MSWD = 2.3, P = 0.078															**92**	**5**		
Mean (of latter five ages) ±2SE (Ma), MSWD = 2.3, P = 0.078															**99**	**5**		
11LX094B	0.384	1.5	0.335	1.9	0.002	13.3	27	4.3	1.2	1.9	1.14	0.66	82.1	1.6	125	7	38.3	3.8E+16
11LX094B	0.583	1.4	0.272	1.9	0.003	13.5	15	4.0	1.2	1.8	2.12	0.72	80.5	1.5	113	6	46.8	3.3E+16
11LX094B	0.797	1.4	0.478	1.9	0.006	6.9	14	6.7	1.2	1.8	1.65	0.75	82.1	1.5	110	6	52.4	4.0E+16
11LX094B	0.652	1.4	0.353	2.0	0.004	11.3	17	4.9	1.2	1.9	1.83	0.76	79.8	1.5	106	6	54.5	2.5E+16
11LX094B	0.529	1.4	0.393	1.9	0.002	11.1	17	5.2	1.2	1.9	1.34	0.72	82.9	1.5	114	6	47.7	3.7E+16
11LX094B	0.852	1.4	0.354	2.1	0.004	9.0	17	6.2	1.2	1.8	2.39	0.71	91.3	1.7	128	7	46.5	3.0E+16
Mean ±2SE (Ma), MSWD = 1.9, P = 0.083															**115**	**5**		

Appendix Table 4.5 Apatite fission-track data for samples in the Sulu UHP belt

Sample ID	N	ρ_s	N_s	ρ_i	N_i	ρ_d	N_d	P(χ2) (%)	Central Age Ma	± σ Ma	N(L)	MTL µm	C-axis projected MTL µm	SD µm	SE µm	Dpar µm	SD µm
10SD010	25	3.984	358	14.877	1337	12.705	5369	99.6	53	3						2.17	0.43
11LX199B	25	0.472	105	0.988	220	7.043	3108	100.0	52	6						2.3	0.25
11LX209	25	1.715	206	3.562	428	7.395	3108	100.0	55	5						2.04	0.25
10JD06B	25	2.859	548	6.375	1222	6.984	3108	100.0	49	3						2.26	0.39
10SD061A	25	4.079	420	7.731	796	6.397	3108	99.6	53	3						2.98	1.00
11LX094B	25	8.068	281	13.437	468	5.810	3108	99.1	54	4						2.08	0.27
11LX178B	25	6.614	467	13.922	983	6.162	3108	99.8	46	3	100	12.7	13.94	1.13	0.11	1.65	0.20
10SD033A	25	2.921	324	9.14	1014	12.538	5369	69.57	62	4						1.75	0.06

N= nubmer of dated apatite grains; ρs(ρi) = spontaneous (induced) track densities (× 10^5 tracks/cm^2); N_s (N_i) = number of counted spontaneous (induced) tracks; ρd = track density of dosimeter (× 10^5 tracks/cm^2); Nd = number of tracks counted on dosimeter; P(χ2) = probability of obtaining chi-square value for N degree of freedom; Dpar = average etch pit diameter of fission tracks; SD = standard deviation; SE= standard error; N(L) = number of confined horizontal tracks counted; MTL = mean of track length. Glass dosimeter CN-5 is used for apatite samples and the zeta value is 312.72 ± 3.45 (Operator: Martin Danišík).

Appendix Table 4.6 Apatite (U-Th)/He data for samples in the Sulu UHP belt

Sample ID	^{232}Th (ng)	±σ (%)	^{238}U (ng)	±σ (%)	^{147}Sm (ng)	±σ (%)	eU ppm	He (ncc)	±σ (%)	TAU (%)	Th/U	Ft	Raw age (Ma)	±1σ (Ma)	Cor. age (Ma)	±1σ (Ma)	Rs (μm)
10JD05	0.172	3.8	0.219	4.2	n/a	n/a	11	0.9	2.0	0.8	3.9	0.85	27	1	32	3	98.8
10JD05	0.126	3.8	0.228	4.2	n/a	n/a	10	1.0	2.0	0.5	4.1	0.85	31	1	37	2	101.9
10JD05	0.111	3.8	0.232	4.1	n/a	n/a	11	0.9	2.1	0.5	4.2	0.84	30	1	35	2	97.2
10JD05	0.070	3.8	0.138	3.9	0.239	0.8	9	0.6	1.4	0.5	2.9	0.82	30	1	37	2	
10JD05	0.150	3.8	0.200	3.9	0.279	0.6	12	0.9	1.4	0.7	3.0	0.84	30	1	36	2	
10JD05	0.068	3.8	0.106	3.9	0.142	0.7	7	0.5	1.4	0.6	3.0	0.83	31	1	37	2	
10JD05	0.048	3.8	0.112	3.9	0.228	0.7	9	0.5	1.4	0.4	2.8	0.81	32	1	40	2	
Mean age ±2SE (Ma), MSWD = 0.67, P = 0.67															**36**	**2**	
10JD06B	0.005	4.4	0.044	4.0	0.031	1.4	19	0.1	1.2	0.1	3.6	0.72	25	1	35	4	52.5
10JD06B	0.011	4.0	0.072	4.0	0.060	1.0	23	0.2	1.2	0.2	3.5	0.76	27	1	35	4	61.5
10JD06B	0.015	3.9	0.116	4.0	0.067	1.0	38	0.5	1.2	0.1	3.6	0.78	34	1	44	5	68.1
10JD06B	0.004	5.0	0.043	4.0	0.021	1.4	19	0.1	1.2	0.1	3.8	0.73	22	1	30	3	55.6
10JD06B	0.016	3.9	0.150	4.0	0.065	0.8	38	0.7	1.2	0.1	3.6	0.78	40	1	51	5	68.3
Mean age (former four ages) ±2SE (Ma), MSWD = 2, P = 0.12															**35**	**4**	
10SD010	0.393	3.8	0.078	4.0	n/a	n/a	68	0.7	2.4	5.0	3.7	0.67	31.7	1.2	48	3	48.0
10SD010	0.120	3.8	0.016	4.0	n/a	n/a	37	0.1	3.3	7.7	4.3	0.60	23.1	1.0	42	3	36.0
10SD010	0.251	3.8	0.034	4.5	n/a	n/a	31	0.3	3.0	7.3	4.1	0.64	29.8	1.2	47	3	44.5
Mean age ±2SE (Ma), MSWD = 1.11, P = 0.33															**45**	**3**	
10SD033A	0.975	3.8	0.396	4.1	n/a	n/a	21	5.6	1.6	2.4	3.3	0.84	72.9	2.4	86	5	100.9

10SD033A	0.797	3.8	0.382	4.4	n/a	n/a	19	4.7	1.7	2.1	3.4	0.87	67.2	2.3	79	5	101.7
10SD033A	1.034	3.8	0.417	4.4	n/a	n/a	23	5.1	1.7	2.5	3.3	0.85	63.8	2.1	74	4	110.6
10SD033A	1.013	3.8	0.384	5.3	n/a	n/a	19	4.6	1.7	2.6	3.5	0.86	60.9	2.1	71	4	109.6
Mean age ± 2SE (Ma), MSWD = 1.9, P = 0.12															**77**	**5**	
10SD069	0.040	3.8	0.028	4.3	n/a	n/a	9	0.1	2.2	1.4	4.0	0.74	29.3	1.1	40	3	58.6
10SD069	0.109	3.8	0.061	4.5	n/a	n/a	7	0.4	2.5	1.8	7.3	0.81	41.0	1.6	51	3	82.7
10SD069	0.025	3.9	0.007	4.1	n/a	n/a	5	0.1	6.8	3.5	6.1	0.68	38.0	2.8	56	5	49.4
10SD069	0.025	3.9	0.008	4.2	n/a	n/a	6	0.1	5.4	3.1	3.2	0.66	43.6	2.7	66	5	46.6
10SD069	0.023	3.8	0.010	4.0	0.223	0.7	5	0.1	1.3	2.3	1.6	0.71	28.5	0.4	40	2	
11LX094B	0.073	3.8	0.042	4.0	0.028	1.3	87	0.1	1.2	1.7	3.1	0.59	13.2	0.4	23	2	37.6
11LX094B	0.184	3.8	0.080	4.0	0.066	0.9	135	0.4	1.2	2.3	2.9	0.62	24.5	0.7	39	4	41.6
11LX094B	0.072	3.8	0.039	4.0	0.020	1.4	62	0.1	1.2	1.8	3.1	0.64	15.1	0.5	24	2	43.1
11LX199B	0.001	21.4	0.027	4.0	0.048	1.1	9	0.2	1.2	0.0	2.6	0.83	51.1	1.3	61	6	90.0
11LX199B	0.004	5.2	0.028	4.0	0.062	1.0	6	0.2	1.2	0.1	2.2	0.86	68.8	1.5	80	8	103.5
11LX199B	0.000	105.1	0.031	4.6	0.049	2.0	7	0.1	1.2	0.0	3.8	0.78	20.8	0.8	27	3	68.1
11LX199B	0.002	7.3	0.030	4.0	0.055	1.1	6	0.1	1.2	0.1	2.9	0.81	35.6	1.0	44	5	77.3
No mean age due to diverse grain size																	
11LX209	0.080	3.8	0.026	4.0	0.088	0.9	33	0.1	1.2	3.1	2.3	0.68	26.4	0.6	39	4	49.2
11LX209	0.132	3.8	0.036	4.0	0.095	0.8	32	0.3	1.2	3.7	2.4	0.71	31.4	0.7	44	5	55.2
11LX209	0.268	3.8	0.068	4.2	0.186	1.5	23	0.6	1.2	3.9	2.3	0.78	36.8	0.9	47	5	72.9
11LX209	0.725	3.8	0.104	4.1	0.383	0.9	46	1.5	1.2	6.9	2.2	0.81	45.1	1.0	56	6	83.4
Mean age ± 2SE (Ma), MSWD = 1.9, P = 0.12															**45**	**5**	

eU = effective Uranium concentration = U + 0.235 × Th; TAU = total analytical uncertainty; Ft = alpha recoil correction factor; Rs = effective radius of apatite grain.

Appendix Table 4.7 Compilation of U-Pb, Ar/Ar, (U-Th)/He results in the Sulu UHP-HP belt

Unit	Sample	Rock type	Mineral	Method	Age (Ma)	error	Locality	References
NUHP	SU11a	Weakly foliated hypabyssal intrusion	K-feldspar	40Ar/39Ar	142-110		30 Km North Of Donghai	*Webb et al.* (2006)
NUHP	SU17	Pseudotachylite	whole rock	40Ar/39Ar	92	1	Lanshan	*Webb et al.* (2006)
NUHP	SU33		muscovite	40Ar/39Ar			Taoyuan	*Webb et al.* (2006)
NUHP	SU45	Quartzofeldspathic gneiss	K-feldspar	40Ar/39Ar	201-102		An Island To North Of Weihai	*Webb et al.* (2006)
NUHP	MH89-26	Mylonite	K-feldspar	40Ar/39Ar	121-96		Sishan-Miaoshan, Rizhao	*Chen et al.* (1992)
NUHP	MH89-37	Amphibolite	hornblende	40Ar/39Ar	213	3	East Of Weihai	*Chen et al.* (1992)
NUHP	MH89-14		biotite	40Ar/39Ar	218	3	Shuhu Village On Tanlu Fault	*Chen et al.* (1992)
NUHP	MH89-14		muscovite	40Ar/39Ar	209	3	Shuhu Village On Tanlu Fault	*Chen et al.* (1992)
NUHP	P23-TW1	Mylonite	muscovite	40Ar/39Ar	159	2.5	Jiaonan	*Song and Lu* (1997)
NUHP	95YZB1	Foliated granite emplaced at 160 Ma	K-feldspar	40Ar/39Ar	104-73		Yazi,Rushan	*Hacker et al.* (2009)
NUHP	95CLSW	Deformed granite but by undeformed dike	K-feldspar	40Ar/39Ar	149-89		South Of Junan	*Hacker et al.* (2009)
NUHP	99SMC06b	Biotite-K-feldspar gneiss	biotite	40Ar/39Ar	149-81		Wendeng	*Hacker et al.* (2009)
NUHP	99DPC2	Granitic orthogneiss	biotite	40Ar/39Ar	126-89		Lanshan	*Hacker et al.* (2009)
NUHP	94YK46	Phengite-K-feldspar granitic gneiss	K-feldspar	40Ar/39Ar	193-107		Yangkou	*Hacker et al.* (2009)
NUHP	94YK46	Phengite-K-feldspar granitic gneiss	muscovite	40Ar/39Ar	209-182		Yangkou	*Hacker et al.* (2009)
NUHP	SD04A	Gneiss	K-feldspar	40Ar/39Ar	111	1.7	Yangkou	*Lin et al.* (2005)
NUHP	SD08A	Gneiss	K-feldspar	40Ar/39Ar	119	1.8	Taohang	*Lin et al.* (2005)
NUHP	SD20C	Gneiss	biotite	40Ar/39Ar	119.6	1.7	Rizhao	*Lin et al.* (2005)
NUHP	SD20D	Gneiss	K-feldspar	40Ar/39Ar	109	1.7	Rizhao	*Lin et al.* (2005)
NUHP	94WHB05	Biotite-K-feldspar augen	biotite	40Ar/39Ar	161-96		Weihai	*Hacker et al.* (2009)

		gneiss						
NUHP	1120807	Granitic mylonite	muscovite	40Ar/39Ar	192	0.5	Zetou	*Zhang et al.* (2007)
NUHP	1121101	Granitic gneiss	biotite	40Ar/39Ar	124	0.2	Xilongjia	*Zhang et al.* (2007)
NUHP	121504	Quartzofeldspathic mylonite	biotite	40Ar/39Ar	123	0.3	Wanggezhuang	*Zhang et al.* (2007)
NUHP	11LX196	Granitic gneiss	biotite	40Ar/39Ar	110-40		Shijuzi	This study
NUHP	10SD062B	Amphibolite	hornblende	40Ar/39Ar	202	15	Weihai	This study
NUHP	11LX199B	Granitic gneiss	muscovite	40Ar/39Ar	216	4	Lanshan	This study
NUHP	11LX199B	Granitic gneiss	zircon	(U-Th)/He	96.9	8.5	Lanshan	This study
NUHP	10SD061A	Grantic gneiss	zircon	(U-Th)/He	102.6	8.6	Laohushan	This study
NUHP	11LX178B	Foliated granite	zircon	(U-Th)/He	173	20.3	Wulian	This study
NUHP	94YK46	Granitic gneiss	zircon	ICP	216.3	2.4	Yangkou	*Hacker et al.* (2006)
NUHP	SL5	Garnet-bearing orthogneiss	zircon	SHRIMP	228	2	Lanshan	*Liu et al.* (2009b)
NUHP	SL5	Garnet-bearing orthogneiss	zircon	SHRIMP	215	3	Lanshan	*Liu et al.* (2009b)
NUHP	B4	Biotite-bearing paragneiss	biotite	40Ar/39Ar	215	0.5	Lanshan	*Liu et al.* (2009b)
NUHP	94WHB05	Augen gneiss	zircon	ICP	223.7	4.9	Weihai	*Hacker et al.* (2006)
NUHP	SL3	Garnet-bearing orthogneisses	zircon	SHRIMP	217	3	Weihai	*Liu et al.* (2009b)
NUHP	SL3	Garnet-bearing orthogneisses	zircon	SHRIMP	202	2	Weihai	*Liu et al.* (2009b)
NUHP	B6	Biotite-bearing paragneiss	biotite	40Ar/39Ar	201	0.6	Weihai	*Liu et al.* (2009b)
NUHP	WH17	Grt-amphibolite	zircon	SHRIMP	230	2	Weihai	*Liu et al.* (2009c)
NUHP	SDY-16	Amphibolized peridotite	zircon	SHRIMP	221	12	Bonan Village, Boyu County	*Yang et al.* (2003)
NUHP	SL4	Garnet-bearing orthogneisses	zircon	SHRIMP	217	4	Taohang	*Liu et al.* (2009b)
NUHP	SL4	Garnet-bearing orthogneisses	zircon	SHRIMP	202	4	Taohang	*Liu et al.* (2009b)
NUHP	SL6	Garnet-bearing orthogneisses	zircon	SHRIMP	218	2	Linshu	*Liu et al.* (2009b)

NUHP	SL6	Garnet-bearing orthogneisses	zircon	SHRIMP	202	2	Linshu	*Liu et al.* (2009b)
NUHP	B5	Biotite-bearing paragneiss	biotite	40Ar/39Ar	203	0.6	Linshu	*Liu et al.* (2009b)
NUHP	SL7	Biotite-bearing orthogneiss	zircon	SHRIMP	218	3	Rizhao	*Liu et al.* (2009b)
NUHP	SL7	Biotite-bearing orthogneiss	zircon	SHRIMP	202	2	Rizhao	*Liu et al.* (2009b)
NUHP	CJ4D	Garnet clinopyroxenite	zircon	SHRIMP	215	2	Rizhao Hujialing	*Zhao et al.* (2007a)
NUHP	DPC2	Layered granitic orthegneiss	zircon	ICP	204.7	2.6	Suoluoshu	*Hacker et al.* (2006)
NUHP	XG13	Garnet peridotite	zircon	SHRIMP	245	8	Xugou	*Liu et al.* (2006a)
NUHP	XG09	Eclogite	zircon	SHRIMP	242	3	Xugou	*Liu et al.* (2006a)
NUHP	XG07	Orphyroblastic eclogite	zircon	SHRIMP	224	3	Xugou	*Liu et al.* (2006a)
NUHP	SD01	Eclogite	zircon	LA-ICP-MS in thin section	230	4	Xugou	*Zong et al.* (2010)
NUHP	SD01	Eclogite	zircon	LA-ICP-MS in thin section	209	4	Xugou	*Zong et al.* (2010)
NUHP	CD01	Eclogite	zircon	SHRIMP	227	3	Rongcheng	*Liu et al.* (2006a)
NUHP	CD01	Eclogite	zircon	SHRIMP	241	5	Rongcheng	*Liu et al.* (2006a)
NUHP	LJ32	Eclogite	zircon	SHRIMP	243	1.4	Junan	*Liu et al.* (2006a)
NUHP	LJ32	Eclogite	zircon	SHRIMP	227.6	3.7	Junan	*Liu et al.* (2006a)
NUHP	MCK7	Eclogite	zircon	SHRIMP	225	2	Macaokuang-Rongcheng	*Zhao et al.* (2007b)
NUHP	CJ4A	Eclogite	zircon	SHRIMP	233	7	Chijiadian	*Zhao et al.* (2006a)
NUHP	CJ4C	Eclogite	zircon	SHRIMP	238	3	Chijiadian	*Zhao et al.* (2006a)
NUHP	CJ4D	Eclogite	zircon	SHRIMP	218	5	Chijiadian	*Zhao et al.* (2006a)
NUHP	05SD34	Gabbro	zircon	Cameca	210	2	Shidao	*Zhao et al.* (2012)
NUHP	05SD37	Gabbro	zircon	Cameca	211	2	Shidao	*Zhao et al.* (2012)
NUHP	05SD38	Gabbro	zircon	Cameca	210	2	Shidao	*Zhao et al.* (2012)
NUHP	05SD42	Syenite	zircon	Cameca	211	2	Shidao	*Zhao et al.* (2012)
NUHP	05SD39	Syenite	zircon	LA-ICP-Ms	204	3	Shidao	*Zhao et al.* (2012)

NUHP	05SD40	Gabbro	zircon	LA-ICP-Ms	210	2	Shidao	*Zhao et al.* (2012)
NUHP	05SD41	Granite	zircon	LA-ICP-Ms	201	2	Shidao	*Zhao et al.* (2012)
NUHP	JZS-3	Syenite	zircon	SHRIMP	215	5	Jiazishan	*Yang et al.* (2005)
SUHP	SU01	Quartzofeldspathic gneiss	hornblende	40Ar/39Ar	No Plateau		Fangshan	*Webb et al.* (2006)
SUHP	SU01	Quartzofeldspathic gneiss	K-feldspar	40Ar/39Ar	249-182		Fangshan	*Webb et al.* (2006)
SUHP	SU03	Quartzofeldspathic gneiss	K-feldspar	40Ar/39Ar	No Plateau		Fangshan	*Webb et al.* (2006)
SUHP	SU04	Quartzofeldspathic gneiss	K-feldspar	40Ar/39Ar	210-171		Fangshan	*Webb et al.* (2006)
SUHP	N1104-1	K-fsp porphyroblast bearing felsic gneiss	hornblende	40Ar/39Ar	213	0.3	Niushan	*Li et al.* (2003)
SUHP	N1103-1a	K-fsp porphyroblast bearing felsic gneiss	K-feldspar	40Ar/39Ar	191	2	Niushan	*Li et al.* (2003)
SUHP	F1031-5	Pod of pegmaite	biotite	40Ar/39Ar	203	0.3	Fangshan	*Li et al.* (2003)
SUHP	F1031-6a	Pod of pegmaite	biotite	40Ar/39Ar	203	0.4	Fangshan	*Li et al.* (2003)
SUHP	CCSD-MH891	Mylonitic paragneiss	biotite	40Ar/39Ar	211	1	Maobei ,Donghai	*Xu et al.* (2006)
SUHP	CCSD-MH960	Mylonitic paragneiss	biotite	40Ar/39Ar	214	4	Maobei ,Donghai	*Xu et al.* (2006)
SUHP	CCSD-MH1097	Mylonitic paragneiss	biotite	40Ar/39Ar	201	1	Maobei ,Donghai	*Xu et al.* (2006)
SUHP	CCSD-MH1130	Mylonitic paragneiss	biotite	40Ar/39Ar	202	1	Maobei ,Donghai	*Xu et al.* (2006)
SUHP	SDX-80	Pl gneiss	muscovite	40Ar/39Ar	218	2	Ganyu	*Xu et al.* (2006)
SUHP	02HS-2	Granitic gneiss	biotite	40Ar/39Ar	180	5	Hushan	*Li* (2003)
SUHP	02HS-2	Granitic gneiss	muscovite	40Ar/39Ar	186	4	Hushan	*Li* (2003)
SUHP	MH89-3	Granitic gneiss	K-feldspar	40Ar/39Ar	203-182		Niushan	*Chen et al.* (1992)
SUHP	1120905	Granitic gneiss	biotite	40Ar/39Ar	126	0.2	Qiandao	*Zhang et al.* (2007)
SUHP	1121002	Granitic gneiss	biotite	40Ar/39Ar	126	0.2	Beiqishan	*Zhang et al.* (2007)
SUHP	1121005	Granitic gneiss	biotite	40Ar/39Ar	126	0.1	Daoxitou	*Zhang et al.* (2007)
SUHP	01120908B	Granitic gneiss	biotite	40Ar/39Ar	189	0.5	Dashijia	*Zhang et al.* (2007)
SUHP	01120908	Granitic gneiss	hornblende	40Ar/39Ar	196	0.3	Dashijia	*Zhang et al.* (2007)

	H							
SUHP	JZS-11	Hornblende syenite	K-feldspar	40Ar/39Ar	221-194		Shidao	*Yang et al.* (2005)
SUHP	10SD033A	Granitic gneiss	zircon	(U-Th)/He	169.3	9.9	Jinghai	This study
SUHP	10SD041B	Quartz syenite	biotite	40Ar/39Ar	212.9	2.5	Shidao	This study
SUHP	10SD041B	Quartz syenite	zircon	(U-Th)/He	177.5	13.2	Shidao	This study
SUHP	94MY08A	Layered granitic orthegneiss	zircon	ICP	229.5	5.6	Moyedao	*Hacker et al.* (2006)
SUHP	95HZ14A	Deformed granite	zircon	ICP	221.8	7.3	Donghai	*Hacker et al.* (2006)
SUHP	R498	Granitic gneiss	zircon	SHRIMP	227	2	Donghai	*Liu et al.* (2004a)
SUHP	R498	Granitic gneiss	zircon	SHRIMP	209	3	Donghai	*Liu et al.* (2004a)
SUHP	S1	Paragneiss	zircon	SHRIMP	228	5	Donghai	*Liu et al.* (2004b)
SUHP	S1	Paragneiss	zircon	SHRIMP	208	4	Donghai	*Liu et al.* (2004b)
SUHP	S2	Orthogneiss	zircon	SHRIMP	232	4	Donghai	*Liu et al.* (2004b)
SUHP	S2	Orthogneiss	zircon	SHRIMP	213	5	Donghai	*Liu et al.* (2004b)
SUHP	SL8	Biotite-bearing orthogneiss	zircon	SHRIMP	228	3	North Of Donghai	*Liu et al.* (2009b)
SUHP	SL8	Biotite-bearing orthogneiss	zircon	SHRIMP	215	2	North Of Donghai	*Liu et al.* (2009b)
SUHP	B3	Biotite-bearing paragneiss	biotite	40Ar/39Ar	212	0.7	Maobei	*Liu et al.* (2009b)
SUHP	G13	Amphibolite	zircon	SHRIMP	231	3	Niushan	*Liu et al.* (2008)
SUHP	G13	Amphibolite	zircon	SHRIMP	214	4	Niushan	*Liu et al.* (2008)
SUHP	G13	Amphibolite	hornblende	40Ar/39Ar	210	0.8	Niushan	*Liu et al.* (2008)
SUHP	00QL16	Eclogite	zircon	Cameca	220	7	Qinglongshan	*Chen et al.* (2011)
SUHP	99QL07	Granitic gneiss	zircon	Cameca	218	2	Qinglongshan	*Chen et al.* (2011)
SUHP	99QL16	Granitic gneiss	zircon	Cameca	219	3	Qinglongshan	*Chen et al.* (2011)
SUHP	00QL27	Granitic gneiss	zircon	Cameca	220	4	Qinglongshan	*Chen et al.* (2011)
SUHP	H4	Marble	zircon	SHRIMP	246	3	Sanqingge	*Liu et al.* (2006d)
SUHP	H4	Marble	zircon	SHRIMP	234	4	Sanqingge	*Liu et al.* (2006d)
SUHP	H4	Marble	zircon	SHRIMP	213	6	Sanqingge	*Liu et al.* (2006d)

SUHP	H2	Eclogite lense in marble	zircon	SHRIMP	244	4	Sanqingge	*Liu et al.* (2007)
SUHP	H2	Eclogite lense in marble	zircon	SHRIMP	233	4	Sanqingge	*Liu et al.* (2007)
SUHP	H2	Eclogite lense in marble	zircon	SHRIMP	214	5	Sanqingge	*Liu et al.* (2007)
SUHP	B441	Grt-biotite paragneiss	zircon	SHRIMP	228	5	CCSD-MH	*Liu et al.* (2006c)
SUHP	B441	Grt-biotite paragneiss	zircon	SHRIMP	213	6	CCSD-MH	*Liu et al.* (2006c)
SUHP	R498	Ep-biotite orthogneiss	zircon	SHRIMP	227	2	CCSD-MH	*Liu et al.* (2004a)
SUHP	R498	Ep-biotite orthogneiss	zircon	SHRIMP	209	3	CCSD-MH	*Liu et al.* (2004a)
SUHP	02-II1(2)A	Eclogite	zircon	SHRIMP	216	3	CCSD-MH	*Zhao et al.* (2006b)
SUHP	02-I4A	Granitic gneiss	zircon	SHRIMP	228	3	CCSD-MH	*Chen et al.* (2007)
SUHP	02-I6A	Eclogite	zircon	LA-ICP-Ms	223	3	CCSD-MH	*Chen et al.* (2007)
SUHP	G12	Amphibolite	zircon	SHRIMP	229	3	CCSD-MH	*Liu et al.* (2008)
SUHP	G12	Amphibolite	zircon	SHRIMP	215	3	CCSD-MH	*Liu et al.* (2008)
SUHP	G12	Amphibolite	hornblende	40Ar/39Ar	210	0.8	CCSD-MH	*Liu et al.* (2008)
SUHP	S3	Ep-biotite orthogneiss	zircon	SHRIMP	227	8	CCSD-PP1	*Liu et al.* (2006b)
SUHP	S3	Ep-biotite orthogneiss	zircon	SHRIMP	213	7	CCSD-PP1	*Liu et al.* (2006b)
SUHP	S4	Ep-biotite orthogneiss (non-UHP orthogneiss)	zircon	SHRIMP	211	6	CCSD-PP1	*Liu et al.* (2006b)
SUHP	S27	Phe-biotite paragneiss	zircon	SHRIMP	230	7	CCSD-PP2	*Liu et al.* (2009a)
SUHP	S27	Phe-biotite paragneiss	zircon	SHRIMP	210	2	CCSD-PP2	*Liu et al.* (2009a)
SUHP	S28	Grt-Phe orthogneiss	zircon	SHRIMP	230	7	CCSD-PP2	*Liu et al.* (2009a)
SUHP	S28	Grt-Phe orthogneiss	zircon	SHRIMP	210	3	CCSD-PP2	*Liu et al.* (2009a)
SUHP	S20	Grt-Amp paragneiss	zircon	SHRIMP	229	4	CCSD-PP2	*Liu et al.* (2005)
SUHP	S21	Grt-Amp paragneiss	zircon	SHRIMP	228	3	Zk2304	*Liu et al.* (2005)
HP	99JP7	Quartzofeldspathic schist	K-feldspar	40Ar/39Ar	192-178		Jinping	*Hacker et al.* (2009)
HP	95YTST01 f	Muscovite schist layer associated with deformed granite	muscovite	40Ar/39Ar	196-145		Lianyungang	*Hacker et al.* (2009)
HP	LYG-20	Mylonitic Ep-Pl gneiss	biotite	40Ar/39Ar	244	3	Pingshan, Lianyungang	*Xu et al.* (2006)
HP	LYG1025-	Mylonitic Ep-Pl gneiss	biotite	40Ar/39Ar	254	3	Xueqigou, Lianyungang	*Xu et al.* (2006)

	08							
HP	SJ-1	Gaucophane schist	Phengite	40Ar/39Ar	245	0.5	Sanjie, Zhangbaling	*Li et al.* (1993)
HP	SU11b	Biotite shear band	biotite	40Ar/39Ar	No Plateau		Jinping	*Webb et al.* (2006)
HP	SU12	Schist	muscovite	40Ar/39Ar	213	1	Jinping	*Webb et al.* (2006)
HP	SU16	Nodule of K-feldspar	K-feldspar	40Ar/39Ar	189-157		Lianyungang Coast	*Webb et al.* (2006)
HP	T98	Muscovite-Plg schist	muscovite	40Ar/39Ar	218	3	Haizhou P Mine	*Li et al.* (2003)
HP	MH89-2	Granitic migmatite	K-feldspar	40Ar/39Ar	199-177		Haizhou Middle Schoool	*Chen et al.* (1992)
HP		Leptite	K-feldspar	40Ar/39Ar	212-166		Jinping P Quarry	*Chen et al.* (1992)
HP	SL1	Biotite-bearing paragneiss	zircon	SHRIMP	245	4	Lianyungang	*Liu et al.* (2009b)
HP	SL1	Biotite-bearing paragneiss	zircon	SHRIMP	231	3	Lianyungang	*Liu et al.* (2009b)
HP	B1	Biotite-bearing paragneiss	biotite	40Ar/39Ar	233	0.9	Lianyungang	*Liu et al.* (2009b)
HP	SL2	Biotite-bearing orthogneiss	zircon	SHRIMP	245	4	Jinping	*Liu et al.* (2009b)
HP	SL2	Biotite-bearing orthogneiss	zircon	SHRIMP	230	2	Jinping	*Liu et al.* (2009b)
HP	B2	Biotite-bearing paragneiss	biotite	40Ar/39Ar	231	0.8	Jinping	*Liu et al.* (2009b)
Granite	10SD010	Granite	zircon	SHRIMP U-Pb	115.6	1.2	Haiyang	This study
Granite	10JD06B	Granite	zircon	SHRIMP U-Pb	159.7	1.3	Queshan	This study
Granite	Washan	Granite	biotite	40Ar/39Ar	130	2	Kunyushan	*Zhang et al.* (1995)
Granite	03R097	Granite	zricon	SHRIMP	160	3	Wuzhuashan	*Hu* (2004)
Granite	03R100	Granite	zircon	SHRIMP	111	3	Sanfoshan	*Hu* (2004)
Granite	04R008	Monzonite	zircon	LA-ICP-MS	114	1	Wendengnan	*Hu* (2004)
Granite	04R009	Dirotire enclace	zircon	LA-ICP-MS	114	1	Wendengnan	*Hu* (2004)
Granite	04R134	Gabbroic diorite	zircon	LA-ICP-MS	113	2	Gongjia	*Hu* (2004)
Granite	03R079	K-feldspar granite	zircon	LA-ICP-MS	111	2	Xiamashan	*Hu* (2004)
Granite	DG49	Granodiorite	zircon	SHRIMP	161	1	Duguoshan	*Guo et al.* (2005)
Granite	WD13	Monzogranite	zircon	SHRIMP	160	3	Wendeng	*Guo et al.* (2005)
Granite	KY15	Leucogranite	zircon	SHRIMP	142	3	Kunyushan	*Guo et al.* (2005)

Granite	KY34	Diorite	zircon	ID ICP	114.5	0.8	Liudushi	*Guo et al.* (2005)
Granite	KY33	Granite	zircon	ID ICP	114	1	Taiboding	*Guo et al.* (2005)
Granite	KY45	Granite	zircon	ID ICP	113	1	Sanfoshan	*Guo et al.* (2005)
Granite	RC13	Granite	zricon	ID ICP	108	2	Weideshan	*Guo et al.* (2005)
Granite	SD-11	Monzograinte	zircon	SHRIMP	118	1	Sanfoshan	*Goss et al.* (2010)
Granite	SD-12	Syenogranite	zircon	SHRIMP	117	1	Sanfoshan	*Goss et al.* (2010)
Granite	SD-30	Monzonite	zircon	SHRIMP	116	1	Yashan	*Goss et al.* (2010)
Granite	SD-31	Monzograinte	zircon	SHRIMP	113	2	Yashan	*Goss et al.* (2010)
Granite	SD-59	Alkali granite	zircon	SHRIMP	115	2	Laoshan	*Goss et al.* (2010)
Granite	06SD01	Mozonite	zircon	LA-ICP-MS	114	3	Sanfoshan	*Zhang et al.* (2010)
Granite	06SD17	Granite	zircon	SHRIMP	116	3	Sanfoshan	*Zhang et al.* (2010)
Granite	06SD12	Granite	zircon	LA-ICP-MS	134	5	Kunyushan	*Zhang et al.* (2010)
Granite	06SD21	Granite	zircon	LA-ICP-MS	141	3	Kunyushan	*Zhang et al.* (2010)
Granite	06SD28	Granite	zircon	LA-ICP-MS	146	4	Kunyushan	*Zhang et al.* (2010)
Granite	00DP02	Granite	zircon	LA-ICP-MS	124	1		*Zhang et al.* (2012)
Granite	00SD02	Granite	zircon	LA-ICP-MS	113	2		*Zhang et al.* (2012)
Granite	00SD04	Granite	zircon	LA-ICP-MS	119	4		*Zhang et al.* (2012)
Granite	00SD07	Granite	zircon	LA-ICP-MS	120	2		*Zhang et al.* (2012)
Granite	00XHY05	Diorite	zircon	LA-ICP-MS	123	2		*Zhang et al.* (2012)
Granite	08LX094	Syenite	zircon	LA-ICP-MS	124	1	Dadian	*Lan et al.* (2011)
Granite	08LX098	Syenite	zircon	LA-ICP-MS	125	1	Dadian	*Lan et al.* (2011)
Granite	QS001	Trachyandesite	zircon	LA-ICP-MS	124	1	Qibaoshan	*Liu et al.* (2009d)
Granite	SD08B	Pegmatite	muscovite	40Ar/39Ar	136.9	1.9	Taohang	*Lin et al.* (2005)
Granite	SD10A	Grantie	K-feldspar	40Ar/39Ar	117.5	1.7	Taohang	*Lin et al.* (2005)
Granite	SD20B2	Grantie	biotite	40Ar/39Ar	125.1	1.8	Rizhao	*Lin et al.* (2005)
Granite	10SD06B	Granite	hornblende	40Ar/39Ar	125.7	2.8	Liujiakuang	This study
Granite	10SD06B	Granite	zircon	(U-Th)/He	96.9	5.3		This study
Granite	10SD010	Granite	hornblende	40Ar/39Ar	116.9	0.9	Haiyang	This study

Granite	10SD010	Granite	biotite	40Ar/39Ar	114.3	1.1	Haiyang	This study
Granite	10SD010	Granite	zircon	(U-Th)/He	87.7	9	Haiyang	This study
Granite	10SD069	Granite	biotite	40Ar/39Ar	114.1	1	Shaizi	This study
Granite	11LX209	Granite	zircon	(U-Th)/He	90.6	13.1	Laoshan	This study
Granite	11lX094B	Granite	zircon	(U-Th)/He	110.6	3.9	Fangzi	This study

References

Chen, R. X., Y. F. Zheng, Z. F. Zhao, J. Tang, F. Y. Wu, and X. M. Liu (2007), Zircon U–Pb age and Hf isotope evidence for contrasting origin of bimodal protoliths for ultrahigh-pressure metamorphic rocks from the Chinese Continental Scientific Drilling project, *Journal of Metamorphic Geology*, *25*(8), 873-894, doi:10.1111/j.1525-1314.2007.00735.x.

Chen, W., T. M. Harrison, M. Heizerler, R. Liu, B. Ma, and J. Li (1992), The cooling history of melange zone in north Jiangsu-South Shandong region: evidence from multiple diffusion domain ^{40}Ar-^{39}Ar thermal geochornology, *Acta Petrologica Sinica*, *8*(1), 1-17.

Chen, Y.-X., Y.-F. Zheng, R.-X. Chen, S.-B. Zhang, Q. Li, M. Dai, and L. Chen (2011), Metamorphic growth and recrystallization of zircons in extremely 18O-depleted rocks during eclogite-facies metamorphism: Evidence from U–Pb ages, trace elements, and O–Hf isotopes, *Geochimica et Cosmochimica Acta*, *75*(17), 4877-4898, doi:10.1016/j.gca.2011.06.003.

Goss, S. C., S. A. Wilde, F. Wu, and J. Yang (2010), The age, isotopic signature and significance of the youngest Mesozoic granitoids in the Jiaodong Terrane, Shandong Province, North China Craton, *Lithos*, *120*(3-4), 309-326, doi:10.1016/j.lithos.2010.08.019.

Guo, J. H., F. K. Chen, X. M. Zhang, W. Siebel, and M. G. Zhai (2005), Evolution of syn-to post-collisional magmatism from north Sulu UHP belt, eastern China: zircon U-Pb geochronology, *Acta Petrologica Sinica*, *21*(4), 1281-1301.

Hacker, B. R., S. R. Wallis, M. O. McWilliams, and P. B. Gans (2009), ^{40}Ar/^{39}Ar Constraints on the tectonic history and architecture of the ultrahigh-pressure Sulu orogen, *Journal of Metamorphic Geology*, *27*(9), 827-844, doi:10.1111/j.1525-1314.2009.00840.x.

Hacker, B. R., S. R. Wallis, L. Ratschbacher, M. Grove, and G. Gehrels (2006), High-temperature geochronology constraints on the tectonic history and architecture of the ultrahigh-pressure Dabie-Sulu Orogen, *Tectonics*, *25*(5), TC5006, doi:10.1029/2005tc001937.

Hu, F. (2004), Magmatism, ore fluid evolution and gold mineralization of the Kunyushan area in the Jiaodong peninsula during the Mesozoic tectonic regime inversion in eastern China, PhD thesis, 189 pp, Institute of Geology and Geophysics, Chinese Academy of Sciences, Beijing, China.

Lan, T.-G., H.-R. Fan, M. Santosh, F.-F. Hu, K.-F. Yang, Y.-H. Yang, and Y. Liu (2011), Geochemistry and Sr–Nd–Pb–Hf isotopes of the Mesozoic Dadian alkaline intrusive complex in the Sulu orogenic belt, eastern China: Implications for crust–mantle interaction, *Chemical Geology*, *285*(1–4), 97-114, doi:10.1016/j.chemgeo.2011.03.013.

Li, J., T. Yang, W. Chen, and S. Zhang (2003), ^{40}Ar/^{39}Ar dating of deformation events and reconstruction of exhumation of ultrahigh-pressure metamorphic rocks in Donghai, East China, *Acta Geologica Sinica - English Edition*, *77*(2), 155-168, doi:10.1111/j.1755-6724.2003.tb00558.x.

Li, Q. (2003), Thermochronology and cooling history of the ultrahigh-pressure metamorphic rocks in the Dabie mountain, PhD thesis, 105 pp, University of Science and Technology of China, Hefei, China.

Li, S., et al. (1993), Collision of the North China and Yangtse Blocks and formation of coesite-bearing eclogites: Timing and processes, *Chemical Geology*, *109*(1–4), 89-111, doi:10.1016/0009-2541(93)90063-o.

Lin, L.-H., P.-L. Wang, C.-H. Lo, C.-H. Tsai, and B.-M. Jahn (2005), ^{40}Ar-^{39}Ar thermochronological constraints on the exhumation of ultrahigh-pressure metamorphic rocks in the Sulu terrane of Eastern China, *International Geology Review*, *47*(8), 872-886, doi:10.2747/0020-6814.47.8.872.

Liu, D., P. Jian, A. Kröner, and S. Xu (2006a), Dating of prograde metamorphic events deciphered from episodic zircon growth in rocks of the Dabie-Sulu UHP complex, China, *Earth and Planetary Science Letters*, *250*(3-4), 650-666, doi:10.1016/j.epsl.2006.07.043.

Liu, F., Z. Xu, and H. Xue (2004a), Tracing the protolith, UHP metamorphism, and exhumation ages of orthogneiss from the SW Sulu terrane (eastern China): SHRIMP U–Pb dating of mineral inclusion-bearing zircons, *Lithos*, *78*(4), 411-429, doi:10.1016/j.lithos.2004.08.001.

Liu, F., J. G. Liou, and Z. Xu (2005), U-Pb SHRIMP ages recorded in the coesite-bearing zircon domains of paragneisses in the southwestern Sulu terrane, eastern China: New interpretation, *American Mineralogist*, *90*(5-6), 790-800, doi:10.2138/am.2005.1677.

Liu, F., J. G. Liou, and H. Xue (2006b), Identification of UHP and non-UHP orthogneisses in the Sulu UHP terrane, eastern China: evidence from SHRIMP U-Pb dating of mineral inclusion-bearing zircons, *International Geology Review*, *48*(12), 1067-1086, doi:10.2747/0020-6814.48.12.1067.

Liu, F., Z. Xu, J. G. Liou, and B. Song (2004b), SHRIMP U–Pb ages of ultrahigh-pressure and retrograde metamorphism of gneisses, south-western Sulu terrane, eastern China, *Journal of Metamorphic Geology*, *22*(4), 315-326, doi:10.1111/j.1525-1314.2004.00516.x.

Liu, F., Z. Xu, H. Xue, and K. Zhou (2006c), Ultrahigh-pressure and retrograde metamorphic ages for Paleozoic protolith of paragneiss in the main drill hole of the Chinese Continental Scientific Drilling Project (CCSD-MH), SW Sulu UHP Terrane, *Acta Geologica Sinica - English Edition*, *80*(3), 336-348, doi:10.1111/j.1755-6724.2006.tb00253.x.

Liu, F., A. Gerdes, L. Zeng, and H. Xue (2008), SHRIMP U–Pb dating, trace elements and the Lu–Hf isotope system of coesite-bearing zircon from amphibolite in the SW Sulu UHP terrane, eastern China, *Geochimica et Cosmochimica Acta*, *72*(12), 2973-3000, doi:10.1016/j.gca.2008.04.007.

Liu, F., A. Gerdes, J. Liou, and P. Liu (2009a), Unique coesite-bearing zircon from allanite-bearing gneisses: U-Pb, REE and Lu-Hf properties and implications for the evolution of the Sulu UHP terrane, China, *European Journal of Mineralogy*, *21*(6), 1225-1250, doi:10.1127/0935-1221/2009/0021-1965.

Liu, F., G. A., R. P. T., H. Xue, and J. Ye (2007), Zoned zircon from eclogite lenses in marbles from the Dabie-Sulu UHP terrane, China: A clear record of ultra-deep subduction and fast exhumation, *Acta Geologica Sinica - English Edition*, *81*(2), 204-225, doi:10.1111/j.1755-6724.2007.tb00945.x.

Liu, F. L., A. Gerdes, and H. M. Xue (2009b), Differential subduction and exhumation of crustal slices in the Sulu HP-UHP metamorphic terrane: insights from mineral inclusions, trace elements, U-Pb and Lu-Hf isotope analyses of zircon in orthogneiss, *Journal of Metamorphic Geology*, *27*(9), 805-825, doi:10.1111/j.1525-1314.2009.00833.x.

Liu, F. L., H. M. Xue, and P. H. Liu (2009c), Genetic mechanism of garnet-bearing amphibolite in the north Sulu ultrahigh-pressure (UHP) metamorphic belt, *Acta Petrological Sinica*, *25*, 1575-1586.

Liu, F. L., A. Gerdes, J. G. Liou, H. M. Xue, and F. H. Liang (2006d), SHRIMP U-Pb zircon dating from Sulu-Dabie dolomitic marble, eastern China: constraints on prograde, ultrahigh-pressure and retrograde metamorphic ages, *Journal of Metamorphic Geology*, *24*(7), 569-589, doi:10.1111/j.1525-1314.2006.00655.x.

Liu, S., R. Hu, S. Gao, C. Feng, B. Yu, Y. Qi, T. Wang, G. Feng, and I. M. Coulson (2009d), Zircon U-Pb age, geochemistry and Sr-Nd-Pb isotopic compositions of adakitic volcanic rocks from Jiaodong, Shandong Province, Eastern China: Constraints on petrogenesis and implications, *Journal of Asian Earth Sciences*, *35*(5), 445-458, doi:10.1016/j.jseaes.2009.02.008.

Song, M., and F. Lu (1997), Primarily study on muscovite from the country rocks of eclogite in Jiaonan area, Shandong Province, *Journal of Mineralogy and Petrology*, *17*(2), 17-21.

Webb, L. E., M. L. Leech, and T. N. Yang (2006), $^{40}Ar/^{39}Ar$ thermochronology of the Sulu terrane: Late Triassic exhumation of high- and ultrahigh-pressure rocks and implications for Mesozoic tectonics in East Asia, *Geological Society of America Special Papers*, *403*, 77-92, doi:10.1130/2006.2403(04).

Xu, Z., L. Zeng, F. Liu, J. Yang, Z. Zhang, M. McWilliams, and J. G. Liou (2006), Polyphase subduction and exhumation of the Sulu high-pressure–ultrahigh-pressure metamorphic terrane, *Geological Society of America Special Papers*, *403*, 93-113, doi:10.1130/2006.2403(05).

Yang, J.-H., S.-L. Chung, S. A. Wilde, F.-y. Wu, M.-F. Chu, C.-H. Lo, and H.-R. Fan (2005), Petrogenesis of post-orogenic syenites in the Sulu Orogenic Belt, East China: geochronological, geochemical and Nd-Sr isotopic evidence, *Chemical Geology*, *214*(1-2), 99-125, doi:10.1016/j.chemgeo.2004.08.053.

Yang, J. S., J. L. Wooden, C. L. Wu, F. L. Liu, Z. Q. Xu, R. D. Shi, I. Katayama, J. G. Liou, and S. Maruyama (2003), SHRIMP U–Pb dating of coesite-bearing zircon from the ultrahigh-pressure metamorphic rocks, Sulu terrane, east China, *Journal of Metamorphic Geology*, *21*(6), 551-560, doi:10.1046/j.1525-1314.2003.00463.x.

Zhang, D., H. Xu, and G. Sun (1995), Emplacement ages of the Denggezhuang gold deposit and the Kunyushan granite and their geological implication, *Geological Review*, *41*(5), 415-425.

Zhang, H., Q. Hou, and D. Cao (2007), Tectono-chronologic constraints on a Mesozoic slip and thrust belt in the eastern Jiaodong Peninsula, *Science in China Series D: Earth Sciences*, *50*(1), 25-32, doi:10.1007/s11430-007-2073-6.

Zhang, J., Z.-F. Zhao, Y.-F. Zheng, and M. Dai (2010), Postcollisional magmatism: Geochemical constraints on the petrogenesis of Mesozoic granitoids in the Sulu orogen, China, *Lithos*, *119*(3-4), 512-536, doi:10.1016/j.lithos.2010.08.005.

Zhang, J., Z.-F. Zhao, Y.-F. Zheng, X. Liu, and L. Xie (2012), Zircon Hf–O isotope and whole-rock geochemical constraints on origin of postcollisional mafic to felsic dykes in the Sulu orogen, *Lithos*, *136–139*, 225-245, doi:10.1016/j.lithos.2011.06.006.

Zhao, R., J. G. Liou, R. Y. Zhang, and T. Li (2006a), SHRIMP U-Pb zircon dating of the Rongcheng eclogite and associated peridotite: New constraints for ultrahigh-pressure metamorphism of mantle-derived mafic-ultramafic bodies from the Sulu terrane, *Geological Society of America Special Papers*, *403*, 115-125, doi:10.1130/2006.2403(06).

Zhao, R., J. G. Liou, T. Tsujimori, and R. Y. Zhang (2007a), Petrology and U-Pb SHRIMP geochronology of a garnet peridotite, Sulu UHP terrane, east-central China, *International Geology Review*, *49*(8), 732-752, doi:10.2747/0020-6814.49.8.732.

Zhao, R., R. Y. Zhang, J. G. Liou, A. L. Booth, E. C. Pope, and C. P. Chamberlain (2007b), Petrochemistry, oxygen isotopes and U-Pb SHRIMP geochronology of mafic–ultramafic bodies from the Sulu UHP terrane, China, *Journal of Metamorphic Geology*, *25*(2), 207-224, doi:10.1111/j.1525-1314.2007.00691.x.

Zhao, Z.-F., Y.-F. Zheng, J. Zhang, L.-Q. Dai, Q. Li, and X. Liu (2012), Syn-exhumation magmatism during continental collision: Evidence from alkaline intrusives of Triassic age in the Sulu orogen, *Chemical Geology*, *328*, 70-88, doi:10.1016/j.chemgeo.2011.11.002.

Zhao, Z. F., Y. F. Zheng, T. S. Gao, Y. B. Wu, B. Chen, F. K. Chen, and F. Y. Wu (2006b), Isotopic constraints on age and duration of fluid-assisted high-pressure eclogite-facies recrystallization during exhumation of deeply subducted continental crust in the Sulu orogen, *Journal of Metamorphic Geology*, *24*(8), 687-702, doi:10.1111/j.1525-1314.2006.00662.x.

Zong, K., Y. Liu, C. Gao, Z. Hu, S. Gao, and H. Gong (2010), In situ U-Pb dating and trace element analysis of zircons in thin sections of eclogite: Refining constraints on the ultra high-pressure metamorphism of the Sulu terrane, China, *Chemical Geology*, *269*(3-4), 237-251, doi:10.1016/j.chemgeo.2009.09.021.

Appendix Figure 4.1 Radiation damage and grain size effects on the AHe, ZHe and ZFT ages

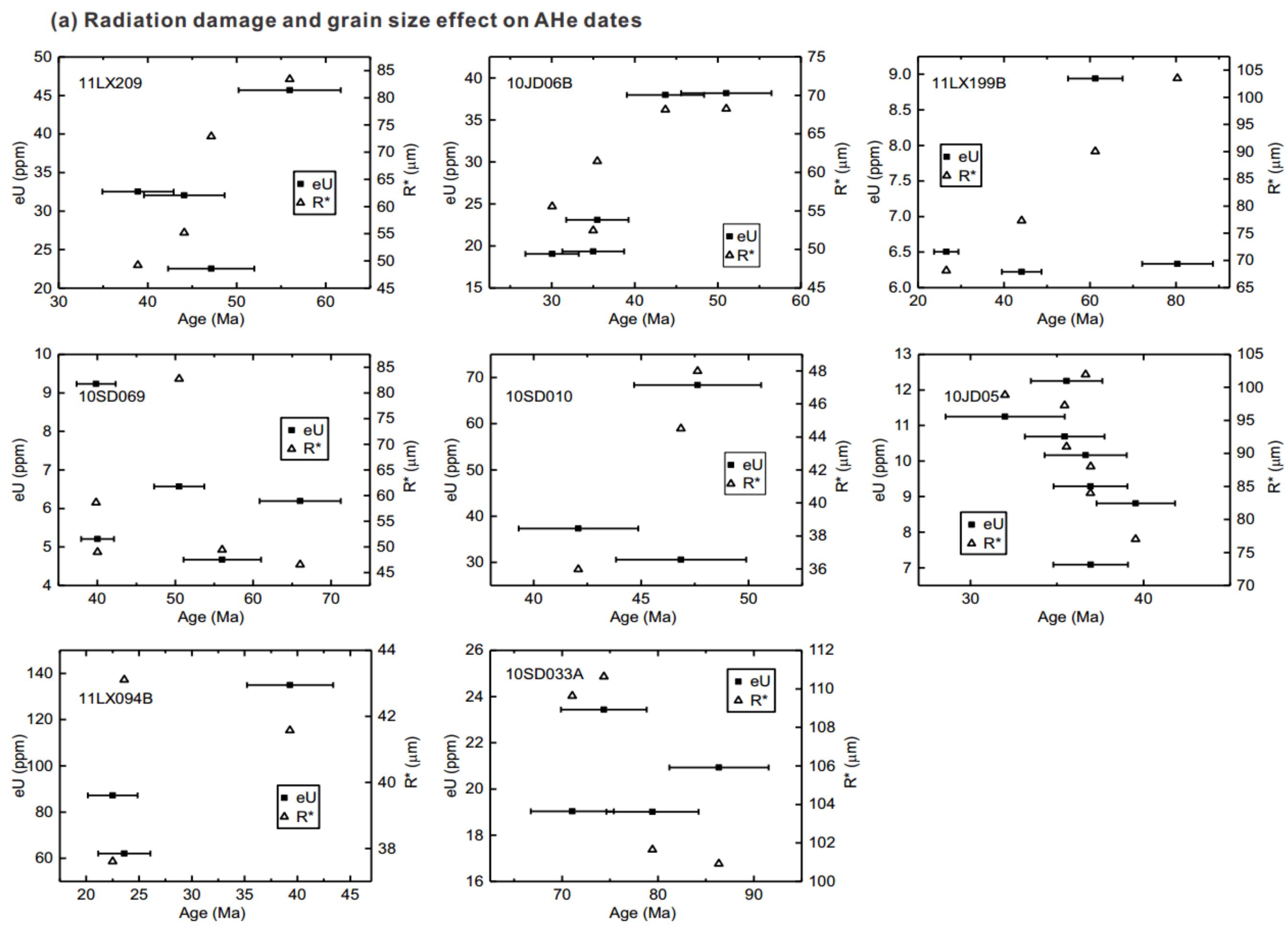

(b) Radiation damage and grain size effect on ZHe dates

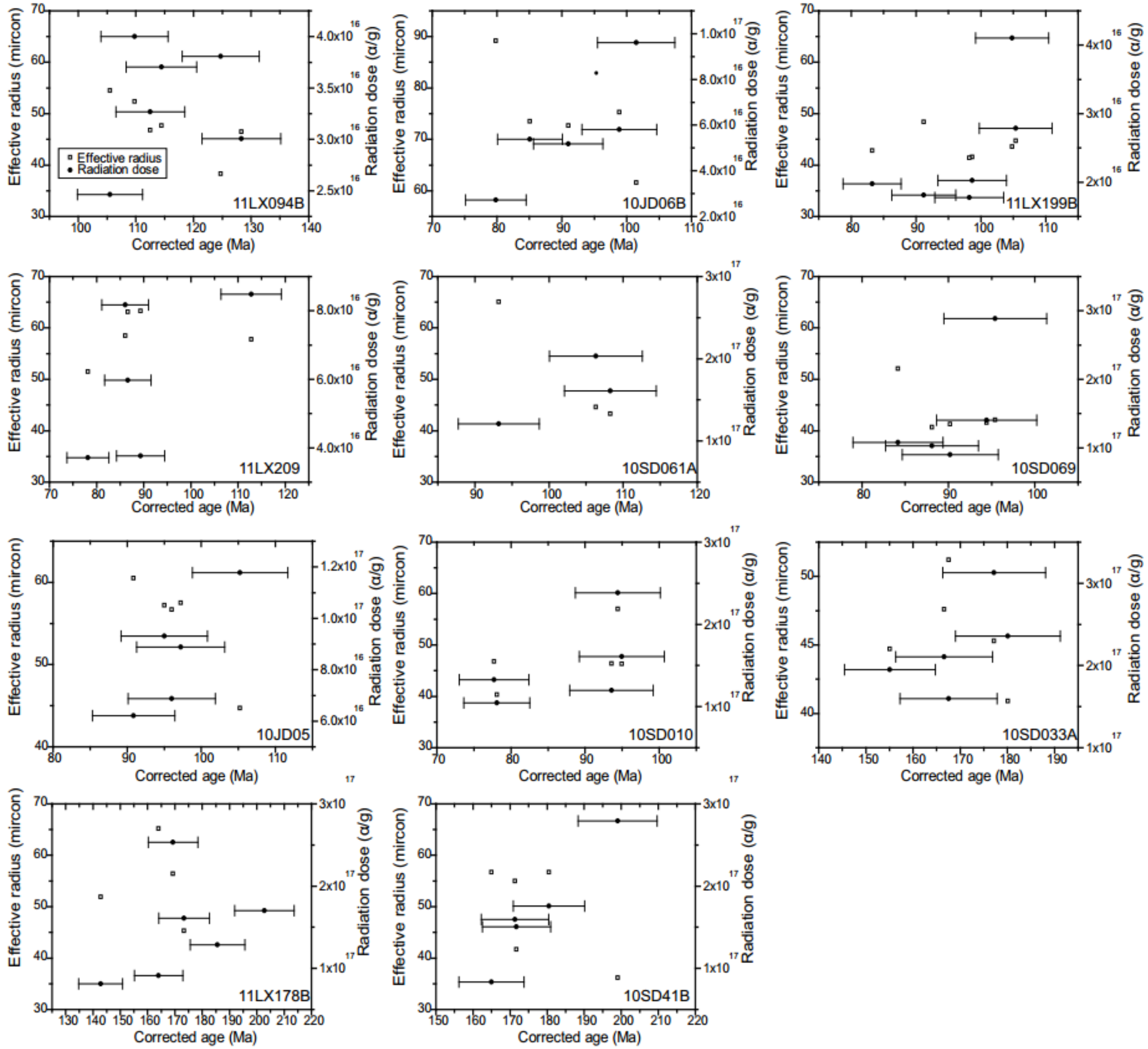

(c)Radiation damage effect on ZFT dates

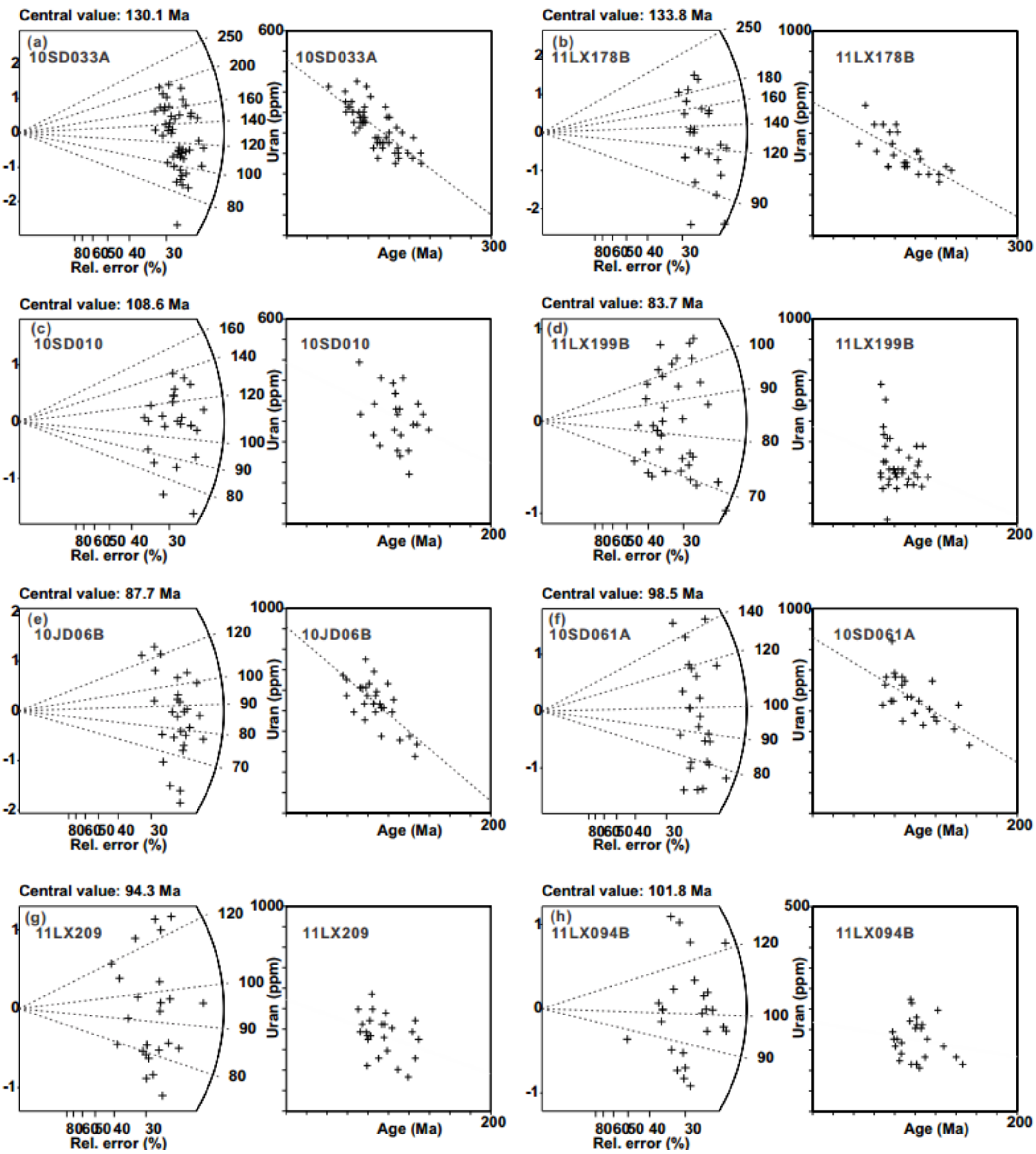

Appendix Table 5.1 Sample information for thermochronology study in the Jiaobei region

Sample ID	**Latitude (° N)**	**Longitude (°E)**	**Elevation (m)**	**Rock type**	**Rock unit**
10JD10	37.1599	121.2426	129	Mylonized granite	Upper Jurassic
10JD20	37.3900	120.8785	115	Mica schist	Fenzishan Group
10JD27	37.9527	120.7351	9	Quartzite	Penglai Group
10JD28	37.9895	120.6852	20	Quartzite	Penglai Group
10JD31	37.5772	121.0878	40	Foliated granite	Upper Jurassic
10JD34	37.5500	120.6560	64	Unfoliated granite	Lower Cretaceous
10SD112	37.6210	121.3514	19	Quartzite	Zhifu Group
10SD121	36.9985	120.3341	116	Granite	Paleoproterzoic
10SD128B	37.0133	120.1533	124	Foliated granite	Upper Jurassic Linglong pluton
10SD128C	37.0133	120.1533	124	Unfoliated granite	Upper Jurassic Linglong pluton
10SD132	36.8699	119.6701	33	Amphibolite	Jingshan Group
10SD134	36.7883	119.6337	42	Marble	Jingshan Group
10SD138	36.4420	119.3724	107	Marble	Jingshan Group
10SD148	37.1253	119.8744	84	Amphibolite	Archean
10SD154	37.3978	120.1861	127	Granite	Upper Jurassic Linglong pluton
10SD180	37.7755	120.6653	76	Gneiss	Archean
10SD198	37.2406	120.7904	149	Gneiss	Archean
10SD201	37.1330	120.7657	163	Amphibolite	Archean
10SD204	37.0647	120.7606	92	Gneiss	Archean
10SD207	36.8536	120.6461	117	Calc-silicate rock	Jingshan Group

11JD006	36.8323	120.6518	57	Grantic gneiss	Fenzishan Group
11JD022	37.4145	121.0070	70	Quartzite	Penglai Group
JB12-02-1	37.1088	120.7614	183	Gneiss	Archean
JB12-02-2	37.1088	120.7614	183	Gneiss	Archean
JB12-05	37.3164	120.8527	164	Granulite	Archean
JB12-06	37.3311	120.8958	248	TTG gneiss	Archean
JB12-10	37.2946	121.1394	130	TTG gneiss	Archean
JB12-12-1	37.6995	120.8748	88	Granite	Archean (?)
JB12-12-2	37.6995	120.8748	88	Gneiss	Archean

Appendix Table 5.2 SHRIMP zircon U-Pb results for samples from the Jiaobei region

Sample spot	U (ppm)	Th (ppm)	$^{232}Th/^{238}U$	$^{206}Pb_c$ (%)	$^{206}Pb^*$ (ppm)	$^{207}Pb^*/^{206}Pb^*$	σ (%)	$^{207}Pb^*/^{235}U$	σ (%)	$^{206}Pb^*/^{238}U$	σ (%)	$^{207}Pb/^{206}Pb$ (Ma)	σ	$^{206}Pb/^{238}U$ (Ma)	σ
10JD10															
10JD10-01	1446	843	0.602	0.03	30.9	0.049	1.2	0.17	1.3	0.025	0.6	128	28	159	0.9
10JD10-02	849	37	0.045	0.28	18.0	0.047	3.2	0.16	3.3	0.025	1.1	53.6	75	157	1.7
10JD10-03	140	78	0.576	0.52	3.0	0.048	7.2	0.17	7.2	0.025	1.0	101	169	159	1.6
10JD10-04	772	258	0.345	0.00	16.6	0.051	1.4	0.18	1.6	0.025	0.6	246	33	159	1.0
10JD10-05	326	17	0.055	--	6.6	0.049	2.6	0.16	2.7	0.024	0.8	140	60	150	1.1
10JD10-06	791	41	0.054	0.30	16.4	0.051	2.4	0.17	2.5	0.024	0.6	244	56	153	0.9
10JD10-07	406	163	0.415	0.09	8.6	0.048	2.6	0.16	2.8	0.025	1.1	101	61	158	1.7
10JD10-08	354	19	0.057	--	7.1	0.051	3.1	0.16	3.3	0.023	1.2	253	72	148	1.8
10JD10-09	535	170	0.327	0.37	11.1	0.051	6.0	0.17	6.0	0.024	0.9	240	137	154	1.4
10JD10-10	740	39	0.055	--	15.7	0.050	2.5	0.17	2.7	0.025	1.1	207	59	158	1.7
10JD10-11	158	89	0.586	--	3.8	0.051	4.9	0.20	5.5	0.028	2.4	237	113	179	4.2
10JD10-12	487	46	0.097	0.27	10.3	0.046	3.4	0.16	3.5	0.025	1.0	17.1	81	158	1.6
10JD10-13	745	42	0.058	0.11	16.0	0.048	2.0	0.17	2.2	0.025	0.9	118	48	160	1.4
10JD10-14	349	11	0.032	--	7.4	0.049	3.3	0.17	3.4	0.025	0.8	151	77	157	1.2
10JD10-15	868	45	0.054	0.11	18.0	0.049	2.0	0.16	2.3	0.024	1.1	131	47	154	1.7
10JD10-16	928	121	0.134	--	20.2	0.051	2.1	0.18	2.4	0.025	1.2	219	48	161	1.9
10JD10-17	666	37	0.057	--	13.9	0.050	1.8	0.17	2.1	0.024	1.0	211	42	155	1.6
10JD10-18	175	11	0.066	1.07	3.7	0.041	10.2	0.14	10.3	0.024	1.5	-270	258	155	2.3
10JD31															
10JD31-1	717	91	0.131	0.19	16	0.0463	2.8	0.1644	2.9	0.02577	0.99	11.6	67	164	1.6
10JD31-2	2203	456	0.214	0.02	52	0.0502	1.0	0.1887	1.2	0.02725	0.55	205	23	173	0.9
10JD31-3	1188	146	0.127	0.14	27	0.0494	1.8	0.1799	1.9	0.02639	0.74	169	42	168	1.2

10JD31-4	2468	338	0.141	0.08	58	0.0487	1.7	0.1834	1.9	0.02729	0.92	135	40	174	1.6
10JD31-5	103	60	0.598	1.82	2	0.0427	18.7	0.1483	18.7	0.02520	1.54	-185	466	160	2.4
10JD31-6	1568	196	0.129	0.00	35	0.0509	1.2	0.1821	1.4	0.02593	0.57	237	28	165	0.9
10JD31-7	1540	232	0.156	--	35	0.0494	1.6	0.1794	1.7	0.02634	0.59	167	37	168	1.0
10JD31-8	188	218	1.200	0.02	84	0.3087	1.0	22.0529	2.0	0.51805	1.74	3515	15	2691	38.2
10JD31-9	837	142	0.176	0.71	18	0.0494	3.6	0.1742	3.7	0.02557	0.81	168	84	163	1.3
10JD31-10	1940	221	0.118	0.16	45	0.0496	1.4	0.1837	1.5	0.02688	0.56	174	33	171	0.9
10JD31-11	1713	366	0.221	0.00	38	0.0494	1.2	0.1775	1.3	0.02604	0.57	169	27	166	0.9
10JD31-12	557	52	0.097	0.00	12	0.0508	3.6	0.1781	3.7	0.02541	0.69	233	84	162	1.1
10JD31-13	1688	221	0.135	0.30	37	0.0487	2.0	0.1718	2.0	0.02560	0.57	132	46	163	0.9
10JD31-14	655	127	0.199	0.40	14	0.0458	3.7	0.1601	3.8	0.02533	0.90	-11	90	161	1.4
10JD31-15	1603	398	0.256	0.25	35	0.0480	1.9	0.1686	2.1	0.02549	0.95	98.4	45	162	1.5
10JD31-16	1452	689	0.490	0.20	32	0.0484	1.8	0.1719	2.0	0.02577	0.68	117	43	164	1.1
10JD31-17	139	33	0.241	2.14	3	0.0398	19.4	0.1367	19.5	0.02488	1.84	-361	501	158	2.9
10JD34															
10JD34-1	224	107	0.49	0.72	3.9	0.041	9.3	0.12	9.3	0.020	0.99	-272	236	130	1.3
10JD34-2	424	221	0.54	--	7.6	0.053	4.6	0.15	4.7	0.021	0.80	349	104	133	1.0
10JD34-3	281	134	0.49	0.55	4.9	0.043	7.0	0.12	7.1	0.020	0.89	-144	174	130	1.1
10JD34-4	298	142	0.49	--	5.2	0.054	5.8	0.15	5.8	0.020	0.88	379	130	130	1.1
10JD34-5	307	125	0.42	0.85	5.3	0.044	7.8	0.12	7.9	0.020	1.31	-105	192	128	1.7
10JD34-6	274	125	0.47	0.20	4.8	0.047	4.9	0.13	5.0	0.020	0.86	34.8	117	131	1.1
10JD34-7	295	130	0.45	0.61	5.0	0.045	7.3	0.12	7.4	0.020	0.89	-36	178	127	1.1
10JD34-8	393	178	0.47	0.42	7.0	0.046	5.3	0.13	5.4	0.021	1.08	-23	129	132	1.4
10JD34-9	343	165	0.50	0.16	5.9	0.049	4.0	0.14	4.2	0.020	1.31	161	94	128	1.7
10JD34-10	322	158	0.51	0.15	5.4	0.045	6.3	0.12	6.4	0.020	0.80	-59	154	125	1.0
10JD34-11	299	116	0.40	--	5.2	0.050	6.2	0.14	6.3	0.020	0.83	180	146	130	1.1
10JD34-12	124	161	1.35	--	33.6	0.112	7.7	4.87	9.5	0.317	5.68	1825	139	1774	88.1
10JD34-	282	121	0.44	--	4.9	0.048	4.8	0.13	4.8	0.020	0.85	88.4	113	128	1.1

12R															
10JD34-13	355	173	0.50	--	6.0	0.051	4.8	0.14	5.1	0.020	1.74	222	110	125	2.2
10JD34-14	301	155	0.53	1.01	5.2	0.042	11.3	0.12	11.4	0.020	0.91	-216	285	129	1.2
10JD34-15	251	117	0.48	0.21	4.3	0.046	5.2	0.13	5.3	0.020	0.88	2.5	126	128	1.1
10JD34-16	336	183	0.56	--	5.7	0.052	4.2	0.14	4.2	0.020	0.80	291	95	127	1.0
10JD34-17	312	150	0.50	0.32	5.4	0.047	5.1	0.13	5.2	0.020	0.82	48.1	122	127	1.0
10JD34-18	301	130	0.45	0.19	5.3	0.048	4.7	0.13	4.9	0.020	1.40	82.0	110	130	1.8
10JD34-19	296	151	0.53	0.00	5.2	0.045	3.3	0.13	3.4	0.020	0.81	-49	79	130	1.0
10JD34-20	254	112	0.46	--	4.4	0.055	7.0	0.15	7.1	0.020	1.45	398	156	128	1.8
10JD34-21	268	118	0.46	0.80	4.6	0.043	8.5	0.12	8.6	0.020	0.93	-162	212	127	1.2
10JD34-22	264	114	0.45	0.19	4.6	0.049	4.6	0.14	4.7	0.020	0.86	155	108	129	1.1
10JD34-23	367	178	0.50	0.14	6.4	0.048	3.7	0.13	4.0	0.020	1.44	74.9	88	129	1.8
10JD34-24	299	130	0.45	0.87	5.2	0.038	9.3	0.11	9.3	0.020	0.90	-477	246	128	1.1
10SD121															
SD121-01C	222	157	0.73	0.12	63	0.113	0.57	5.1	1.0	0.33	0.8	1847	10	1838	13
SD121-01R	461	30	0.07	0.04	131	0.113	0.36	5.1	0.8	0.33	0.7	1841	7	1838	11
SD121-02R	613	38	0.06	0.02	173	0.112	0.30	5.1	1.0	0.33	1.0	1840	5	1828	16
SD121-02C	266	176	0.68	0.10	76	0.112	0.76	5.1	1.1	0.33	0.8	1838	14	1847	13
SD121-03C	386	283	0.76	0.01	109	0.113	0.38	5.1	1.0	0.33	0.9	1844	7	1836	15
SD121-03R	382	18	0.05	0.03	107	0.112	0.39	5.1	1.2	0.33	1.1	1836	7	1822	18
SD121-04C	223	170	0.79	--	62	0.113	0.50	5.0	1.2	0.32	1.1	1851	9	1804	18
SD121-04R	424	33	0.08	--	119	0.112	0.36	5.1	1.1	0.33	1.0	1839	7	1829	16
SD121-05R	380	24	0.06	0.02	107	0.112	0.38	5.1	0.8	0.33	0.7	1839	7	1831	11

SD121-05C	262	200	0.79	0.07	74	0.113	0.49	5.1	0.9	0.33	0.8	1851	9	1823	12
SD121-06C	251	195	0.80	0.08	70	0.112	0.82	5.0	1.1	0.33	0.8	1833	15	1820	13
SD121-06R	556	32	0.06	0.04	157	0.112	0.34	5.1	0.8	0.33	0.7	1836	6	1834	11
SD121-07C	198	140	0.73	0.12	56	0.113	0.61	5.2	1.0	0.33	0.9	1851	11	1839	14
SD121-07R	420	22	0.05	0.03	118	0.113	0.37	5.1	0.8	0.33	0.7	1846	7	1823	11
SD121-08B	302	227	0.77	0.03	86	0.112	0.45	5.1	0.9	0.33	0.8	1833	8	1840	12
SD121-08L	231	185	0.83	0.15	65	0.112	0.59	5.1	1.0	0.33	0.8	1826	11	1837	13
SD121-09R	496	29	0.06	0.03	138	0.111	0.35	5.0	1.0	0.32	0.9	1819	6	1807	15
SD121-09C	229	182	0.82	0.00	65	0.114	0.49	5.1	0.9	0.33	0.8	1858	9	1829	13
SD121-10R	394	22	0.06	0.01	110	0.112	0.39	5.0	1.0	0.32	0.9	1836	7	1807	14
SD121-10C	233	181	0.80	0.07	66	0.112	0.54	5.1	1.0	0.33	0.8	1839	10	1846	13
10SD154															
SD154-1R	95	31	0.34	--	2.0	0.081	16.0	0.278	16.2	0.02495	2.1	1215	315	159	3.3
SD154-1C	236	5	0.02	--	7.3	0.061	6.9	0.303	6.9	0.03603	1.0	635	148	228	2.3
SD154-2	187	64	0.35	--	4.0	0.050	6.4	0.168	6.5	0.02458	1.0	180	149	157	1.6
SD154-3	734	4	0.01	--	18.8	0.052	2.7	0.214	2.8	0.02986	0.7	283	63	190	1.2
SD154-2R	198	6	0.03	--	4.3	0.054	6.5	0.189	6.6	0.02520	1.0	392	146	160	1.6
SD154-4R	708	270	0.39	--	15.2	0.052	4.0	0.181	4.1	0.02495	0.7	307	91	159	1.1
SD154-7R	170	16	0.10	0.00	3.7	0.046	5.2	0.158	5.3	0.02509	1.0	-13	125	160	1.6
SD154-7C	105	3	0.03	--	2.8	0.061	10.5	0.263	10.7	0.03136	2.2	631	226	199	4.3
SD154-8C	307	97	0.33	0.00	6.5	0.046	3.6	0.154	3.9	0.02458	1.3	-25	88	157	2.0

SD154-8R	98	6	0.06	--	2.1	0.084	15.8	0.286	15.9	0.02470	2.1	1292	307	157	3.3
SD154-9	626	73	0.12	0.09	13.0	0.050	2.8	0.166	2.9	0.02413	0.7	185	65	154	1.0
SD154-10	272	9	0.03	--	5.7	0.050	5.0	0.169	5.1	0.02433	0.9	208	116	155	1.4
SD154-11	753	193	0.27	--	15.9	0.052	2.7	0.175	2.8	0.02464	1.0	269	61	157	1.5
SD154-12C	278	353	1.31	--	28.4	0.064	1.7	1.052	1.9	0.11897	0.9	745	36	725	5.9
SD154-12R	93	6	0.06	--	2.0	0.067	17.9	0.229	18.0	0.02461	1.9	851	373	157	2.9
SD154-14C	445	570	1.321	--	45.0	0.0632	1.2	1.026	1.4	0.1177	0.74	715	25	717	5.0
SD154-14R	282	38	0.140	--	5.7	0.0524	7.9	0.172	8.0	0.0237	0.97	304	181	151	1.4
SD154-15C	1243	62	0.051	--	39.6	0.0539	1.6	0.275	1.7	0.0371	0.60	365	36	235	1.4
SD154-15R	162	27	0.171	--	3.4	0.0645	9.6	0.217	9.7	0.0244	1.28	757	204	155	2.0
SD154-16C	724	683	0.975	--	58.8	0.0639	1.2	0.833	1.4	0.0946	0.66	738	25	583	3.7
SD154-16R	520	208	0.414	--	10.9	0.0543	4.4	0.183	4.4	0.0244	0.76	384	98	155	1.2
SD154-17	386	95	0.255	--	8.1	0.0494	4.7	0.167	4.8	0.0244	0.80	169	110	156	1.2
SD154-18C	586	52	0.092	--	16.3	0.0522	2.1	0.233	2.3	0.0323	0.96	293	47	205	1.9
SD154-18R	326	47	0.148	--	6.6	0.0635	10.0	0.205	10.1	0.0235	1.07	724	213	150	1.6
SD154-19C	166	23	0.142	--	5.2	0.0492	3.8	0.249	4.0	0.0367	1.02	157	89	232	2.3
SD154-19R	324	41	0.131	--	7.0	0.0514	6.6	0.177	6.7	0.0250	0.82	257	152	159	1.3
SD154-20C	93	32	0.356	--	38.9	0.1869	0.7	12.504	1.4	0.4852	1.24	2715	12	2550	26
SD154-20R	417	89	0.220	0.67	8.8	0.0438	6.4	0.148	6.5	0.0245	0.81	-121	159	156	1.2
SD154-	786	88	0.116	--	23.8	0.0506	1.8	0.246	1.9	0.0352	0.64	224	43	223	1.4

21C															
SD154-21R	346	28	0.083	--	7.2	0.0512	4.7	0.170	4.7	0.0241	0.83	250	107	154	1.3
10SD185															
SD185-1	351	125	0.37	0.02	131	0.169	0.7	10.12	1.6	0.435	1.42	2544	11	2329	27.8
SD185-2	136	59	0.45	1.52	3	0.037	18.9	0.13	18.9	0.025	1.35	-527	505	161	2.1
SD185-3	1354	213	0.16	0.00	552	0.175	0.2	11.46	0.9	0.475	0.84	2606	3	2505	17.4
SD185-3R	738	71	0.10	0.02	271	0.159	0.3	9.33	0.8	0.427	0.79	2441	5	2291	15.3
SD185-4	1661	146	0.09	0.40	37	0.049	2.0	0.17	2.2	0.026	0.73	142	47	165	1.2
SD185-5	3046	475	0.16	0.16	71	0.049	1.1	0.18	1.4	0.027	0.91	165	26	173	1.6
SD185-6	145	38	0.27	1.03	3	0.045	11.9	0.16	12.0	0.025	1.29	-51	290	161	2.1
SD185-7	343	76	0.23	0.04	88	0.159	0.5	6.53	2.1	0.299	2.05	2440	8	1685	30.4
SD185-8	3351	777	0.24	0.20	82	0.048	1.2	0.19	1.4	0.028	0.70	109	29	181	1.3
SD185-9	134	3	0.02	0.32	32	0.112	1.2	4.25	1.6	0.276	1.18	1829	21	1570	16.4
SD185-9R	405	29	0.07	0.19	37	0.099	1.1	1.44	1.8	0.106	1.43	1603	20	647	8.8
SD185-10	1649	236	0.15	0.11	50	0.111	1.3	0.54	1.6	0.036	0.98	1808	24	225	2.2
SD185-11	357	91	0.26	--	139	0.167	0.4	10.38	1.0	0.452	0.91	2525	6	2403	18.2
SD185-12	3700	642	0.18	0.20	85	0.048	1.7	0.18	2.0	0.027	0.93	117	41	171	1.6
SD185-12C	255	116	0.47	0.10	55	0.139	1.1	4.84	2.3	0.253	1.99	2211	19	1454	25.9
SD185-13	565	144	0.26	0.28	13	0.047	3.2	0.17	3.3	0.026	0.83	59.8	77	164	1.3
SD185-14	302	95	0.32	0.85	7	0.059	4.8	0.23	5.0	0.028	1.46	565	103	178	2.6
SD185-15	252	166	0.68	0.03	102	0.165	0.4	10.68	1.5	0.470	1.47	2507	7	2481	30.3
SD185-16R	3481	734	0.22	0.28	84	0.049	1.1	0.19	1.4	0.028	0.79	155	27	179	1.4
SD185-16C	1182	87	0.08	0.03	446	0.159	0.3	9.66	1.1	0.439	1.11	2450	5	2348	21.7
SD185-17	2924	616	0.22	0.38	68	0.050	1.6	0.19	1.8	0.027	0.82	210	38	171	1.4
SD185-18	3228	1256	0.40	0.09	75	0.051	1.0	0.19	1.3	0.027	0.80	229	22	171	1.3
SD185-19	207	90	0.45	0.00	76	0.153	0.5	9.00	1.1	0.428	1.02	2377	9	2295	19.7

SD185-20	650	291	0.46	0.58	16	0.046	12.1	0.18	12.2	0.029	1.30	-4	293	181	2.3
SD185-21	406	111	0.28	0.06	94	0.155	0.8	5.72	2.0	0.269	1.80	2397	13	1534	24.6
SD185-22	1641	547	0.34	0.33	65	0.099	1.6	0.63	2.6	0.046	2.03	1608	31	291	5.8
10SD128C															
128c-01c	31	22	0.73	--	9	0.1366	2.9	6.45	3.7	0.343	2.31	2185	51	1899	38.0
128c-01	191	88	0.47	--	4	0.0570	11.4	0.17	11.5	0.022	1.36	490	252	141	1.9
128c-02	316	244	0.80	--	35	0.0676	1.4	1.19	1.7	0.128	0.93	856	29	774	6.8
128c-03	885	720	0.84	--	95	0.0660	0.9	1.13	1.2	0.124	0.76	807	20	756	5.5
128c-03r	98	28	0.29	--	2	0.0471	6.3	0.17	6.5	0.027	1.33	56.5	151	169	2.2
128c-04	364	235	0.67	--	7	0.0599	7.0	0.19	7.1	0.023	1.03	599	152	146	1.5
128c-05	236	108	0.47	--	25	0.0673	3.1	1.14	3.3	0.122	1.04	847	65	744	7.3
128c-6r	453	225	0.51	0.46	9	0.0478	5.5	0.15	5.6	0.023	0.90	89.9	130	146	1.3
128c-6c	631	574	0.94	--	12	0.0541	4.0	0.17	4.1	0.023	0.83	374	90	144	1.2
128c-7c	139	60	0.44	1.21	3	0.0558	11.3	0.22	11.4	0.029	1.40	443	251	184	2.5
128c-7r	379	156	0.43	--	7	0.0582	7.8	0.18	7.8	0.023	1.04	538	170	147	1.5
128c-8c	175	196	1.16	0.12	19	0.0658	2.1	1.15	2.3	0.127	1.11	799	43	769	8.0
128c-8r	798	768	0.99	--	16	0.0477	4.9	0.15	5.0	0.023	0.78	83.5	117	146	1.1
128c-9	209	197	0.97	0.17	23	0.0654	2.1	1.16	2.3	0.128	1.06	788	43	779	7.8
128c-10	327	128	0.40	--	6	0.0548	5.8	0.17	5.9	0.023	0.99	404	130	144	1.4
128c-11	416	231	0.57	--	44	0.0645	1.6	1.11	1.8	0.125	0.90	757	34	757	6.4
128c-12	2082	44	0.02	0.34	46	0.0480	2.1	0.17	2.2	0.026	0.70	101	49	164	1.1
128c-12r	1685	489	0.30	0.27	34	0.0478	2.4	0.15	2.5	0.023	0.72	87.5	56	148	1.0
128c-13	449	418	0.96	0.00	49	0.0655	1.1	1.14	1.4	0.126	0.86	789	23	767	6.2
128c-14	389	226	0.60	--	8	0.0499	4.9	0.16	5.0	0.023	0.92	188	114	145	1.3
128c-15	671	644	0.99	2.30	13	0.0624	6.6	0.20	6.6	0.023	0.93	686	140	146	1.3
128c-16r	188	69	0.38	--	4	0.0565	9.6	0.19	9.7	0.024	1.26	472	213	152	1.9
128c-16c	257	337	1.36	0.00	27	0.0637	1.6	1.08	1.9	0.123	1.01	731	34	748	7.1
128c-17	331	169	0.53	0.20	6	0.0464	7.6	0.15	7.7	0.023	1.50	16.2	182	145	2.1

128c-18	302	113	0.39	1.13	6	0.0421	10.8	0.13	10.8	0.022	1.08	-223	271	138	1.5
128c-19	637	253	0.41	0.00	13	0.0520	2.5	0.16	2.7	0.023	1.15	285	56	146	1.7
128c-20	190	73	0.40	0.39	4	0.0495	8.0	0.16	8.1	0.023	1.16	171	187	147	1.7
128c-21	1599	49	0.03	--	45	0.0513	1.7	0.23	1.8	0.033	0.72	255	39	207	1.5
128c-22	833	507	0.63	0.07	158	0.1116	0.5	3.39	1.3	0.220	1.18	1825	9	1282	13.7
128c-23	566	229	0.42	--	11	0.0519	4.7	0.16	4.8	0.023	0.86	283	108	146	1.2
128c-24	452	321	0.73	0.00	46	0.0658	1.2	1.07	1.5	0.117	0.87	799	26	716	5.9
128c-24r	312	79	0.26	--	6	0.0573	6.7	0.19	6.9	0.024	1.52	504	147	150	2.2
128c-25	815	530	0.67	5.63	85	0.1002	3.4	1.67	3.5	0.121	0.83	1628	63	736	5.8
128c-25r	491	299	0.63	15.02	11	0.1637	13.5	0.59	13.9	0.026	3.29	2494	227	167	5.4
128c-26	776	830	1.11	--	16	0.0521	3.3	0.17	3.5	0.023	0.97	289	76	149	1.4
128c-27	337	145	0.44	--	7	0.0627	8.4	0.21	8.4	0.024	1.18	699	178	153	1.8
128c-28	252	137	0.56	0.05	27	0.0649	1.7	1.10	2.0	0.123	1.01	770	36	749	7.1
128c-29c	577	196	0.35	--	28	0.0626	1.9	0.48	2.0	0.056	0.83	693	40	351	2.8
128c-29r	1006	1167	1.20	--	20	0.0499	2.6	0.16	2.8	0.023	0.76	192	62	149	1.1
128c-30	378	221	0.60	--	7	0.0582	9.2	0.18	9.2	0.023	1.02	539	201	144	1.4
128c-31	373	178	0.49	0.41	7	0.0472	6.2	0.15	6.2	0.022	0.95	61.1	147	143	1.3
128c-32	382	196	0.53	--	8	0.0556	6.5	0.18	6.6	0.023	0.99	436	145	147	1.4
128c-33	332	240	0.75	0.08	33	0.0633	1.6	1.00	1.9	0.115	0.93	718	34	699	6.1
128c-34	182	248	1.41	--	20	0.0684	2.1	1.23	2.4	0.130	1.13	880	44	790	8.4
128c-35	612	541	0.91	0.43	24	0.0588	2.5	0.37	2.7	0.045	1.03	558	55	286	2.9

Appendix Table 5.3 $^{40}Ar/^{39}Ar$ results for granites and metamorphic rocks in the Jiaobei region

Step	Power (W) /T(°C)	36Ar (V)	± σ36 (%)	37Ar (V)	± σ37 (%)	38Ar (V)	± σ38 (%)	39Ar (V)	± σ39 (%)	40Ar (V)	± σ40 (%)	40Ar* (%)	Age (Ma)	± 2σ (Ma)	K/Ca
Sample: 10SD134, Phlogopite, Irradiation disk: I15t40h, J=0.00341900 ± 0.00000615															
1	57.5	2.17E-06	297.4	6.36E-05	181.2	7.76E-06	67.2	1.87E-04	5.4	0.03	0.48	97.9	781.2	107.3	1.5
2	58.0	1.58E-05	44.3	4.99E-05	237.8	1.05E-05	49.7	1.76E-04	5.2	0.05	0.20	89.7	1059.9	116.2	1.8
3	58.3	-1.36E-06	424.3	-2.99E-05	390.5	1.30E-07	#####	2.89E-04	4.6	0.13	0.15	100.3	1683.4	104.8	-5.0
4	58.7	1.05E-05	65.4	-7.06E-05	150.2	9.59E-06	69.8	6.66E-04	2.5	0.32	0.11	99.0	1755.3	57.7	-4.9
5	59.1	1.39E-05	38.9	-8.82E-05	121.7	7.54E-06	67.9	2.07E-04	5.5	0.10	0.30	95.9	1717.2	127.4	-1.2
6	59.6	6.57E-06	116.3	-1.24E-04	93.3	1.18E-05	40.6	4.78E-04	3.9	0.24	0.08	99.2	1801.8	91.2	-2.0
7	60.1	1.85E-05	33.9	-1.31E-04	86.2	2.53E-05	22.0	1.63E-03	1.3	0.78	0.06	99.3	1733.3	29.4	-6.5
8	61.0	3.12E-05	20.6	-5.73E-05	188.2	6.07E-05	9.5	4.04E-03	0.9	2.30	0.04	99.6	1942.8	21.3	-36.5
9	62.0	1.35E-05	46.0	-6.59E-05	166.6	5.23E-05	13.7	3.41E-03	1.2	1.91	0.03	99.8	1926.4	28.7	-26.8
10	63.0	6.85E-06	92.2	-1.51E-04	76.5	7.27E-05	8.9	4.88E-03	0.9	2.58	0.04	99.9	1857.4	20.7	-16.7
11	64.0	5.83E-06	115.4	-9.64E-05	115.0	4.31E-05	17.5	3.30E-03	1.4	1.80	0.03	99.9	1893.8	32.9	-17.7
12	66.0	8.25E-05	12.3	3.31E-03	5.6	3.52E-04	4.3	2.37E-02	0.7	12.59	0.03	99.8	1864.7	15.3	3.7
13	**70.0**	**1.15E-04**	**33.8**	**8.17E-03**	**6.8**	**7.81E-04**	**6.6**	**5.35E-02**	**0.7**	**31.15**	**0.03**	**99.9**	**1974.1**	**17.4**	**3.4**
14	**70.0**	**1.15E-04**	**33.8**	**8.17E-03**	**6.8**	**7.81E-04**	**6.6**	**5.35E-02**	**0.7**	**31.15**	**0.03**	**99.9**	**1974.1**	**17.4**	**3.4**
Sample: 10SD138, Muscovite, Irradiation disk: I15t40h, J = 0.00341900 ± 0.00000600															
1	56.9	1.06E-05	90.6	8.26E-05	137.8	2.98E-06	197.3	1.04E-04	15.5	0.04	0.45	91.5	1354.7	335.8	0.6
2	57.1	2.68E-05	27.0	6.43E-05	174.9	6.38E-06	87.4	2.53E-04	5.2	0.11	0.14	92.6	1536.5	115.7	2.0
3	57.3	5.78E-05	14.7	8.63E-05	134.4	1.55E-05	34.0	4.87E-04	3.1	0.21	0.17	91.7	1527.1	70.4	2.9
4	57.5	8.06E-05	12.3	1.36E-04	78.5	2.61E-05	21.1	1.34E-03	2.0	0.59	0.03	95.9	1598.6	44.3	5.1
5	57.8	8.11E-05	11.6	1.43E-04	77.1	6.98E-05	8.2	3.72E-03	1.4	1.50	0.04	98.4	1547.5	29.7	13.5
6	58.0	2.53E-05	31.8	3.02E-05	382.6	4.86E-05	17.4	3.19E-03	1.1	1.26	0.04	99.4	1531.7	23.0	54.7
7	58.3	1.33E-05	66.3	2.23E-05	532.1	3.22E-05	17.1	2.03E-03	1.5	0.79	0.06	99.5	1520.0	31.6	47.2

8	58.7	3.48E-05	34.9	8.78E-05	123.0	9.88E-05	8.6	6.58E-03	0.8	2.45	0.02	99.6	1474.6	16.5	38.8
9	59.1	9.96E-06	93.7	2.68E-05	444.0	1.08E-04	6.7	7.67E-03	0.9	2.73	0.04	99.9	1433.3	18.6	148.0
10	59.6	2.22E-05	37.5	8.71E-05	140.5	1.35E-04	7.1	8.72E-03	0.8	3.50	0.03	99.8	1555.9	16.8	51.9
11	60.1	2.20E-06	363.6	6.26E-05	173.6	6.33E-05	13.1	4.28E-03	1.0	1.55	0.05	100.0	1454.7	19.9	35.4
12	61.0	1.54E-05	67.9	7.39E-05	156.8	2.11E-04	5.8	1.51E-02	0.4	5.84	0.02	99.9	1520.8	8.5	105.5
13	62.0	-3.58E-06	222.6	5.68E-05	190.2	4.15E-06	137.5	3.07E-04	5.3	0.11	0.22	100.9	1482.3	115.7	2.8
Sample: 10JD20, Muscovite, Irradiation disk: I15t40h, J = 0.00341900 ±0.00000615															
1	56.9	1.82E-05	46.1	-1.95E-05	548.4	4.39E-06	128.0	3.92E-04	3.8	0.10	0.29	94.66	1098.0	75.3	-10.4
2	57.1	6.82E-06	86.2	3.61E-05	324.0	-4.68E-06	128.3	1.17E-04	7.7	0.03	0.79	93.66	1137.3	163.7	1.7
3	57.3	8.27E-06	68.8	-8.73E-06	1312.8	3.98E-07	#####	3.03E-04	3.9	0.09	0.36	97.25	1237.2	78.6	-18.0
4	57.5	7.43E-06	72.3	-1.24E-05	1082.0	6.45E-06	93.8	7.81E-04	2.0	0.34	0.09	99.34	1628.1	45.0	-32.6
5	57.8	-1.49E-07	4327.0	7.11E-05	151.8	1.45E-05	38.3	1.68E-03	1.7	0.75	0.07	100.01	1670.8	37.9	12.3
6	58.0	2.00E-06	366.5	-4.37E-05	252.5	2.58E-05	27.7	1.98E-03	1.0	0.91	0.05	99.93	1705.2	22.0	-23.5
7	58.3	2.30E-06	328.7	4.83E-05	225.4	5.53E-05	13.5	4.65E-03	1.0	2.21	0.03	99.97	1737.4	22.1	49.9
8	58.7	-1.31E-06	632.0	-6.10E-05	204.9	7.21E-05	13.8	6.57E-03	0.7	3.31	0.04	100.01	1805.5	16.7	-55.8
9	59.1	**-6.86E-07**	**1189.9**	**4.80E-05**	**232.1**	**1.77E-04**	**4.3**	**1.36E-02**	**0.7**	**6.96**	**0.01**	**100.00**	**1819.6**	**15.4**	**147.1**
10	59.6	**-1.05E-05**	**92.7**	**-2.79E-05**	**462.5**	**2.47E-04**	**3.7**	**1.87E-02**	**0.6**	**9.68**	**0.02**	**100.03**	**1837.0**	**13.4**	**-347.1**
11	60.1	**-2.14E-06**	**371.5**	**1.29E-04**	**87.3**	**2.36E-04**	**4.0**	**1.81E-02**	**0.7**	**9.35**	**0.02**	**100.01**	**1833.5**	**16.9**	**72.7**
12	61.0	**-3.45E-06**	**221.5**	**1.11E-04**	**109.4**	**1.82E-04**	**3.5**	**1.29E-02**	**0.5**	**6.71**	**0.01**	**100.02**	**1838.0**	**10.9**	**60.3**
13	62.0	**-1.32E-05**	**43.6**	**2.37E-05**	**507.5**	**6.84E-05**	**10.4**	**5.24E-03**	**0.6**	**2.70**	**0.03**	**100.15**	**1834.5**	**13.9**	**114.5**
14	63.0	**-4.05E-06**	**185.6**	**1.67E-04**	**74.5**	**5.84E-05**	**14.2**	**5.42E-03**	**1.0**	**2.79**	**0.03**	**100.04**	**1828.1**	**22.2**	**16.8**
15	64.0	**-3.96E-06**	**163.2**	**1.90E-04**	**63.8**	**5.50E-05**	**12.8**	**3.80E-03**	**1.0**	**1.96**	**0.03**	**100.06**	**1830.3**	**22.1**	**10.4**
16	66.0	**-8.09E-06**	**78.6**	**2.29E-05**	**491.7**	**1.77E-05**	**38.7**	**2.07E-03**	**1.6**	**1.09**	**0.07**	**100.22**	**1857.3**	**37.7**	**46.8**
17	70.0	**-1.33E-05**	**59.6**	**1.38E-04**	**93.9**	**7.67E-06**	**73.0**	**4.81E-04**	**3.0**	**0.25**	**0.16**	**101.60**	**1846.3**	**73.2**	**1.8**
Sample: 10SD201, Hornblende package, Irradiation disk: I15t40h, J = 0.00341900 ±0.00000615															
1	650	5.37E-05	137.6	8.33E-06	233.0	1.04E-05	82.3	3.32E-04	4.5	0.14	13.58	88.54	1532.7	494.8	17.1
2	750	9.73E-05	76.5	-9.36E-06	214.6	2.78E-05	30.9	5.67E-04	3.9	0.24	7.87	87.97	1535.8	296.0	-26.1
3	850	2.42E-05	306.5	3.21E-05	68.4	3.30E-05	27.1	1.18E-03	1.8	0.48	3.92	98.51	1616.1	136.4	15.8

4	920	5.82E-05	127.5	1.30E-05	166.9	1.14E-04	8.5	5.91E-03	0.8	2.76	0.69	99.37	1767.7	29.6	195.9
5	**975**	**5.17E-04**	**17.1**	**8.83E-04**	**4.2**	**1.49E-03**	**3.9**	**8.50E-02**	**0.5**	**42.10**	**0.08**	**99.63**	**1838.6**	**12.1**	**41.4**
6	**1000**	**4.30E-04**	**22.5**	**1.98E-03**	**4.2**	**2.28E-03**	**5.4**	**1.33E-01**	**0.4**	**65.46**	**0.07**	**99.80**	**1832.0**	**10.4**	**29.0**
7	1025	3.74E-05	199.2	4.97E-05	39.4	2.92E-04	5.2	1.71E-02	0.5	8.19	0.24	99.86	1798.9	14.2	148.5
8	1050	3.80E-05	195.1	3.00E-06	584.8	1.21E-04	9.1	6.72E-03	0.5	3.11	0.61	99.64	1762.8	24.3	962.2
9	**1075**	**8.71E-05**	**85.3**	**2.67E-05**	**78.5**	**2.66E-04**	**4.9**	**1.48E-02**	**0.7**	**7.35**	**0.27**	**99.65**	**1844.2**	**19.1**	**237.6**
10	**1100**	**2.50E-04**	**30.9**	**8.51E-04**	**6.9**	**1.31E-03**	**4.1**	**8.09E-02**	**0.5**	**39.55**	**0.07**	**99.81**	**1825.3**	**11.9**	**40.9**
11	**1125**	**2.08E-04**	**36.8**	**8.23E-04**	**8.5**	**8.80E-04**	**5.0**	**5.01E-02**	**0.7**	**24.71**	**0.09**	**99.75**	**1834.7**	**16.4**	**26.2**
12	**1150**	**1.27E-05**	**583.1**	**-9.76E-07**	**1900.9**	**2.18E-05**	**36.1**	**1.15E-03**	**1.8**	**0.58**	**3.28**	**99.35**	**1852.0**	**124.2**	**-508.3**
13	**1175**	**3.35E-06**	**2203.1**	**9.09E-06**	**228.5**	**1.71E-05**	**46.6**	**1.06E-03**	**1.7**	**0.52**	**3.68**	**99.81**	**1819.8**	**135.1**	**50.2**
14	**1200**	**1.50E-05**	**494.8**	**-3.87E-06**	**492.5**	**1.46E-05**	**61.3**	**2.70E-04**	**4.5**	**0.12**	**15.28**	**96.41**	**1720.0**	**548.2**	**-30.0**
15	**1300**	**2.15E-05**	**345.3**	**-1.92E-05**	**103.7**	**8.93E-06**	**87.9**	**1.08E-04**	**9.6**	**0.05**	**37.45**	**87.35**	**1631.5**	**1431.0**	**-2.4**
16	**1400**	**-7.81E-05**	**95.3**	**-1.43E-06**	**1289.8**	**1.67E-05**	**50.2**	**1.22E-03**	**1.9**	**0.59**	**3.24**	**103.97**	**1855.5**	**120.0**	**-365.2**
Sample: 11JD006, Biotite, Irradiation disk: I15t40h, J = 0.00341900 ± 0.00000615															
1	56.4	8.27E-06	62.9	1.15E-04	69.5	4.64E-06	82.4	1.98E-04	5.0	0.03	0.83	92.51	759.4	89.3	0.9
2	56.5	1.31E-05	49.0	1.11E-04	96.1	1.75E-05	25.3	9.53E-04	2.5	0.19	0.22	97.93	913.0	38.6	4.5
3	56.6	5.93E-06	91.2	2.04E-05	402.9	7.54E-06	60.6	8.02E-04	1.7	0.16	0.19	98.88	920.7	29.2	20.3
4	56.7	1.26E-05	56.0	-9.44E-05	89.9	4.51E-05	13.8	3.17E-03	0.9	0.63	0.09	99.40	935.7	13.8	-17.4
5	56.8	8.10E-06	71.2	-1.36E-04	67.0	1.10E-04	7.7	6.94E-03	0.9	1.38	0.07	99.82	932.9	13.4	-26.4
6	56.9	4.16E-05	19.0	-4.77E-05	174.8	2.25E-04	5.3	1.53E-02	0.6	2.98	0.03	99.58	917.1	8.6	-166.1
7	57.0	6.54E-05	14.3	-8.76E-05	102.9	3.88E-04	3.1	2.80E-02	0.4	5.38	0.02	99.64	907.4	6.5	-165.7
8	57.1	5.97E-05	11.8	-8.92E-05	98.6	4.13E-04	3.4	2.94E-02	0.4	5.62	0.02	99.68	904.9	5.6	-170.6
9	57.2	4.47E-05	21.2	-5.82E-05	157.2	2.71E-04	3.9	1.85E-02	0.4	3.54	0.03	99.62	905.1	6.3	-164.4
10	57.3	1.50E-05	56.4	-4.78E-05	193.0	6.42E-05	12.3	4.77E-03	0.7	0.91	0.07	99.51	902.6	11.0	-51.7
11	57.4	5.74E-07	1011.6	-1.14E-04	77.3	5.61E-05	9.3	4.30E-03	0.7	0.80	0.09	99.98	885.2	10.5	-19.5
12	58.0	8.74E-05	10.2	-5.21E-06	1703.5	6.60E-04	3.0	4.64E-02	0.4	8.76	0.02	99.70	895.1	5.7	-4617.5
13	60.0	9.31E-05	7.0	1.68E-04	51.7	6.35E-04	2.7	4.62E-02	0.5	8.76	0.02	99.68	898.1	6.4	142.4

Sample: 10SD207, Biotite, Irradiation disk: I12t25h, J = 0.00881500 ± 0.00002204

1	56.5	3.29E-05	12.9	3.31E-04	262.4	4.24E-05	10.3	9.52E-04	3.0	0.76	0.08	98.71	3734.0	95.3	1.2
2	56.8	1.89E-05	19.7	-9.83E-04	81.3	3.56E-05	14.2	1.88E-03	1.0	0.50	0.05	98.84	2146.2	24.9	-0.8
3	57.2	4.63E-05	17.0	4.94E-05	1559.8	1.49E-04	3.9	9.20E-03	0.9	1.10	0.02	98.75	1287.8	16.2	80.1
4	57.5	7.79E-05	10.6	-5.47E-04	145.8	6.23E-04	1.3	4.45E-02	0.6	3.05	0.43	99.23	846.1	10.1	-35.0
5	57.7	2.69E-06	180.5	2.16E-04	380.3	1.36E-04	6.6	9.90E-03	0.8	0.37	0.08	99.79	509.4	8.0	19.7
6	57.9	2.68E-05	24.4	-6.24E-04	153.4	6.85E-04	2.0	5.49E-02	0.4	1.77	0.05	99.54	449.3	3.5	-37.8
7	58.0	1.56E-05	26.7	-1.86E-04	398.9	2.69E-04	3.6	2.15E-02	0.5	0.64	0.05	99.27	418.1	3.9	-49.6
8	58.1	4.35E-06	99.0	-2.71E-04	307.5	3.99E-05	7.8	3.61E-03	0.8	0.11	0.15	98.80	425.9	10.9	-5.7
9	58.3	3.66E-06	91.5	7.33E-04	111.5	5.86E-05	10.8	4.77E-03	0.7	0.14	0.15	99.29	424.8	7.6	2.8
Sample: 10JD31, Biotite, Irradiation disk:I12t25h, J = 0.00881500 ±0.00002204															
1	56.3	1.52E-04	4.6	1.09E-04	634.8	1.64E-04	6.2	9.28E-03	1.2	0.11	0.15	57.96	104.1	7.3	36.4
2	56.5	2.14E-04	4.1	2.97E-04	211.7	3.37E-04	3.8	2.16E-02	0.5	0.23	0.13	72.28	118.1	3.9	31.4
3	**56.7**	**1.62E-04**	**5.7**	**1.84E-04**	**412.9**	**6.56E-04**	**1.8**	**4.71E-02**	**0.6**	**0.43**	**0.06**	**88.69**	**123.4**	**2.2**	**109.7**
4	**56.9**	**1.96E-05**	**25.9**	**-1.37E-03**	**50.1**	**1.43E-04**	**5.3**	**1.02E-02**	**0.6**	**0.09**	**0.10**	**93.26**	**123.8**	**4.6**	**-3.2**
5	**57.2**	**2.80E-05**	**21.1**	**7.59E-04**	**71.7**	**5.62E-04**	**2.5**	**4.43E-02**	**0.5**	**0.37**	**0.06**	**97.73**	**124.2**	**1.7**	**25.1**
6	**57.5**	**7.89E-05**	**7.7**	**2.00E-03**	**34.8**	**2.03E-03**	**1.4**	**1.53E-01**	**0.4**	**1.26**	**0.09**	**98.14**	**124.1**	**1.0**	**33.0**
7	**57.7**	**5.83E-06**	**87.7**	**-2.57E-04**	**339.2**	**2.41E-04**	**5.0**	**1.81E-02**	**0.5**	**0.15**	**0.16**	**98.79**	**122.4**	**2.8**	**-30.3**
8	**58**	**8.70E-06**	**68.5**	**-1.66E-04**	**376.1**	**4.80E-04**	**2.1**	**3.93E-02**	**0.4**	**0.32**	**0.05**	**99.17**	**123.5**	**1.7**	**-101.7**
9	**58.3**	**1.33E-05**	**48.6**	**1.33E-03**	**41.2**	**9.53E-04**	**1.8**	**7.43E-02**	**0.4**	**0.61**	**0.26**	**99.36**	**124.4**	**1.5**	**24.0**
10	**58.6**	**1.34E-05**	**47.8**	**1.78E-03**	**33.6**	**4.88E-04**	**4.6**	**3.82E-02**	**0.4**	**0.31**	**0.08**	**98.76**	**124.4**	**1.8**	**9.2**
11	**59**	**7.53E-06**	**88.4**	**1.08E-03**	**52.6**	**4.65E-04**	**4.0**	**3.54E-02**	**0.5**	**0.29**	**0.09**	**99.24**	**124.1**	**2.1**	**14.1**
12	**59.5**	**1.87E-06**	**307.6**	**2.97E-04**	**231.5**	**3.44E-04**	**3.6**	**2.81E-02**	**0.4**	**0.23**	**0.15**	**99.76**	**123.3**	**2.1**	**40.7**
13	**60**	**3.25E-06**	**160.2**	**1.81E-03**	**41.5**	**8.22E-05**	**9.3**	**5.34E-03**	**1.0**	**0.04**	**0.31**	**98.13**	**124.0**	**9.0**	**1.3**
Sample: 10SD185, Biotite, Irradiation disk:I12t25h, J = 0.00881500 ±0.00002204															
1	55.5	1.87E-04	5.2	1.30E-03	75.1	1.36E-04	5.8	8.05E-03	0.8	0.12	0.20	52.46	117.4	10.9	2.7
2	55.8	2.93E-06	203.4	1.42E-03	66.0	8.06E-07	347.4	4.05E-04	3.0	0.00	4.05	80.19	116.3	131.9	0.1
3	56.2	2.21E-04	3.8	-1.91E-04	500.2	2.94E-04	3.4	1.99E-02	0.6	0.22	0.15	70.16	120.1	4.0	-44.7
4	**56.5**	**7.95E-05**	**8.9**	**5.86E-04**	**188.5**	**5.58E-04**	**1.8**	**4.41E-02**	**0.4**	**0.38**	**0.09**	**93.68**	**122.4**	**1.8**	**32.3**

5	**56.7**	**6.26E-06**	**102.3**	**7.70E-04**	**118.2**	**2.82E-04**	**4.0**	**2.21E-02**	**0.4**	**0.18**	**0.14**	**98.99**	**124.1**	**2.8**	**12.4**
6	**57.0**	**1.50E-05**	**30.5**	**5.79E-04**	**102.1**	**9.32E-04**	**1.5**	**7.40E-02**	**0.4**	**0.60**	**0.04**	**99.26**	**124.3**	**1.1**	**54.9**
7	**57.1**	**6.09E-06**	**71.5**	**1.66E-04**	**385.2**	**3.36E-04**	**3.6**	**2.66E-02**	**0.5**	**0.21**	**0.12**	**99.15**	**122.7**	**1.9**	**68.7**
8	**57.3**	**-1.51E-07**	**2454.1**	**1.58E-03**	**35.7**	**2.31E-04**	**3.5**	**1.74E-02**	**0.5**	**0.14**	**0.24**	**100.12**	**124.4**	**2.2**	**4.7**
9	**57.5**	**-7.52E-09**	**######**	**-1.14E-04**	**518.5**	**3.68E-04**	**3.1**	**2.93E-02**	**0.6**	**0.24**	**0.10**	**99.99**	**124.1**	**2.0**	**-110.3**
10	**57.7**	**1.12E-05**	**29.4**	**-4.92E-04**	**119.6**	**6.29E-04**	**2.4**	**5.03E-02**	**0.4**	**0.40**	**0.06**	**99.15**	**122.2**	**1.2**	**-43.9**
11	**58.0**	**4.05E-07**	**894.2**	**-2.51E-04**	**233.4**	**9.96E-05**	**9.7**	**8.56E-03**	**0.6**	**0.07**	**0.15**	**99.78**	**122.5**	**4.0**	**-14.7**
Sample: 10SD154, Biotite, Irradiation disk:I12t25h, J = 0.00881500 ± 0.00002204															
1	56.3	2.48E-05	23.4	-4.37E-04	267.6	4.66E-05	11.9	2.72E-03	1.5	0.02	0.60	66.55	84.4	19.5	-2.7
2	56.5	2.68E-04	3.8	5.60E-04	210.7	3.20E-04	2.5	2.10E-02	0.5	0.23	0.08	65.28	110.1	4.5	16.1
3	56.6	7.42E-06	79.6	-6.76E-05	1842.5	7.95E-05	10.6	6.43E-03	1.0	0.05	0.18	95.90	124.1	8.5	-40.9
4	56.8	7.77E-05	11.8	8.39E-04	139.5	6.10E-04	3.9	4.76E-02	0.4	0.40	0.10	94.18	120.9	2.0	24.4
5	**57.0**	**1.52E-05**	**48.4**	**7.38E-04**	**160.5**	**5.46E-04**	**3.1**	**4.19E-02**	**0.5**	**0.34**	**0.10**	**98.68**	**123.7**	**1.9**	**24.4**
6	**57.2**	**5.25E-06**	**79.2**	**8.14E-04**	**146.4**	**5.20E-04**	**4.1**	**4.13E-02**	**0.5**	**0.33**	**0.07**	**99.54**	**123.8**	**1.4**	**21.8**
7	**57.4**	**4.16E-06**	**122.7**	**2.30E-03**	**51.6**	**6.38E-04**	**2.9**	**5.11E-02**	**0.6**	**0.42**	**0.14**	**99.74**	**125.4**	**1.7**	**9.5**
8	**57.6**	**1.49E-05**	**31.1**	**2.83E-03**	**42.5**	**1.13E-03**	**1.6**	**8.74E-02**	**0.5**	**0.71**	**0.09**	**99.40**	**123.6**	**1.4**	**13.3**
9	**57.7**	**-9.78E-06**	**59.1**	**-5.46E-04**	**154.0**	**3.81E-05**	**12.9**	**3.20E-03**	**1.3**	**0.03**	**0.37**	**111.14**	**136.8**	**16.3**	**-2.5**
10	**57.8**	**6.48E-07**	**905.1**	**4.15E-04**	**221.2**	**2.59E-04**	**2.9**	**2.09E-02**	**0.5**	**0.17**	**0.13**	**99.90**	**122.8**	**2.7**	**21.6**
11	**57.9**	**-4.26E-07**	**1156.8**	**3.16E-04**	**279.3**	**1.01E-04**	**5.5**	**7.77E-03**	**0.6**	**0.06**	**0.18**	**100.24**	**123.2**	**5.8**	**10.6**
12	**58.1**	**-1.16E-08**	**######**	**1.48E-05**	**5994.4**	**7.34E-05**	**4.5**	**5.17E-03**	**0.8**	**0.04**	**0.28**	**100.01**	**124.1**	**10.7**	**150.1**
13	**58.4**	**7.70E-06**	**69.7**	**6.10E-04**	**145.9**	**4.25E-04**	**2.8**	**3.40E-02**	**0.6**	**0.28**	**0.12**	**99.18**	**123.7**	**1.9**	**24.0**
14	**58.7**	**7.14E-06**	**73.9**	**-8.04E-04**	**110.4**	**3.03E-04**	**2.8**	**2.40E-02**	**0.5**	**0.19**	**0.13**	**98.85**	**122.1**	**2.3**	**-12.8**
15	**59.1**	**2.07E-06**	**261.4**	**8.51E-04**	**96.0**	**3.23E-04**	**2.7**	**2.50E-02**	**0.6**	**0.20**	**0.20**	**99.72**	**123.4**	**2.5**	**12.6**
16	**59.5**	**4.04E-06**	**127.3**	**-1.18E-03**	**70.3**	**2.11E-04**	**4.8**	**1.68E-02**	**0.6**	**0.14**	**0.24**	**99.03**	**122.5**	**3.1**	**-6.1**
17	**61.0**	**9.86E-06**	**44.1**	**-1.53E-03**	**42.4**	**2.52E-04**	**4.2**	**1.88E-02**	**0.5**	**0.15**	**0.16**	**97.97**	**121.4**	**2.4**	**-5.3**
Sample: 10SD128B, Biotite, Irradiation disk:I12t25h, J = 0.00881500 ± 0.00002204															
1	**56.3**	**7.34E-05**	**10.5**	**-2.87E-04**	**244.1**	**2.03E-04**	**3.7**	**1.56E-02**	**0.5**	**0.15**	**0.19**	**85.44**	**126.3**	**4.6**	**-23.4**
2	**56.6**	**2.70E-05**	**26.0**	**-1.50E-04**	**494.0**	**2.00E-04**	**4.6**	**1.51E-02**	**0.7**	**0.13**	**0.23**	**93.82**	**124.2**	**4.4**	**-43.3**

3	**56.9**	**2.29E-05**	**29.6**	**8.21E-04**	**96.7**	**4.86E-04**	**2.9**	**3.72E-02**	**0.5**	**0.31**	**0.10**	**97.81**	**125.3**	**2.0**	**19.5**
4	**57.2**	**1.09E-05**	**34.4**	**9.61E-04**	**50.1**	**1.48E-04**	**5.3**	**1.27E-02**	**0.6**	**0.11**	**0.09**	**96.98**	**123.0**	**3.0**	**5.7**
5	**57.4**	**5.30E-07**	**658.5**	**6.35E-04**	**85.1**	**1.57E-04**	**4.8**	**1.30E-02**	**0.7**	**0.11**	**0.18**	**99.90**	**127.2**	**2.9**	**8.8**
Sample: 10JD34, Biotite, Irradiation disk:I12t25h, J = 0.00881500 ±0.00002204															
1	**56.0**	**7.32E-05**	**10.6**	**7.42E-04**	**126.9**	**1.78E-04**	**8.1**	**1.40E-02**	**0.5**	**0.13**	**0.08**	**83.22**	**118.4**	**5.1**	**8.1**
2	**56.2**	**2.22E-05**	**21.1**	**2.33E-04**	**433.3**	**1.31E-04**	**4.6**	**1.05E-02**	**0.6**	**0.09**	**0.12**	**92.73**	**123.4**	**4.2**	**19.3**
3	**56.4**	**5.09E-05**	**13.3**	**-2.45E-04**	**426.0**	**1.54E-04**	**6.7**	**1.13E-02**	**0.5**	**0.10**	**0.17**	**85.43**	**120.9**	**5.4**	**-19.9**
4	**56.7**	**1.70E-04**	**8.2**	**1.64E-03**	**59.6**	**4.71E-04**	**2.9**	**3.46E-02**	**0.6**	**0.33**	**0.11**	**84.71**	**124.2**	**3.8**	**9.1**
5	**56.9**	**1.45E-04**	**8.9**	**5.71E-05**	**1810.9**	**5.73E-04**	**2.1**	**4.28E-02**	**0.4**	**0.38**	**0.12**	**88.70**	**122.2**	**2.9**	**322.3**
6	**57.1**	**2.17E-05**	**26.0**	**-8.09E-04**	**129.0**	**2.79E-04**	**4.1**	**2.22E-02**	**0.5**	**0.18**	**0.12**	**96.43**	**122.2**	**2.6**	**-11.8**
7	**57.4**	**2.53E-05**	**19.9**	**-7.63E-04**	**125.9**	**7.21E-04**	**2.4**	**5.65E-02**	**0.4**	**0.46**	**0.11**	**98.33**	**122.4**	**1.3**	**-31.9**
8	**57.6**	**7.34E-06**	**50.0**	**1.30E-03**	**68.3**	**3.87E-04**	**3.2**	**2.96E-02**	**0.7**	**0.24**	**0.42**	**99.12**	**122.9**	**2.2**	**9.8**
9	**57.9**	**-3.64E-06**	**116.2**	**2.21E-04**	**447.6**	**3.13E-04**	**4.3**	**2.59E-02**	**0.5**	**0.21**	**0.17**	**100.52**	**124.3**	**1.9**	**50.3**
10	**58.2**	**1.43E-05**	**38.4**	**8.23E-04**	**110.4**	**7.71E-04**	**2.1**	**5.81E-02**	**0.5**	**0.47**	**0.10**	**99.09**	**121.9**	**1.4**	**30.4**
11	**58.5**	**1.95E-06**	**172.7**	**1.45E-03**	**70.2**	**4.23E-04**	**3.0**	**3.41E-02**	**0.5**	**0.27**	**0.08**	**99.82**	**123.6**	**1.4**	**10.1**
Sample: 10JD34, Hornblende, Irradiation disk:I12t25h, J = 0.00881500 ±0.00002204															
1	61	2.83E-05	27.2	-7.81E-04	200.4	9.88E-06	43.6	3.51E-05	13.2	0.09	0.27	90.39	5466.0	468.9	-0.02
2	62	1.32E-04	7.0	2.14E-04	722.0	6.27E-05	10.7	1.49E-04	7.9	0.49	0.05	91.99	5991.8	275.4	0.30
3	62.5	1.54E-05	52.7	1.44E-04	1164.9	8.18E-06	70.8	2.65E-05	19.5	0.05	0.24	91.05	5063.5	704.1	0.08
4	63.2	7.77E-05	12.9	-1.95E-04	859.9	3.22E-05	13.1	1.25E-04	4.7	0.26	0.05	91.00	5160.7	169.0	-0.28
5	63.7	5.43E-05	17.0	2.47E-04	654.3	2.31E-05	20.9	1.73E-04	5.7	0.11	0.13	85.15	3144.4	191.5	0.30
6	64.2	5.25E-05	16.0	-1.39E-03	114.2	2.59E-05	16.2	2.90E-04	2.9	0.10	0.25	84.83	2346.6	107.2	-0.09
7	65	1.09E-04	9.5	1.92E-03	96.0	3.26E-05	19.1	1.06E-03	1.6	0.18	0.12	81.81	1433.4	52.8	0.24
8	66	1.03E-04	9.8	3.70E-03	45.3	4.94E-05	14.5	2.23E-03	1.6	0.12	0.15	74.72	551.1	35.6	0.26
9	67	9.16E-05	11.7	4.74E-03	36.5	5.42E-05	10.1	2.46E-03	1.2	0.09	0.17	71.49	391.7	34.5	0.22
10	68	1.85E-04	6.5	1.09E-02	15.9	1.06E-04	6.7	5.32E-03	0.7	0.19	0.15	70.96	358.9	18.2	0.21
11	69	3.61E-04	3.8	1.44E-02	12.4	2.07E-04	4.7	1.22E-02	0.7	0.31	0.08	65.06	241.3	9.8	0.37
12	70	4.72E-04	3.8	5.35E-02	6.6	4.41E-04	2.8	2.65E-02	0.5	0.44	0.09	68.76	172.0	6.1	0.21

13	70.8	5.59E-05	13.9	3.55E-02	5.7	1.65E-04	5.8	1.09E-02	0.8	0.11	0.23	87.08	130.5	6.7	0.13
14	71.6	2.33E-04	6.6	2.30E-01	4.6	8.26E-04	2.3	5.20E-02	0.5	0.55	0.08	90.85	146.8	3.0	0.10
15	72.1	6.90E-04	2.6	6.27E-01	4.5	2.15E-03	2.1	1.32E-01	0.4	1.46	0.07	89.51	151.3	1.8	0.09
16	72.4	1.30E-03	3.5	1.86E+00	4.5	6.19E-03	0.9	3.84E-01	0.4	3.88	0.02	94.03	145.1	1.6	0.09
17	72.5	7.68E-04	2.7	1.35E+00	4.5	4.43E-03	1.2	2.83E-01	0.4	2.68	0.06	95.68	138.7	1.4	0.09
18	72.6	8.38E-04	2.1	1.52E+00	4.5	5.00E-03	1.0	3.18E-01	0.4	2.99	0.03	95.92	138.5	1.3	0.09
19	72.7	3.32E-04	3.9	6.40E-01	4.5	2.15E-03	1.4	1.36E-01	0.4	1.22	0.05	96.30	132.5	1.4	0.09
20	72.8	2.16E-04	8.1	3.63E-01	4.6	1.21E-03	2.5	7.73E-02	0.4	0.71	0.07	95.21	133.8	2.4	0.09
21	73	4.50E-04	3.0	8.97E-01	4.5	3.00E-03	1.2	1.91E-01	0.4	1.74	0.04	96.61	134.7	1.3	0.09
22	79.4	8.51E-06	101.6	1.47E-02	24.6	4.52E-05	18.2	3.32E-03	1.1	0.03	1.23	95.95	142.5	23.5	0.10
23	79.7	1.26E-05	71.6	2.81E-02	13.3	9.01E-05	11.4	6.14E-03	0.8	0.06	0.65	97.71	146.8	13.3	0.09
24	80.2	5.32E-05	18.3	7.81E-02	6.8	2.43E-04	5.0	1.57E-02	0.5	0.15	0.27	93.74	136.6	5.8	0.09
25	80.8	7.17E-04	3.2	1.50E+00	4.6	4.99E-03	1.4	3.16E-01	0.4	2.92	0.03	97.00	137.5	1.3	0.09
26	81.5	2.49E-03	1.8	4.99E+00	4.6	1.62E-02	0.9	1.03E+00	0.4	9.37	0.05	96.56	134.8	1.2	0.09
27	82	6.66E-05	23.2	9.21E-02	5.9	2.62E-04	5.8	1.59E-02	0.6	0.15	0.35	92.06	136.0	8.8	0.07
Sample 10SD148, Hornblende, Irradiation disk: I15t40h, J=0.00345700 ± 0.00000500															
1	56.2	1.03E-05	58.6	1.35E-03	31.1	1.39E-05	31.1	4.76E-04	3.8	0.34	0.06	99.12	2220.7	97.3	0.18
2	56.5	1.41E-05	59.4	8.74E-03	5.8	4.09E-05	13.0	2.48E-03	0.8	1.26	0.05	99.72	1825.7	19.1	0.15
3	56.7	-2.46E-07	2886.4	7.04E-03	7.1	2.66E-05	17.8	2.14E-03	1.4	1.05	0.03	100.06	1789.2	33.2	0.16
10SD204, Biotite, Irradiation disk: I15t40h, J=0.00341900 ± 0.00000615															
1	56.9	2.64E-04	2.5	-6.81E-06	483.2	4.90E-05	15.5	9.10E-04	2.6	0.34	0.10	76.93	1241.5	49.1	-57.50
2	57.1	1.91E-04	4.1	-6.86E-06	474.7	6.55E-05	11.0	2.16E-03	0.9	0.85	0.09	93.24	1466.0	19.5	-135.08
3	57.4	1.84E-04	6.3	-2.73E-05	119.5	1.57E-04	2.8	9.40E-03	0.6	4.67	0.08	98.82	1780.8	14.7	-148.00
4	57.7	7.02E-05	12.3	-1.82E-05	191.6	9.94E-05	6.2	5.84E-03	0.8	3.06	0.08	99.31	1848.7	18.8	-138.28
5	58.0	5.06E-05	12.9	-1.55E-05	216.8	6.70E-05	10.6	3.87E-03	1.1	1.85	0.09	99.18	1740.6	24.5	-107.31
6	58.3	7.48E-06	74.2	1.58E-06	2107.5	1.65E-05	18.6	8.87E-04	2.4	0.43	0.14	99.49	1772.7	54.9	241.17
7	65.0	9.66E-06	47.7	-2.82E-05	112.7	-1.05E-06	308.2	1.53E-04	5.7	0.09	0.14	96.73	1932.8	139.9	-2.33

Appendix Table 5.4 Zircon and apatite (U-Th)/He data for samples in the Jiaobei region

Sample	^{232}Th (ng)	σ (%)	^{238}U (ng)	σ (%)	^{147}Sm (ng)	σ (%)	eU ppm	He (ncc)	σ (%)	TAU (%)	Th/U	Ft	Cor. age (Ma)	±1σ (Ma)
ZIRCON														
Precambrian rocks														
JB12-02-1a	0.254	1.5	4.190	2.0	0.007	7.5	976	95.17	1.5	2.4	0.06	0.69	262	15
JB12-02-1b	0.696	1.5	3.578	2.0	0.016	4.8	768	91.63	1.5	2.4	0.19	0.73	271	15
JB12-02-1c	0.348	1.5	1.766	2.0	0.003	16.2	806	40.66	1.2	2.2	0.20	0.70	254	14
JB12-02-1d	0.369	1.5	4.118	2.0	0.013	6.8	945	98.81	1.2	2.3	0.09	0.72	264	14
JB12-02-1e	0.576	1.5	2.913	2.0	0.023	3.9	1027	62.09	1.2	2.2	0.20	0.66	250	14
Mean Age ±95% conf. uncertainty (Ma), MSWD = 0.33 , P = 0.86													**260**	**13**
JB12-02-2a	0.366	1.5	1.748	2.0	0.004	37.5	497	45.63	1.2	2.2	0.21	0.73	275	15
JB12-02-2b	0.263	1.5	1.168	2.0	0.007	77.8	409	28.62	1.2	2.2	0.22	0.70	269	15
JB12-02-2c	0.331	1.5	0.910	2.0	0.009	44.9	309	22.08	1.2	2.2	0.36	0.70	258	14
JB12-02-2d	0.251	1.5	1.060	2.0	0.003	14.6	465	24.17	1.2	2.2	0.24	0.69	253	14
Mean Age ±95% conf. uncertainty (Ma), MSWD = 0.46 , P = 0.71													**263**	**14**
11JD022a	0.233	1.5	0.252	1.9	0.003	29.7	25	4.89	1.2	2.0	0.92	0.69	188	10
11JD022b	0.172	1.5	0.257	1.9	0.008	75.7	20	5.60	1.2	2.0	0.66	0.72	213	12
11JD022c	0.174	1.5	0.259	1.9	0.011	5.6	22	5.04	1.2	2.0	0.67	0.71	193	10
11JD022d	0.688	1.4	0.581	1.9	0.008	13.7	27	13.45	1.2	1.9	1.18	0.76	194	10
11JD022e	0.365	1.5	0.349	1.9	0.003	15.1	24	7.37	1.2	1.9	1.04	0.71	193	10
Mean Age ±95% conf. uncertainty (Ma), MSWD = 0.80 , P = 0.52													**196**	**9**
JB12-10a	0.922	1.5	3.432	2.0	0.001	20.0	232	62.21	1.2	2.2	0.27	0.72	192	10
JB12-10b	0.287	1.5	2.101	2.0	0.004	29.9	213	31.07	1.2	2.3	0.14	0.67	174	10
JB12-10c	0.810	1.5	4.520	1.9	0.002	17.8	427	72.67	1.2	2.2	0.18	0.69	182	10
JB12-10d	0.579	1.5	2.728	2.0	0.002	29.9	255	45.65	1.2	2.2	0.21	0.70	185	10

JB12-10e	0.517	1.5	3.577	2.0	0.010	8.0	295	62.45	1.2	2.3	0.14	0.71	193	11
Mean Age ± 95% conf. uncertainty (Ma), MSWD = 0.62 , P = 0.65													**185**	**9**
10SD132a	0.508	1.4	1.552	1.8	0.001	26.0	95	22.64	1.2	2.1	0.32	0.71	154	8
10SD132b	0.196	1.5	0.731	1.8	0.001	21.9	69	9.74	1.2	2.1	0.27	0.64	160	9
10SD132c	0.263	1.5	0.975	1.8	0.001	22.5	118	14.18	1.2	2.1	0.27	0.63	176	10
10SD132d	0.272	1.5	0.995	1.8	0.001	28.1	105	13.05	1.2	2.1	0.27	0.62	162	9
10SD132e	0.181	1.5	0.683	1.9	0.004	78.1	55	9.68	1.2	2.1	0.26	0.67	163	9
10SD132f	0.310	1.5	1.199	1.8	0.001	45.9	104	18.18	1.2	2.1	0.26	0.67	173	9
Mean Age ± 95% conf. uncertainty (Ma), MSWD = 0.84 , P = 0.52													**164**	**7**
10JD28a	0.207	3.7	0.3	2.7	NULL	NULL	122	4.21	1.7	4.9	0.82	0.73	153	11
10JD28b	0.557	3.7	0.8	2.8	NULL	NULL	513	14.19	2.5	5.3	0.74	0.72	177	13
10JD28c	0.462	3.7	0.9	2.8	NULL	NULL	356	15.14	2.5	5.3	0.53	0.74	166	12
10JD28d	0.488	3.7	0.5	2.8	NULL	NULL	289	10.65	2.5	5.3	0.93	0.75	178	13
Mean Age ± 95% conf. uncertainty (Ma), MSWD = 1.06, P = 0.36													**167**	**12**
10JD27a	0.254	1.5	0.222	1.8	0.003	10.4	11	4.51	1.2	1.9	1.13	0.71	183	10
10JD27b	0.573	1.4	0.920	1.8	0.003	9.0	25	16.95	1.2	2.0	0.62	0.77	169	9
10JD27c	0.423	1.4	0.510	1.8	0.005	7.2	19	8.70	1.2	2.0	0.82	0.79	147	8
10JD27d	1.062	1.4	0.722	1.8	0.007	6.4	34	17.94	1.2	1.8	1.46	0.71	211	11
10JD27e	0.288	1.5	0.487	1.8	0.003	9.6	22	8.95	1.2	2.0	0.59	0.75	174	9
10JD27f	0.248	1.5	0.361	1.9	0.002	13.2	26	5.67	1.2	2.0	0.68	0.77	144	8
													No mean age	
JB12-06a	0.074	1.7	0.258	2.1	0.002	20.6	113	3.50	1.2	2.3	0.28	0.68	152	8
JB12-06b	0.067	1.7	0.304	2.0	0.004	44.9	108	3.99	1.2	2.3	0.22	0.67	152	8
JB12-06c	0.104	1.6	0.351	2.0	0.000	27.5	95	4.97	1.2	2.2	0.30	0.68	158	9
JB12-06d	0.061	1.7	0.296	2.0	0.003	59.0	129	3.86	1.2	2.3	0.20	0.67	151	8
Mean Age ± 95% conf. uncertainty (Ma), MSWD = 0.15, P = 0.93													**153**	**8**
JB12-12-2a	0.529	1.5	7.717	2.0	0.005	29.7	663	77.66	1.5	2.5	0.07	0.70	115	6
JB12-12-2b	0.641	1.5	5.364	2.0	0.021	55.7	699	52.16	1.5	2.4	0.12	0.66	117	7

JB12-12-2c	0.232	1.5	2.795	2.0	0.002	14.3	458	28.76	1.5	2.4	0.08	0.73	113	6
Mean Age ±95% conf. uncertainty (Ma), MSWD = 0.46, P = 0.71													**115**	**7**
JB12-05a	0.012	3.1	0.185	1.9	0.003	53.6	92	2.24	1.2	2.2	0.06	0.77	126	7
JB12-05b	0.090	1.5	0.479	1.9	0.001	21.0	166	5.46	1.2	2.1	0.19	0.74	120	7
JB12-05c	0.043	1.7	0.369	1.8	0.001	24.6	123	4.29	1.2	2.1	0.12	0.73	126	7
JB12-05d	0.016	3.1	0.255	1.9	0.001	41.5	141	2.30	1.2	2.2	0.06	0.65	112	6
JB12-05e	0.046	1.7	0.237	1.8	0.006	31.4	119	2.80	1.2	2.1	0.19	0.75	123	7
JB12-05f	0.024	2.1	0.291	1.8	0.002	26.5	163	2.95	1.2	2.1	0.08	0.69	118	6
Mean Age ±95% conf. uncertainty (Ma), MSWD = 0.76, P = 0.58													**120**	**5**
JB12-12-1a	0.050	1.8	0.404	2.0	0.001	20.8	81	3.94	1.5	2.5	0.12	0.68	114	6
JB12-12-1b	0.111	1.5	0.737	2.0	0.001	23.8	74	7.99	1.5	2.5	0.15	0.71	120	7
JB12-12-1c	0.218	1.5	1.929	2.0	0.002	14.0	109	20.89	1.5	2.5	0.11	0.74	116	6
JB12-12-1d	0.076	1.6	0.474	2.0	0.002	14.2	75	4.88	1.5	2.4	0.16	0.69	117	7
Mean Age ±95% conf. uncertainty (Ma), MSWD = 0.17, P = 0.92													**117**	**6**
10SD112a	2.423	1.4	4.461	1.8	0.006	6.2	29	63.05	1.3	2.1	0.54	0.84	121	7
10SD112b	1.741	1.4	2.825	1.8	0.004	8.6	35	35.37	1.4	2.1	0.61	0.82	109	6
10SD112c	0.624	1.4	1.104	1.8	0.005	7.9	20	13.23	1.3	2.1	0.56	0.80	108	6
10SD112d	1.380	1.4	1.218	1.8	0.007	5.6	11	18.35	1.3	2.0	1.12	0.83	117	6
10SD112e	2.171	1.4	3.449	1.9	0.010	5.3	23	42.52	1.3	2.1	0.63	0.86	102	6
Mean Age ±95% conf. uncertainty (Ma), MSWD = 1.50, P = 0.20													**111**	**9**
10SD121a	1.482	4.0	3.840	3.0	0.004	31.7	806	56.36	1.2	3.0	0.38	0.83	132	8
10SD121b	2.002	4.0	3.628	2.9	0.059	5.8	861	56.65	1.2	2.9	0.55	0.82	137	8
10SD121c	2.152	4.0	3.872	2.9	0.005	26.4	706	64.26	1.2	2.9	0.55	0.84	143	8
10SD121d	1.108	4.0	2.112	2.9	0.002	32.4	809	31.45	1.2	2.9	0.52	0.78	139	8
10SD121e	1.899	4.0	5.613	2.9	0.004	25.3	849	97.17	1.2	3.0	0.34	0.77	169	10
													No mean age	
10SD148a	0.028	4.3	0.126	3.0	0.005	35.8	101	1.30	1.2	3.1	0.22	0.72	111	7
10SD148b	0.019	4.7	0.125	3.1	0.003	43.5	131	1.26	1.2	3.2	0.15	0.69	115	7

10SD148c	0.022	4.4	0.114	3.0	0.005	36.3	112	1.31	1.2	3.2	0.19	0.72	124	7
10SD148d	0.018	4.7	0.111	3.0	0.006	36.7	102	1.16	1.2	3.3	0.16	0.73	113	7
10SD148e	0.010	6.0	0.081	3.0	0.002	42.5	74	0.84	1.2	3.2	0.12	0.64	129	8
Mean Age ± 95% conf. uncertainty (Ma), MSWD = 1.18, P = 0.32													**118**	**6**
10SD198a	0.329	2.0	1.056	2.3	0.003	10.5	27	9.50	1.2	2.4	0.31	0.78	88	5
10SD198b	0.293	1.5	0.767	1.8	0.002	12.4	28	6.79	1.2	2.1	0.38	0.75	89	5
10SD198c	0.343	1.5	0.894	1.8	0.002	13.8	29	8.98	1.2	2.1	0.38	0.78	97	5
10SD198d	0.266	1.5	0.795	1.8	0.003	9.8	28	7.34	1.2	2.1	0.33	0.74	94	5
10SD198e	0.395	1.4	0.999	1.8	0.002	26.8	27	9.68	1.2	2.1	0.39	0.75	97	5
10SD198f	0.571	1.4	1.096	1.8	0.002	11.2	26	12.67	1.2	2.0	0.52	0.78	107	6
Mean Age ± 95% conf. uncertainty (Ma), MSWD = 1.7, P = 0.13													**95**	**7**
Meosozoic igenous rocks														
10JD10a	0.795	1.4	2.648	1.8	0.004	9.2	93	24.37	1.2	2.1	0.30	0.73	96	5
10JD10b	0.495	1.4	1.332	1.8	0.001	13.2	73	11.42	1.2	2.0	0.37	0.70	92	5
10JD10c	0.244	1.5	1.073	1.8	0.002	12.2	38	8.55	1.2	2.1	0.23	0.74	83	5
10JD10d	0.413	1.4	2.337	1.8	0.001	15.4	71	21.42	1.2	2.1	0.18	0.78	93	5
10JD10e	0.521	1.4	3.316	1.8	0.001	16.4	91	33.38	1.2	2.1	0.16	0.75	106	6
													No mean age	
10JD31a	2.642	4.0	6.270	2.9	0.008	20.5	577	75.45	1.2	2.9	0.42	0.72	124	7
10JD31b	1.199	4.0	3.818	2.9	0.005	27.1	367	39.13	1.2	3.0	0.31	0.77	101	6
10JD31c	3.651	4.0	5.751	2.9	0.008	26.1	655	68.57	1.2	2.9	0.63	0.74	114	7
10JD31d	0.440	3.7	0.964	2.8	NULL	NULL	423	8.10	1.4	2.9	0.47	0.67	93	5
10JD31e	0.272	3.7	2.445	2.9	NULL	NULL	1447	20.29	2.6	3.8	0.11	0.67	99	6
													No mean age	
10SD128Ba	0.253	3.7	0.5	2.7	NULL	NULL	487	4.97	1.7	2.9	0.53	0.64	116	7
10SD128Bb	1.176	3.7	1.7	2.7	NULL	NULL	1201	16.72	2.5	3.5	0.72	0.68	104	6
10SD128Bc	0.612	3.7	1.6	2.7	NULL	NULL	1053	13.39	2.5	3.5	0.39	0.70	91	6
10SD128Bd	0.242	3.7	1.2	2.7	NULL	NULL	1578	9.98	2.5	3.5	0.21	0.61	108	7

													No mean age	
10SD154a	0.595	3.8	2.4	2.7	NULL	NULL	345	24.82	2.5	3.6	0.25	0.81	98	6
10SD154b	0.264	3.8	1.2	2.7	NULL	NULL	374	12.54	2.5	3.6	0.23	0.75	111	7
10SD154c	0.481	3.8	1.8	2.7	NULL	NULL	275	20.74	2.5	3.6	0.27	0.80	108	7
10SD154d	0.718	3.8	5.7	2.7	NULL	NULL	470	68.07	2.5	3.6	0.13	0.84	112	7
10SD154e	0.176	3.8	1.4	2.7	NULL	NULL	386	13.53	2.5	3.7	0.13	0.76	101	6
Mean Age ±95% conf. uncertainty (Ma), MSWD = 0.96, P = 0.43													**106**	**6**
10JD34a	0.228	3.7	1.2	2.8	NULL	NULL	340	7.84	1.4	3.0	0.20	0.75	70	4
10JD34b	0.420	3.7	0.9	2.8	NULL	NULL	628	8.00	1.4	2.9	0.45	0.69	91	5
10JD34c	0.268	3.7	0.9	2.7	NULL	NULL	507	8.48	1.3	2.9	0.29	0.68	101	6
10JD34d	0.472	3.7	0.9	2.7	NULL	NULL	499	8.65	1.3	2.8	0.51	0.71	94	5
10JD34e	0.282	3.7	0.8	2.9	NULL	NULL	489	6.84	1.5	3.0	0.36	0.68	95	6
Mean Age ±95% conf. uncertainty (Ma), MSWD = 0.61, P = 0.61													**95**	**5**
10SD185a	0.708	3.7	4.1	2.9	NULL	NULL	1990	41.38	2.5	3.7	0.18	0.70	114	7
10SD185b	0.384	3.7	3.5	2.8	NULL	NULL	1909	31.84	2.5	3.7	0.11	0.67	108	7
10SD185c	0.563	3.7	2.8	2.7	NULL	NULL	1027	24.38	2.5	3.6	0.20	0.72	93	6
10SD185d	0.788	3.8	5.2	2.8	NULL	NULL	1216	51.91	2.5	3.7	0.15	0.76	103	6
10SD185e	0.432	3.7	2.6	2.8	NULL	NULL	1151	28.17	2.5	3.7	0.17	0.69	125	8
													No mean age	
							APATITE							
10JD31a	0.025	4.1	0.035	4.4	NULL	NULL	12.2	0.170	2.9	4.6	0.70	0.69	49	3
10JD31b	0.054	3.8	0.104	4.1	NULL	NULL	16.4	0.524	2.5	4.3	0.52	0.77	48	3
10JD31c	0.012	3.9	0.045	3.9	0.050	1.1	14.7	0.231	1.3	3.1	0.27	0.71	56	3
10JD31d	0.015	3.9	0.019	4.0	0.028	1.4	9.0	0.097	1.5	2.9	0.78	0.67	52	3
10JD31e	0.010	4.0	0.020	4.0	0.023	1.5	13.5	0.105	1.5	3.1	0.49	0.65	59	3
Mean Age ±95% conf. uncertainty (Ma), MSWD = 1.8, P = 0.12													**52**	**5**
10JD34a	0.054	3.8	0.020	4.3	NULL	NULL	16.3	0.130	3.1	4.2	2.68	0.62	53	3
10JD34b	0.059	3.8	0.026	4.2	NULL	NULL	23.1	0.125	3.2	4.3	2.27	0.62	42	3

10JD34c	0.096	3.8	0.033	4.3	NULL	NULL	20.6	0.191	3.1	4.2	2.90	0.65	44	3
10JD34d	0.058	3.9	0.023	4.6	NULL	NULL	14.8	0.145	3.4	4.5	2.50	0.66	50	3
10JD34e	0.076	3.8	0.025	4.2	NULL	NULL	15.4	0.171	2.9	4.1	3.04	0.67	49	3
Mean Age ± 95% conf. uncertainty (Ma), MSWD = 2.3, P = 0.05													**47**	**6**
10SD128Ba	0.041	3.8	0.054	4.2	NULL	NULL	11.8	0.314	2.9	4.5	0.77	0.79	51	3
10SD128Bb	0.067	3.8	0.079	4.1	NULL	NULL	9.5	0.405	2.7	4.3	0.84	0.80	44	3
10SD128Bc	0.026	3.9	0.036	4.1	NULL	NULL	5.6	0.193	3.1	4.6	0.72	0.81	47	3
Mean Age ± 95% conf. uncertainty (Ma), MSWD =1.5, P = 0.23													**47**	**9**
10SD185a	0.006	4.3	0.009	4.0	0.01	1.7	11.1	0.042	1.3	2.9	0.65	0.53	59	6
10SD185b	0.015	3.9	0.015	4.0	0.020	1.6	17.4	0.076	1.3	2.9	0.96	0.54	60	6
10SD185c	0.016	3.9	0.014	4.0	0.02	1.8	17.1	0.067	1.3	3.0	1.08	0.58	52	5
Mean Age ± 95% conf. uncertainty (Ma), MSWD =0.59, P = 0.55													**57**	**7**
10SD132a	0.259	3.8	0.086	4.0	0.03	1.4	66.2	0.587	1.2	2.9	2.99	0.74	44	5
10SD132b	0.088	3.8	0.111	4.0	0.03	1.3	50.2	0.260	1.2	3.5	0.79	0.77	21	2
10SD132c	0.119	3.8	0.207	4.0	0.04	1.0	84.9	0.698	1.2	3.6	0.57	0.74	33	3
													No mean age	
10SD180a	0.087	3.8	0.171	4.0	0.02	1.3	79.3	0.955	1.2	3.6	0.51	0.76	54	6
10SD180b	0.086	3.8	0.113	4.0	0.02	1.5	39.9	0.477	1.2	3.5	0.76	0.75	39	4
10SD180c	0.030	3.8	0.055	4.0	0.02	1.6	14.8	0.169	1.2	3.6	0.55	0.76	29	3
10SD180d	0.081	3.8	0.091	4.4	0.03	1.7	28.2	0.539	1.2	3.6	0.88	0.77	52	6
10SD180e	0.098	3.8	0.088	4.0	0.02	2.0	35.6	0.465	1.2	3.4	1.10	0.73	47	5
													No mean age	

Appendix Table 6.1 Zircon and apatite fission-track results for the Luxi region

Sample ID	# of crystals	RhoS	Ns	RhoI	Ni	RhoD	Nd	P(χ^2) (%)	U (ppm)	Central Age (Ma)	± 1σ	Non-projected MTL	C-axis projected MTL (μm) ± SD	Dpar (μm)	SD
Zircon															
11LX153	25	229.505	1089	47.418	225	10.713	4488	100	161.6	309	24				
11LX049A	25	248.683	1180	37.302	177	11.251	4488	99.46	121.0	442	37				
11LX026	25	236.459	1122	94.204	447	11.431	4488	80.61	300.8	173	10				
Apatite															
11LX137	25	7.568	813	14.261	1532	6.515	3108	99.0	28.3	54	3	13.9	14.8 ±0.8 (n=119)	2.16	0.4
11LX049A	25	1.732	309	3.346	597	5.986	3108	100.0	7.0	48	4			2.29	0.36
11LX053A	25	1.94	280	3.686	532	7.336	3108	100.0	6.5	60	5			2.87	0.76
11LX116A	25	1.479	293	3.094	613	6.691	3108	100.0	5.7	50	4			2.34	0.48
11LX118	25	2.534	284	4.979	558	6.045	3108	100	10.7	48	4			2.04	0.26
11LX119	25	3.361	229	5.914	403	5.517	3108	99.1	13.5	49	4			1.67	0.21
11LX120	25	1.083	116	2.361	253	6.221	3108	100.0	5.0	44	5			2.14	0.65
11LX121	26	0.965	163	2.096	354	5.634	3108	100.0	4.7	40	4			1.77	0.23
11LX030	25	12.099	465	12.697	488	5.752	3108	100.0	26.9	85	6	14.2	15.1 ±1.0 (n=111)	2.96	0.53

Appendix Table 6.2 Zircon and apatite (U-Th)/He results for the Luxi region

Sample	^{232}Th	σ	^{238}U	σ	^{147}Sm	σ	eU	He	σ	TAU	Th/U	Ft	Cor. age	±1σ
	(ng)	(%)	(ng)	(%)	(ng)	(%)	ppm	(ncc)	(%)	(%)			(Ma)	(Ma)
							Zircon							
10SD001C-1	0.149	1.5	0.372	1.9	0.002	55.8	12.3	4.447	1.2	2.1	0.40	0.75	118.3	6.4
10SD001C-2	0.125	1.5	0.339	1.9	0.001	20.9	7.3	4.128	1.2	2.1	0.37	0.80	114.8	6.2
10SD001C-3	0.139	1.5	0.323	1.9	0.001	25.1	11.3	3.965	1.2	2.0	0.43	0.79	115.8	6.3
10SD001C-4	0.245	1.5	0.562	1.9	0.001	25.3	12.5	7.316	1.2	2.0	0.43	0.81	119.5	6.5
10SD001C-5	0.205	1.5	0.447	1.9	0.001	21.1	11.3	5.631	1.2	2.1	0.46	0.80	116.5	6.3
10SD001C-6	0.102	1.5	0.320	1.9	0.001	23.5	6.6	4.091	1.2	2.1	0.32	0.78	123.8	6.7
Weighted Mean age ± error (95% confidence) (MSWD = 0.25, P = 0.94)													118 ± 5 Ma	
11LX005-1	2.335	1.4	1.574	1.8	0.016	6.1	230.9	6.477	1.2	1.8	1.47	0.68	36.8	2.0
11LX005-2	2.968	1.4	2.666	1.8	0.061	2.2	458.0	8.049	1.2	1.9	1.11	0.63	31.1	1.7
11LX005-3	3.099	1.4	2.771	1.8	0.085	5.8	448.2	8.956	1.2	1.9	1.11	0.58	36.3	1.9
11LX005-4	1.956	1.4	1.919	1.9	0.058	2.9	295.1	6.240	1.2	1.9	1.01	0.66	32.7	1.7
11LX005-5	3.656	1.4	3.103	1.8	0.047	2.7	389.8	11.190	1.2	1.9	1.17	0.64	36.4	1.9
11LX005-6	7.082	1.4	3.346	1.8	0.051	2.7	698.1	11.016	1.2	1.8	2.10	0.62	29.0	1.5
11LX018-1	0.688	1.4	0.567	1.9	0.006	7.3	46.0	8.543	1.2	1.9	1.20	0.71	134	7
11LX018-2	0.215	1.5	0.149	1.9	0.002	20.5	10.8	5.155	1.2	1.9	1.43	0.68	307	16
11LX018-3	0.058	1.7	0.071	2.1	0.003	63.3	10.9	2.093	1.2	2.1	0.80	0.61	328	18
11LX018-4	0.053	1.6	0.105	1.9	0.003	32.2	13.5	2.039	1.2	2.1	0.50	0.64	218	12
11LX018-5	0.131	1.5	0.216	1.9	0.007	75.6	18.6	4.217	1.2	2.0	0.60	0.68	203	11
11LX018-6	0.226	1.5	0.121	1.9	0.001	19.6	16.6	3.383	1.2	1.8	1.85	0.64	245	13
11LX026-1	0.752	1.4	1.067	1.9	0.004	9.1	19.1	31.603	1.2	2.0	0.70	0.82	250	13

11LX026-2	0.295	1.5	0.292	1.9	0.002	11.2	6.6	7.687	1.2	1.9	1.00	0.79	218	12
11LX026-3	0.909	1.4	1.952	1.8	0.005	8.6	44.7	34.636	1.2	2.0	0.46	0.79	165	9
11LX026-4	0.515	1.4	1.501	1.9	0.008	24.0	20.0	21.476	1.2	2.1	0.34	0.82	131	7
11LX026-5	0.367	1.5	1.125	1.8	0.002	12.0	26.7	13.200	1.2	2.1	0.32	0.80	111	6
11LX026-6	0.257	1.5	0.469	1.9	0.002	11.7	9.2	10.153	1.2	2.1	0.54	0.82	189	10
11LX049A-1	0.309	1.5	0.598	1.9	0.007	15.0	7.1	53.930	1.2	2.0	0.51	0.84	738	40
11LX049A-2	0.212	1.5	0.391	1.9	0.004	8.0	5.7	29.766	1.2	2.0	0.54	0.82	643	35
11LX049A-3	0.246	1.5	0.480	1.9	0.005	7.5	6.7	26.638	1.2	2.1	0.51	0.81	484	26
11LX049A-4	0.348	1.5	0.856	1.8	0.005	8.2	9.9	54.465	1.2	2.1	0.40	0.83	550	30
11LX049A-5	0.190	1.5	0.516	1.9	0.005	9.0	8.7	35.228	1.2	2.1	0.37	0.82	597	32
11LX049A-6	0.212	1.5	0.341	1.9	0.003	8.2	7.1	27.422	1.2	2.0	0.62	0.81	680	37
11LX053A-1	0.453	1.4	1.089	1.8	0.003	8.4	25.4	16.459	1.3	2.1	0.41	0.78	144.1	7.8
11LX053A-2	0.190	1.5	0.257	1.9	0.003	9.8	5.4	3.627	1.3	2.0	0.73	0.80	122.5	6.6
11LX053A-3	0.647	1.4	2.620	1.8	0.003	8.4	52.7	36.934	1.3	2.1	0.25	0.78	139.1	7.6
11LX053A-4	0.302	1.5	0.390	1.9	0.001	15.1	6.9	6.316	1.3	2.0	0.77	0.77	145.4	7.8
11LX053A-5	0.498	1.4	1.736	1.8	0.002	11.6	39.9	24.782	1.3	2.1	0.29	0.77	140.8	7.7
11LX053A-6	0.325	1.5	1.336	1.8	0.004	8.1	34.3	19.226	1.3	2.2	0.24	0.75	146.9	8.0
Weighted Mean age ± error (95% confidence) (MSWD = 1.7, P = 0.14)													139 ± 10 Ma	
11LX115-1	0.666	1.4	2.221	1.8	0.009	5.2	44.4	37.193	1.2	2.1	0.30	0.79	161.3	8.7
11LX115-2	0.160	1.5	1.279	1.8	0.019	4.3	42.4	23.591	1.2	2.1	0.12	0.77	188.4	10.2
11LX115-3	1.706	1.4	3.202	1.8	0.057	2.2	70.7	44.307	1.2	2.0	0.53	0.78	128.7	6.9
11LX115-4	0.436	1.4	1.838	1.8	0.011	4.8	31.2	21.920	1.2	2.1	0.24	0.81	113.5	6.2
11LX115-5	0.508	1.4	2.404	1.8	0.019	3.7	63.8	20.928	1.2	2.1	0.21	0.77	88.4	4.8
11LX116A-1	0.190	1.5	0.553	1.8	0.008	27.0	23.3	21.390	1.2	2.1	0.34	0.72	398.1	21.5
11LX116A-2	0.196	1.5	0.707	1.9	0.006	12.5	23.3	21.815	1.2	2.1	0.28	0.76	306.3	16.6

11LX116A-3	0.120	1.5	0.603	1.9	0.005	25.3	32.1	7.703	1.2	2.1	0.20	0.73	136.7	7.4
11LX116A-4	0.153	1.5	0.806	1.8	0.009	11.9	27.7	12.323	1.2	2.1	0.19	0.76	157.5	8.5
11LX116A-5	0.112	1.5	0.643	1.8	0.005	7.3	35.2	14.145	1.2	2.1	0.17	0.72	239.0	13.0
11LX120-1	0.079	1.6	0.374	1.9	0.003	12.1	17.2	4.920	1.2	2.1	0.21	0.72	141.1	7.7
11LX120-2	0.091	1.5	0.373	1.9	0.002	12.3	17.1	4.790	1.2	2.1	0.24	0.75	132.7	7.2
11LX120-3	0.134	1.5	0.729	1.8	0.006	7.1	29.3	9.156	1.2	2.1	0.18	0.74	133.3	7.2
11LX120-4	0.121	1.5	0.475	1.8	0.003	10.5	18.0	5.650	1.2	2.1	0.25	0.75	122.0	6.6
11LX120-5	0.115	1.5	0.465	1.9	0.003	10.8	24.2	4.970	1.2	2.1	0.24	0.73	113.0	6.1
Weighted Mean age ± error (95% confidence) (MSWD = 2.6, P = 0.03)													127 ± 14	
11LX121-1	0.198	1.5	0.271	1.9	0.001	15.3	23.4	3.989	1.2	2.0	0.73	0.69	149.0	8.0
11LX121-2	0.104	1.5	0.279	1.9	0.000	34.1	32.8	3.453	1.2	2.1	0.37	0.68	137.1	7.4
11LX121-3	0.408	1.4	0.593	1.8	0.004	15.9	30.3	8.384	1.2	2.0	0.68	0.69	142.8	7.7
11LX121-4	0.153	1.5	0.674	1.8	0.002	13.4	53.8	4.839	1.2	2.1	0.23	0.66	84.5	4.6
11LX135-1	0.537	1.4	0.858	1.8	0.045	2.2	42.4	13.594	1.2	2.0	0.62	0.74	151.8	8.2
11LX135-3	0.711	1.4	0.833	1.8	0.024	20.2	57.8	6.663	1.2	1.9	0.85	0.64	85.3	4.6
11LX135-4	0.709	1.4	1.431	1.8	0.023	3.2	63.8	6.632	1.2	2.0	0.49	0.68	50.4	2.7
11LX135-5	1.374	1.4	1.479	1.8	0.030	3.0	87.8	5.887	1.2	1.9	0.92	0.67	39.8	2.1
11LX135-6	1.044	1.4	3.935	1.9	0.087	1.7	135.4	15.065	1.2	2.1	0.26	0.76	38.7	2.1
11LX137-1	1.767	1.4	2.770	1.8	0.009	5.0	106.4	21.814	1.2	2.0	0.63	0.77	72.6	3.9
11LX137-2	1.237	1.4	0.985	1.8	0.010	5.2	38.8	28.824	1.2	1.9	1.25	0.73	250.1	13.3
11LX137-3	1.378	1.4	1.658	1.8	0.010	5.2	61.6	12.981	1.2	1.9	0.82	0.75	71.7	3.8
11LX137-4	1.469	1.4	1.488	1.8	0.008	6.3	51.4	17.734	1.2	1.9	0.98	0.78	100.7	5.4
11LX137-5	0.799	1.4	0.811	1.8	0.004	11.0	47.4	12.301	1.2	1.9	0.98	0.71	140.4	7.5
11LX153-1	0.686	1.4	0.582	1.8	0.005	7.0	11.2	92.768	1.2	1.9	1.17	0.82	1136	61

11LX153-2	0.442	1.4	0.534	1.8	0.006	6.8	21.1	65.408	1.2	2.0	0.82	0.74	1053	57
11LX153-3	0.420	1.4	0.575	1.9	0.005	7.1	13.5	73.760	1.2	2.0	0.73	0.79	1045	56
11LX153-4	0.914	1.4	0.743	1.8	0.013	12.7	15.2	96.372	1.2	1.9	1.22	0.80	964	52
11LX153-5	0.494	1.4	0.342	1.9	0.005	9.0	8.8	31.766	1.2	1.9	1.43	0.80	681	36
Apatite														
10SD001C-1	0.001	19.7	0.039	4.2	0.017	1.7	18.0	0.120	1.3	4.1	0.03	0.68	36.8	4.0
10SD001C-2	0.007	4.2	0.069	4.0	0.042	1.2	16.3	0.272	1.2	3.6	0.11	0.80	39.5	4.2
10SD001C-3	0.009	5.1	0.038	4.2	0.015	2.2	17.7	0.109	1.2	3.9	0.24	0.76	29.7	3.2
10SD001C-4	0.004	7.4	0.041	4.4	0.019	2.0	15.2	0.152	1.2	4.1	0.10	0.76	38.9	4.2
Weighted Mean age ± error (95% confidence) (MSWD = 1.6, P = 0.18)													35 ± 8 Ma	
11LX018-1	0.089	3.8	0.045	4.0	0.037	1.1	70.6	0.224	1.2	2.9	1.99	0.65	43.2	4.5
11LX018-2	0.028	3.8	0.037	4.0	0.022	1.5	35.5	0.122	1.2	3.4	0.75	0.69	33.0	3.5
11LX018-3	0.037	3.8	0.071	4.0	0.133	1.0	60.8	0.325	1.2	2.8	0.52	0.70	47.1	4.9
11LX018-4	0.106	3.8	0.058	4.6	0.040	1.8	66.7	0.304	1.2	3.3	1.82	0.69	43.3	4.5
Weighted Mean age ± error (95% confidence) (MSWD = 2.4, P = 0.07)													40 ± 10 Ma	
11LX030-1	0.236	3.8	0.197	4.0	0.184	0.7	57.4	0.963	1.2	3.0	1.19	0.77	40.1	4.2
11LX030-2	0.368	3.8	0.307	4.0	0.287	0.6	81.9	1.410	1.2	3.0	1.19	0.81	35.9	3.7
11LX030-3	0.387	3.8	0.222	4.0	0.244	0.6	47.6	1.130	1.2	2.8	1.72	0.81	36.4	3.8
11LX030-4	0.169	3.8	0.060	4.0	0.338	0.4	18.1	0.367	1.2	2.0	2.80	0.82	35.9	3.7
Weighted Mean age ± error (95% confidence) (MSWD = 0.25, P = 0.86)													37 ± 4 Ma	
11LX040-1	1.256	3.8	0.826	4.0	1.041	0.4	84.8	5.542	1.2	2.6	1.51	0.74	54.0	5.6
11LX040-2	0.299	3.8	0.217	4.0	0.221	0.5	92.9	2.562	1.2	2.5	1.37	0.76	95.7	9.9
11LX040-3	0.477	3.8	0.306	4.0	0.424	0.5	73.5	3.374	1.2	2.3	1.55	0.82	79.7	8.2
11LX040-4	0.404	3.8	0.293	4.0	0.506	0.4	69.3	2.409	1.2	2.4	1.37	0.80	62.9	6.5
11LX040-5	0.663	3.8	0.370	4.0	0.702	0.5	93.2	3.874	1.2	2.2	1.78	0.81	73.5	7.5
11LX049A-1	0.013	3.9	0.084	4.0	0.099	0.9	24.6	0.615	1.2	2.8	0.15	0.79	72.5	7.5
11LX049A-2	0.022	3.9	0.072	4.0	0.080	0.8	18.2	0.650	1.2	2.7	0.30	0.80	85.0	8.8

11LX049A-3	0.007	4.3	0.052	4.0	0.043	1.2	10.6	0.274	1.2	3.3	0.13	0.83	50.0	5.3
11LX049A-4	0.004	4.7	0.115	4.0	0.075	0.9	32.5	0.902	1.2	3.2	0.03	0.78	81.8	8.6
11LX049A-5	0.013	3.9	0.076	4.0	0.112	0.7	16.3	0.576	1.2	2.6	0.17	0.78	75.2	7.8
11LX053A-1	0.362	3.8	0.096	4.0	0.141	0.7	65.8	1.212	1.2	2.4	3.74	0.75	73.0	7.5
11LX053A-2	0.549	3.8	0.127	4.0	0.148	0.7	84.8	1.383	1.2	2.6	4.30	0.76	57.8	6.0
11LX053A-3	0.073	3.8	0.049	4.0	0.085	0.9	28.3	0.349	1.2	2.5	1.46	0.71	59.7	6.2
11LX053A-4	0.005	4.8	0.029	4.0	0.091	0.9	22.5	0.262	1.2	1.9	0.16	0.71	97.1	9.9
11LX053A-5	0.008	4.1	0.027	4.0	0.054	1.0	19.1	0.102	1.2	2.9	0.28	0.71	40.5	4.2
11LX115-1	0.002	8.2	0.040	4.0	0.061	0.9	15.3	0.196	1.2	3.0	0.04	0.75	51.9	5.4
11LX115-2	0.042	3.8	0.107	4.0	0.188	0.5	19.2	0.765	1.2	2.5	0.39	0.80	66.5	6.8
11LX115-3	0.011	3.9	0.100	4.0	0.116	0.7	15.9	0.543	1.2	3.0	0.11	0.82	52.6	5.5
11LX115-4	0.014	3.9	0.098	4.0	0.125	0.7	10.9	0.770	1.2	2.7	0.14	0.86	71.6	7.4
11LX115-5	0.050	3.8	0.082	4.0	0.165	0.7	10.5	0.638	1.2	2.3	0.60	0.84	65.7	6.7
Weighted Mean age ± error (95% confidence) (MSWD = 2.0, P = 0.09)													60 ± 11 Ma	
11LX116A-1	0.004	4.6	0.045	4.0	0.012	2.2	17.3	0.244	1.2	3.8	0.10	0.76	57.0	6.1
11LX116A-2	0.002	7.5	0.121	4.1	0.007	3.5	42.9	0.669	1.2	4.2	0.02	0.80	56.3	6.1
11LX116A-3	0.003	5.3	0.070	4.0	0.013	1.9	31.9	0.462	1.2	3.8	0.05	0.75	71.1	7.6
11LX116A-4	0.005	4.7	0.065	4.0	0.014	2.3	16.7	0.371	1.2	3.8	0.08	0.79	57.9	6.2
11LX116A-5	0.005	5.2	0.059	4.2	0.012	2.5	21.5	0.376	1.2	4.0	0.09	0.78	65.4	7.0
Weighted Mean age ± error (95% confidence) (MSWD = 0.86, P = 0.49)													61 ± 6 Ma	

Appendix Table 7.1 Sample locations and mineral assemblages for the late Mesozoic igneous rocks in the Jiaobei region

Sample No.	Unit	GPS	Lithology	Average magnetic suscecibility (10-3) SI	Mineral assemblage	Age ±2SE, Ma	Inherited zircon ages
13JD062B	Luanjiahe	N 37.242700 °, E 120.559080 °	Granite	0.3	Qz+Afs+Pl+Bt+Ttn+Fe oxide	159 ±1	2.5, 2.6Ga
13JD009B	Linglong	N 36.814200 °, E 120.017100 °	Granite	0.06	Qz+Pl+Afs+Bt+Ep+Aln	157 ±2	770 ,710 Ma; 1.8, 2.2, 2.4 Ga
13JD054B	Linglong	N 37.516930 °, E 120.529850 °	Granite	4.8	Qz+Afs+Pl+Bt+Chl+Hbl+Aln+ Ap	155 ±3	200, 220, 240 Ma;1.8, 2.5, 2.7 Ga
13JD054D	Linglong	N 37.516930 °, E 120.529850 °	Enclave in host granite	0.3	Pl+Afs+Qz+Hbl+Bt+Chl+Ep+ Ttn+Aln+Ap+Zrn	154 ±4	1.6, 1.8, 2.2 Ga
13JD060A	Linglong	N 37.454930 °, E 120.559600 °	Granite	2.5	Qz+Pl+Asf+Bt+Chl	155 ±2	210 Ma, 2.5, 3.3 Ga
13JD040I	Linglong	N 37.471860 °, E 120.224720 °	Granodiorite	12.2	Pl+Afs+Qz+Hbl+Bt+Chl+Aln+ Ap+Fe oxide	154 ±2	210, 230, 280 Ma;1.9, 2.3, 2.5 Ga
13JD048B	Linglong	N 37.474990 °, E 120.520130 °	Granite	5.2	Pl+Afs+Qz+Hbl+Bt+Chl+Aln+ Ap+Fe oxide	149 ±1	2.1 Ga
13JD057A	Guojialing	N 37.555370 °, E 120.597070 °	Granodiorite	2.2	Pl+Qz+Afs+Hbl+Bt+Chl+Ttn+ Ap+Fe oxide	127 ±1	2.2 Ga
13JD057C	Guojialing	N 37.555370 °, E 120.597070 °	mafic granular enclave	0.3	Pl+Hbl+Bt+Asf+Qz+Ttn+Ap+ Fe oxide+Zrn	127 ±1	2.5, 2.8 Ga

13JD040A	Dioritic intrusion	N 37.471860°, E 120.224720°	Gabbro-diorite	0.4	Pl+Hbl+Bt+Afs+Qz+Ttn+Aln+Ap+Fe oxide+Zrn	123 ± 2	1.4, 2.3, 2.4, 2.5 Ga
13JD040F	Dioritic intrusion	N 37.471860°, E 120.224720°	Monzonite	1.1	Pl+Afs+Qz+Hbl+Bt+Aln+Ttn	122 ± 3	2.3, 2.5 Ga

Appendix Table 7.2 LA-ICP-MS zircon U-Th-Pb isotope data for the late Mesozoic igneous rocks from the Jiaobei region

Spot No.	Type	U	Th/U	Isotope ratios						Corrected ages (Ma)					
				207Pb /235U	2 Se	206Pb /238U	2 Se	207Pb/206Pb	2 Se	207Pb /235U	2 Se	206Pb /238U	2 Se	207Pb/206Pb	2 Se
13JD009B															
X009B_1	rim	785	0.16	0.178	0.01	0.025	0.0005	0.0526	0.0035	165	11	156.4	3.2	290	140
X009B_2	core	116	0.52	8.360	0.4	0.409	0.0100	0.1482	0.0043	2272	46	2208	46	2323	51
X009B_3	rim	174	0.28	2.460	0.31	0.161	0.0180	0.1109	0.0055	1228	96	950	100	1792	92
X009B_4	core	130	0.39	4.920	0.22	0.316	0.0055	0.1125	0.0043	1804	38	1770	27	1830	68
X009B_5	rim	1306	0.09	0.177	0.02	0.025	0.0008	0.0518	0.0047	165	13	160.5	5.1	280	190
X009B_6	rim	1447	0.10	0.165	0.02	0.024	0.0005	0.0492	0.0056	155	16	154.8	3	160	230
X009B_7	rim	861	0.09	0.162	0.01	0.024	0.0004	0.0484	0.0039	153	12	152	2.4	140	150
X009B_8	core	257	0.81	9.580	0.41	0.439	0.0075	0.1567	0.0046	2394	40	2344	34	2412	51
X009B_9	rim	449	0.80	4.500	0.18	0.251	0.0042	0.1136	0.0036	1728	33	1444	21	1847	57
X009B_10	rim	100	0.11	0.207	0.04	0.030	0.0013	0.0512	0.009	184	30	188.2	8.4	240	320
X009B_11	core	573	0.10	0.248	0.02	0.034	0.0007	0.0523	0.0037	224	13	213.7	4.6	280	140
X009B_12	rim	1128	0.10	0.173	0.02	0.022	0.0007	0.0495	0.0045	162	14	140.1	4.1	160	180
X009B_13	rim	347	1.38	1.161	0.06	0.127	0.0027	0.0669	0.0035	782	31	768	16	800	110
X009B_14	rim	230	0.51	3.830	0.24	0.252	0.0110	0.1104	0.0041	1584	50	1450	58	1810	67
X009B_15	homo	302	0.24	7.360	0.49	0.374	0.0180	0.1337	0.0046	2139	64	2050	86	2173	55
X009B_16	rim	71	0.41	0.176	0.04	0.026	0.0014	0.0520	0.012	166	34	162.7	9.1	180	370
X009B_17	rim	368	0.41	0.189	0.02	0.024	0.0007	0.0564	0.0063	176	19	155.3	4.4	370	220
X009B_18	rim	1130	0.20	0.164	0.02	0.025	0.0008	0.0480	0.0053	154	15	157.5	4.8	100	210
X009B_19	core	202	1.62	1.043	0.08	0.113	0.0019	0.0648	0.0043	720	40	690	11	760	150
X009B_20	rim	174	0.28	0.203	0.03	0.025	0.0007	0.0584	0.0079	190	22	158.8	4.6	470	260

X009B_21	core	192	0.03	0.206	0.03	0.031	0.0009	0.0453	0.0068	185	26	198.7	5.8	40	260
X009B_22	rim	1220	0.11	0.163	0.01	0.024	0.0005	0.0482	0.0037	153	11	155.6	3.1	110	150
X009B_23	rim	495	0.88	0.148	0.01	0.021	0.0005	0.0454	0.0038	141	11	131.1	3.3	70	160
X009B_24	core	211	0.63	1.038	0.07	0.117	0.0020	0.0628	0.004	720	34	713	12	680	130
X009B_25	rim	328	0.01	0.212	0.02	0.032	0.0007	0.0477	0.0043	195	16	200.6	4.3	120	160
X009B_26	rim	1440	0.16	0.173	0.02	0.025	0.0005	0.0491	0.004	161	13	160.4	3	180	170
X009B_27	rim	3900	0.10	0.135	0.01	0.020	0.0004	0.0498	0.0021	128.5	6.7	124.6	2.7	179	94
X009B_28	rim	386	0.43	0.729	0.04	0.085	0.0023	0.0629	0.0036	559	26	526	14	680	120
X009B_29	rim	92	0.22	0.164	0.04	0.025	0.0012	0.0530	0.012	147	31	158.7	7.4	110	370
X009B_30	rim	1069	0.12	0.176	0.01	0.025	0.0005	0.0501	0.0029	164.4	9.2	159.7	2.9	180	120
X009B_31	rim	1483	0.12	0.172	0.02	0.025	0.0007	0.0494	0.0059	161	18	158.5	4.3	160	240
X009B_32	rim	1353	0.18	0.185	0.01	0.025	0.0005	0.0527	0.004	172	12	160.8	3.3	290	160
X009B_33	rim	842	0.07	0.167	0.01	0.024	0.0004	0.0497	0.0036	156	11	153.8	2.7	170	140
X009B_34	core	69	0.43	5.350	0.28	0.343	0.0078	0.1116	0.0053	1883	49	1897	38	1848	91
X009B_35	rim	1327	0.20	0.180	0.01	0.025	0.0006	0.0529	0.0036	172	12	158.4	3.8	330	150
X009B_36	core	87	0.81	1.203	0.1	0.126	0.0038	0.0660	0.0055	803	46	767	22	790	150
X009B_37	rim	2470	0.12	0.129	0.01	0.018	0.0004	0.0500	0.0032	122.9	7.6	117.3	2.6	180	130
X009B_38	core	111	0.12	0.200	0.03	0.025	0.0010	0.0579	0.01	183	30	157.3	6.1	440	330
13JD048B															
X48B_1	core	49	0.85	0.209	0.06	0.025	0.0015	0.0720	0.021	182	49	156.9	9.6	330	500
X48B_2	rim	1480	0.09	0.251	0.03	0.023	0.0007	0.0807	0.0087	224	24	147	4.2	1040	230
X48B_3	rim	80	0.54	0.162	0.04	0.022	0.0008	0.0530	0.013	148	37	142.5	5	50	400
X48B_4	mix	780	0.38	0.175	0.01	0.024	0.0005	0.0530	0.0041	163	12	150.8	3.1	300	160
X48B_5	core	72	0.55	0.201	0.05	0.024	0.0012	0.0600	0.014	173	40	149.4	7.7	270	430
X48B_6	rim	769	0.51	0.155	0.01	0.023	0.0005	0.0484	0.0044	145	12	146.7	3.1	100	170
X48B_7	rim	704	0.13	0.162	0.02	0.024	0.0005	0.0488	0.0042	152	13	150.7	3.3	160	170
X48B_8	rim	1236	0.51	0.169	0.01	0.024	0.0005	0.0524	0.0042	158	11	149.7	3.4	270	160

X48B_9	core	101	0.55	0.147	0.04	0.023	0.0010	0.0440	0.012	135	33	147.4	6.3	-70	390
X48B_10	homo	88	0.27	0.212	0.05	0.024	0.0013	0.0590	0.014	183	39	153.9	8.2	310	400
X48B_11	rim	983	0.92	0.163	0.01	0.023	0.0004	0.0517	0.0039	154.3	11	146.2	2.7	290	160
X48B_12	rim	568	0.24	0.164	0.02	0.023	0.0004	0.0515	0.0049	153	13	147.7	2.8	230	190
X48B_13	core	88	0.53	0.168	0.04	0.024	0.0011	0.0460	0.011	149	32	151.2	7	-60	350
X48B_14	homo	89	0.65	0.183	0.04	0.024	0.0012	0.0570	0.011	164	30	149.6	7.5	330	350
X48B_15	homo	115	0.86	0.165	0.03	0.024	0.0011	0.0504	0.0097	149	28	152.3	6.9	70	320
X48B_16	rim	398	0.92	0.149	0.02	0.024	0.0005	0.0458	0.005	139	15	150.5	3.2	60	180
X48B_17	rim	536	0.26	0.150	0.02	0.023	0.0005	0.0462	0.0046	141	13	148.3	3.3	20	180
X48B_18	rim	89	0.61	0.173	0.03	0.023	0.0012	0.0570	0.011	156	29	144.2	7.5	380	370
X48B_19	core	339	0.24	0.167	0.02	0.024	0.0006	0.0514	0.0058	155	16	150.2	3.4	230	200
X48B_20	homo	66	0.43	0.205	0.05	0.019	0.0012	0.0720	0.017	178	37	123.8	7.3	400	410
X48B_21	homo	89	0.28	0.176	0.04	0.024	0.0013	0.0520	0.012	156	33	153.3	8.3	110	370
X48B_22	homo	45	0.43	0.199	0.05	0.024	0.0018	0.0700	0.018	172	40	152	11	380	470
X48B_23	rim	804	0.54	0.162	0.01	0.023	0.0005	0.0493	0.004	151	12	148.5	3	180	160
X48B_24	homo	78	0.57	0.229	0.04	0.023	0.0011	0.0730	0.013	205	36	148.4	6.8	700	370
X48B_25	core	47	0.49	0.148	0.04	0.023	0.0015	0.0450	0.012	131	35	149.2	9.2	-80	410
X48B_26	rim	142	0.95	0.176	0.03	0.024	0.0010	0.0565	0.0089	164	24	151.8	6.1	270	290
X48B_27	core	84	0.41	0.228	0.05	0.025	0.0012	0.0670	0.014	197	38	156.2	7.6	420	390
X48B_28	rim	711	0.25	0.163	0.01	0.023	0.0004	0.0504	0.0043	153	12	147.3	2.7	220	170
X48B_29	core	123	0.56	0.153	0.03	0.025	0.0010	0.0475	0.0085	141	23	156.1	6.4	40	290
X48B_30	rim	269	0.15	0.175	0.02	0.024	0.0007	0.0520	0.0065	171	19	151.3	4.2	350	220
X48B_31	core	474	0.31	4.620	0.66	0.241	0.0250	0.1339	0.0068	1670	130	1370	130	2125	91
X48B_32	homo	114	0.80	0.205	0.03	0.023	0.0010	0.0640	0.011	183	28	148.4	6.1	550	330
X48B_33	homo	137	0.83	0.184	0.03	0.023	0.0009	0.0588	0.0095	167	25	146.1	5.7	350	300
X48B_34	rim	724	0.99	0.175	0.02	0.023	0.0004	0.0555	0.0047	166	13	147.5	2.7	380	170
X48B_35	homo	211	1.28	0.162	0.02	0.023	0.0007	0.0473	0.007	149	21	148.2	4.6	140	260

13JD057A

X57A_1	rim	46	0.20	0.151	0.03	0.019	0.0008	0.0590	0.011	145	25	122.5	5.1	390	360
X57A_2	core	6	0.02	0.270	0.04	0.033	0.0010	0.0585	0.0082	240	30	206.1	6.5	460	290
X57A_3	rim	62	0.22	3.410	0.66	0.163	0.0280	0.1380	0.012	1300	190	950	150	2080	210
X57A_4	rim	74	0.16	0.530	0.13	0.043	0.0075	0.0798	0.0081	389	74	271	45	1050	220
X57A_5	homo	72	0.33	0.130	0.02	0.020	0.0006	0.0458	0.0073	121	18	126.6	3.7	-30	260
X57A_6	homo	202	0.52	0.144	0.02	0.020	0.0005	0.0533	0.0059	135	14	125.6	3.4	270	210
X57A_7	homo	178	0.48	0.163	0.02	0.021	0.0006	0.0569	0.0064	151	16	132	3.5	390	220
X57A_8	homo	169	0.44	0.128	0.02	0.020	0.0006	0.0442	0.0051	121	14	128.2	3.7	-40	190
X57A_9	homo	41	0.16	0.147	0.02	0.018	0.0007	0.0495	0.0057	137	16	115.8	4.2	290	220
X57A_10	homo	196	0.42	0.136	0.02	0.020	0.0006	0.0506	0.0049	130	13	125.1	3.5	200	190
X57A_11	homo	132	0.40	0.124	0.02	0.020	0.0005	0.0455	0.0066	117	16	125.8	3.3	-10	240
X57A_12	homo	70	0.18	0.142	0.02	0.020	0.0006	0.0507	0.0062	133	15	125.2	3.5	240	220
X57A_13	homo	179	0.51	0.136	0.02	0.020	0.0006	0.0477	0.0052	128	13	129	3.6	110	200
X57A_14	rim	110	0.42	0.153	0.02	0.020	0.0006	0.0549	0.0055	143	15	125.5	3.6	370	200
X57A_15	homo	194	0.49	0.141	0.02	0.020	0.0006	0.0506	0.0056	133	14	125.2	3.6	170	200
X57A_16	homo	156	0.44	0.135	0.02	0.020	0.0005	0.0496	0.0075	128	18	124.9	3.2	120	260
X57A_17	homo	172	0.52	0.155	0.02	0.020	0.0005	0.0567	0.0072	148	17	129.3	3.4	380	240
X57A_18	rim	73	0.28	0.232	0.03	0.021	0.0006	0.0780	0.01	207	25	132.9	3.5	1040	280
X57A_19	core	70	0.58	7.360	0.33	0.381	0.0069	0.1378	0.0055	2158	40	2077	32	2198	69
X57A_20	homo	211	0.51	0.142	0.02	0.020	0.0006	0.0513	0.0071	132	17	126.5	4	200	250
X57A_21	homo	131	0.41	0.136	0.02	0.019	0.0005	0.0510	0.0065	128	15	121.4	3.2	200	230
X57A_22	homo	162	0.51	0.128	0.02	0.020	0.0005	0.0481	0.0064	127	14	128	3.3	150	220
X57A_23	homo	51	0.20	0.163	0.02	0.024	0.0007	0.0499	0.0066	151	19	150.8	4.2	110	230
X57A_24	core	7	0.08	0.218	0.04	0.036	0.0013	0.0419	0.0076	191	34	228.3	8	-130	280
X57A_25	rim	143	0.26	0.137	0.01	0.020	0.0007	0.0483	0.0053	129	13	130.6	4.1	110	210
X57A_26	rim	138	0.40	0.106	0.02	0.020	0.0006	0.0393	0.0053	103	14	127.8	3.6	-250	200

13JD057C															
X57C_1	rim	17	0.06	0.230	0.14	0.023	0.0040	0.0650	0.043	167	97	144	25	-60	830
X57C_2	homo	343	0.37	0.139	0.02	0.020	0.0005	0.0503	0.0055	133	14	126.1	3.3	260	200
X57C_3	homo	191	0.26	0.136	0.02	0.021	0.0006	0.0471	0.0068	129	18	131.9	3.8	70	250
X57C_4	rim	259	0.21	0.142	0.02	0.020	0.0005	0.0529	0.0066	135	15	125.5	3.3	250	220
X57C_5	homo	217	0.28	0.139	0.02	0.020	0.0007	0.0517	0.0077	130	18	126.2	4.3	190	270
X57C_6	homo	168	0.33	0.152	0.02	0.021	0.0007	0.0530	0.0082	140	20	131.5	4.4	240	280
X57C_7	homo	305	0.39	0.128	0.02	0.020	0.0005	0.0470	0.0058	120	14	125.3	2.9	120	210
X57C_8	homo	230	0.29	0.133	0.02	0.019	0.0005	0.0508	0.0059	126	14	124.3	3.3	150	210
X57C_9	rim	245	0.44	0.144	0.02	0.020	0.0006	0.0513	0.0061	137	15	128.9	3.8	230	210
X57C_10	homo	300	0.34	0.134	0.02	0.020	0.0006	0.0470	0.0056	126	15	125.3	3.6	80	210
X57C_11	homo	319	0.36	0.134	0.02	0.020	0.0006	0.0467	0.005	127	14	128.9	3.7	50	190
X57C_12	homo	252	0.31	0.136	0.02	0.020	0.0007	0.0505	0.0055	132	15	127.9	4.1	250	210
X57C_13	homo	196	0.28	0.129	0.02	0.020	0.0007	0.0464	0.0061	122	15	127.4	4.5	110	220
X57C_14	homo	313	0.37	0.133	0.02	0.020	0.0006	0.0483	0.0055	126	14	128.6	3.7	120	210
X57C_15	homo	271	0.35	0.129	0.02	0.020	0.0005	0.0487	0.0065	122	15	124.6	3.4	60	230
X57C_16	rim	235	0.36	0.152	0.02	0.019	0.0006	0.0585	0.0065	142	15	122	3.7	410	220
X57C_17	homo	288	0.37	0.134	0.02	0.021	0.0006	0.0448	0.0056	126	15	133.4	3.5	30	210
X57C_18	homo	289	0.34	0.147	0.02	0.020	0.0006	0.0526	0.0057	138	15	125	3.7	310	210
X57C_19	rim	240	0.31	0.146	0.02	0.021	0.0006	0.0518	0.0057	141	16	132	3.8	220	210
X57C_20	core	94	0.30	14.180	0.54	0.512	0.0084	0.2001	0.0059	2759	37	2663	36	2824	50
X57C_21	rim	303	0.42	0.165	0.02	0.020	0.0005	0.0611	0.0065	154	15	125.2	3	530	200
X57C_22	rim	303	0.39	0.140	0.01	0.020	0.0007	0.0526	0.0052	132	13	126.3	4.1	280	190
X57C_23	core	290	0.50	0.144	0.02	0.020	0.0007	0.0507	0.0065	139	17	127.7	4.4	250	240
X57C_24	rim	541	0.25	0.125	0.01	0.020	0.0005	0.0467	0.004	120.2	9.7	125.3	2.9	100	160
X57C_25	core	427	0.19	7.790	0.7	0.345	0.0260	0.1633	0.0047	2203	83	1910	120	2489	47
X57C_26	homo	332	0.33	0.156	0.02	0.020	0.0005	0.0540	0.0073	144	19	127.2	3.3	350	250
X57C_27	homo	310	0.37	0.131	0.02	0.020	0.0007	0.0482	0.0061	132	15	127	4.5	210	210

X57C_28	rim	302	0.23	0.152	0.02	0.020	0.0007	0.0565	0.0079	144	19	126	4.3	360	270
X57C_29	core	185	0.16	13.200	0.5	0.419	0.0072	0.2022	0.0059	2692	36	2255	33	2847	46
X57C_30	homo	298	0.38	0.122	0.02	0.020	0.0006	0.0463	0.0069	115	17	126.8	3.6	40	260
X57C_31	rim	366	0.44	0.139	0.02	0.020	0.0006	0.0490	0.0068	132	17	130.1	3.9	100	240
X57C_32	core	154	0.43	0.119	0.03	0.017	0.0007	0.0470	0.01	110	23	106.8	4.3	-30	340
X57C_33	rim	497	0.24	0.127	0.02	0.019	0.0004	0.0485	0.0056	120	14	120.4	2.8	100	210
X57C_34	core	73	0.33	10.560	0.49	0.452	0.0083	0.1681	0.0064	2483	42	2402	37	2545	64
13JD062B															
X62B_1	rim	37	0.24	0.192	0.08	0.029	0.0033	0.0520	0.022	169	62	185	21	-200	580
X62B_2	rim	377	0.07	0.170	0.02	0.029	0.0007	0.0427	0.0039	160	13	183	4.1	-60	160
X62B_3	core	154	0.21	0.260	0.03	0.034	0.0009	0.0576	0.0064	237	25	214.8	5.6	440	210
X62B_4	rim	63	0.58	0.133	0.04	0.025	0.0014	0.0410	0.011	120	30	158.1	8.8	-230	370
X62B_5	core	42	0.41	0.244	0.09	0.027	0.0027	0.0690	0.022	206	68	171	17	520	630
X62B_6	rim	279	0.18	0.171	0.03	0.028	0.0024	0.0463	0.009	168	33	177	15	20	340
X62B_7	core	225	0.42	12.030	0.47	0.482	0.0075	0.1810	0.0049	2610	34	2536	32	2665	43
X62B_8	homo	239	0.17	0.251	0.03	0.032	0.0009	0.0540	0.0059	230	20	205.2	5.7	400	200
X62B_9	rim	312	0.22	0.151	0.02	0.025	0.0007	0.0426	0.0048	141	15	159.2	4.5	-100	190
X62B_10	rim	311	0.20	0.184	0.02	0.026	0.0011	0.0507	0.0056	169	17	168.1	6.8	220	210
X62B_11	core	247	0.08	0.259	0.03	0.035	0.0010	0.0530	0.0068	230	27	223.1	6.2	280	230
X62B_12	rim	988	0.02	0.199	0.01	0.029	0.0005	0.0502	0.0027	183.4	9.5	181.4	3.1	220	110
X62B_14	rim	342	0.13	0.139	0.02	0.025	0.0006	0.0420	0.0042	133	13	157.5	3.7	-140	160
X62B_15	rim	1113	0.28	0.172	0.02	0.025	0.0006	0.0487	0.0043	161	13	156.4	3.7	130	180
X62B_16	rim	444	0.14	0.181	0.02	0.025	0.0005	0.0509	0.0047	168	14	161.2	3.3	220	180
X62B_17	core	91	0.10	0.288	0.06	0.034	0.0018	0.0580	0.012	244	49	213	12	380	400
X62B_18	rim	731	0.17	0.161	0.01	0.025	0.0005	0.0458	0.004	151	11	156.4	3.1	30	160
X62B_19	homo	607	0.13	0.174	0.01	0.024	0.0005	0.0504	0.0039	163	12	152.7	3	210	160
X62B_20	rim	275	0.10	0.199	0.03	0.030	0.0010	0.0475	0.0057	181	21	188.5	6	190	210

X62B_21	core	457	0.27	0.237	0.05	0.028	0.0014	0.0630	0.015	219	44	177.6	8.8	460	460
X62B_22	rim	1560	0.18	0.161	0.02	0.025	0.0005	0.0472	0.0044	152	14	159.1	3.3	50	170
X62B_23	rim	3240	0.25	0.178	0.01	0.025	0.0004	0.0501	0.0034	165.4	10	159.9	2.2	240	130
X62B_24	core	233	0.76	0.286	0.05	0.038	0.0017	0.0580	0.011	245	39	240	11	250	310
X62B_25	rim	1304	0.07	0.178	0.02	0.024	0.0005	0.0526	0.005	165	15	155.1	3.4	290	190
X62B_26	core	702	0.25	6.070	0.51	0.258	0.0190	0.1694	0.0055	1973	76	1466	96	2560	54
X62B_27	rim	570	0.17	0.199	0.02	0.029	0.0011	0.0512	0.0063	190	18	184.3	7.2	260	210
X62B_28	rim	280	0.46	0.134	0.03	0.025	0.0013	0.0382	0.0095	123	29	158.6	8.4	-290	340
X62B_29	rim	2520	0.09	0.171	0.01	0.025	0.0005	0.0503	0.0031	159.8	9.1	159	3.2	190	120
X62B_30	core	456	0.05	0.176	0.04	0.021	0.0018	0.0520	0.011	161	37	134	11	210	410
X62B_31	rim	987	0.42	0.185	0.02	0.025	0.0006	0.0516	0.0053	173	16	162.2	3.8	250	190
X62B_32	core	904	0.63	0.438	0.04	0.055	0.0031	0.0580	0.004	363	29	341	19	480	150
X62B_33	rim	1720	0.14	0.170	0.01	0.025	0.0005	0.0482	0.0036	159	11	161.2	3.3	120	140
X62B_34	rim	1091	0.44	0.176	0.02	0.024	0.0006	0.0518	0.0041	166	12	155.4	3.5	250	150
X62B_35	rim	454	0.14	0.620	0.07	0.062	0.0031	0.0637	0.0057	484	43	388	19	700	190
X62B_36	rim	431	0.20	0.168	0.02	0.025	0.0008	0.0480	0.0065	157	21	157.8	5.2	110	240
X62B_37	rim	1377	0.17	0.171	0.01	0.025	0.0005	0.0501	0.0038	159	12	157.6	3.2	190	150
X62B_38	core	10	0.17	0.230	0.13	0.042	0.0063	0.1570	0.099	143	86	261	39	-210	700
X62B_39	rim	189	0.35	0.217	0.05	0.029	0.0011	0.0510	0.011	188	38	185.2	6.9	200	370
13JD060A															
L60A_1	rim	1076	0.13	0.156	0.01	0.024	0.0006	0.0455	0.0033	148	11	155.7	3.6	0	130
L60A_2	core	12	1.00	0.240	0.11	0.037	0.0047	0.0490	0.024	167	76	238	30	-600	510
L60A_3	core	274	0.33	0.219	0.03	0.034	0.0011	0.0472	0.0064	197	24	212.1	6.7	100	240
L60A_4	rim	915	0.14	0.168	0.02	0.025	0.0008	0.0489	0.0045	161	13	156.2	4.9	120	170
L60A_5	core	406	0.14	0.157	0.02	0.024	0.0008	0.0491	0.0065	153	18	153.6	5.2	100	230
L60A_6	rim	386	0.33	0.160	0.02	0.025	0.0008	0.0453	0.0059	150	19	159.2	4.8	80	230
L60A_7	core	90	0.50	0.180	0.04	0.024	0.0013	0.0530	0.012	158	36	149.4	8.3	190	380

L60A_8	homo	178	0.50	0.141	0.03	0.023	0.0010	0.0452	0.0096	129	25	147.3	6.2	-40	320
L60A_9	rim	677	0.20	0.160	0.02	0.024	0.0008	0.0491	0.0046	149	13	151	4.8	180	170
L60A_10	core	133	0.50	0.175	0.03	0.024	0.0010	0.0498	0.0089	158	27	153.7	5.9	40	300
L60A_11	homo	221	1.00	0.179	0.03	0.024	0.0010	0.0571	0.0095	162	25	154.1	6.5	340	310
L60A_12	rim	495	0.20	0.163	0.02	0.024	0.0008	0.0476	0.0064	151	19	155.4	5	90	240
L60A_13	core	330	0.33	0.180	0.03	0.024	0.0009	0.0476	0.0068	164	23	155.3	5.5	130	260
L60A_14	rim	176	1.00	0.137	0.03	0.024	0.0011	0.0393	0.0075	126	24	149.7	7	-240	280
L60A_15	core	126	0.08	0.273	0.05	0.034	0.0016	0.0620	0.011	235	40	215	10	460	350
L60A_16	rim	1351	0.20	0.189	0.01	0.024	0.0006	0.0538	0.0032	175	11	153.5	3.8	350	130
L60A_17	rim	1091	0.20	0.171	0.02	0.026	0.0007	0.0496	0.0048	160	15	166.3	4.3	160	180
L60A_18	rim	4616	0.07	0.108	0.01	0.015	0.0004	0.0520	0.0024	103.6	5.2	95.9	2.3	300	100
L60A_19	homo	222	0.25	0.156	0.03	0.024	0.0009	0.0439	0.0072	146	23	155.8	5.6	-90	260
L60A_20	rim	892	0.25	0.168	0.01	0.024	0.0006	0.0505	0.004	157	12	154.8	4	180	150
L60A_21	homo	78	1.00	0.287	0.06	0.022	0.0013	0.0860	0.017	238	47	141.9	8.2	880	420
L60A_22	core	536	0.33	0.536	0.1	0.044	0.0046	0.0773	0.005	400	54	274	28	1080	140
L60A_23	homo	113	1.00	0.176	0.04	0.025	0.0014	0.0510	0.011	156	33	156	8.6	120	370
L60A_24	core	40	0.04	0.243	0.07	0.034	0.0024	0.0520	0.014	207	54	218	15	10	430
L60A_25	rim	504	0.33	0.182	0.02	0.026	0.0008	0.0529	0.0059	167	20	166.5	5.3	290	210
L60A_26	mix	136	1.00	1.070	0.11	0.110	0.0036	0.0672	0.0066	735	55	675	21	850	200
L60A_27	homo	565	0.11	0.182	0.02	0.025	0.0008	0.0503	0.0053	168	16	159.9	4.7	260	190
L60A_28	rim	1305	0.25	0.170	0.01	0.024	0.0006	0.0532	0.0033	162	11	153.1	3.9	310	130
L60A_29	core	179	1.00	0.242	0.03	0.025	0.0010	0.0667	0.0084	220	26	161.8	6.2	740	260
L60A_30	core	678	0.33	23.560	0.63	0.571	0.0140	0.2739	0.0062	3253	28	2912	56	3324	35
L60A_31	rim	1065	0.33	0.183	0.02	0.027	0.0009	0.0493	0.0041	170	13	170.1	5.6	180	170
L60A_32	rim	182	0.50	0.264	0.04	0.024	0.0010	0.0810	0.012	231	30	154.3	6.3	1030	290
L60A_33	rim	666	0.33	0.194	0.02	0.025	0.0008	0.0565	0.0057	178	18	161.8	5.2	380	200
L60A_34	rim	428	1.00	0.200	0.02	0.027	0.0008	0.0555	0.0054	183	16	169.2	5.1	370	200
L60A_35	core	213	0.50	0.164	0.03	0.025	0.0010	0.0480	0.0086	149	25	156.1	6	40	290

L60A_36	rim	358	0.33	2.600	0.29	0.143	0.0130	0.1286	0.0053	1292	87	857	74	2088	67
L60A_37	core	1174	0.13	8.840	0.2	0.392	0.0086	0.1611	0.0024	2321	20	2133	40	2470	24
L60A_38	rim	1626	0.17	0.185	0.01	0.025	0.0007	0.0507	0.0034	172.1	9.5	161.6	4.2	240	130
L60A_39	rim	420	0.50	0.174	0.02	0.024	0.0008	0.0526	0.0069	163	20	154.4	5.1	280	240
L60A_40	rim	644	0.33	0.159	0.02	0.023	0.0007	0.0500	0.0049	149	13	143.5	4.5	170	180
13JD040I															
X40I_1	rim	449	0.17	0.166	0.02	0.025	0.0007	0.0506	0.0067	153	19	156.1	4.4	130	230
X40I_2	rim	296	0.08	0.174	0.03	0.024	0.0010	0.0500	0.0076	159	22	152.6	6.2	190	280
X40I_3	core	472	0.33	0.192	0.02	0.030	0.0010	0.0463	0.0059	175	21	191	6.1	70	220
X40I_4	rim	617	0.20	0.172	0.02	0.024	0.0007	0.0524	0.0056	164	13	151.6	4.3	270	180
X40I_5	rim	126	0.05	0.209	0.05	0.024	0.0013	0.0640	0.014	175	36	151.5	7.9	280	380
X40I_6	core	161	0.50	0.333	0.05	0.045	0.0019	0.0521	0.0077	281	39	283	12	190	260
X40I_7	rim	640	0.17	0.158	0.02	0.024	0.0008	0.0476	0.0048	148	14	153.3	5.2	50	180
X40I_8	rim	212	0.05	0.191	0.04	0.024	0.0011	0.0590	0.012	170	32	154.1	6.9	260	340
X40I_9	core	275	0.33	6.930	0.32	0.311	0.0110	0.1463	0.0041	2096	42	1751	51	2297	49
X40I_10	rim	147	0.05	0.236	0.04	0.026	0.0012	0.0630	0.011	206	33	163.4	7.8	510	340
X40I_11	core	143	0.20	0.273	0.05	0.037	0.0016	0.0551	0.0099	234	39	230.8	9.9	300	320
X40I_12	core	244	0.33	8.920	0.28	0.395	0.0099	0.1640	0.0045	2329	28	2151	44	2498	44
X40I_13	rim	247	0.05	0.182	0.03	0.026	0.0011	0.0519	0.0081	173	24	162.4	6.9	230	280
X40I_14	core	190	0.14	10.480	0.45	0.471	0.0130	0.1595	0.0042	2473	41	2491	58	2452	45
X40I_15	rim	315	0.02	0.191	0.03	0.027	0.0009	0.0532	0.0071	176	23	169.7	5.6	230	240
X40I_16	rim	547	0.14	0.156	0.02	0.024	0.0006	0.0474	0.0059	145	17	151.6	4	70	220
X40I_17	core	435	0.50	0.178	0.04	0.027	0.0015	0.0530	0.011	163	31	174	9.3	250	400
X40I_18	core	193	0.50	11.020	0.32	0.478	0.0120	0.1650	0.0039	2522	27	2515	51	2511	40
X40I_19	rim	128	0.08	0.221	0.04	0.030	0.0014	0.0550	0.01	198	36	190.5	8.7	190	330
X40I_20	rim	454	0.11	0.149	0.02	0.024	0.0008	0.0428	0.0066	138	19	154.7	5.2	-130	230
X40I_21	rim	637	0.25	0.150	0.02	0.024	0.0008	0.0451	0.0049	141	14	150.5	4.9	-30	180

X40I_22	core	235	0.50	0.718	0.06	0.078	0.0025	0.0664	0.0054	550	32	483	15	820	160
X40I_23	rim	86	0.06	0.219	0.05	0.026	0.0018	0.0590	0.016	186	44	164	11	150	430
X40I_24	rim	1221	0.20	0.169	0.02	0.024	0.0007	0.0510	0.0041	159	12	151.2	4.4	220	160
X40I_25	core	733	0.14	10.070	0.32	0.439	0.0110	0.1646	0.0031	2437	29	2344	47	2503	32
X40I_26	rim	203	0.05	0.180	0.03	0.027	0.0011	0.0473	0.0079	163	25	168.7	7.1	100	290
X40I_27	rim	642	0.11	0.219	0.02	0.032	0.0010	0.0490	0.0043	201	17	205.5	6.4	200	170
X40I_28	core	208	1.00	0.871	0.08	0.104	0.0052	0.0631	0.0043	630	39	638	31	670	140
X40I_29	rim	230	0.02	0.177	0.03	0.024	0.0009	0.0540	0.01	159	28	155.1	5.5	200	320
X40I_30	mix	422	0.17	0.259	0.03	0.029	0.0017	0.0636	0.0067	229	26	184	11	630	210
X40I_31	core	29	1.00	5.350	0.46	0.317	0.0110	0.1230	0.011	1878	77	1778	57	1950	170
X40I_32	rim	636	0.14	0.170	0.02	0.021	0.0007	0.0526	0.0047	158	13	136.4	4.4	270	170
13JD054B															
X54B_1	homo	58	1.00	0.223	0.06	0.023	0.0016	0.0760	0.022	186	48	147	10	420	500
X54B_2	core	74	0.25	10.390	0.5	0.398	0.0130	0.1676	0.0066	2457	45	2154	62	2549	65
X54B_3	rim	814	0.17	0.168	0.01	0.024	0.0007	0.0505	0.004	156	12	150.8	4.5	230	150
X54B_4	rim	1510	0.20	0.150	0.01	0.023	0.0009	0.0481	0.003	141.6	9.7	147.2	5.5	170	120
X54B_5	core	570	0.50	1.021	0.04	0.109	0.0029	0.0658	0.0025	712	20	669	17	813	81
X54B_6	rim	952	0.09	0.174	0.02	0.025	0.0007	0.0495	0.0048	161	14	161.1	4.3	130	180
X54B_7	rim	204	0.09	0.239	0.04	0.033	0.0014	0.0510	0.01	208	35	210.2	8.7	140	320
X54B_8	core	655	0.11	0.203	0.03	0.032	0.0010	0.0469	0.0061	202	20	202.9	6.4	80	230
X54B_9	homo	36	1.00	0.213	0.08	0.026	0.0025	0.0710	0.027	166	61	166	16	-60	550
X54B_10	rim	1030	0.17	0.160	0.02	0.025	0.0008	0.0461	0.0044	152	13	159.2	5	30	180
X54B_11	homo	47	0.50	0.134	0.05	0.022	0.0018	0.0470	0.018	114	40	137	11	-470	450
X54B_12	rim	685	0.25	0.160	0.02	0.024	0.0008	0.0477	0.0048	150	14	153.9	4.8	70	180
X54B_13	homo	39	1.00	0.211	0.07	0.026	0.0021	0.0580	0.019	170	55	167	13	-70	500
X54B_14	rim	976	0.33	0.199	0.02	0.026	0.0011	0.0565	0.0048	185	19	163.1	6.8	410	170
X54B_15	core	550	0.01	4.720	0.15	0.297	0.0068	0.1140	0.0029	1771	26	1677	34	1859	46

X54B_16	rim	1278	0.33	0.175	0.01	0.024	0.0006	0.0539	0.0036	163	10	151.3	3.6	320	140
X54B_17	core	129	0.50	0.204	0.04	0.026	0.0013	0.0600	0.013	179	35	163.7	8.1	280	370
X54B_18	homo	173	1.00	0.579	0.06	0.077	0.0022	0.0561	0.006	463	38	479	13	360	200
X54B_19	rim	710	0.20	0.182	0.02	0.026	0.0008	0.0499	0.0039	171	13	167.8	4.8	210	150
X54B_20	core	427	0.04	0.285	0.04	0.038	0.0013	0.0554	0.0078	251	33	237.3	8.3	390	290
X54B_21	rim	856	0.20	0.169	0.02	0.024	0.0007	0.0515	0.0045	158	13	153.4	4.2	270	180
X54B_22	core	81	0.50	0.186	0.05	0.027	0.0019	0.0520	0.015	166	44	173	12	70	440
X54B_23	rim	1146	0.14	0.161	0.01	0.023	0.0007	0.0498	0.0039	150	11	149	4.2	170	150
X54B_24	core	789	0.05	0.263	0.02	0.035	0.0009	0.0537	0.0029	236	12	224.6	5.4	350	120
X54B_25	core	18	0.20	0.280	0.12	0.036	0.0044	0.0570	0.026	192	80	224	27	-270	570
X54B_26	rim	467	0.13	0.165	0.02	0.025	0.0009	0.0463	0.0062	152	20	159.7	5.3	-20	220
X54B_27	rim	1245	0.25	0.167	0.02	0.025	0.0008	0.0483	0.0038	161	13	159.4	5	140	160
X54B_28	core	123	1.00	12.710	0.48	0.480	0.0130	0.1858	0.0053	2663	34	2524	55	2706	44
X54B_29	core	169	0.25	11.740	0.46	0.463	0.0120	0.1766	0.0055	2575	38	2452	51	2616	55
X54B_30	rim	326	0.33	0.145	0.03	0.025	0.0014	0.0460	0.01	133	26	160.1	8.6	-90	340
X54B_31	core	207	1.00	8.700	0.56	0.355	0.0160	0.1663	0.0052	2296	62	1954	76	2509	54
X54B_32	core	313	0.14	0.251	0.03	0.035	0.0011	0.0504	0.0063	229	25	221.2	6.7	280	230
X54B_33	rim	521	0.09	0.213	0.02	0.032	0.0012	0.0496	0.0051	197	17	201.8	7.4	170	190
X54B_34	rim	901	0.14	0.171	0.01	0.025	0.0006	0.0513	0.0041	161	11	156.4	4	230	150
X54B_35	core	161	0.25	0.222	0.04	0.036	0.0015	0.0445	0.0082	195	34	227.9	9.3	-110	290
13JD054D															
X54D_1	rim	53	0.50	0.105	0.05	0.024	0.0019	0.0300	0.014	88	40	150	12	-800	420
X54D_2	core	173	0.50	0.168	0.03	0.023	0.0011	0.0500	0.011	151	29	148.8	6.9	70	350
X54D_3	rim	72	0.50	0.135	0.05	0.026	0.0017	0.0370	0.013	107	40	168	10	-510	400
X54D_4	rim	469	0.17	0.183	0.02	0.023	0.0007	0.0563	0.0061	168	17	148.7	4.5	380	220
X54D_5	rim	210	0.50	0.189	0.03	0.024	0.0011	0.0549	0.0094	170	27	155.3	6.7	260	310
X54D_6	core	234	1.00	0.181	0.03	0.023	0.0009	0.0599	0.0098	168	26	148.1	5.8	400	310

X54D_7	rim	1024	0.11	0.170	0.01	0.024	0.0007	0.0503	0.0037	160	12	155.1	4.1	200	150
X54D_8	homo	83	0.33	0.173	0.04	0.023	0.0014	0.0590	0.016	151	37	144.9	8.9	30	420
X54D_9	homo	131	0.50	0.174	0.04	0.023	0.0011	0.0560	0.012	159	33	143.8	7.1	250	380
X54D_10	homo	619	0.33	0.191	0.02	0.026	0.0009	0.0522	0.0051	177	16	167.5	5.5	260	190
X54D_11	rim	311	0.14	0.148	0.02	0.024	0.0011	0.0430	0.0064	140	22	151.7	7.2	-60	250
X54D_12	rim	59	0.33	0.236	0.06	0.023	0.0018	0.0740	0.019	200	44	148	11	560	480
X54D_13	core	174	0.33	0.210	0.04	0.028	0.0015	0.0580	0.011	187	31	175.7	9.5	320	330
X54D_14	core	1464	0.06	0.178	0.01	0.026	0.0006	0.0482	0.0029	167	9.8	163.7	3.8	130	120
X54D_15	rim	1585	0.07	0.209	0.02	0.025	0.0007	0.0576	0.0053	191	17	158.5	4.6	450	180
X54D_16	homo	69	0.50	0.155	0.04	0.024	0.0018	0.0520	0.013	143	34	153	11	30	400
X54D_17	rim	926	0.25	0.177	0.02	0.019	0.0006	0.0679	0.0067	166	14	123.3	3.7	740	200
X54D_18	homo	68	0.33	0.201	0.05	0.024	0.0016	0.0590	0.017	172	42	154	10	230	460
X54D_19	rim	183	0.50	0.131	0.02	0.022	0.0010	0.0448	0.0081	122	20	141.5	6.2	-20	290
X54D_20	core	86	1.00	0.162	0.04	0.023	0.0011	0.0530	0.014	143	34	145.5	7	150	420
X54D_21	rim	363	0.07	0.166	0.03	0.022	0.0009	0.0538	0.0082	156	22	142.8	5.5	280	270
X54D_22	homo	108	0.50	0.193	0.04	0.024	0.0013	0.0600	0.015	169	36	150.3	8.1	240	400
X54D_23	rim	906	0.17	0.273	0.02	0.020	0.0006	0.1015	0.007	245	17	126.4	3.9	1630	130
X54D_24	core	448	0.33	0.181	0.02	0.026	0.0008	0.0495	0.0054	167	17	165.1	5	150	200
X54D_25	homo	77	0.50	0.232	0.06	0.025	0.0016	0.0690	0.019	186	42	160.2	9.9	290	440
X54D_26	rim	368	0.20	0.161	0.02	0.023	0.0009	0.0485	0.0066	149	19	148.7	5.4	150	240
X54D_27	core	94	0.50	0.171	0.04	0.026	0.0015	0.0500	0.012	156	36	164.8	9.3	-40	370
X54D_28	rim	237	0.20	2.300	0.12	0.144	0.0040	0.1113	0.0053	1214	38	868	23	1798	90
X54D_29	core	685	0.11	3.500	0.1	0.214	0.0062	0.1175	0.0026	1527	23	1251	33	1910	40
X54D_30	rim	106	0.50	0.196	0.04	0.024	0.0011	0.0590	0.013	173	34	153.2	7	270	380
X54D_31	core	427	0.33	2.592	0.1	0.130	0.0032	0.1459	0.0049	1301	26	785	18	2296	59
X54D_32	homo	78	0.50	0.118	0.04	0.025	0.0017	0.0340	0.011	105	32	160	11	-510	380
X54D_33	homo	48	0.33	0.163	0.05	0.025	0.0020	0.0590	0.019	141	39	158	12	100	480

10JD040A

X40A_1	rim	1530	1.07	0.134	0.01	0.017	0.0006	0.0536	0.0053	127	13	110.5	3.7	310	200
X40A_2	core	514	0.80	0.151	0.02	0.020	0.0009	0.0551	0.0084	143	20	124.7	5.7	350	290
X40A_3	homo	160	0.50	10.850	0.52	0.463	0.0120	0.1675	0.0082	2509	43	2453	51	2539	80
X40A_4	mix	354	0.77	0.650	0.08	0.043	0.0024	0.1070	0.012	511	53	268	15	1690	220
X40A_5	rim	631	0.81	0.119	0.02	0.019	0.0007	0.0440	0.0073	112	17	124.1	4.3	-80	260
X40A_6	homo	278	0.19	0.183	0.04	0.025	0.0010	0.0520	0.011	163	32	156.4	6.3	120	350
X40A_7	rim	288	0.60	0.112	0.03	0.020	0.0011	0.0400	0.01	103	25	125.4	6.7	-180	360
X40A_8	core	98	0.82	10.330	0.63	0.442	0.0130	0.1648	0.01	2462	58	2362	56	2514	110
X40A_9	core	115	0.22	0.156	0.05	0.023	0.0021	0.0570	0.018	134	40	145	13	0	470
X40A_10	rim	330	0.70	0.095	0.02	0.020	0.0010	0.0349	0.0088	89	21	125.9	6.2	-380	330
X40A_11	rim	564	0.81	0.151	0.02	0.020	0.0008	0.0579	0.009	140	20	127	5	300	280
X40A_12	rim	490	0.63	0.148	0.02	0.019	0.0008	0.0559	0.0088	137	19	120.2	4.9	310	290
X40A_13	rim	450	0.74	0.122	0.02	0.021	0.0009	0.0436	0.0086	114	22	133	5.7	-80	310
X40A_14	rim	512	0.87	0.131	0.02	0.019	0.0009	0.0501	0.0088	122	20	123.9	5.6	160	310
X40A_15	rim	387	0.64	0.118	0.02	0.019	0.0009	0.0465	0.0089	110	20	122.1	5.9	0	300
X40A_16	rim	411	0.89	0.130	0.02	0.019	0.0008	0.0484	0.0092	121	21	121	4.9	30	310
X40A_17	rim	391	0.75	0.097	0.02	0.018	0.0008	0.0392	0.0074	94	18	116	5.1	-220	280
X40A_18	rim	400	0.60	0.121	0.03	0.020	0.0008	0.0441	0.0094	112	23	127	5	-40	330
X40A_19	homo	455	0.05	7.030	0.34	0.346	0.0093	0.1462	0.0066	2109	43	1913	45	2315	79
X40A_20	homo	118	0.28	7.790	0.5	0.389	0.0130	0.1424	0.0077	2222	55	2123	58	2251	88
X40A_21	homo	392	0.85	0.112	0.02	0.018	0.0009	0.0456	0.0094	104	20	116.2	5.5	-30	330
X40A_22	rim	247	0.49	0.123	0.03	0.019	0.0012	0.0570	0.018	111	30	122.3	7.3	-70	420
X40A_23	core	306	0.36	9.080	0.43	0.416	0.0110	0.1561	0.0068	2344	43	2241	51	2404	75
X40A_24	rim	255	0.56	0.124	0.03	0.020	0.0010	0.0430	0.012	116	28	124.4	6.2	-110	380
X40A_25	rim	192	0.60	0.146	0.03	0.020	0.0012	0.0500	0.011	132	29	124.7	7.8	160	380
X40A_26	core	342	0.69	0.130	0.03	0.020	0.0009	0.0484	0.0098	120	23	127.3	5.5	20	330
X40A_27	rim	24	0.73	3.640	0.55	0.263	0.0140	0.1030	0.015	1510	130	1510	70	1440	320

X40A_28	rim	72	0.08	0.300	0.09	0.039	0.0034	0.0590	0.018	240	69	248	21	90	470
13JD040F															
X40F_1	rim	514	0.68	0.154	0.02	0.019	0.0007	0.0582	0.0086	143	19	122.5	4.4	400	290
X40F_2	rim	494	0.61	0.137	0.02	0.020	0.0009	0.0508	0.0091	127	21	125.6	5.4	120	310
X40F_3	core	472	0.62	0.110	0.02	0.021	0.0008	0.0374	0.0071	103	19	130.8	5	-350	260
X40F_4	core	211	0.27	0.168	0.04	0.026	0.0011	0.0510	0.011	159	32	162.6	7.1	60	350
X40F_5	core	487	0.86	0.137	0.02	0.019	0.0009	0.0545	0.0093	130	19	122.6	5.6	250	300
X40F_6	rim	423	0.76	0.121	0.02	0.020	0.0009	0.0412	0.0072	113	18	127.8	5.7	-40	280
X40F_7	rim	506	0.64	0.110	0.02	0.020	0.0009	0.0401	0.0081	106	19	124.8	5.5	-120	310
X40F_8	rim	460	0.60	0.126	0.02	0.019	0.0008	0.0502	0.008	118	18	118.3	5.1	180	290
X40F_9	core	354	0.80	0.113	0.02	0.020	0.0010	0.0395	0.0087	105	22	128.9	6.3	-280	300
X40F_10	homo	71	0.38	0.092	0.04	0.024	0.0024	0.0400	0.016	80	35	153	15	-610	430
X40F_11	rim	399	0.69	0.175	0.03	0.020	0.0009	0.0640	0.01	160	23	129.3	5.6	500	310
X40F_12	rim	355	0.75	0.278	0.04	0.019	0.0008	0.1020	0.015	240	35	119.9	5.2	1540	310
X40F_13	homo	445	0.55	0.160	0.03	0.019	0.0007	0.0640	0.01	147	23	118.2	4.7	490	320
X40F_14	homo	62	0.24	8.480	0.52	0.380	0.0130	0.1615	0.0097	2282	56	2079	58	2455	110
X40F_15	rim	390	0.65	0.120	0.02	0.019	0.0010	0.0440	0.0081	117	21	122.2	6	20	310
X40F_16	rim	310	0.54	0.153	0.03	0.018	0.0008	0.0600	0.012	139	27	115.7	5.2	250	350
X40F_17	rim	388	0.68	0.139	0.02	0.021	0.0008	0.0520	0.009	130	19	131.9	5.3	120	280
X40F_18	rim	468	0.69	0.149	0.02	0.018	0.0010	0.0614	0.01	138	19	115.9	6.3	410	310
X40F_19	rim	360	0.58	0.140	0.02	0.020	0.0010	0.0505	0.0085	133	20	130.2	6.3	180	300
X40F_20	rim	390	1.30	0.081	0.02	0.015	0.0007	0.0490	0.01	79	15	94	4.7	80	330
X40F_21	rim	358	0.60	0.143	0.02	0.020	0.0008	0.0488	0.0073	133	20	126.2	5.3	140	270
X40F_22	mix	91	0.33	0.103	0.04	0.025	0.0019	0.0300	0.01	92	31	159	12	-570	380
X40F_23	core	104	0.76	0.167	0.05	0.023	0.0018	0.0610	0.019	145	39	144	12	60	460
X40F_24	rim	79	0.54	0.229	0.06	0.030	0.0021	0.0590	0.016	191	49	187	13	100	440
X40F_25	rim	426	0.59	0.156	0.02	0.019	0.0010	0.0610	0.01	144	21	123.2	6.2	410	310

X40F_26	rim	466	0.56	0.129	0.02	0.018	0.0008	0.0539	0.0079	121	17	112.5	4.7	220	270
X40F_27	rim	311	0.62	0.130	0.03	0.019	0.0010	0.0530	0.014	123	28	123.1	6.6	30	390
X40F_28	rim	645	0.61	0.138	0.03	0.018	0.0010	0.0538	0.01	128	23	115.8	6.3	230	330
X40F_29	homo	121	0.09	6.370	0.43	0.316	0.0120	0.1448	0.01	2024	58	1767	57	2270	120
X40F_30	rim	328	1.28	0.133	0.03	0.020	0.0009	0.0467	0.0094	123	22	126.3	5.9	30	320
X40F_31	rim	476	0.58	0.150	0.02	0.019	0.0007	0.0558	0.0082	139	20	123.8	4.7	310	280
X40F_32	rim	458	0.56	0.123	0.02	0.018	0.0009	0.0484	0.0076	121	18	115.2	5.5	80	270

Appendix Table 7.3 LA-ICPMS zircon Hf isotope data for the late Mesozoic igneous rocks from the Jiaobei region

Spots	Type	t (Ma)	$^{176}Lu/^{177}Hf$	1 sigma	$^{176}Hf/^{177}Hf$	1 sigma	I_{Hf}	$\varepsilon_{Hf}(t)$	1 sigma	$f_{Lu/Hf}$	T_{DM1}	1 sigma	T_{DM2}	1 sigma
13JD040I														
L40I-01	rim	156	0.000747	0.000030	0.282113	0.000010	0.282111	-20.0	0.4	-0.98	1595	14	2453	22
L40I-02	rim	153	0.000390	0.000006	0.282054	0.000011	0.282053	-22.1	0.4	-0.99	1661	15	2582	24
L40I-03	core	191	0.000111	0.000005	0.281969	0.000010	0.281969	-24.2	0.4	-1.00	1765	14	2742	22
L40I-04	rim	152	0.000565	0.000025	0.282046	0.000009	0.282044	-22.4	0.3	-0.98	1680	12	2601	20
L40I-05	rim	152	0.000675	0.000031	0.282055	0.000010	0.282053	-22.1	0.4	-0.98	1672	14	2582	22
L40I-06	core	283	0.001498	0.000055	0.282085	0.000010	0.282077	-18.4	0.4	-0.95	1667	14	2449	22
L40I-07	rim	153	0.000745	0.000010	0.282032	0.000009	0.282030	-22.9	0.3	-0.98	1707	12	2632	20
L40I-08	rim	154	0.000482	0.000010	0.282014	0.000015	0.282013	-23.5	0.5	-0.99	1720	21	2669	33
L40I-09	core	1751	0.000457	0.000012	0.281439	0.000010	0.281424	-8.7	0.4	-0.99	2500	14	2960	22
L40I-10	rim	163	0.000459	0.000009	0.282052	0.000019	0.282051	-21.9	0.7	-0.99	1667	26	2581	41
L40I-11	core	231	0.000675	0.000088	0.282131	0.000016	0.282128	-17.7	0.6	-0.98	1567	22	2369	35
L40I-12	core	2151	0.000271	0.000005	0.281468	0.000025	0.281457	1.6	0.9	-0.99	2449	34	2636	55
L40I-13	rim	162	0.000493	0.000017	0.282077	0.000012	0.282076	-21.1	0.4	-0.99	1634	16	2527	26
L40I-14	core	2491	0.000712	0.000100	0.281381	0.000014	0.281347	5.5	0.5	-0.98	2595	20	2659	32
L40I-15	rim	170	0.000457	0.000010	0.282073	0.000013	0.282072	-21.1	0.5	-0.99	1638	18	2531	28
L40I-16	rim	152	0.000814	0.000029	0.282036	0.000008	0.282034	-22.8	0.3	-0.98	1704	11	2624	17
L40I-18	core	2515	0.000292	0.000021	0.281383	0.000009	0.281369	6.8	0.3	-0.99	2565	13	2596	20
L40I-19	rim	191	0.000117	0.000033	0.282179	0.000010	0.282179	-16.8	0.4	-1.00	1479	14	2283	22
L40I-20	rim	156	0.000571	0.000010	0.282059	0.000010	0.282057	-21.9	0.3	-0.98	1662	13	2570	21
L40I-21	rim	151	0.000426	0.000006	0.282025	0.000015	0.282024	-23.2	0.5	-0.99	1702	21	2646	33
L40I-23	rim	164	0.000787	0.000027	0.282098	0.000012	0.282096	-20.3	0.4	-0.98	1618	17	2482	26
L40I-24	rim	151	0.000803	0.000047	0.282058	0.000011	0.282056	-22.0	0.4	-0.98	1674	15	2577	24
L40I-25	core	2344	0.000407	0.000007	0.281363	0.000025	0.281345	2.0	0.9	-0.99	2599	34	2758	54

L40I-26	rim	169	0.000584	0.000013	0.282094	0.000010	0.282092	-20.3	0.4	-0.98	1615	14	2486	22
L40I-27	rim	206	0.000815	0.000041	0.282083	0.000020	0.282080	-20.0	0.7	-0.98	1640	28	2490	44
L40I-28	core	638	0.002150	0.000063	0.282253	0.000025	0.282227	-5.2	0.9	-0.94	1455	36	1898	55
L40I-29	rim	155	0.000347	0.000008	0.282079	0.000010	0.282078	-21.2	0.4	-0.99	1625	14	2526	22
L40I-31	core	1778	0.000196	0.000003	0.281372	0.000009	0.281365	-10.2	0.3	-0.99	2573	12	3070	20
13JD054B														
L54B-01	homo	147	0.000343	0.000004	0.281943	0.000009	0.281942	-26.1	0.3	-0.99	1811	13	2827	20
L54B-03	rim	151	0.000505	0.000010	0.281957	0.000010	0.281956	-25.6	0.3	-0.98	1799	13	2795	21
L54B-04	rim	147	0.001175	0.000034	0.282131	0.000011	0.282128	-19.6	0.4	-0.96	1588	15	2422	24
L54B-06	rim	161	0.000735	0.000015	0.282010	0.000010	0.282008	-23.5	0.3	-0.98	1737	13	2675	21
L54B-07	rim	210	0.000122	0.000010	0.282039	0.000009	0.282039	-21.3	0.3	-1.00	1670	12	2578	19
L54B-08	core	203	0.000050	0.000002	0.282042	0.000014	0.282042	-21.4	0.5	-1.00	1663	19	2575	31
L54B-09	homo	166	0.000349	0.000016	0.281971	0.000011	0.281970	-24.9	0.4	-0.99	1773	15	2759	24
L54B-10	rim	159	0.001408	0.000043	0.282130	0.000010	0.282126	-19.9	0.4	-0.96	1599	14	2431	22
L54B-11	homo	137	0.000245	0.000008	0.281978	0.000010	0.281977	-24.7	0.4	-0.99	1758	14	2746	22
L54B-12	rim	154	0.000954	0.000024	0.282155	0.000011	0.282152	-18.3	0.4	-0.97	1545	15	2356	24
L54B-13	homo	167	0.000241	0.000007	0.281983	0.000009	0.281982	-24.3	0.3	-0.99	1751	12	2729	19
L54B-14	rim	164	0.000443	0.000017	0.281945	0.000015	0.281944	-25.7	0.5	-0.99	1813	21	2813	33
L54B-16	rim	151	0.000475	0.000009	0.281981	0.000006	0.281980	-24.7	0.2	-0.99	1765	8	2743	13
L54B-17	core	164	0.000475	0.000009	0.281981	0.000006	0.281980	-24.4	0.2	-0.99	1765	8	2735	13
L54B-19	rim	168	0.000704	0.000014	0.282047	0.000008	0.282045	-22.0	0.3	-0.98	1684	11	2590	17
L54B-20	core	237	0.000939	0.000034	0.282020	0.000018	0.282016	-21.6	0.6	-0.97	1732	25	2611	39
L54B-20	core	237	0.000431	0.000012	0.282162	0.000013	0.282160	-16.4	0.5	-0.99	1515	18	2295	29
L54B-21	rim	153	0.000436	0.000013	0.281995	0.000010	0.281994	-24.2	0.3	-0.99	1744	13	2711	21
L54B-23	rim	149	0.000542	0.000040	0.282056	0.000011	0.282054	-22.1	0.4	-0.98	1665	15	2581	24
L54B-24	mix	225	0.001291	0.000004	0.282227	0.000009	0.282222	-14.5	0.3	-0.96	1458	13	2168	20
L54B-25	core	224	0.000583	0.000110	0.282190	0.000009	0.282188	-15.8	0.3	-0.98	1482	13	2243	19
L54B-27	rim	160	0.000322	0.000003	0.281857	0.000017	0.281856	-28.9	0.6	-0.99	1927	23	3006	37

L54B-32	core	221	0.000129	0.000006	0.282114	0.000009	0.282113	-18.4	0.3	-1.00	1568	12	2407	19
L54B-35	core	228	0.000613	0.000110	0.282163	0.000009	0.282160	-16.6	0.3	-0.98	1521	14	2300	20
L54B-02	core	2549	0.000365	0.000006	0.281064	0.000008	0.281046	-3.9	0.3	-0.99	2996	11	3274	18
L54B-15	core	1677	0.000666	0.000012	0.281211	0.000014	0.281190	-18.7	0.5	-0.98	2822	19	3511	30
L54B-29	core	2452	0.000240	0.000010	0.281061	0.000011	0.281050	-6.0	0.4	-0.99	2991	15	3328	24
L54B-31	core	1954	0.000857	0.000026	0.281346	0.000010	0.281314	-8.0	0.3	-0.97	2653	13	3070	21
13JD054D														
L54D-01	rim	150	0.000225	0.000004	0.281935	0.000013	0.281934	-26.3	0.5	-0.99	1816	18	2842	28
L54D-02	core	149	0.000456	0.000010	0.281969	0.000013	0.281968	-25.2	0.5	-0.99	1780	18	2770	28
L54D-03	rim	169	0.000209	0.000004	0.281965	0.000011	0.281964	-24.9	0.4	-0.99	1774	15	2765	24
L54D-05	rim	155	0.000272	0.000011	0.281966	0.000008	0.281965	-25.1	0.3	-0.99	1776	10	2772	17
L54D-06	core	148	0.000255	0.000016	0.281957	0.000011	0.281956	-25.6	0.4	-0.99	1787	15	2795	24
L54D-07	rim	155	0.000482	0.000003	0.281966	0.000010	0.281965	-25.2	0.4	-0.99	1786	14	2773	22
L54D-08	homo	145	0.000216	0.000013	0.281963	0.000013	0.281962	-25.5	0.5	-0.99	1777	18	2784	28
L54D-09	homo	144	0.000296	0.000010	0.281941	0.000014	0.281940	-26.3	0.5	-0.99	1811	19	2833	30
L54D-10	homo	168	0.000610	0.000049	0.282152	0.000034	0.282150	-18.3	1.2	-0.98	1536	47	2360	75
L54D-11	rim	152	0.001166	0.000015	0.282139	0.000024	0.282136	-19.2	0.8	-0.96	1576	34	2401	53
L54D-13	core	176	0.000250	0.000005	0.281979	0.000013	0.281978	-24.2	0.5	-0.99	1757	18	2731	28
L54D-14	core	164	0.000115	0.000005	0.282675	0.000007	0.282675	0.2	0.3	-1.00	799	10	1200	16
L54D-16	rim	153	0.000433	0.000019	0.281916	0.000009	0.281915	-27.0	0.3	-0.99	1852	12	2882	19
L54D-18	homo	154	0.000152	0.000007	0.281928	0.000010	0.281928	-26.5	0.4	-1.00	1822	14	2854	22
L54D-18	homo	154	0.000329	0.000009	0.282016	0.000013	0.282015	-23.4	0.5	-0.99	1710	18	2664	28
L54D-21	rim	143	0.000173	0.000011	0.282086	0.000009	0.282086	-21.1	0.3	-0.99	1608	12	2516	19
L54D-22	homo	150	0.000212	0.000013	0.281975	0.000015	0.281974	-24.9	0.5	-0.99	1761	20	2755	33
L54D-24	core	165	0.000716	0.000028	0.282026	0.000050	0.282024	-22.8	1.8	-0.98	1714	69	2638	109
L54D-25	homo	160	0.000486	0.000023	0.281970	0.000013	0.281969	-24.9	0.5	-0.99	1780	18	2761	28
L54D-26	rim	149	0.000309	0.000019	0.281980	0.000008	0.281979	-24.8	0.3	-0.99	1759	11	2745	18
L54D-27	core	165	0.000163	0.000004	0.281920	0.000009	0.281919	-26.5	0.3	-1.00	1833	12	2865	19

L54D-33	homo	158	0.000062	0.000003	0.281946	0.000008	0.281946	-25.8	0.3	-1.00	1793	11	2812	18
L54D-12	rim	148	0.000274	0.000013	0.282030	0.000021	0.282029	-23.0	0.7	-0.99	1689	29	2636	46
L54D-30	rim	153	0.000113	0.000007	0.281791	0.000015	0.281791	-31.4	0.5	-1.00	2005	20	3151	32
L54D-31	core	785	0.000409	0.000012	0.281450	0.000010	0.281444	-29.7	0.4	-0.99	2482	13	3514	21
L54D-32	homo	160	0.000261	0.000006	0.281904	0.000013	0.281903	-27.2	0.5	-0.99	1860	18	2903	28
13JD057A														
L57A-01	rim	122	0.000524	0.000014	0.282377	0.000008	0.282376	-11.3	0.3	-0.98	1222	11	1891	17
L57A-05	homo	127	0.000700	0.000016	0.282270	0.000011	0.282268	-15.0	0.4	-0.98	1376	15	2125	24
L57A-06	homo	126	0.000661	0.000013	0.282368	0.000012	0.282366	-11.6	0.4	-0.98	1239	17	1909	27
L57A-08	homo	128	0.000538	0.000017	0.282352	0.000014	0.282351	-12.1	0.5	-0.98	1257	19	1943	31
L57A-10	homo	125	0.000636	0.000012	0.282356	0.000011	0.282355	-12.0	0.4	-0.98	1255	15	1936	24
L57A-11	homo	126	0.000622	0.000008	0.282331	0.000013	0.282330	-12.9	0.5	-0.98	1289	18	1991	29
L57A-12	homo	125	0.000565	0.000020	0.282293	0.000009	0.282292	-14.2	0.3	-0.98	1339	13	2075	21
L57A-13	homo	129	0.000597	0.000011	0.282365	0.000009	0.282364	-11.6	0.3	-0.98	1241	13	1914	21
L57A-15 begining signal	homo	125	0.000633	0.000010	0.282335	0.000025	0.282334	-12.8	0.9	-0.98	1284	35	1983	55
L57A-16	homo	125	0.000401	0.000005	0.282329	0.000010	0.282328	-13.0	0.3	-0.99	1284	13	1995	21
L57A-17	homo	129	0.000501	0.000028	0.282335	0.000011	0.282334	-12.7	0.4	-0.98	1279	15	1980	24
L57A-20	homo	126	0.000499	0.000025	0.282321	0.000012	0.282320	-13.2	0.4	-0.98	1298	17	2012	26
L57A-21	homo	121	0.000530	0.000004	0.282327	0.000008	0.282326	-13.1	0.3	-0.98	1291	11	2002	17
L57A-22	homo	128	0.000438	0.000024	0.282314	0.000020	0.282313	-13.4	0.7	-0.99	1306	28	2026	44
L57A-23	homo	151	0.000181	0.000004	0.281874	0.000014	0.281873	-28.5	0.5	-0.99	1896	19	2973	30
L57A-24	core	228	0.000144	0.000016	0.282154	0.000009	0.282153	-16.9	0.3	-1.00	1515	12	2316	20
L57A-02	core	206	0.000308	0.000024	0.282331	0.000008	0.282330	-11.1	0.3	-0.99	1278	11	1941	18
L57A-07	rim	132	0.000569	0.000012	0.282348	0.000013	0.282347	-12.2	0.5	-0.98	1263	18	1949	29
L57A-09	homo	116	0.002138	0.000063	0.282115	0.000011	0.282110	-20.9	0.4	-0.94	1653	16	2479	24

L57A-14 begining signal	rim	126	0.000575	0.000013	0.282338	0.000029	0.282337	-12.6	1.0	-0.98	1277	40	1975	64
L57A-18	rim	133	0.000257	0.000002	0.282338	0.000013	0.282337	-12.5	0.5	-0.99	1267	18	1969	29
L57A-19	core	2198	0.000532	0.000005	0.281276	0.000009	0.281254	-4.6	0.3	-0.98	2725	12	3048	20
L57A-26	homo	128	0.000420	0.000017	0.282326	0.000011	0.282325	-13.0	0.4	-0.99	1289	15	2000	24
13JD057C														
L57C-02	homo	126	0.000519	0.000014	0.282317	0.000009	0.282316	-13.4	0.3	-0.98	1305	13	2021	21
L57C-03	homo	132	0.000523	0.000005	0.282366	0.000008	0.282365	-11.5	0.3	-0.98	1237	10	1909	17
L57C-04	rim	126	0.000428	0.000024	0.282292	0.000015	0.282291	-14.3	0.5	-0.99	1336	21	2076	33
L57C-05	homo	126	0.000596	0.000011	0.282366	0.000008	0.282365	-11.6	0.3	-0.98	1239	12	1913	18
L57C-06	homo	132	0.000537	0.000009	0.282363	0.000008	0.282362	-11.6	0.3	-0.98	1242	11	1916	17
L57C-07	homo	125	0.000505	0.000020	0.282329	0.000009	0.282328	-13.0	0.3	-0.98	1288	13	1995	20
L57C-08	homo	124	0.000551	0.000013	0.282327	0.000009	0.282326	-13.1	0.3	-0.98	1292	13	2001	21
L57C-09	rim	129	0.000501	0.000008	0.282338	0.000009	0.282337	-12.6	0.3	-0.98	1275	12	1973	19
L57C-10	homo	125	0.000576	0.000026	0.282305	0.000009	0.282304	-13.8	0.3	-0.98	1323	12	2049	20
L57C-11	homo	129	0.000605	0.000031	0.282376	0.000007	0.282375	-11.2	0.2	-0.98	1226	10	1890	15
L57C-12	homo	128	0.000396	0.000015	0.282272	0.000016	0.282271	-14.9	0.6	-0.99	1362	22	2119	35
L57C-13	homo	127	0.000515	0.000026	0.282344	0.000009	0.282343	-12.4	0.3	-0.98	1267	13	1961	21
L57C-14	homo	129	0.000335	0.000015	0.282385	0.000007	0.282384	-10.9	0.3	-0.99	1205	10	1868	16
L57C-15	homo	125	0.000536	0.000025	0.282391	0.000011	0.282390	-10.8	0.4	-0.98	1203	15	1858	24
L57C-17	homo	133	0.000700	0.000022	0.282367	0.000007	0.282365	-11.5	0.2	-0.98	1241	9	1908	15
L57C-18	homo	125	0.000635	0.000026	0.282368	0.000011	0.282367	-11.6	0.4	-0.98	1238	15	1910	24
L57C-19	rim	132	0.000487	0.000024	0.282384	0.000009	0.282383	-10.9	0.3	-0.99	1211	12	1869	19
L57C-22	rim	126	0.000473	0.000024	0.282375	0.000005	0.282374	-11.3	0.2	-0.99	1223	7	1893	12
L57C-26	homo	127	0.000486	0.000021	0.282406	0.000010	0.282405	-10.2	0.4	-0.99	1181	14	1824	22
L57C-27	homo	127	0.000562	0.000020	0.282423	0.000006	0.282422	-9.6	0.2	-0.98	1159	8	1786	13
L57C-28	rim	126	0.000448	0.000019	0.282116	0.000010	0.282115	-20.5	0.4	-0.99	1579	14	2463	22

L57C-30 repeat	homo	127	0.000698	0.000005	0.282341	0.000009	0.282339	-12.5	0.3	-0.98	1277	12	1969	19
L57C-31	rim	130	0.000475	0.000017	0.282337	0.000030	0.282336	-12.6	1.1	-0.99	1276	41	1974	66
L57C-01	core	144	0.000606	0.000067	0.281985	0.000011	0.281983	-24.7	0.4	-0.98	1765	15	2739	24
L57C-16	homo	122	0.000568	0.000013	0.282395	0.000011	0.282394	-10.7	0.4	-0.98	1198	15	1851	24
L57C-20	core	2824	0.000896	0.000053	0.281164	0.000010	0.281116	4.9	0.4	-0.97	2902	14	2949	23
L57C-21	homo	125	0.000499	0.000016	0.282408	0.000009	0.282407	-10.2	0.3	-0.98	1178	13	1821	20
L57C-25	core	2489	0.000769	0.000011	0.281373	0.000014	0.281336	5.0	0.5	-0.98	2610	19	2683	31
L57C-29 repeat	core	2847	0.000831	0.000050	0.281112	0.000015	0.281067	3.7	0.5	-0.97	2968	21	3041	33
L57C-32	core	107	0.000983	0.000033	0.282330	0.000013	0.282328	-13.4	0.5	-0.97	1302	18	2006	29
13JD040A														
L40A-02	core	125	0.000750	0.000012	0.281642	0.000028	0.281640	-37.3	1.0	-0.98	2242	38	3492	60
L40A-05	rim	124	0.000993	0.000020	0.282136	0.000053	0.282134	-19.9	1.9	-0.97	1573	74	2423	116
L40A-07	rim	125	0.000823	0.000010	0.282263	0.000027	0.282261	-15.3	1.0	-0.98	1390	38	2142	59
L40A-09	core	145	0.000324	0.000034	0.281418	0.000016	0.281417	-44.7	0.6	-0.99	2520	22	3957	34
L40A-11	rim	127	0.000796	0.000063	0.282235	0.000020	0.282233	-16.3	0.7	-0.98	1428	28	2203	44
L40A-12	rim	120	0.000779	0.000018	0.282152	0.000012	0.282150	-19.4	0.4	-0.98	1543	17	2389	26
L40A-13	rim	133	0.000864	0.000013	0.282211	0.000020	0.282209	-17.0	0.7	-0.97	1464	28	2252	44
L40A-14	rim	124	0.000932	0.000011	0.282121	0.000022	0.282119	-20.4	0.8	-0.97	1592	31	2455	48
L40A-15	rim	122	0.000844	0.000031	0.282152	0.000016	0.282150	-19.3	0.6	-0.97	1545	22	2388	35
L40A-16	rim	121	0.000911	0.000026	0.282171	0.000024	0.282169	-18.7	0.8	-0.97	1521	33	2347	53
L40A-18	rim	127	0.000925	0.000039	0.282179	0.000020	0.282177	-18.3	0.7	-0.97	1511	28	2326	44
L40A-21	homo	116	0.000425	0.000008	0.281360	0.000015	0.281359	-47.4	0.5	-0.99	2604	20	4098	32
L40A-22	rim	122	0.000783	0.000023	0.282080	0.000012	0.282078	-21.9	0.4	-0.98	1642	17	2545	26
L40A-24	rim	124	0.000966	0.000009	0.282092	0.000022	0.282090	-21.4	0.8	-0.97	1634	31	2519	48
L40A-26	core	127	0.001626	0.000016	0.281369	0.000026	0.281365	-47.0	0.9	-0.95	2675	36	4078	55

L40A-28	homo	248	0.001120	0.000060	0.282136	0.000024	0.282131	-17.2	0.8	-0.97	1579	34	2353	53
L40A-27	homo	1510	0.000877	0.000025	0.282107	0.000019	0.282082	9.2	0.7	-0.97	1609	26	1669	42
L40A-03	rim	2453	0.000783	0.000011	0.282119	0.000028	0.282082	30.7	1.0	-0.98	1588	39	1056	63
L40A-04	mix	268	0.000694	0.000016	0.281994	0.000037	0.281991	-21.8	1.3	-0.98	1757	51	2647	81
L40A-17	rim	116	0.001145	0.000023	0.282109	0.000021	0.282107	-21.0	0.7	-0.97	1618	29	2487	46
L40A-19	mix	1913	0.000764	0.000012	0.282143	0.000019	0.282115	19.5	0.7	-0.98	1554	26	1335	42
L40A-20	mix	2123	0.000650	0.000005	0.281986	0.000020	0.281960	18.8	0.7	-0.98	1766	27	1546	45
L40A-23	core	2241	0.000802	0.000011	0.281945	0.000018	0.281911	19.8	0.6	-0.98	1830	25	1578	40
13JD040F														
L40F-01	rim	122	0.000895	0.000011	0.282144	0.000030	0.282142	-19.6	1.1	-0.97	1558	42	2406	66
L40F-02	rim	126	0.001061	0.000014	0.282121	0.000019	0.282119	-20.4	0.7	-0.97	1597	26	2455	42
L40F-04	core	163	0.000837	0.000007	0.281476	0.000024	0.281473	-42.4	0.8	-0.97	2474	33	3826	51
L40F-05	core	123	0.001408	0.000023	0.282162	0.000037	0.282159	-19.0	1.3	-0.96	1554	52	2368	81
L40F-06	rim	128	0.000875	0.000031	0.282116	0.000049	0.282114	-20.5	1.7	-0.97	1596	68	2464	107
L40F-07	rim	125	0.000924	0.000040	0.282181	0.000032	0.282179	-18.2	1.1	-0.97	1508	45	2323	70
L40F-15 REPEAT	rim	122	0.001107	0.000003	0.282071	0.000041	0.282068	-22.2	1.5	-0.97	1669	57	2567	90
L40F-16	rim	116	0.001228	0.000046	0.282160	0.000030	0.282157	-19.2	1.1	-0.96	1550	42	2376	66
L40F-17	rim	132	0.001077	0.000010	0.282244	0.000028	0.282241	-15.9	1.0	-0.97	1426	39	2182	62
L40F-18	rim	116	0.001207	0.000019	0.282110	0.000020	0.282107	-21.0	0.7	-0.96	1619	28	2485	44
L40F-21	rim	126	0.001350	0.000025	0.282178	0.000020	0.282175	-18.4	0.7	-0.96	1529	28	2331	44
L40F-23	core	144	0.000923	0.000027	0.282005	0.000024	0.282003	-24.1	0.8	-0.97	1752	33	2697	52
L40F-24	rim	187	0.000810	0.000020	0.282151	0.000021	0.282148	-18.0	0.7	-0.98	1545	29	2352	46
L40F-25	rim	123	0.001298	0.000011	0.282110	0.000022	0.282107	-20.8	0.8	-0.96	1623	31	2482	48
L40F-26	rim	112	0.000891	0.000010	0.282171	0.000020	0.282169	-18.9	0.7	-0.97	1521	28	2352	44
L40F-27	rim	123	0.000984	0.000014	0.282051	0.000032	0.282049	-22.9	1.1	-0.97	1691	44	2609	70
L40F-28	rim	116	0.000837	0.000022	0.282174	0.000022	0.282172	-18.7	0.8	-0.97	1514	31	2343	48

L40F-30	rim	126	0.001085	0.000013	0.282113	0.000023	0.282110	-20.6	0.8	-0.97	1609	32	2472	50
L40F-31	rim	124	0.000984	0.000018	0.282140	0.000027	0.282138	-19.7	1.0	-0.97	1568	38	2414	59
L40F-32	rim	115	0.000800	0.000066	0.282149	0.000019	0.282147	-19.6	0.7	-0.98	1548	26	2399	42
L40F-29	homo	1767	0.000903	0.000050	0.282020	0.000029	0.281990	11.7	1.0	-0.97	1731	40	1709	64
L40F-03	core	131	0.001620	0.000025	0.282023	0.000041	0.282019	-23.8	1.5	-0.95	1760	58	2669	89
L40F-10	homo	153	0.000581	0.000016	0.282003	0.000011	0.282001	-23.9	0.4	-0.98	1739	15	2694	24
L40F-11	rim	129	0.000622	0.000034	0.281996	0.000023	0.281995	-24.7	0.8	-0.98	1751	32	2724	50
L40F-13	homo	118	0.001597	0.000110	0.282038	0.000038	0.282034	-23.5	1.3	-0.95	1737	54	2643	83
L40F-22	mix	159	0.000951	0.000013	0.282151	0.000022	0.282148	-18.6	0.8	-0.97	1551	31	2370	48

Appendix Table 7.4 Major and trace element data for the late Mesozoic igneous rocks in the Jiaobei region

Sample No	13JD009A	13JD009B	13JD009C	13JD009D	13JD040I	13JD040J	13JD048B	13JD048C	13JD054A	13JD054B	13JD054C
Unit	Linglong	Linglong	Linglong	Linglong	Linglong	Linglong	Linglong	Linglong	Linglong	Linglong	Linglong
SiO2	75.41	73.47	72.74	72.69	68.86	67.68	73.28	72.70	72.63	71.95	72.74
Al2O3	13.75	14.70	14.99	14.98	16.59	17.37	14.45	14.88	14.93	15.14	14.80
TiO2	0.07	0.09	0.10	0.10	0.31	0.34	0.13	0.16	0.23	0.23	0.21
Fe2O3T	0.84	1.17	1.41	1.43	2.24	2.25	1.05	1.26	1.52	1.51	1.37
MgO	0.10	0.13	0.17	0.17	0.57	0.58	0.21	0.23	0.32	0.32	0.29
MnO	0.02	0.02	0.03	0.03	0.02	0.04	0.02	0.03	0.03	0.03	0.03
CaO	1.43	1.67	1.72	1.71	3.16	3.48	1.39	1.52	1.89	1.98	1.81
Na2O	3.81	4.38	4.25	4.32	4.65	4.37	3.89	4.28	3.75	3.81	3.74
K2O	3.80	3.57	3.78	3.80	2.52	2.89	4.56	4.03	3.84	4.13	4.14
P2O5	0.01	0.01	0.01	0.01	0.09	0.09	0.02	0.04	0.05	0.05	0.04
L.O.I	0.17	0.21	0.23	0.17	0.47	0.38	0.40	0.29	0.29	0.34	0.32
Total	99.41	99.41	99.42	99.42	99.48	99.49	99.41	99.41	99.49	99.49	99.49
Li	16.6	22.8	22.8	18.9	10.2	11.1	4.8	15.1	23.1	21.3	20.9
Be	1.4	1.5	1.4	1.5	1.4	1.2	1.9	1.8	1.5	1.6	1.4
P	92	92	109	109	431	372	133	223	249	236	228
Sc	0.48	0.56	0.72	0.66	2.40	1.69	1.13	1.25	2.4	2.4	2.2
Ti	295	389	471	453	1781	1680	626	740	1307	1326	1182
V	2.53	3.19	2.95	2.70	16.73	13.78	2.59	4.00	8.3	7.7	7.7
Cr	6.14	7.68	6.37	5.05	10.68	3.65	27.57	6.06	6.24	0.89	2.41
Mn	108	151	193	182	144	246	142	176	199	203	174
Co	0.215	0.315	0.369	0.378	2.372	2.226	0.364	0.692	1.713	1.626	1.643
Ni	0.216	0.462	0.373	0.388	3.341	3.088	0.332	0.407	2.373	2.414	3.624
Cu	0.729	1.119	1.057	1.111	3.042	1.684	1.550	2.005	1.159	1.277	1.617

Zn	19.8	22.2	27.7	27.0	38.4	45.8	24.4	41.1	49.3	51.3	44.5
Ga	13.6	15.4	15.4	15.1	19.3	17.7	17.2	19.6	19.7	19.8	19.6
Ge	0.93	1.08	0.92	1.02	0.71	0.47	0.91	0.94	0.78	0.81	0.72
Rb	85.9	82.9	87.2	90.6	45.3	48.0	103.2	98.2	101.7	105.9	104.3
Sr	658	687	747	719	1544	1161	530	569	789	799	778
Y	2.99	3.52	4.28	4.12	10.09	7.99	4.39	4.72	7.27	7.53	7.34
Zr	89	64	80	81	113	139	24	142	150	148	142
Nb	2.87	3.69	4.11	5.56	7.92	6.58	4.87	5.06	7.68	7.81	7.69
Cs	1.023	1.059	0.865	1.025	0.449	0.430	0.582	0.659	1.135	1.146	1.080
Ba	2578	2049	2566	2450	2809	2536	1931	1505	2141	2241	2188
La	7.72	4.70	6.97	5.67	53.66	45.51	26.26	28.92	32.84	39.79	31.89
Ce	13.44	8.92	12.46	9.85	95.68	80.06	47.13	54.41	57.55	69.95	55.70
Pr	1.47	0.97	1.32	1.04	10.06	8.52	4.88	5.59	6.07	7.33	5.83
Nd	4.94	3.48	4.45	3.55	33.08	28.16	15.92	18.30	19.99	23.76	19.14
Sm	0.94	0.74	0.80	0.69	4.54	3.88	2.47	2.83	2.71	3.17	2.63
Eu	0.36	0.29	0.36	0.32	1.26	1.14	0.61	0.69	0.82	0.87	0.79
Gd	0.83	0.67	0.63	0.62	2.90	2.47	1.57	1.78	1.73	1.97	1.74
Tb	0.115	0.111	0.100	0.103	0.365	0.320	0.214	0.225	0.227	0.244	0.232
Dy	0.58	0.62	0.60	0.64	1.93	1.63	0.96	1.03	1.27	1.36	1.26
Ho	0.104	0.125	0.132	0.140	0.370	0.313	0.170	0.180	0.261	0.275	0.257
Er	0.28	0.35	0.43	0.43	0.90	0.70	0.42	0.42	0.61	0.65	0.61
Tm	0.04	0.05	0.08	0.06	0.14	0.10	0.05	0.06	0.10	0.10	0.10
Yb	0.29	0.39	0.53	0.46	0.86	0.62	0.31	0.39	0.63	0.67	0.65
Lu	0.05	0.07	0.09	0.08	0.12	0.09	0.05	0.06	0.10	0.10	0.10
Hf	2.55	1.95	2.16	2.31	3.29	4.17	0.54	4.14	5.06	5.04	4.76
Ta	0.14	0.22	0.24	0.48	0.50	0.20	0.12	0.16	0.56	0.56	0.51
Pb	24.1	23.9	24.0	24.1	22.5	13.6	30.2	31.6	28.4	26.8	29.2
Th	1.40	1.32	1.37	1.14	8.80	7.50	6.07	6.69	5.80	6.68	5.73
U	0.40	0.41	0.65	0.47	1.04	0.40	0.37	0.70	0.81	1.00	0.84
A/CNK	1.06	1.04	1.05	1.05	1.03	1.04	1.04	1.05	1.08	1.06	1.06
Gd/Yb	2.8	1.7	1.2	1.4	3.4	4.0	5.1	4.6	2.7	3.0	2.7

La/Yb	26.5	12.2	13.3	12.4	62.6	73.3	86.1	74.3	51.8	59.6	49.2
T_{Zr}(°C)	743	713	730	731	751	767	645	777	780	778	778

Sample No	**13JD060A**	**13JD060B**	**13JD054D**	**13JD054E**	**13JD062B**	**13JD062C**	**13JD040A**	**13JD040B**
Unit	**Linglong**	**Linglong**	**Linglong MME**	**Linglong MME**	**Luanjiahe**	**Luanjiahe**	**Dioritic intrusion**	**Dioritic intrusion**
SiO2	72.95	73.11	64.08	69.39	75.48	73.23	54.23	54.80
Al2O3	14.81	14.65	13.86	15.02	13.87	14.20	14.84	15.20
TiO2	0.18	0.16	0.41	0.31	0.09	0.10	1.12	1.04
Fe2O3T	0.94	1.06	5.76	2.50	0.69	0.91	7.61	7.66
MgO	0.24	0.23	3.74	1.70	0.13	0.13	5.57	5.24
MnO	0.04	0.04	0.13	0.05	0.04	0.04	0.12	0.12
CaO	1.39	1.46	4.39	2.96	0.42	1.42	7.18	7.06
Na2O	4.08	4.00	3.11	3.83	3.88	4.11	3.53	3.73
K2O	4.13	4.20	3.13	2.98	4.05	3.79	2.99	3.05
P2O5	0.03	0.03	0.18	0.11	0.01	0.01	0.68	0.58
L.O.I	0.62	0.46	0.69	0.62	0.76	1.47	1.60	1.01
Total	99.40	99.41	99.49	99.48	99.41	99.42	99.48	99.48
Li	21.5	19.6	45.3	41.5	13.0	23.3	14.7	10.6
Be	2.5	3.5	2.5	1.8	1.7	1.9	3.1	1.8
P	209	194	844	527	110	111	3087	1448
Sc	1.1	1.0	11.0	5.1	0.6	0.8	17.6	13.6
Ti	782	710	2388	1805	383	420	6785	3327
V	4.8	5.3	72.4	36.5	4.1	6.0	124.4	67.7
Cr	10.00	7.64	187.19	66.12	5.64	11.37	150.59	75.27
Mn	261	243	982	361	254	265	964	543
Co	0.669	0.687	10.714	6.039	0.212	0.342	20.448	11.611
Ni	1.208	0.386	83.412	25.296	0.327	0.573	111.959	54.037

Cu	4.144	1.031	2.339	2.417	1.068	0.979	7.222	4.807
Zn	71.5	48.9	125.3	59.8	16.7	24.7	156.6	84.3
Ga	19.4	18.9	22.0	19.3	15.2	15.6	24.8	15.8
Ge	1.22	1.18	1.30	0.68	1.67	1.68	1.46	0.68
Rb	139.8	137.7	95.7	94.1	159.6	148.1	46.6	39.4
Sr	606	596	939	1203	251	294	2933	2038
Y	6.48	6.01	13.81	9.51	7.20	8.22	34.98	28.43
Zr	109	108	131	122	72	66	355	179
Nb	8.72	7.88	7.85	6.79	7.48	8.19	16.32	9.00
Cs	2.204	2.184	1.914	1.950	2.983	2.971	0.234	0.409
Ba	1794	1750	2046	2237	1040	937	4636	3517
La	25.94	28.46	43.32	43.79	9.11	10.81	302.35	213.88
Ce	46.05	49.32	81.03	81.26	16.08	20.30	553.92	369.48
Pr	4.75	5.24	8.96	8.90	1.77	2.15	66.42	48.66
Nd	15.62	17.18	32.03	30.32	5.84	7.06	229.17	173.36
Sm	2.43	2.65	5.18	4.25	1.01	1.25	30.85	24.36
Eu	0.66	0.69	1.25	1.16	0.26	0.31	7.27	5.71
Gd	1.69	1.77	3.70	2.81	0.89	1.04	18.79	14.72
Tb	0.234	0.238	0.471	0.344	0.151	0.176	1.898	1.543
Dy	1.15	1.16	2.47	1.76	0.96	1.08	7.79	6.56
Ho	0.212	0.213	0.494	0.352	0.218	0.238	1.271	1.067
Er	0.54	0.54	1.26	0.83	0.71	0.80	2.95	2.44
Tm	0.08	0.07	0.18	0.13	0.13	0.15	0.38	0.32
Yb	0.51	0.50	1.21	0.87	1.06	1.18	2.39	1.93
Lu	0.08	0.07	0.19	0.14	0.21	0.23	0.33	0.27
Hf	3.23	3.32	4.32	3.93	2.57	2.30	8.27	5.47
Ta	0.59	0.56	0.39	0.38	0.55	0.59	0.83	0.44
Pb	28.6	29.4	20.7	28.3	26.2	35.2	20.8	12.9
Th	6.28	6.83	9.47	9.51	4.59	4.32	41.81	29.32
U	1.13	0.97	2.00	1.93	0.89	0.81	2.90	1.43
A/CNK	1.08	1.06	0.84	1.01	1.20	1.05	0.67	0.68

Gd/Yb	3.3	3.6	3.1	3.2	0.8	0.9	7.9	7.6
La/Yb	51.2	57.5	35.7	50.1	8.6	9.2	126.5	110.6
T_{Zr}(°C)	758	755	735	756	737	716	757	707

Sample No	**13JD040F**	**13JD040G**	**13JD057A**	**13JD057B**	**13JD057C**	**13JD057D**
Unit	**Dioritic intrusion**	**Dioritic intrusion**	**Guojialing**	**Guojialing**	**Guojialing MME**	**Guojialing MME**
SiO2	58.94	61.41	70.65	69.67	53.15	46.48
Al2O3	16.90	17.22	14.85	15.30	15.08	14.49
TiO2	0.78	0.69	0.28	0.28	1.28	1.76
Fe2O3T	5.12	4.20	1.93	1.84	10.67	14.60
MgO	3.17	2.27	1.11	1.09	5.76	7.79
MnO	0.08	0.06	0.04	0.04	0.16	0.21
CaO	4.98	4.04	2.70	2.52	4.13	4.54
Na2O	4.23	4.30	4.48	4.18	3.49	2.84
K2O	4.03	4.30	2.91	4.05	4.01	4.69
P2O5	0.42	0.32	0.09	0.09	0.51	0.76
L.O.I	0.84	0.67	0.37	0.37	1.28	1.41
Total	99.48	99.48	99.42	99.42	99.52	99.56
Li	14.8	14.7	27.6	28.3	131.8	201.1
Be	2.4	2.1	2.8	2.3	2.9	2.9
P	1839	1388	491	500	2727	4157
Sc	10.1	7.3	3.2	3.3	11.5	14.8
Ti	4376	3750	1393	1373	6764	9201
V	78.6	60.4	27.0	27.7	129.0	181.2
Cr	78.46	43.40	29.19	33.41	108.90	157.50
Mn	573	429	253	251	1142	1515
Co	12.417	9.655	3.876	3.763	23.160	31.190

Ni	49.835	29.532	8.940	9.283	54.630	75.040
Cu	5.994	4.443	2.181	3.284	10.150	10.990
Zn	95.1	73.7	47.3	44.4	234.7	313.9
Ga	23.3	23.0	20.3	19.9	34.6	39.3
Ge	0.96	0.82	1.00	0.96	1.63	1.88
Rb	62.9	65.3	90.1	104.9	238.8	330.5
Sr	3087	3135	848	952	605	411
Y	26.10	21.10	6.04	6.17	15.81	20.85
Zr	303	300	113	137	350	340
Nb	11.84	11.08	4.89	4.76	14.53	19.53
Cs	0.586	0.550	5.768	4.007	15.060	18.410
Ba	6389	6943	845	1786	577	533
La	240.15	218.79	20.48	25.57	37.73	49.26
Ce	428.94	391.64	38.54	45.59	76.96	99.69
Pr	50.40	45.13	4.22	4.91	9.15	12.03
Nd	169.44	148.90	14.74	16.63	33.56	44.06
Sm	22.55	19.07	2.51	2.74	6.09	8.13
Eu	5.49	4.74	0.69	0.75	1.53	1.97
Gd	13.47	11.03	1.82	1.90	4.34	5.73
Tb	1.392	1.153	0.237	0.245	0.586	0.776
Dy	5.90	4.84	1.15	1.22	2.93	3.86
Ho	0.977	0.801	0.214	0.227	0.548	0.726
Er	2.22	1.81	0.58	0.59	1.52	1.95
Tm	0.28	0.24	0.08	0.08	0.21	0.27
Yb	1.77	1.49	0.54	0.55	1.37	1.80
Lu	0.25	0.21	0.09	0.09	0.23	0.29
Hf	7.16	6.91	3.27	3.86	9.40	9.25
Ta	0.59	0.53	0.29	0.29	0.71	0.94
Pb	30.6	30.5	34.1	37.9	21.1	23.4
Th	35.74	33.41	8.65	9.86	15.42	19.91
U	2.23	2.23	1.14	1.47	2.51	2.73

A/CNK	0.83	0.90	0.96	0.97	0.86	0.81
Gd/Yb	7.6	7.4	3.3	3.5	3.2	3.2
La/Yb	135.6	146.8	37.8	46.6	27.5	27.4
T_{Zr}(°C)	789	805	746	761	799	770